Theoretical Investigations of Novel Materials for Nitrogen Fixation

Howalt, Jakob Geelmuyden

Publication date:
2013

Document Version
Publisher's PDF, also known as Version of record

Jakob Geelmuyden Howalt

Theoretical investigations of novel materials for nitrogen fixation

Submitted in candidacy for the degree Doctor of Philosophy

Supervisors
Tejs Vegge, DTU Energy Conversion
Thomas Bligaard, SLAC National Accelerator Laboratory

Theoretical investigations of novel materials for nitrogen fixation

Author
Jakob Geelmuyden Howalt
E-mail: jhow@dtu.dk

Supervisors
Prof. Tejs Vegge
Atomic scale Modeling and Materials
DTU Energy Conversion and Storage
Technical University of Denmark
E-mail: teve@dtu.dk

Deputy Director, Senior Staff Scientist, Dr. Thomas Bligaard
SUNCAT Center for Interface Science & Catalysis
SLAC National Accelerator Laboratory
Stanford University
E-mail: bligaard@stanford.edu

Atomic Scale Modeling and Materials,
DTU Energy Conversion and Storage
Technical University of Denmark
Frederiksborgvej 399
DK-4000 Roskilde
Denmark

www.ecs.dtu.dk
Tel: (+45) 46 77 58 00
E-mail: info@ecs.dtu.dk

Center for Atomic-scale Materials Design,
DTU Physics
Technical University of Denmark
Fysikvej 311
DK-2800 Kongens Lyngby
Denmark

www.camd.dtu.dk
Tel: (+45) 45 25 32 24
E-mail: info@camd.dtu.dk

Release date: August 31st, 2013

Abstract

This thesis is dedicated to the investigation and design of new catalyst materials for electrochemical ammonia production and especially the properties of the under-coordinated reaction sites on nanoparticles has been studied in great detail. Additionally, a universal transition state relation governing a large number of (de)hydrogenation reactions has been developed. The approach throughout the work is to use Density Functional Theory (DFT) to understand chemical reactions occurring at surfaces.

I present an analysis of the transition state energies for 249 hydrogenation/dehydrogenation reactions of atoms and simple molecules over close-packed and stepped surfaces as well as nanoparticles of transition metals. Linear energy scaling relations are observed for the transition state structures leading to transition state scaling relations for all the investigated reactions. With a suitable choice of reference systems the transition state scaling relations form a universality class that can be approximated with one single linear relation describing the entire range of reactions over all types of surfaces and nanoclusters.

Theoretical studies of producing ammonia electrochemically at ambient temperature and pressure without direct N_2 dissociation are presented. The computational hydrogen electrode was used to calculate the free energy profile for the reduction of N_2 admolecules and N adatoms with an applied potential on transition metal nanoclusters in contact with an acidic electrolyte.

In a study, the extreme under-coordinated M12 nanocluster was used as a model system for very under-coordinated reaction sites. The work resulted in establishing linear scaling relations for reaction intermediates for the *dissociative* and the *associative* reaction mechanism, and for the key adsorbates hydrogen and nitrogen. These scaling relations and free energy corrections are used to establish volcanoes describing the onset potential for electrochemical ammonia production and hence describe the potential determining steps for the electrochemical ammonia production. The competing hydrogen evolution reaction has also been analyzed for comparison. The most promising candidates from this study were found to be Mo and Fe which would require potentials of -0.5 V to electochemically form ammonia. These metals still have a tight competition with hydrogen evolution reaction.

On the basis of the M12 study, a molybdenum nanocluster of 13 atoms in the cuboctahedral structure was analyzed. Pathways for electrochemical am-

monia production via direct protonation of N adatoms and N_2 admolecules was analyzed and the results was found to match the predictions from the M12 nanocluster study. Calculations presented here, show that N_2 dissociation at either nitrogen vacancies or a clean molybdenum particle, is unlikely to occur. The calculations suggest that nitrogen will be favored at the surface compared to hydrogen even at potentials used to produce ammonia and the Faradaic losses due to hydrogen evolution reaction should be low.

For electro-catalysts the presence of water is very difficult to avert. Water will give rise to oxygen adsorption on most surfaces and the oxygen atoms will occupy important surfaces sites, which results in a decrease or a total hindrance of other chemical reactions taking place at that site. We therefore present theoretical investigations of the influence of oxygen adsorption and reduction on a molybdenum nanocluster with the purpose of understanding the issues with oxygen poisoning the catalyst. The calculations show that the molybdenum nanocluster will preferentially bind oxygen over nitrogen and hydrogen. The potentials required to reduce oxygen off the surface are -0.72 V or lower for all oxygen coverages studied. Exposure of the molybdenum nanoclusters to air or water, should not be an issue, since it is possible to reduce oxygen blocking the active sites off the surface. At lower oxygen coverage, nitrogen molecules can adsorb to the surface and electrochemical ammonia production at potentials between -0.45 V and -0.7 V are observed.

My conclusion is that the molybdenum nanocluster should be a good electrocatalyst for electrochemical ammonia production at ambient conditons. This should open for another pathway for the production of ammonia.

Resumé

Denne afhandling omhandler undersøgelse og design af nye katalysatorer til elektrokemisk produktion af ammoniak, og især indflydelsen af de under-koordinerede reaktionssteder på nanopartikler er blevet udførligt undersøgt. Derudover er der blevet udviklet en universel overgangstilstandsenergirelation for et stort antal (de)hydrogeneringsreaktioner. Den gennemgående tilgang for hele arbejdet har været brugen af tætheds-funktional-teori (DFT) med henblik på at forstå kemiske reaktioner på overflader.

Jeg præsenterer en analyse af overgangstilstandsenergier for 249 hydrogeneringsog dehydrogeneringsreaktioner af atomer og simple molekyler på tætpakkede og step overflader samt nanopartikler af overgangsmetaller. Lineære energirelationer observeres for overgangstilstandsstrukturer, der fører til overgangstilstandsenergirelationer for alle de undersøgte reaktioner. Med et passende valg af referencesystemer vil overgangstilstandsenergirelationerne danne en universalitetsklasse. Denne klasse kan tilnærmelsesvis beskrives med en enkelt lineær sammenhæng, som dækker hele spektret af reaktioner på alle typer overflader og nanopartikler.

Der præsenteres teoretiske studier for elektrokemisk produktion af ammoniak ved stuetemperatur og atmosfærisk tryk uden at involvere den direkte dissociationsreaktion af N_2. I undersøgelsen er den beregningsmæssige brint-elektrode blevet anvendt til at beregne den frie energi-profil for reduktion af adsorberede N_2 molekyler og adsorberede N atomer på nanopartikler af overgangsmetaller, der er i kontakt med en sur elektrolyt.

Der er blevet udført en undersøgelse af den ekstremt under-koordinerede M12 nanopartikel, som har fungeret som et modelsystem for meget underkoordinerede reaktionssteder. Arbejdet resulterede i dannelsen af lineære energirelationer for reaktions mellemprodukter for den *dissociative* og den *associative* reaktion, samt energirelationer for de vigtige adsorbater brint og kvælstof. Energirelationerne og beregnede fri-energi korrektioner er blevet brugt til at etablere vulkaner, som beskriver det påkrævede potential for elektrokemisk ammoniakproduktion. Denne metode påviser, hvilke reaktionstrin som er potentialbestemmende for den elektrokemiske ammoniakproduktion. Til sammenligning er den konkurrerende brintudviklings-reaktion også blevet analyseret. De mest lovende kandidater fra denne undersøgelse var molybdæn og jern, der kræver et over potential på omkring -0,5 V for elektrokemisk ammoniakproduk-

tion.

På grundlag af undersøgelsen om M12 model systemet er en molybdæn nanopartikel bestående af 13 atomer i den cuboctahedral struktur blevet analyseret. På denne partikel er der blevet undersøgt adskillige reaktionsveje, som elektrokemisk kan producere ammoniak. De undersøgte reaktionsveje er en direkte protonisering af adsorberede kvælstof atomer og molekyler med sammenlignelige potentialer med de i M12 undersøgelsen påviste potentialer. Beregninger præsenteret i denne afhandling viser, at kvælstof dissociation for kvælstof adsorberet på enten ledige kvælstof adsorptionssteder for en delvist kvælstof dækket molybdæn nanopartikel eller på rene molybdæn partikler er usandsynlig. Beregningerne tyder på, at kvælstof i forhold til brint vil være det favoriserede adsorbat på overfladen, også selv ved potentialer op til -0,8 V. Dette indikere, at den elektrokemiske effektivitet vil være relativ høj som følge af en formodet lav brintudvikling.

Ved brugen af våde elektrolytter er det meget vanskeligt at forhindre tilstedeværelsen af vand. Når vand kommer i forbindelse med katalytiske overflader vil det oftest give anledning til ilt adsorption og iltatomerne vil besætte vigtige overflader adsorptionssteder, hvilket resulterer i en reduktion eller total hindring af andre kemiske reaktioner som kunne have fundet sted her. Vi har derfor præsenteret undersøgelser af adsorption og reduktion af ilt på molybdæn nanopartiklen med henblik på at forstå egenskaberne for ilt forgiftning af overfladerne på katalysatorer. Beregningerne viser, at molybdæn nanopartiklen fortrinsvis vil binde ilt i forhold til kvælstof og brint. Potentialerne der er nødvendige for at kunne reducere ilt fra overfladen er -0,72 V eller lavere for alle undersøgte ilt dækningsgrader. Eksponering af molybdæn nanopartikler med luft eller vand, bør derfor ikke være et problem, da det er muligt at reducere ilt af overfladen. Det er også fundet, at selv ved lavere ilt dækning, kan kvælstof molekyler adsorbere til overfladen og elektrokemisk ammoniak produktion er muligt for potentialer mellem -0,45 V og -0,7 V.

Vores konklusioner er, at molybdæn nanopartikler vil være en rigtig god elektrokatalysator for elektrokemisk ammoniakproduktion ved stue temperatur og atmosfærisk tryk. Vi har derved vist, at en anden måde at producere ammoniak er muligt.

Preface

This thesis is submitted in candidacy for the Ph.D. degree from the Technical University of Denmark (DTU) and is based on work that has been carried out between September 2010 and August 2013 at the Department of Energy Conversion and Storage and Center for Atomic-scale Materials Design at Department of Physics and with an external stay at SUNCAT Center for Interface Science & Catalysis, SLAC National Accelerator Laboratory, Stanford, CA, USA.

The project was supervised by Professor and Head of Section for Atomic Scale Modeling and Materials at the Department of Energy Conversion and Storage, Tejs Vegge, and co-supervised by Deputy Director and Senior Staff Scientist at SUNCAT Center for Interface Science & Catalysis, Thomas Bligaard.

The work was financially funded by the Catalysis for Sustainable Energy (CASE) initiative, that is funded by the Danish Ministry of Science, Technology and Innovation. I would also like to thank the Danish Center for Scientific Computing for access to the supercomputer at DTU and civil engineer Frants Allings Grant for kindly supporting my research visit at SLAC, Stanford financially.

First and foremost, I would like to thank my supervisor Tejs Vegge for his positive attitude, the never ending stream of suggestions and ideas for what to investigate and his ability to always keep me focused on the essential. I would also like to thank my co-supervisor Thomas Bligaard for his hospitality at SLAC, for his guidance and expertise and not the least for convincing me to start this adventure years ago.

Thanks to the computer staff Ole, Marcin and Jens Jørgen at CAMD, for always keeping Niflheim crunching and for help on software related issues.

I would also like to thank my office mates and colleagues through the years at DTU and at SLAC. I thank you all for interesting and entertaining discussions and the social activities we did together. Furthermore, I thank you for inspiring work related discussions, help on literature searches, computational methods, and a never ending contribution to a good working environment. Special thanks go to Vladimir, Jon Steinar, Steen, and Peter for the help with proof-reading of the thesis. Thank you also, Lene Danielsen, for always helping out with a smile.

My warmest thanks to my friends and family who have been an extraordinary support for me in these times with their love and encouragements.

Last, but not the least, Dorthe, thank you for all your support, patience and good times home and abroad. More to come.

Kgs. Lyngby, August 2013
Jakob Geelmuyden Howalt

Contents

List of Figures

List of Tables

Chapter 1

Introduction

In the past decade, it has become more apparent than ever that mankind needs to move towards more sustainable energy consumption with significantly smaller carbon foot print per capita. In Denmark there is a large political force pushing the country towards more renewable energy as the Danish Government in 2011 released its energy policy for the coming decades. The goal is to make Denmark independent of fossil fuels by 2050 [1].

There are a number of possible ways that could potentially be used to reduce the global carbon foot print and a number of technologies have already been implemented to generate electrical power more or less sustainable, such as for example wind turbines, solar cells, biomass fired power plants, etc. With time, some of these may become economically competitive with fossil resources. A more difficult problem to address is that of substituting transportation fuels. To make sustainable transportation fuels economically viable, one needs not only a inexpensive way to harvest a sustainable source of energy, but also to store the energy in a convenient form with a high enough volumetric and gravimetric energy densities, and in a form that can easily be transferred to vehicles. Since catalysis can facilitate the efficient synthesis of chemicals with high energy contents, it will play a key role in many of the potential scenarios for reducing our dependence on fossil resources. Fig. 1.1 presents the different routes to create fuel from renewable energy sources, all of which have been thoroughly studied in the research initiative 'Catalysis for Sustainable Energy' (CASE) at the Technical University of Denmark.

1.1 Ammonia synthesis

One chemical compound of great versatility is ammonia. Ammonia is primarily used for making fertilizers, ultimately sustaining roughly two-fifth of the World's population [2, 3].

> What is the most important invention of the twentieth century? Aeroplanes, nuclear energy, space flight, television and computers will be the most common answers. Yet none of these can match

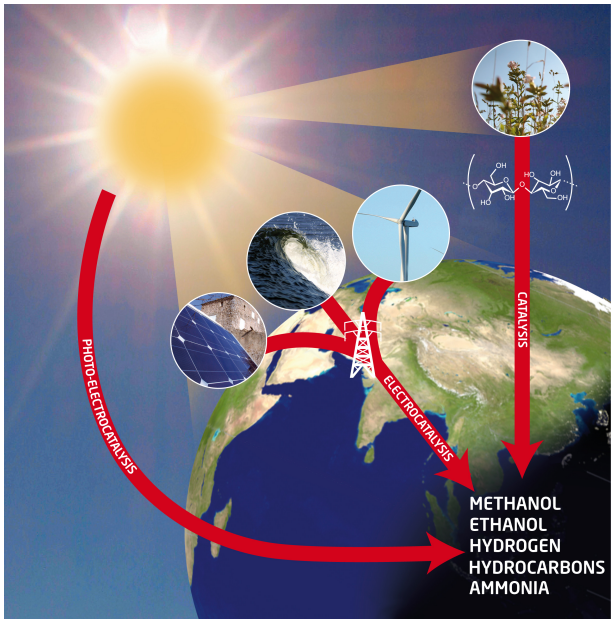

Figure 1.1: *The energy coming from the sun is orders of magnitude larger than the human energy consumption and there are several different pathways of harvesting it. One route is through biomass production (top right) and reforming it into a useful fuel. The second route is conversion of electricity created by photovoltaic cells, windmills or wave energy into fuel. The last pathway (lower left) is the combination of photovoltaics and electrocatalysis to create fuel in a one step reaction and should lower the loss due to energy transformation from one type to another in one step, but is significantly more difficult to master due to increased material requirements and other constraints.*

> the synthesis of ammonia from its elements. The world might be better off without Microsoft and CNN, and neither nuclear reactors nor space shuttles are critical to human well-being. But the world's population could not have grown from 1.6 billion in 1900 to todays six billion without the Haber-Bosch process.
> Vaclav Smil, Nature, 1999 [2]

In terms of reducing the carbon foot print, ammonia is interesting for a number of reasons. First, there is a potential for improving the sustainability of the already huge industrial catalytic production of ammonia, which is on the order of over 100 million metric tons annually, and responsible for 1-2% of the global energy consumption. Secondly, ammonia is becoming increasingly interesting as a potential transportation fuel [4, 5]. As an energy carrier, ammonia has the benefit that it can be used in fuel cells such as the solid oxide fuel cell (SOFC) or a direct ammonia fuel cell (DAFC). Furthermore, it has an interesting feature of not emitting CO_2, while having a high energy density that is comparable with traditional fossil fuels, both volumetrically and gravimetrically [4, 6]. A highly energy-efficient method for the synthesis of ammonia (NH_3) from molecular nitrogen (N_2) in air is therefore desirable.

Currently, ammonia synthesis is achieved by the Haber-Bosch process that initially dissociates the N_2 bond and then protonates each nitrogen atom [7]. This is the so-called *dissociative mechanism*. The Haber-Bosch process is energy-

intensive and centralized due to the high required temperature and pressure because of the very difficult task of splitting the nitrogen molecule at the catalyst surface. Production of ammonia therefore require facilities that are capable of facilitating high pressures of 150-250 bar and temperatures of between 300-550 °C efficiently [3, 7, 8]. This can be achieved at large production plants and together with required essential infrastructure the building of these plants are associated with very high capital costs. In contrast, the natural enzymatic process in Nitrogenase takes place at room temperature by initially weakening the N-N bond through successive protonations until the dissociation barrier is low enough that the N-N bond breaks; this process is referred to as the *associative mechanism* [9]. Furthermore, the enzyme Nitrogenase utilizes an electrochemical reduction of the nitrogen molecule to produce ammonia at the active site, the iron-molybdenum cofactor [10], and it is a completely different pathway. However, Nitrogenase is also a very good hydrogen evolution catalyst.

What we aim for is the electricity-based production of ammonia utilizing electrochemistry, thus allowing small production scales and the use of renewable energy sources like windmills or solar cells. The issue with windmills and solar cells, is that storing the excess electricity when the electricity production exceeds the demand is crucial to fully cover the energy demand at all times. When the demand exceeds the production the stored energy can be used to cover the gap. We see ammonia as an excellent fuel, both because of the energy densities, storage capabilities [4,5] and because of the interplay with electricity production coming largely by unreliable but renewable energy sources.

Over the years, numerous experimental studies [8, 11–24] and theoretical studies [10, 25–36] have examined ammonia synthesis, and they offer excellent insight into the challenges faced when developing new catalytic materials for this reaction. It has been shown in previous studies that ammonia synthesis is very structure sensitive and primarily occurs on the surface steps of Fe and Ru [25, 37, 38]. One could expect the associative mechanism to be even more structure sensitive. The competing hydrogen evolution reaction (HER) is structure insensitive [39], and we have therefore looked at highly under-coordinated nanoclusters as a way to overcome the problem of losing efficiency to HER.

Furthermore, it has been shown that a similar reaction, CO oxidation, can be performed on transition metal nanoparticles consisting of more noble metals at lower temperature [38, 40] than traditionally-used catalysts for this reaction. The results show that, in general, nanoparticles can actually be useful if one wants to examine new material surfaces to alter the reaction kinetics.

1.2 Density functional theory

The most successful theory to determine the electronic structure of systems of particular interest for heterogeneous and electro catalysis is density functional theory (DFT). The strength of DFT lies in the trade-off between accuracy and demand for CPU time. In the research fields of chemistry, physics and material science the success of density functional theory has been recognized by a Nobel prize in 1999 to the founder, Walter Kohn [41].

The improvements to density functional theory and the continued advances

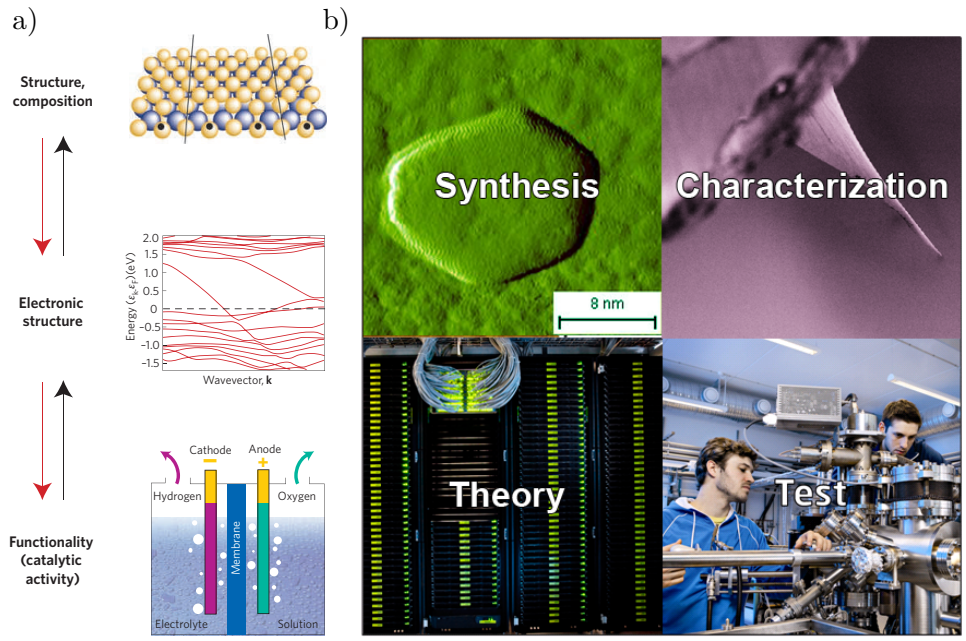

Figure 1.2: *The work flow using density functional theory as a tool to gain insight into chemistry, physics and material science. a) shows how the electronic structure is the link between the functionality and the material structure and composition. Adapted from [42]. b) shows the crucial role theory plays in the work flow employed in the research initiative 'Catalysis for Sustainable Energy' (CASE) at the Technical University of Denmark to find new catalytic materials.*

to computer power extending Moore's law, the basis for catalyst design based on theoretical leads, is becoming reality [42]. Fig. 1.2 shows the key role density functional theory plays in present day research; the specific catalytic properties one can obtain (Fig. 1.2a) from DFT calculations and the interplay with experimentalists (Fig. 1.2b) in the design loop. Theoretical calculations in the form of density functional theory can determine catalytic properties of materials for both heterogeneous catalysis and electrocatalysis; adsorption energy of reaction intermediates, activation barriers, stability of catalysts, diffusion barriers, vibrational calculations to obtain the entropy and zero point energy corrections using statistical physics. Some of these properties can be simplified in linear scaling relations and thereby DFT starts to have a predictive power. The obtained information can be used either to tailor the material structure and/or the composition to improve the desired functionality. This can be achieved through screening or genetic algorithm studies within the DFT framework. In many cases the simplistic approaches utilized in present day DFT studies and the continuing limitation to the model system size due to the scaling of computer demand, one can describe and understand the key reaction mechanism of many reactions. But the complexity of the unsolved problems calls for increased collaboration between the experimental and theoretical disciplines. In many high profiled research topics the interplay between theory and experimentalist is of paramount importance, because both research approaches can provide valuable information that are inaccessible with other tools.

1.3 Outline of the Thesis

Chapter 2 will introduce the fundamental aspects of DFT. The implementation of DFT that has been used in this work is the code `GPAW`, that is based upon the real-space-based projector augmented-wave method. Some of the methods used within the atomic simulation environment (`ASE`) will be briefly explained.

Chapter 3 will theoretical methods through which the reactivity of surfaces can be described and introduce relations which simplify modeling of reactions on surfaces. Here, the results from the Newns-Anderson model will be presented and the consequences on the surface reactivity will be described by the d-band model. Other relations such as linear scaling relations and the Brøndsted-Evans-Polanyi relation will be addressed.

Chapter 4 presents the electrochemical cell required to produce ammonia electrochemically. The chapter will also describe the reaction pathways that have been simulated and how the proton and electron transfer reactions are modelled using the computational hydrogen electrode.

Chapter 5 will present an extensive study of (de)hydrogenation reactions performed on a large number of metals and surfaces. The study shows a universal transition state scaling relation for (de)hydrogenation reactions for intermediates containing nitrogen, oxygen or carbon atoms.

Chapter 6 will present a study, which investigates the role of under-coordinated sites for electrochemical formation of ammonia on a model system. For this model system, linear scaling relations will be determined and used to make a volcano describing the onset potential for electrochemical ammonia formation at ambient conditions.

Chapter 7 will present a study on the molybdenum nanocluster used to examine the electrochemical production of ammonia. The chapter will discuss coverage effects of nitrogen and hydrogen, the competition between hydrogen and nitrogen and the potentials required for forming ammonia.

Chapter 8 will present a study of the oxygen presence on the molybdenum nanocluster. The adsorption free energies of oxygen will be compared to the adsorption free energies presented in chapter 7 of nitrogen and hydrogen. The reduction of oxygen off the molybdenum nanocluster will be discussed for the following cases: oxygen acting as a contaminator, a pure oxygen skin and oxygen skin with nitrogen molecules present. The electrochemical production of ammonia is considered at low oxygen coverages.

Chapter 9 will give an outlook of the work presented in this thesis.

List of Included Publications

The included papers do not contain additional information to the material presented in the chapters 5-8.

Paper A

Universal transition state scaling relations for (de)hydrogenation over transition metals
Wang, Shengguang; Petzold, Vivienne; Tripkovic, Vladimir; Kleis, Jesper; Howalt, Jakob Geelmuyden; Skúlason, Egill; Fernández, Eva M.; Hvolbæk, Britt; Jones, Glenn; Toftelund, Anja; Falsig, Hanne; Björketun, Mårten; Studt, Felix; Abild-Pedersen, Frank; Rossmeisl, Jan; Nørskov, Jens K.; Bligaard, Thomas.
Phys. Chem. Chem. Phys., Vol. 13, No. 46, 2011, p. 20760-20765.

Paper B

DFT based study of transition metal nano-clusters for electrochemical NH_3 production
Howalt, Jakob Geelmuyden; Bligaard, Thomas; Rossmeisl, Jan; Vegge, Tejs.
Phys. Chem. Chem. Phys., Vol. 15, 2013, p. 7785-7795.

Paper C

Electrochemical ammonia production on molybdenum nitride nanoclusters
Howalt, Jakob Geelmuyden; Vegge, Tejs.
Phys. Chem. Chem. Phys., *accepted*

Paper D

The role of oxygen and water on molybdenum nanoclusters for electro catalytic ammonia production
Howalt, Jakob Geelmuyden; Vegge, Tejs.
submitted, 2013.

List of Publications Not Included

Bookchapter

Computational design of catalysts , electrolytes and materials for energy storage
T. Vegge, J. G. Howalt, S. Lysgaard, J. S. G. Mýrdal, N. Bork, and J. S. Hummelshøj
New and future developments in catalysis: Batteries, hydrogen storage and fuel cells
ed. S. L. Suib, Elsevier, (2013)

Chapter 2

Density Functional Theory and Computational Methods

2.1 Overview

To understand chemical reactions on metallic surfaces, where the adsorption and reactivity depends on the electronic structure a framework is needed to determine the electronic structure. To describe the electronic structure using computational methods, one can use and implement the fundamental physical theories of quantum mechanics. One approach is to employ density functional theory (DFT) to obtain the electronic structure. This approach has been used intensively to gain insight into chemical reactions on surfaces [42]. It is possible to evaluate the complete kinetics for chemical reactions based solely on DFT calculations; one can obtain reaction energies and enthalpies, entropies for adsorbed reaction intermediates and activation barriers [33, 43]. Recent improvements to DFT have greatly enhanced its ability to be used for computer based catalyst design [44]. The accuracy of computational methods is now of such quality that computational methods can be used to capture trends in reactivity of e.g. transition metal surfaces.
This chapter will present the fundamental equations for density functional theory. All work presented in this thesis is based on the density functional theory implementation in the code `GPAW` [45, 46]. In addition important tools implemented in the atomic simulation environment `ASE` [47] will be briefly presented.

2.2 Quantum Calculations

At nanometer scale quantum mechanics describes the dominating phenomena. The mutual interactions of electrons and the nuclei describe the chemical properties of atoms and molecules in this region and are dominant over the Newtonian forces. The quantum mechanic interactions are described by the Hamiltonian operator, which depends on the electronic and ionic degrees of freedom. For systems of already just a few atoms, this operator is too complex, and approx-

imations are therefore necessary for it to be solved computationally. Since the mass of the electrons is much lower than the mass of the nucleus, the Born-Oppenheimer approximation can be used to decouple the electronic and ionic contributions. In the Born-Oppenheimer approximation the electronic part is solved first while the nuclei are held fixed [48, 49]. This leads to an electronic many-body problem that must obey the Schrödinger equation

$$\widehat{H}\Psi = E\Psi. \tag{2.1}$$

In Eq. 2.1 the many-body wavefunction $\Psi = \Psi(\mathbf{r}_1, \mathbf{r}_2, ..., \mathbf{r}_N)$ depends on the spatial coordinates $\mathbf{r}_i$ and excludes the spin variable for the electrons. The Hamiltonian for this system is given by

$$\widehat{H} = \sum_{i=1}^{N}(-\frac{1}{2}\nabla_i^2) + \sum_{i=1}^{N} v_i + \sum_{i<j}^{N} \frac{1}{|\mathbf{r}_i - \mathbf{r}_j|}. \tag{2.2}$$

The first term is the kinetic energy operator, while the second term is the external potential that arises from the attractive interaction between the nuclei and the electrons where $v(\mathbf{r}_i) = -\sum_A \frac{Z_A}{|\mathbf{r}_i - \mathbf{r}_A|}$. Here, $\mathbf{r}_A$ is the spatial coordinates and Z_A is the charge of the nuclei. The last term accounts for electron-electron interactions.

Solving the many-body problem exactly with respect to the wavefunctions is in practice impossible for systems consisting of more than few atoms. Many approximations exist for solving the electronic problem; however, most of them are extremely computationally demanding.

2.2.1 Density functional theory

An alternative approach to solving the Schrödinger equation exactly was proposed in the Hohenberg-Kohn theorem in 1964 by Hohenberg and Kohn, which states that there is a one-to-one correspondence between the electronic density of the ground state and the external potential [50]. This means that all physical quantities that can be derived from a given Hamiltonian depend on the electronic density $n(\mathbf{r})$. A re-formulation of the Schrödinger equation with the energy as a functional of the electron density can therefore be written as,

$$E[n_0] = \langle \Psi[n_0] | \widehat{H} | \Psi[n_0] \rangle. \tag{2.3}$$

They also showed that the ground state energy, E_0, will always be equal to or lower than the energy from any trial density. The groundstate energy, E_0, can be found in a variational way,

$$E_0 = \min_n E[n]. \tag{2.4}$$

This method uniquely yields the ground state density and is hence a ground state theory. Therefore, more advanced methods must be taken to describe other physically interesting properties such as excited states and time dependent phenomena.

In 1965, the Kohn-Sham Ansatz proposed a practical way to determine the ground state density [51]. The basic principle is to replace the original many-body problem with an auxiliary independent particle problem. The assumption here is that the ground state density of the original interacting system is equivalent to the ground state density of the non-interacting system. This results in the Kohn-Sham equations, which can be seen below,

$$\widehat{h}_s[n(\mathbf{r})]\Psi_n(\mathbf{r}) = \epsilon_n \Psi_n(\mathbf{r}) \tag{2.5}$$

where the single particle Kohn-Sham hamiltonian is,

$$\widehat{h}_s[n(\mathbf{r})] = -\frac{1}{2}\nabla^2 + v_{ext}(\mathbf{r}) + v_H[n](\mathbf{r}) + v_{XC}[n(\mathbf{r})] \tag{2.6}$$

The first term represents the kinetic contribution, the external potential is given by v_{ext}, and the Hartree potential is given by v_H, as shown below:

$$v_H[n(\mathbf{r})] = \int d^3\mathbf{r}' \frac{n(\mathbf{r}')}{|\mathbf{r} - \mathbf{r}'|}. \tag{2.7}$$

The last term, the exchange-correlation potential, $\mathrm{v_{XC}}(\mathbf{r})$, has the form,

$$v_{XC}[n(\mathbf{r})] = \frac{\partial E_{XC}[n(\mathbf{r}')]}{\partial n(\mathbf{r})}. \tag{2.8}$$

To this point, the density functional theory formalism is exact, but the difficult part, $E_{XC}[n(\mathbf{r})]$, is yet to be discussed.

XC-functionals

In principle the Kohn-Sham scheme is exact, if one could find an expression for the exchange-correlation functional. In this approximation, the derivation of the ground state energy is limited by the accuracy of v_{XC}. In principle it should be possible to find the exact exchange-correlation functional but in practice it has not been possible to determine it. The exchange-correlation energy functional is given by:

$$E_{XC}[n] = \frac{1}{2}\int\int d^3r d^3r' \frac{\bar{n}_{XC}(r, r')n(r)}{|\mathbf{r} - \mathbf{r}'|} \tag{2.9}$$

Here $\bar{n}_{XC}(r, r')$ is the average exchange-correlation hole. The average exchange-correlation hole is given by $\bar{n}_{XC}(r, r') = \int_0^1 d\lambda n^{\lambda}_{XC}(r, r')$, where λ is the coupling strength: the non-interacting system has a λ value of 0 and the fully interacting system has a λ value of 1.

The depletion of electrons around a single electron gives rise to $\bar{n}_{XC}(r, r')$, because an electron at position r repulses other electrons close to the position r and the probability of finding other electrons near r is hence reduced. This is a consequence of the Pauli exclusion principle and gives rise to the sum rule: The integration of $\bar{n}_{XC}(r, r')$ over all space gives -1 and the electron hole has numerically the same charge but with an opposite sign as the electron.

In the following, approximations to the exchange-correlation functional, will be presented.

Local Density Approximation, LDA

The first and most simple approximation is the Local Density Approximation [51] or LDA. Here the local environment around the electrons, the exchange-correlation hole, is set to resemble that of the uniform electron gas with the same density.

$$E_{XC}^{LDA}[n] = \int n(\mathbf{r})\epsilon_{XC}(n(\mathbf{r}))d\mathbf{r} \tag{2.10}$$

The approximation should only work for slow varying densities, but it has worked very well in many cases. LDA obeys the sum rule and the spherical averages used for E_{XC} have made LDA rather successful. But for chemical properties the LDA functional lacks in accuracy. It tends to have issues with over-binding [52].

Generalized Gradient Approximation, GGA

Where LDA only takes the average density into consideration, the Generalized Gradient Approximation also includes the gradient. The GGA takes care that the sum rule is fulfilled.

$$E_{XC}^{GGA}[n] = \int n(\mathbf{r})\epsilon_{XC}(n(\mathbf{r}), \nabla n(\mathbf{r}))d\mathbf{r} \tag{2.11}$$

LDA can be seen as the first order approximation with an universal form, GGA is the second order approximation and its implementation is not universal. This has given rise to many GGA functionals; PW91 [53], PBE [54], revPBE [55], and RPBE [44] are some examples. The main differences between these functionals are in the implementation of the local enhancement factor and their form. Some of the GGA's fulfill the local Lieb-Oxford bound [56], while others do not. Strictly fulfilling the Lieb-Oxford bound is not required, but theoretically it ties the approximation together more as a whole. The GGA functionals describe with varying efficiency physical properties, some excel in one area, while others excel in others.

One can include even more complexity to the exchange-correlation functional, and the increase in complexity is denoted as the 'Jacobs ladder of density functional approximations for the exchange-correlation energy' by Perdew and Schmidt in 2000 and the ladder can be seen on Fig. 2.1.

Jacob's ladder of density functional approximations

Applying GGA one soon realizes that the approximation describes many systems inadequately. Among some examples, the band gab (DFT a ground state theory - do not describe excited states), adsorption due to van der Waal forces, delocalization of states that should be localized (charged vacancies) etc. To describe such physical properties the route of increasing the complexity of the exchange-correlation functional has been pursued. The increasing complexity also increases the computational cost.

In meta-GGA the second derivative of the density ($\nabla^2 n(\mathbf{r})$) or the orbital kinetic energy density $\tau(\mathbf{r})$ is included. The last two steps on Jacob's Ladder are exact exchange (EEX) in various forms. These approximations are classes

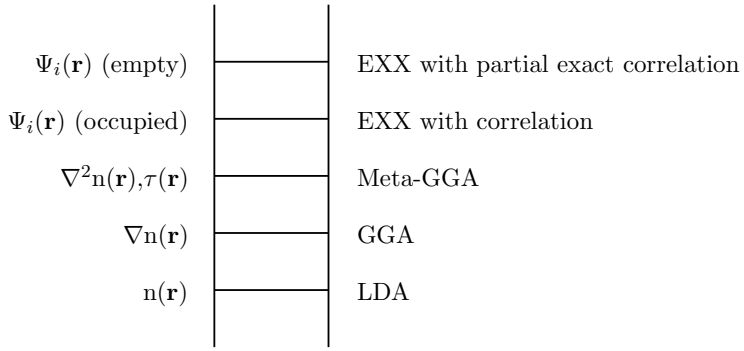

Figure 2.1: *Jacobs ladder of density functional approximations for the xc energy.* Adapted from [57]

of hybrid functionals that implement a portion of exact exchange from Hartree-Fock theory [58, 59] to the exchange-correlation energy functional. They are expressed in terms of the Kohn-Sham orbitals instead of the density. The SIC method [60] tries to correct for the unphysical self-interactions that is present in many functionals for exchange and correlation. The LDA + U [61] is method that uses a Hubbard U to add the orbital-dependent interactions on the basis of LDA or GGA type calculations.

2.3 Atomic forces

Density functional theory determines the electronic structure of a given atomic configuration. In most cases, the newly established electronic structure is determined for a positioning that is not at its local minimum at the potential energy surface and determining the local minima is crucial to model physical properties. Forces, similar to real world forces, can be used to point the system towards the configuration with lowest potential energy and forces is the negative gradient of the energy [62–64],

$$F(\mathbf{r}) = -\nabla E(\mathbf{r}). \tag{2.12}$$

Many various techniques exist for performing minimizations in as few iterations as possible. Some use the curvature of a given point and assume quadratic environment [65], while others adjust the step size simulating velocity [66] and yet others use the change in fictional velocity [67].

2.4 GPAW formalism

The calculations in this study, as previously stated, have been carried out using the `GPAW` code [68], which is a real-space-based implementation of the projector augmented-wave method (PAW) [69, 70]. The single-particle all electron wave-functions from the Hohenberg-Kohn formulation of DFT are used to describe the core, semi-core and valence states. Due to the orthogonality requirement, all electron wave functions, Ψ_n, oscillate strongly at the nucleus. Conversely, in the PAW method a smooth pseudo wave function, $\tilde{\Psi}_n$, is used instead in

this region and its implementation saves computational resources. The external potential is assumed not to influence the core states near the nucleus, which is referred to as the frozen core approximation. A linear transformation between the smooth pseudo wave functions and the all electron wave functions can be performed,

$$\Psi_n(\mathbf{r}) = \hat{\mathcal{T}}\tilde{\psi}_n(\mathbf{r}). \tag{2.13}$$

The transformation operator $\hat{\mathcal{T}}$ is given in terms of atom-centered all electron partial waves, $\phi_i^a(\mathbf{r})$, the corresponding smooth partial waves, $\tilde{\phi}_i^a(\mathbf{r})$, and the projector functions, $\tilde{p}_i^a(\mathbf{r})$. Here the partial waves expand the smooth pseudo waves near the nucleus and are given by,

$$|\tilde{\psi}_n\rangle = \sum_i \sum_n c_{ni}^a |\tilde{\phi}_i^a\rangle \tag{2.14}$$

and the projector functions close to the nucleus are given by

$$\langle \tilde{p}_{i1}^a | \tilde{\phi}_{i2}^a \rangle = \delta_{i1,i2}. \tag{2.15}$$

The transformation operator is given as

$$\hat{\mathcal{T}} = 1 + \sum_a \sum_i \left(|\phi_i^I\rangle - |\tilde{\phi}_i^a\rangle \right) \langle \tilde{p}_i^a |. \tag{2.16}$$

Here a is the index of a given atom, while the principal, angular and magnetic moment quantum numbers, are covered by the index i. Outside a cut-off radius, the atom-centered all electron and pseudo wavefunctions are identical.

The use of real-space grids in the GPAW code instead of plane waves enables efficient parallelization due to local and semi-local operations relative to the fast Fourier transformations of the plane waves (as implemented in e.g. the DACAPO plane wave code) that are non-local in nature. Furthermore, the real-space grid allows for the possibility to use non-periodic boundary conditions, whereas, the plane waves always require periodic boundary conditions. The accuracy of the real-spaced grid calculations can be improved by decreasing the grid spacing and increasing the k-point sampling [46].

2.5 Other computational method

In the previous section the fundamental theory of density functional theory and the implementation of those in the GPAW code have been described. The calculational methods used to calculate some of the key properties needed to describe the catalytic activity of studied systems: (1) how the optimization of the adsorbate position is carried out, (2) finding the minimum energy path, locating the transition state and determining the corresponding activation barrier, (3) definition of the adsorption energy, (4) how to calculate density of states, (5) calculating the vibrational frequencies which then can be used for free energy corrections.

2.5.1 Relaxation method

Modeling chemical reactions the (semi)-stable adsorption sites and positions are needed for the reaction intermediates. The bond lengths and bond angles vary for different metals and even the preferred adsorption site can change from metal to metal.

When determining how the reaction intermediates for ammonia synthesis or oxygen containing adsorbates will bind to the model surfaces, an guess for the initial position is used with a specific adsorption site (e.q. ontop, bridge, hollow), but the optimal angles and length have to be calculated. The work presented in this thesis has been carried out using two relaxation methods to optimize the position of the adsorbate on the surface, BFGS and FIRE [47,65,67]. A maximum force for these optimizers has been set to 0.05 eV/Å, and it is my experience that this value ensures stable configurations and very close to optimal adsorption energy. Using a lower maximum force will not significantly change the adsorption energy, deviations of only ±0.01 eV have been observed. A more strict choice for the maximum force would increase the requirements for computer power.

2.5.2 Determining activation barriers

A crucial part of determining whether a given surface will be a good catalyst or not is to determine the activation energies for all reaction steps. In the presented work two different methods have been used to calculate the activation energies: (1) the nudged elastic band method and (2) the bond stretching method.

Nudged elastic band method

The first method is a formal approach for finding a minimum energy path (MEP) between initial and final states, shown schematically in fig. 2.2. The MEP goes through a transition state, which is defined as the point where the energy is the highest on the MEP path. The transition state is a saddle point, an approximation in the harmonic transition state theory, on the potential energy surface and will therefore have the maximum energy along the reaction coordinate, while also being a minimum in all other directions. It is therefore not possible to determine transition states, or saddle points, using normal minimization methods.

The nudged elastic band method (NEB) is used to find the MEP. The NEB method was developed by Jónsson *et al.* [71,72] and will most often find the MEP if the initial and final states are given. As the initial guess in the NEB method, the initial and final states are connected with a linear chain of interpolated images. Between two adjacent images, which are points on the potential energy surface, a spring potential is applied. The total force of such system is

$$F(\mathbf{R}_1, \mathbf{R}_2, ..., \mathbf{R}_{N-1}) = \sum_{i=1}^{N-1} V(\mathbf{R}_i) + \sum_{i=1}^{N-1} \frac{k_{sp}}{2}(\mathbf{R}_i - \mathbf{R}_{i+1}). \tag{2.17}$$

The first term is the energy of the individual images while the second term is the energy from the spring that connects the images. The total energy of the

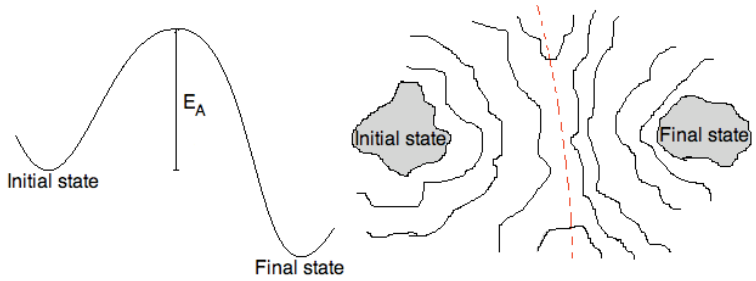

Figure 2.2: Left: a *1-D schematic description of an activation barrier between the initial and the final state. The activation energy for the forward reaction is marked by the energy difference, E_A, between the transition state (the point with the highest energy) and the initial state.* Right: *a 2-D schematic model of the potential energy surface around the initial and final state. The highest energy line between these states is marked with the dotted line. The transition state is a saddle point that has the highest energy in the reaction coordinate direction, while it also has the lowest energy on the dotted line between the initial and final states.*

system is then minimised until the magnitude of the forces along the chain of images is decreased below a specified tolerance. Using more images will describe the MEP in more details. We can see in fig. 2.3 how the images move from the starting chain (black colored line) to the MEP (red colored line). It is noted that because of the applied spring force the distance between the images does not need to be equally-spaced. The NEB method is computationally very demanding because the images are internally connected to each other and it require that all images are calculated for every step in method.

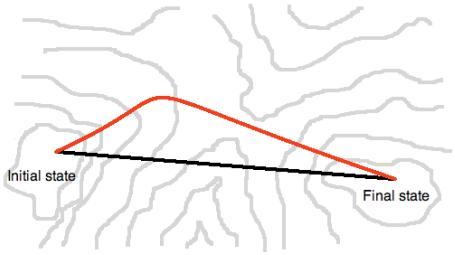

Figure 2.3: *The black colored line shows the initial chain of images before the nudged elastic band method has been applied. The red colored line shows the MEP determined from using the NEB. The distance between the images does not necessarily need to be equally-spaced.*

The bond stretching method

The bond stretching method forces a desired bond to break by fixing the distance between two of the adsorbate atoms and letting the species relax. Sequentially increasing the bond length and calculating the energies will map out the energy for a possible reaction path. The bond stretching method is much faster than the NEB method because a number of independent images along the reaction pathway are obtained quickly, compared to the NEB method where the images

are dependent on each other. Unfortunately, the bond stretching method does not always find the minimum energy path, whereas the NEB method more often does.

2.5.3 Adsorption energy

With DFT it is possible to calculate the adsorption energy, ΔE, of all intermediates of interest. In this study adsorbates containing nitrogen, hydrogen and oxygen have primarily been studied. For intermediates that do not contain oxygen, the adsorption energy is calculated with respect to the gas phase molecules of hydrogen and nitrogen and the studied metallic model system (close-packed, stepped, cuboctahedral Mo_{13} nanocluster or a M_{12} nanocluster) where the reaction is modeled:

$$\Delta E_{surf-N_xH_y} = E_{surf-N_xH_y^*} - (E_{surf} + \frac{x}{2}E_{N_2(g)} + \frac{y}{2}E_{H_2(g)}), \tag{2.18}$$

where $E_{surf-N_xH_y}$ is the calculated total energy of the combined system of the model system and the adsorbed N_xH_y adsorbates, E_{surf} is the calculated total energy of only the model system, while $E_{N_2(g)}$ and $E_{H_2(g)}$ are the calculated gas-phase energies of nitrogen and hydrogen molecules, respectively.

For oxygen containing adsorbates, there is a slight change with respect to the reference. The total energy of oxygen molecules has been reported to have a very high discrepancy compared to what is observed experimentally [73, 74], the reference here has therefore been set to H_2O. One here has to account for the extra hydrogen atoms in the reference and it carried out in this way:

$$\Delta E_{surf-N_xH_yO_z} = E_{surf-N_xH_yO_z} - (E_{sur} + \frac{x}{2}E_{N_2(g)} + \frac{y-2z}{2}E_{H_2(g)} + zE_{H_2O(g)}). \tag{2.19}$$

2.5.4 Density of states and d-band center

A very useful tool when seeking information about the reactivity of a given surface, is to determine the d-band center for a surface atom. According to the Newns Anderson model (see section B) and the d-band model (see section 3.4), an approximation for the reactivity of a given surface can be obtained when investigating the d-band. To calculate the d-band center the density of states of the metal is needed. Knowing the eigenvalues ϵ_n and the corresponding eigenvectors Ψ_n for a given system [75], the density of states is defined by

$$\rho(\epsilon) = \sum_n \langle \Psi_n | \Psi_n \rangle \delta(\epsilon - \epsilon_n).$$

When inserting a complete orthonormal basis, we can rewrite this as

$$\rho(\epsilon) = \sum_i \rho_i(\epsilon)$$

and in this study the density of states will be projected (PDOS) onto the atomic orbitals. The atomic orbitals have previously been introduced in the PAW transformation, see section 2.4, and will here be used to determine the density of states

for each of the orbitals (s, p, d, f). The PDOS will be calculated in the following way,

$$\rho_i^a(\epsilon) = \sum_n |\langle \tilde{p}_i^a | \tilde{\psi}_n \rangle|^2 \delta(\epsilon - \epsilon_n) \approx \sum_n |\langle \tilde{\phi}_i^a | \psi_n \rangle|^2 \delta(\epsilon - \epsilon_n)$$

The atomic all electron partial waves, $\tilde{\phi}_i^a$, do not form an orthonormal basis and the PDOS then gives a qualitative description of a local atomic DOS. The d-band center of the PDOS is calculated in the following way,

$$\epsilon_d = \frac{\int \rho_i^a(\epsilon)\epsilon d\epsilon}{\int \rho_i^a(\epsilon) d\epsilon}.$$

For magnetic materials the density of states can be determined for both spins.

2.5.5 Vibrational frequencies

In order to describe the thermodynamics of adsorbates on a surface, changes in entropy and zero point energy must be determined. This can be done by finding the vibrational frequencies of the adsorbates bonded to the surface using the normal mode analysis. We have assumed that the vibrations for an adsorbate can be described by harmonic potential. This is often a good assumption since the potential energy surface around stable bonding sites tends to have the form of a harmonic potential well. The vibrations are well described if the potential energy surface is not too flat.

For the case of a molecule consisting of N atoms, there are 3N-5 normal modes for a linear molecule and 3N-6 modes for a non-linear molecule. The subtraction of 5 and 6 modes comes from 3 translational and either 2 or 3 rotational modes for the linear or non-linear molecule, respectively. For example, in the linear CO_2 molecule, there are 4 normal modes as shown in fig. 2.4.

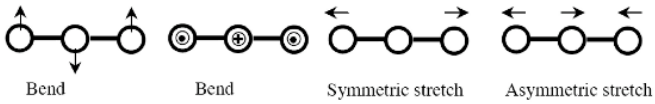

Figure 2.4: *The four normal modes for the linear CO_2 molecule.*

An adsorbed atom on a surface has 3 normal modes, because it is assumed that the atom is not diffusing on the surface and there will be no translational modes. The rotational modes are all zero in this case, because there is only one atom and hence it can not rotate in its binding site. The atom can vibrate in three directions (the x, y and z directions). If the potential energy $V(x, y, z)$ is known for the adsorbed atom, then the force constant k can be calculated as the second derivative of the potential $V(x, y, z)$, as shown below for the x-direction:

$$k_i = \frac{d^2V(x, y, z)}{dx^2}.$$

This gives the vibrational frequencies

$$\nu_i = \frac{1}{2\pi}\sqrt{\frac{k_i}{m}}$$

where m is the mass of the adsorbed atom. The frequencies for the y and z direction are calculated in a similar way.

To find the potential energy $V(x, y, z)$ for an adsorbed atom, the atom is displaced slightly in each direction around the minimum on the potential energy surface, where the energy is calculated. These calculations produce a potential energy curve for each of the three directions; the curvature (or the second derivative) of the parabolic fit to these potential energy curves gives the force constants k_i. The wave number is found by dividing the frequencies by the speed of light, and is commonly reported in units of cm^{-1}.

2.6 Free energy

In the previous sections, it has been shown how one can use density functional theory to calculate adsorption energies and activation energy barriers for reaction intermediates. These energies are obtained at zero kelvin and must therefore be thermodynamically corrected to the desired reaction conditions of temperature and pressure. In this section, thermodynamic corrections are made to model the Gibbs free energy of the reaction intermediates. A scheme for implementing corrections to the calculated adsorption energies will be presented. The free energy of the intermediates is defined as:

$$\Delta G = \Delta E + \Delta E_{ZPE} - T\Delta S \tag{2.20}$$

The entropy S and the zero point energy E_{ZPE} will be calculated using statistical mechanics for the surface intermediates, and for the gas-phase species the Schomate equations will be used [76–78]. The thermodynamical corrections are calculated for the framework of adsorbates outlined in section 2.5.3, where the gas-phase molecules of N_2, H_2O, H_2 and NH_3 are used as reference molecules for the reaction intermediate.

To determine the thermodynamic corrections based on statistical mechanics the vibrational frequencies of the adsorbates are needed. The vibrational frequencies will be calculated using the normal mode analysis described in section 2.5.5 which is a module contained in ASE. The surface species were only allowed to vibrate, while the surface atoms were kept fixed and the thermodynamic of the surfaces are not considered.

From the vibrational frequencies it is possible to calculate the zero point energy, E_{ZPE}, and the entropy, S, at the given reaction conditions. The zero point energy term is given as

$$E_{ZPE}^{V} = \sum_i \frac{1}{2} h\nu_i. \tag{2.21}$$

An example of the vibrational entropic contribution is calculated explicitly using standard equation from statistical mechanics and is shown below:

$$S_{vib} = R \sum_i \left(\frac{\Theta_{vi}/T}{\exp(\Theta_{vi}/T) - 1} - \ln\left[1 - \exp\left(\frac{-\Theta_{vi}}{T}\right)\right] \right) \tag{2.22}$$

In these expressions, the characteristic vibrational temperature, Θ_{vi}, is equal to $h\nu_i/k_B$. Here R is the gas constant, h is Plancks constant, k_B is Boltzmanns constant and T is the temperature and ν is the vibrational frequency.

The rotational contribution of the zero point energy term are,

$$E^R_{ZPE} = \frac{J(J+1)h^2}{8\pi^2 I} \tag{2.23}$$

where J is the rotational quantum number, and I is the moment of intertia of the molecule. For the entropy the corrections are presented for both the linear and the non-linear molecule:

$$S_{rot,lin} = \ln\left(\frac{T}{\sigma\Theta_r}\right) + 1 \tag{2.24}$$

$$S_{rot,nonlin} = \ln\left(\frac{\sqrt{T^3\pi}}{\sigma\sqrt{\Theta_a\Theta_b\Theta_c}}\right) + \frac{3}{2} \tag{2.25}$$

Where the characteric rotational temperature are $\Theta_r = \frac{h^2}{8\pi^2 Ik}$ and $\Theta_{a,b,c} = \frac{h^2}{8\pi^2 I_{a,b,c}k}$. σ is the symmetry number, and has for instance the value of 3 for NH_3 and 2 for H_2O. On the surface, some of the rotational modes will be frustrated, because the surface restricts the adsorbed molecule to not rotate in some of the orientations. The frustated modes of an adsorbed CO molecule can be seen on Fig. 2.5.

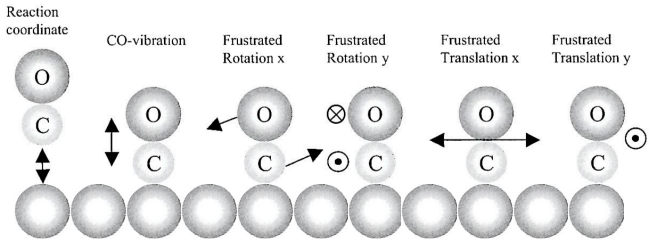

Figure 2.5: *The six modes for an adsorbed CO molecule on a surface. One is the reaction coordinate for adsorption/desorption on the surface, while the two other translational modes are frustrated modes. For the two rotational modes, the bond between C and the surface constrain theses. The last mode is the internal vibration of the C and O with respect to each other.* Adapted from [79].

The translational contribution to the free energy corrections are for the gas phase molecules

$$E^T_{ZPE} = \frac{3}{2}k_B T \tag{2.26}$$

where each direction contributes with $1/2\mathrm{k}_b\mathrm{T}$. A molecule adsorbed on the surface will, because it is tightly bonded to one site, have frustrated translational modes (will essentially behave as vibrational modes) in two of the direction, and these will typically be very soft with energies $\mathrm{h}\nu << \mathrm{k}_B\mathrm{T}$.

$$S_{tran} = \ln\left[\left(\frac{2\pi mkT}{h^2}\right)\frac{kT}{P}\right] + \frac{5}{2} \tag{2.27}$$

Combining all contributions:

$$E^{Total}_{ZPE} = E^V_{ZPE} + E^R_{ZPE} + E^T_{ZPE} \tag{2.28}$$

$$S^{Total} = S^V + S^R + S^T \tag{2.29}$$

Due to the frustated modes on the surface, it is only the vibrational modes that determine the free energy corrections for adsorbates, while for the gas-phase molecules one need to determine all contributions.

2.6.1 Entropy and Zero Point Energy corrections

The thermodynamic corrections used in this thesis are presented in table 2.1. These thermodynamic corrections have been calculated for all ammonia synthesis reaction intermediates on the Ru M12 nanocluster and have been used as a first order approximation for the entropy and zero point energy terms for the other metals and later tested on Mo. It is reasonable to expect that the difference in the correction terms across the metals are small because the type of adsorption site for each reaction intermediate is very similar. For the thermodynamic corrections of O*, OH* and H_2O*, the presented values are taken with respect to H_2O(g) and H_2(g) in gas phase and the corrections are taken from a paper by Nørskov et al. [80].

Table 2.1: The thermodynamic corrections for the reaction intermediates on the M12 nanocluster calculated at 298 K. The corrections for the reaction intermediates O*, OH* and H_2O are already with respect to gas-phase molecules H_2(g) and H_2O(g) and are taken for the paper by Nørskov et al. [80]

Gas-phase at 298 K		
Molecule	E_{ZPE} (eV)	TS (eV/K)
N_2(g)	0.211	0.592
H_2(g)	0.344	0.404
NH_3(g)	0.985	0.596
M12 nanocluster at 298 K		
Molecule	E_{ZPE} (eV)	TS (eV/K)
N*	0.076	0.020
H*	0.171	0.014
N_2*	0.182	0.033
NH*	0.365	0.032
NH_2*	0.713	0.041
NH_3*	1.036	0.058
N_2H*	0.480	0.057
N_2H_2*	0.796	0.067
N_2H_3*	1.135	0.063
Pt fcc 111 at 298 K		
Molecule	ΔE_{ZPE} - $T\Delta S$ (eV)	
O*	0.05	
OH*	0.35	
H_2O*	0.67	

2.7 Computational system setup

The general computational setup employed for the calculations presented in this thesis will here briefly be outlined.

The exchange-correlation functional RPBE in the generalized gradient approximation has been used. The main characteristic of this functional is the accurate description of the adsorption of molecules and surface intermediates [44], which are key components in this study. The RPBE paper states that the average error on this functional is 0.25 eV for adsorption energies. But the lattice constant of bulk structures are being overestimated by approximately 2-3 % [44]

For the calculations in GPAW the applied settings are as follows. The grid spacing has been chosen to be 0.18 Å and the number of free bands above the Fermi level has been set to 20. The convergence criteria for solving the electronic density self-consistently were chosen such that the change in energy had to be less than 10^{-5} eV and the change in density less than 10^{-4} eV. For spin polarized metals, such as Fe, Ni, Co, spin polarized calculations were performed. The Atomic Simulation Environment (ASE) [47] was used to set up the atomic structure of these systems.

Fermi Temperature

At 0 K the Fermi-Dirac distribution is a unit step function, and hence the occupation number of any state is either 0 or 1, see fig. 2.6. When trying to compute the density and energy a numerical problem often arises because the system is constrained because of this limitation. An artificial temperature can broaden the Fermi-Dirac distribution and smoothen the convergence. When the convergence is achieved at finite temperature, one must extrapolate the result back to 0 K. Higher Fermi temperature results in faster convergence, but too

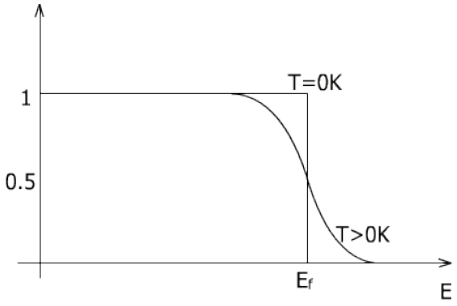

Figure 2.6: *Fermi-Dirac distribution of electrons at 0 K and $T > 0$ K.*

high temperatures violates the basic foundation of extrapolating back to 0 K. A Fermi smearing of 0.1 eV for magnetic metals and 0.0001 eV for the other metals were applied in the calculations.

2.7.1 Ensuring computational precision

Some computational details are important to optimize for each specific system. They are crucial because once converged they can ensure as small errors as the exchange-correlation functional allows. Choosing too strict computational

settings, the gain in accuracy is not worth the added computational time. In general, errors of energy differences are smaller than the errors of the total energy and are often less than 0.2 eV, since the larger errors on the total energy values mostly cancels out. Energy differences can be found for a system consisting of a slab with and without an adsorbate and the corresponding energy for the adsorbate in the gas phase, see eq. 4.8 and eq. 2.19.

For calculations using the GPAW code numerous computational parameters can be tuned such that the energy differences due to computational settings are lower than a desired precision. In appendix A illustrations are presented for proper choice of k-point sampling, number of layers and vacuum and here I will outline why these three parameters must be chosen properly.

k-point sampling

GPAW is based on real-space uniform grids and one can choose to either perform Γ point calculation or for instance using the Monkhorst-Pack k-point sampling [81]. The Γ point calculation allows for choosing the wave functions to be real. If choosing to use the Monkhorst-Pack k-point sampling, the periodic boundary conditions one must employ will restrict the k-point to the first Brillouin zone. Even though restricted to the first Brillouin zone the number of k-points can be infinite but countable. In practice the number of k-points needed are small for accurate evaluation of the wave functions. High accuracy and small k-point set methods are, besides Monkhorst-Pack sampling, the Chadi and Cohen methods [82].

When determining which number of k-points the calculations should be performed with, it is important to remember that the variational principle does not apply to the number of k-points. The energy does not continually decrease when the number of k-points is increased, but will oscillate around the ground state. In GPAW there is the phenomena of an egg-box effect, where oscillations depending on where the k-points are positioned vary the total energy, however these effects are much smaller than the error from XC-functional.

Layers

In calculations with slabs (close-packed or stepped surfaces) there are a number of parameters that one must consider. The size of the surface area is a way to model different coverages and will have an impact on the calculations performed [83]. The other calculational parameter to be optimized is the number of layers the slab consists of. Too few layers and the calculations will not include the bulk effects that are present for surface calculations. Too many layers and the calculation will be too computationally expensive and the gain in accuracy will be trivial. If the bulk behavior should be present in the slab, either the middle layer of the slab should be fixed or the bottom layer(s) should be fixed. In this thesis the bottom layers have always been kept fixed.

Vacuum

The amount of vacuum on top a surface or around a nanocluster is an important computational detail. The presence of vacuum helps in the convergence of the

system and will help ensure a smooth transition from areas with high electron densities to areas with no electron densities. This is often the case in calculations of slabs (one direction) or of gas phase molecules (three directions) or nanoclusters (three directions). If we choose too little vacuum in one of these directions, the electronic density will be forced to be zero at the edge of the unit cell and the rest of the density distribution will be affected and therefore the energy will be incorrect. Choosing more vacuum in the setup will most often ensure more correct energies, but on the compensation of more computational time.

Chapter 3

Surface Reactivity

3.1 Overview

The present chapter will introduce the theories that describe the reactivity of metal surfaces, and the resulting relations that simplify the modeling of surface reactions. Understanding the origin of catalysis is evident for continued improvements in the field. Reactions with a high activation barrier when not catalyzed, see the black line on Fig. 3.1, can be enhanced by introducing a catalyst. The catalyst will take part in the reaction, but will not be consumed by the reaction, and will introduce new elementary reaction steps that have lower activation barriers, see the red lines on Fig 3.1.

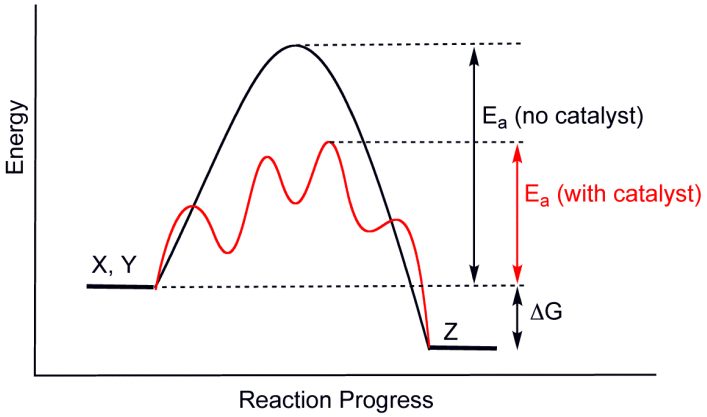

Figure 3.1: *The introduction of a catalyst to a chemical reaction. The black line presents the energy profile of a reaction with no catalyst aid and subsequently a large activation barrier is dominating the reaction. On the contrary, the red line shows the impact a catalyst has on the reaction, lower the activation and introduces elementary reactions on the surface.* Courtesy to http://en.wikipedia.org/wiki/Catalysis for the image.

The aim of this chapter is to describe why and how the energy profile of the catalyzed reaction pathway is changed. To do so, it is important to understand the interactions that influences the energetics of the reactants, reaction interme-

diates and products on the surface. To understand the interplay between catalyst and adsorbates, the results from the Newns-Anderson model will be introduced and the resulting consequences formulated in the d-band model will be presented. Linear scaling relations is the simplification often used when describing trends of the adsorption energies of reaction intermediates for a given reaction and the Brøndsted-Evans-Polanyi relation formulates a relation between the activation barrier and the adsorption energy of the products. Both approximations will be discussed in the end of the chapter.

3.2 Newns-Anderson model

The Newns-Anderson model [84, 85] describes the chemisorption of an atom on a surface. The interaction between a simple adsorbed atom on a metal surface will in the following be outlined. Starting from an assumption that the atom has only one valence electron (a crude but important assumption) with an energy of ϵ_a and a corresponding wave function Φ_a. For most surfaces consisting of transition metals it is accurate to assume a continuum of electronic states Φ_k with the resulting energies ϵ_k. The wave function basis is assumed orthogonal and therefore the matrix elements $\int \Phi_a \Phi_k$ will disappear.

The Hamiltonian H describes the interaction between the atom and the surface through the matrix element $V_{ak} = \int \Phi_a H \Phi_k$. The solution to this eigenvalue problem is, assuming that the solution Φ_i will be a linear combination of the separated wave functions of the atom and the surface, given by:

$$\Phi_i = c_{ai}\Phi_a + \sum_k c_{ik}\Phi_k,$$

where c_{ai} and c_{ik} are constants. This leads to an eigenvalue problem for the system on the following form

$$H\Psi_i = \epsilon_i \Psi_i.$$

The solution of this eigenvalue problem is the new states for the adsorbate defined as

$$n_a(\epsilon) = \frac{1}{\pi} \frac{\Delta(\epsilon)}{[\epsilon - \epsilon_a - \Lambda(\epsilon)]^2 + \Delta(\epsilon)^2} \tag{3.1}$$

where

$$\Delta(\epsilon) = -\mathrm{Im}\left(\sum_k \frac{V_{ak}^2}{(\epsilon - \epsilon_k + i\delta)}\right) \rightarrow \pi \sum_k V_{ak}^2 \delta(\epsilon - \epsilon_k) \quad \text{for} \quad \delta \rightarrow 0^+$$

and

$$\Lambda(\epsilon) = \frac{1}{\pi} \int_{-\infty}^{\infty} \frac{\Delta(x)}{x - \epsilon} dx.$$

The last term, $\Lambda(\epsilon)$, is the Kronig-Kramer transformation of $\Delta(\epsilon)$. $\Delta(\epsilon)$ is essentially a hopping matrix element between the metal state k and the adsorbate level a and accounts for the projection of the metal states onto the adsorbate state. The terms $\Delta(\epsilon)$ and $\Lambda(\epsilon)$ express the interaction between the adsorbate and the metal surface. These terms account for the overlap between the states of the metal and the adsorbate states. For a full derivation of the Newns-Anderson model, see appendix B.

3.3 Interpretation of the Newns-Anderson model

The Newns-Anderson model accounts successfully for the behaviour of chemical bonding. The bonding between a diatomic molecule and a transition metal surface will be used to illustrate the interaction between the surface and the molecule and why transition metals are so special and are extensively used as catalysts.

3.3.1 Diatomic molecules

The homonuclear diatomic molecule consists of the same two atoms bonded together, such as H_2, N_2 and O_2. In such molecules, the energy levels for each of the atoms in isolation are equal to one another, $\epsilon_a = \epsilon_b = \epsilon$. The energy levels for the homo-nuclear diatomic molecule can be showed to be [79, 86],

$$E_{\pm} \cong \epsilon \pm \beta - S\beta.$$

The off-diagonal Hamiltonian element, β, describes the interaction and S is the overlap integral between the two atoms A and B. The overlap will here be assumed small. Since the interaction β is negative, both levels are shifted upwards due to electron-electron repulsion, which is accounted for by the term $-S\beta$, and shown as the upward shifted dotted horizontal lines in fig. 3.2a. The bonding state, E_+, and the anti bonding state, E_-, are formed, and the energy difference between these states are

$$\Delta E = 2|\beta|$$

which is proportional to the interaction between the orbitals. In this model of the homonuclear molecule the repulsive interaction between the electrons have been neglected.

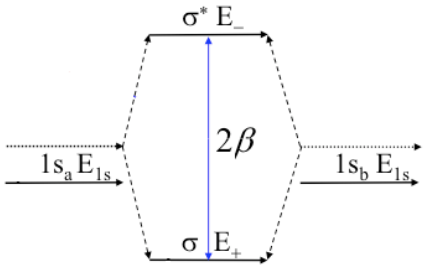

Figure 3.2: *The schematic energy diagram for a homo-nuclear diatomic molecule consisting of two identical atoms. A bonding and an anti bonding state are formed. The energy of splitting the two states is $|2\beta|$ and is proportional to the interaction β of the atomic orbitals.*

The homonuclear diatomic molecule, and the bit more complicated heteronuclear diatomic molecule, have bonding and antibonding states. In gas phase, the bonding states will first be filled and then the antibonding states will be filled. In the next section, the interaction between a diatomic molecule and a metal surface as the molecule adsorbs will be described, and focus will be specifically

on the internal bonding in the molecule. The interaction from the surface onto the internal bonding in a adsorbed molecule are one of the most important factors in heterogeneous catalysis and the reason for why heterogeneous catalysis plays a key role in the chemical industry and the modern society.

Adsorption of a molecule on a transition metal

The chemisorption of a diatomic molecule onto a transition metal surface is shown in fig. 3.3. The interaction between the molecule and the *d*-band results in splitting of the bonding state: one is shifted down in energy and the other is shifted up in energy. A similar effect occurs for the antibonding states, in which filling of the antibonding states strengthens the interaction with the surface, but at the same time weakens the intramolecular bond making it easier for the molecule to dissociate. These effects are the key to understanding dissociation of molecules on transition metal surfaces, which is a vital part of catalytic reactions.

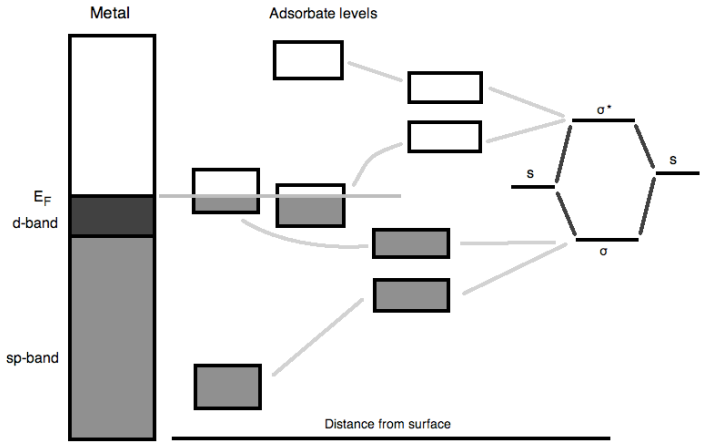

Figure 3.3: *A transition metal consisting of the broad sp-band and the narrow d-band interacts with a molecule with bonding orbitals σ and antibonding orbitals σ∗. The sp-band gives rise to a lowering and broadening of the bands, whereas the d-band gives rise to a splitting into bonding and antibonding orbitals. Filling of the antibonding orbitals of the molecule weakens the internal molecular bonding and may result in dissociation of the molecule.*

3.4 d-band model

In this section qualitative arguments will be given for the bonding of atoms and molecules to a metal surface on the basis of the *d*-band model [87,88]. Especially the late transition metals will be accounted for and expressions for the bonding energy of atoms and molecules will be introduced for these metals.

First it is noted that the *sp*-band for all metals is half filled and the small deviations in the broad *sp*-band will not account for the differences in adsorption energy among the late transition metals. The contribution to the adsorption energy from these bands are therefore estimated to be constant for all metals, both noble and reactive metals. The biggest part of the bonding energy arises

from the *sp*-contribution and is significantly larger than the *d*-band contribution. The down shift due to the interaction with the *sp*-band of the energy levels for both an atom, can be seen on fig. 3.4a(2), and for the diatomic molecule, on Fig. 3.4b(2).

Instead the narrow *d*-band centered at ϵ_d will behave as a pertubation ontop of the adsorption energy contribution caused by the *sp*-band electrons. Here ϵ_d is given by,

$$\epsilon_d = \frac{\int g(\epsilon)\epsilon d\epsilon}{\int g(\epsilon)d\epsilon}, \tag{3.2}$$

where $d(\epsilon)$ is the density of states for the *d*-electrons. For the simple case of an atom adsorbed onto the transition metal surface, the energy splits in bonding and antibonding components. The additional gain in bonding energy from the *d*-band is given by the hybridization energy E_{d-hyp}:

$$E_{d-hyb} = -(1-f)\frac{2\beta^2}{(\epsilon_a - \epsilon_d)} + 2(1+f)\gamma\beta^2. \tag{3.3}$$

Here f is the filling degree of the *d*-band, ϵ_a is the original energy level of the adsorbate electron and ϵ_d is the center of the *d*-band and β is the interaction matrix element as formulated previously, and it has been assumed that $\epsilon_a - \epsilon_d \gg 4\beta^2$. The hybridization energy in eq. 3.3 consists of two terms, the first is an attractive part while the second is the repulsive part.

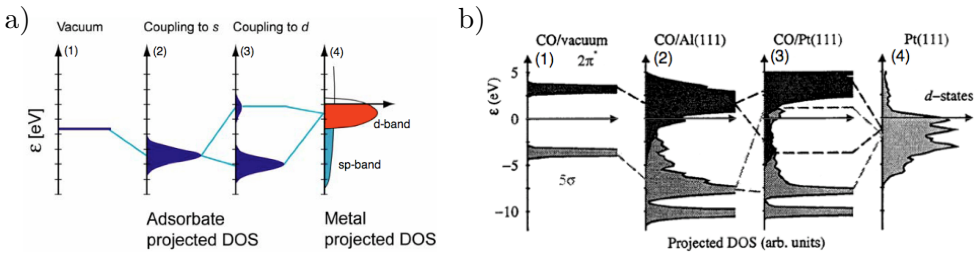

Figure 3.4: *The schematic illustration of the change in local electronic structure of; a) an atom and b) a CO molecule while adsorbed onto a transition metal surface. In (1) for both a) and b) the electronic structure of the atom and the molecule is seen in vacuum and in (4) the electronic structure of the sp-band and the d-band of the transition metal. In (2) the atom and molecule have coupled to the sp-band and energy levels are lowered and broadened. In (3) bonding and antibonding parts are recognised for both the atom and the CO molecule.* The figures are adapted from ref. [87] and ref. [89] respectively.

For the diatomic molecule, CO, the hybridization energy can be formulated in a similar way as for an atom. For the adsorption of a CO onto the late transition metals the hybrization energy can be computed to

$$\begin{aligned}\Delta E_{d-hyb} &= -2\frac{(1-f)\beta_{5\sigma}^2}{|\epsilon_d - \epsilon_{5\sigma}|} - 2f\frac{\beta_{2\pi}^2}{\epsilon_{2\pi} - \epsilon_d} + 2(1+f)\gamma_{5\sigma}\beta_{5\sigma}^2 + 2f\gamma_{2\pi}\beta_{2\pi}^2 \\ &\approx -2f\frac{\beta_{2\pi}^2}{\epsilon_{2\pi} - \epsilon_d} + 2f\gamma_{2\pi}\beta_{2\pi}^2.\end{aligned}$$

Again the hybridization energy have an attractive and a repulsive part.

To summarize, the *d*-band model states that the bonding energy of an atom or a molecule consists of two terms. The first is the *sp*-band contribution which is close to identical for all transition metals while the second term is the narrow *d*-band that act as a pertubation on the chemisorption energies caused by the *sp*-band and the *d*-band supply each of the transition metals with its unique chemisorption properties. The overall hybridization energy depends on three properties,

1. the filling degree of the *d*-band
2. the interaction matrix element β
3. the energy difference between the original electron levels of the adsorbate and the center of the *d*-band.

The *d*-band center and the interaction matrix element have uniquely been calculated for all transition metals, see [87, 90]. The reactivity of surfaces is therefore dependent on the *d*-center, and a higher lying *d*-band center will result in a more reactive surface. Looking at the periodic table, the *d*-band model explains the trends in reactivity that has been observed, where the *d*-band center is moving up when going from the noble metals (Au, Ag, Cu) and to the left. Furthermore, the reactivity decreases while going down through the group (e.g. Cu -> Ag -> Au), because of the broadening of the *d*-band and hence there will be less overlap with adsorbate states.

3.5 Scaling relations

In many studies scaling relations for adsorption energies of a large number of reaction intermediates has been reported. On Fig. 3.5 scaling relations for CH_x, (x = 0, 1, 2, 3) and NH_x, (x = 0, 1, 2) on close-packed and stepped transition metal surfaces are presented, and other scaling relations exists for OH_x and SH_x [91]. A model for scaling relations for hydrogen containing adsorbates will be presented. The model accounts to a large extent for the slopes found in the scaling relations, presented in Fig. 3.5. It is based upon the *d*-electrons and the hydrogen valency of the adsorbate. It is observed that the relations follow a linear form,

$$\Delta E^{AH_x} = \alpha(x)\Delta E^{A} + \kappa. \tag{3.4}$$

The slope $\alpha(x)$ is given as

$$\alpha(x) = \frac{x_{max} - x}{x_{max}} \tag{3.5}$$

where x_{max} is the maximum number of hydrogen that can bind to the central atom, 3 and 4 for N and C respectively. The most important part is to realise that the adsorption energy of AH_x, E^{AH_x}, depends on the adsorption energy

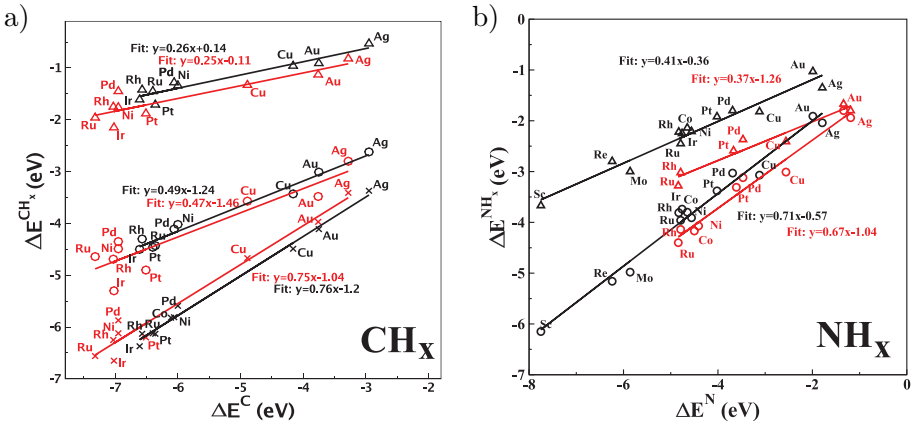

Figure 3.5: a)*Adsorption energy of CH_x intermediates (crosses: $x = 1$, circles: $x = 2$, triangles: $x = 3$) plotted against the adsorption energy of C.* b) *Adsorption energies of NH_x intermediates (circles: $x = 1$, triangles: $x = 2$) plotted against the adsorption energy of N. The black colored data points represent results on close-packed transition metal surfaces, while the red colored data points represent stepped transition metal surfaces.* Adapted from ref. [91]

of A, E^A. κ is a constant and depends on the surface type and the valency is defined as (x_{max}-x).

The adsorption energy of adsorbates with similar electronic structure (N and NH_x) on transition metal surfaces can result in linear scaling relations. The interaction between transition metals and the adsorbates is to a large extent described by the *d*-band model. In the following a qualitative argumentation for the existence of the linear scaling relations will be outlined. The *d*-band model proposes a decoupling of the *sp*- and *d*-band interaction between the adsorbate and the surface.

$$\Delta E = \Delta E_{sp} + \Delta E_d \tag{3.6}$$

As stated earlier, see section 3.4, the coupling to the *sp* states contribute equally for all transition metals to the hybridization energy. However, the main contribution to the variations in bond energy from one transition metal to another comes from the coupling to the *d*-band. The variations observed on Fig. 3.5 must then be given by the term ΔE_d and it signifies that the x dependance in the ΔE^{AH_x} can only be due to the coupling to the d states. Reformulating eq. 3.4 according to these contentions,

$$\Delta E^{AH_x} = \Delta E_d^{AH_x} + \Delta E_{sp}^{AH_x} = \alpha(x)\Delta_d^A + \Delta E_{sp}^{AH_x} = \alpha(x)\Delta E^A + \xi \tag{3.7}$$

where everything concerning the *sp* states have been put into the constant $\xi = \Delta E_{sp}^{AH_x} - \alpha(x)E_{sp}^A$. On the basis of the effective medium theory (EMT) [91,92] one can to a first approximation argue that the coupling strength, $V_{ad}^2(x)$, and the energy contribution from coupling to d states correlates. When a atom A is hydrogenated, it needs less electronic density, n_{surf}, from the surface to reach a optimum electroninc density. The coupling strength is correlated with n_{surf}, bacause the decay of the d states outside the surface correlates with n_{surf}. In

short,

$$\Delta E_d(x) \propto V_{ad}^2(x) \propto n_{surf}(x) \propto \frac{x_{max} - x}{x_{max}} = \alpha(x). \tag{3.8}$$

It shows that the form of the scaling relations to a large extent is elucidated from the *d*-band model and EMT.

The scaling relations presented on Fig. 3.5 show that there is a shift between the close-packed and the stepped surfaces is defined as a geometric effect. The movement along the line is defined as an electronic effect. From the d-band model, one can explain the increase in reactivity observed for stepped surfaces compared to close-packed surfaces. The step atoms have fewer nearest neighbors, which result in a narrow d-band. The d-band then moves up, such that the Fermi level is still aligned with d electrons. This result in less antibonding states and hence the step atoms are more reactive.

The shifts noticed for the scaling relations of both the CH_x and NH_x species betwen close packed and stepped surface show that increasing the under-coordination of the catalytic surface can be one route to change the catalytic properties of the active sites. We have tried to exploit this phenomena in the investigation of new metal facets for electrochemical ammonia production. Furthermore, this can also be used to enhance one reaction pathway compared to another, if the first is structure sensitive, while the other is reported to be structure insensitive (like hydrogen evolution reaction).

3.6 Brøndsted-Evans-Polanyi relations

In catalysis the activation barrier for a given reaction step constitutes a vital part of the catalysis. In this section the Brøndsted-Evans-Polanyi (BEP) relations [93, 94] that describes the activation barrier for a given reaction step will be presented. Using DFT it has been shown that linear relations for the N_2 and CO dissociation and for the CH bond breaking [31, 95, 96] can be established. Examples of these relations can be found on fig. 3.6 where the dissociation energy for NO, CO, N_2 and O_2 have been calculated. It is seen that the activation energy has the following form;

$$E_a = \beta \Delta E + \gamma. \tag{3.9}$$

The BEP line is universal for all four adsorbates, NO, CO, N_2 and O_2, on each of the geometries (close-packed and steps).

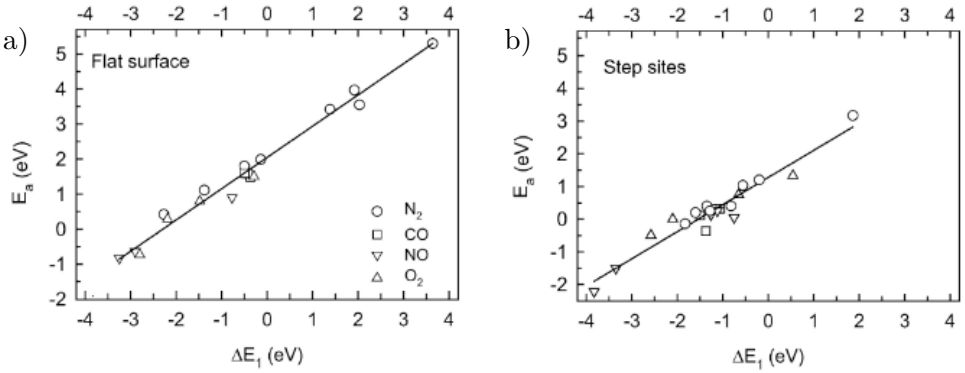

Figure 3.6: *The calculated activation energy for dissociation of the molecules NO, CO, N_2 and O_2 on close-packed surfaces a) and on stepped surfaces b) plotted against the calculated dissociative chemisorption energy for the dissociation products. The close-packed and stepped surfaces show similar trends, but a shift of the lines is observed and is due to a geometric effect.* Adabted from ref. [97]

3.7 Sabatier's principle

In the two previous sections the scaling relations and BEP lines have been introduced. The overall reaction energy diagram can approximately be described using these two models. The activation energy, E_a, determines the rate of dissociation while the stability of the products, ΔE, dictates the product removal. This gives rise to two extrema, (1) the intermediates have a strong bond to the surface (which is due to high adsorbate-surface interaction) resulting in the poisoning of the surface because the end product cannot desorb from the surface. However in this case, the dissociation barrier will be very small or non existing. In the other case, (2) the adsorbates will bond weakly to the surface (low adsorbate-surface interaction) resulting in high barriers for dissociation, and the reaction cannot proceed.

An optimal catalyst has low activation barriers and not too weak or too strong bonding of the intermediates. Due to the fact that the activation energy and the bonding energy often are correlated the best catalyst comes from a compromise such that the adsorbate-surface interaction are neither too strong nor too weak, which is known as Sabatiers principle.

The Sabatier principle can be seen in the form of a volcano plot on fig. 3.7, which shows the activities of a given reaction (in this case the methanation reaction) with respect to the CO dissociation energy. Here the activity follows a volcano where on one side, the surface intermediates are bonded too strongly to the surface (left), whereas on the other side (right) the dissociation barrier is too high and the optimum of the volcano is in the middle.

The Sabatier principle can also be applied to determine the optimum catalysts for electrochemical reactions, where atleast two proton transfer reactions will be limiting the overall effeciency of the electro-catalyst. Introducing the electrochemical cell and the computational hydrogen electrode approach will enable us to describe electro-catalyst with volcano plots illuminating the limiting re-

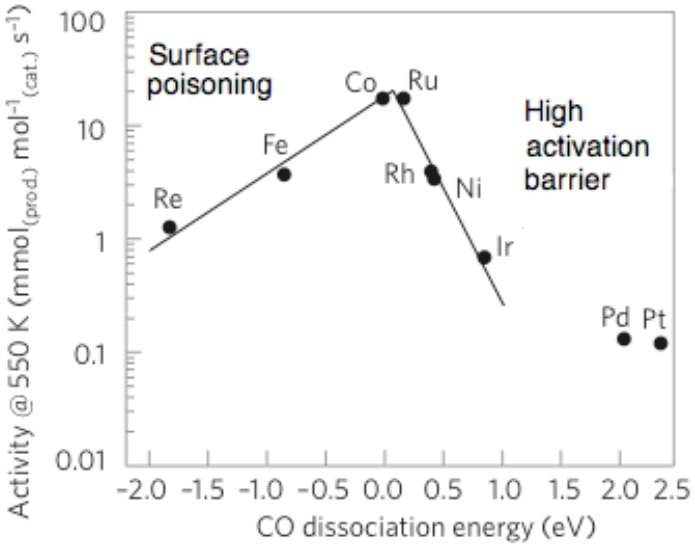

Figure 3.7: *The activity of the methanation reaction ($CO + 3H_2 \rightarrow CH_4 + H_2O$) on various metals. On the right hand side of the maximum, the kinetics is limited by the dissociation barrier, while on the left hand side the intermediates binds too strongly to the surface and will hence poison the surface. This gives a volcano of the activity described with a given parameter (The CO dissociation energy in this case).* Adapted from ref. [42, 98]

action steps and the required potentials to drive the electrochemical reaction forward.

Chapter 4

Electrochemical cell and how to model it

The present chapter will outline the composition of the electrochemical cell that could be used for production of ammonia. In addition the methods for modeling electrochemical reactions will be presented. The challenges faced when creating ammonia electrochemically will briefly be discussed.

4.1 The electrochemical cell

The production of ammonia electrochemically requires an electrochemical cell. Fig. 4.1 shows three examples of such cells. For all of them, the cell requires a cathode and an anode with an electrolyte combining them. The requirements for each of the components are dependent on the choice of cell type. The cell layout that we have envisioned is Fig. 4.1a where hydrogen is the source of protons and electrons. A combination of water splitting and ammonia production as in Fig. 4.1b would be the ideal implementation for production of ammonia.

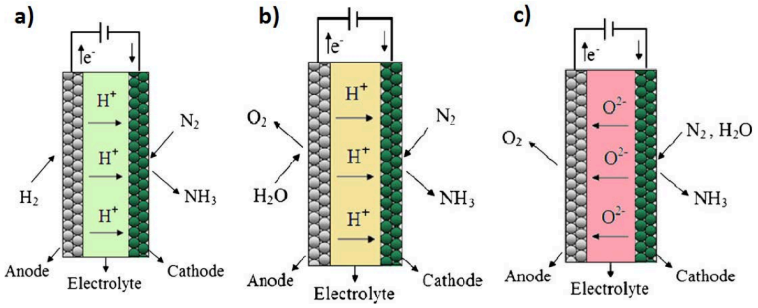

Figure 4.1: *Schematic of three different types of electrochemical cell for ammonia synthesis: a) proton conducting electrolyte, where protons and electrons come from H_2, b) proton conducting electrolyte, where protons and electrons come from the splitting of water at the anode, c) oxide-ion conducting electrolyte, where oxygen is formed on the anode and at the cathode water is split into oxygen ions and protons. For all three types nitrogen is protonated to form ammonia.* Adapted from Amar et al. [99]

In addition to ammonia production rates, the main issue for ammonia electrocatalysts is the competition with hydrogen production and oxygen poisoning. Hydrogen evolution is inevitable, but in the search for new catalysts it should be minimized compared to ammonia production. Oxygen poisoning is a more difficult task to solve, because oxygen binding on most surfaces is stronger than the binding of nitrogen and would result in deactivation of the catalyst. The cathode should therefore operate under very low pressures of water and oxygen. In that respect, it would be suitable to use an proton conducting electrolyte in dry conditions (i.e. at very low partial pressures) or an ionic liquid which do not contain oxygen and is not decomposed by the catalyst.

In solving the electrochemical production of ammonia, it is of highest importance to increase efficiency of electrolytes, such that the chemical process is not limited by an inadequate electrolyte. This can be achieved by either reducing the electrolyte resistance (increasing the conductivity) or decreasing the thickness of the electrolyte. This task is non-trivial.

In the work presented in this thesis, the sole purpose has been to find new catalysts for the cathode reactions outlined in Fig. 4.1a and 4.1b.

4.2 The catalytic processes at the cathode

4.2.1 Volmer-Tafel or Heyrovsky reaction

The protonation processes modeled on the cathode catalyst surface have been simulated using the Heyrovski-type [100] reaction, which can both the describe the electrochemical ammonia formation through both the dissociative mechanism and associative mechanism and also for water formation from adsorbed oxygen adatoms. The Heyrovski-type mechanism is a process where an proton coming from the electrolyte directly attaches to either an adatom or admolecule on the catalyst surface taking up an electron coming from the surface to form a hydrogen atom bonded directly to the molecule. The process is outlined in Fig. 4.2. In this study, the adsorbed species of nitrogen adatoms, nitrogen admolecules or oxygen adatoms are directly protonated to form NH_x or N_2H_x (x={1,2,3}) or OH_y (y={1, 2}) species on the surface. In principle, a Volmer-Tafel-type reaction also exists and could have been modeled. The Volmer-Tafel-

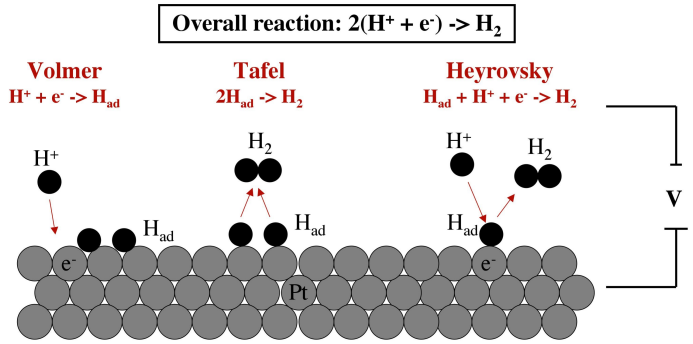

Figure 4.2: *A schematic of the possible elementary reactions in this case to form hydrogen molecules. Adapted from [101]*

type protonation reaction is first a recombination of an electron and a proton on the surface into a hydrogen atom. Then this hydrogen will react with a reaction intermediate, to form the next reaction intermediate in the synthesis pathway. Modeling the Volmer-Tafel reaction will require the reaction barriers for the hydrogenation steps for all reaction intermediates [36, 102] and will therefore often require a higher temperature to drive the process forward.

4.2.2 Reaction pathways

In the process of describing the production of ammonia electrochemically, it is convenient to model the anode reaction

$$H_2 \rightleftharpoons 2H^+ + 2e^- \tag{4.1}$$

as the source of electrons and protons, presented in Fig. 4.1a. The electrons are transported to the cathode side through an external circuit, while the protons are introduced into the proton-conducting electrolyte maintaining the equilibrium while diffusing to the cathode. At the cathode, nitrogen will react with protons and electrons in one of two reactions to form ammonia. The overall reduction reaction for the nitrogen molecule is

$$N_2 + 3H_2 \rightarrow 2NH_3 \tag{4.2}$$

through the dissociative mechanism or the associative mechanism. The studied reaction pathways for the electrochemical ammonia production are presented in detail below. We address first the dissociative mechanism.

$$N_2(g) + 6(H^+ + e^-) + 2^* \rightleftharpoons N_2^{**} + 6(H^+ + e^-) \tag{4.3a}$$
$$N_2^{**} + 6(H^+ + e^-) \rightleftharpoons 2N^* + 6(H^+ + e^-) \tag{4.3b}$$
$$2N^* + 6(H^+ + e^-) \rightleftharpoons NH^* + N^* + 5(H^+ + e^-) \tag{4.3c}$$
$$NH^* + N^* + 5(H^+ + e^-) \rightleftharpoons NH_2^* + N^* + 4(H^+ + e^-) \tag{4.3d}$$
$$NH_2^* + N^* + 4(H^+ + e^-) \rightleftharpoons NH_3^* + N^* + 3(H^+ + e^-) \tag{4.3e}$$
$$NH_3^* + N^* + 3(H^+ + e^-) \rightleftharpoons NH_3^* + NH^* + 2(H^+ + e^-) \tag{4.3f}$$
$$NH_3^* + NH^* + 2(H^+ + e^-) \rightleftharpoons NH_3^* + NH_2^* + (H^+ + e^-) \tag{4.3g}$$
$$NH_3^* + NH_2^* + (H^+ + e^-) \rightleftharpoons 2NH_3^* \tag{4.3h}$$
$$2NH_3^* \rightleftharpoons NH_3^* + NH_3(g) + ^* \tag{4.3i}$$
$$NH_3(g) + NH_3^* + ^* \rightleftharpoons 2NH_3(g) + 2^* \tag{4.3j}$$

Modeling the dissociative mechanism requires the activation barrier for the N-N bond breaking in eq. 4.3b. This part of the reaction is often the rate limiting step for most catalyst surfaces.

Next, the *associative Heyrovski mechanism* is considered, where a nitrogen molecule is directly protonated until it splits into two molecules in the form of NH_x species which later form gaseous ammonia. In the equations below, the N-N bond split is set to happen at the fourth protonation step. The calculations performed in the presented work suggests that the splitting occur at this reaction step and in some cases even earlier. The N-N bond is one of the strongest and

breaking it can be very difficult, but through successive protonations the internal N-N bond is weakened and thus can be more easily cleaved.

$$N_2(g) + 6(H^+ + e^-) + 2^* \rightleftharpoons N_2^{**} + 6(H^+ + e^-) \quad (4.4a)$$
$$N_2^{**} + 6(H^+ + e^-) \rightleftharpoons N_2H^{**} + 5(H^+ + e^-) \quad (4.4b)$$
$$N_2H^{**} + 5(H^+ + e^-) \rightleftharpoons N_2H_2^{**} + 4(H^+ + e^-) \quad (4.4c)$$
$$N_2H_2^{**} + 4(H^+ + e^-) \rightleftharpoons N_2H_3^{**} + 3(H^+ + e^-) \quad (4.4d)$$
$$N_2H_3^{**} + 3(H^+ + e^-) \rightleftharpoons NH_2^* + NH_2^* + 2(H^+ + e^-) \quad (4.4e)$$
$$NH_2^* + NH_2^* + 2(H^+ + e^-) \rightleftharpoons NH_3^* + NH_2^* + (H^+ + e^-) \quad (4.4f)$$
$$NH_3^* + NH_2^* + (H^+ + e^-) \rightleftharpoons 2NH_3^* \quad (4.4g)$$
$$2NH_3^* \rightleftharpoons NH_3^* + NH_3(g) + ^* \quad (4.4h)$$
$$NH_3^* + NH_3(g) + ^* \rightleftharpoons 2NH_3(g) + 2^* \quad (4.4i)$$

The reaction steps described above are either purely electrochemical or thermal steps and together they describe the full catalytic cycle of ammonia synthesis.

An alternative reaction pathway for ammonia production, is the reduction of an adsorbed nitrogen atom. Here, a nitrogen adatom already sits at the surface and only reaction steps for this specific type of reaction, are eq. 4.3c to eq. 4.3e. It is only taking the successive protonations into account and then the release of ammonia from the surface.

$$N + 3H^+ + 3e^- \rightarrow NH_3. \quad (4.5)$$

This process removes nitrogen atoms from the surface and will require their regeneration to continue the production of ammonia. Therefore, this presented pathway below does not describe a full catalytic cycle of producing ammonia; only the reduction of the studied nitride.

4.2.3 Reduction of oxygen

Poisoning of oxygen at the surface, is a occuring event. The reduction of such oxygen atoms is a two step proton and electron transfer process. The reaction pathway for reducing oxygen is as follows:

$$O* + 2(H^+ + e^-) \rightleftharpoons OH* + (H^+ + e^-) \quad (4.6a)$$
$$OH* + (H^+ + e^-) \rightleftharpoons H_2O* \quad (4.6b)$$
$$H_2O* \rightleftharpoons H_2O(g) + * \quad (4.6c)$$

Reducing oxygen to water can be a way to remove the oxygen from the surface.

4.3 Electrochemical modeling

With DFT it is possible to calculate the reaction energy, ΔE, using the Heyrovski type protonation process for each of the reaction intermediates described above; the dissociative mechanism, reduction of nitrogen or oxygen adatoms or the associative mechanism. The reaction energy is calculated with respect to the gas phase molecules of hydrogen and nitrogen according to the following equation.

$$\Delta E = E_{surf-N_xH_y^*} - (E_{surf} + \frac{x}{2}E_{N_2(g)} + \frac{y}{2}E_{H_2(g)}), \quad (4.7)$$

where $E_{surf-N_xH_y}$ is the total energy of the surface and the adsorbate N_xH_y, E_{surf} is the total energy of the system containing only the investigated surface, while $E_{N_2(g)}$ and $E_{H_2(g)}$ are the calculated gas-phase energies of nitrogen and hydrogen molecules, respectively.

For the oxygen containing species, the reference energy of the gas-phase molecule O_2 is wrong in the RPBE exchange-correlation functional. The reason is an erroneous description of the triplet state by DFT [103]. Instead, the energy of water, $E_{H_2O(g)}$ and $E_{H_2(g)}$, has been used. The reaction energy is then calculated as:

$$\Delta E = E_{surf-O_xH_y^*} - (E_{surf} + xE_{H_2O(g)} + \frac{y-2x}{2}E_{H_2(g)}), \tag{4.8}$$

For a thorough understanding, free energy corrections for each reaction intermediate is incorporated.

$$\Delta G = \Delta E + \Delta E_{ZPE} - T\Delta S, \tag{4.9}$$

where ΔE_{ZPE} and ΔS are the reaction zero point energy and reaction entropy, respectively. The corrections for the zero point energy and entropy can be found in section 2.6.

4.3.1 Computational hydrogen electrode

In addition to the entropy and zero point energy corrections, the applied potential driving the electrochemical reaction will influence the free energy landscape for the reactions. To include the effect of an applied potential, the computational hydrogen electrode [80] has been employed, which has previously been very successful in describing a number of electrochemical reactions, such as oxygen [104–106], nitrogen [37,107] and CO_2 reduction [73] reactions. The procedure of employing the computational hydrogen electrode is briefly outlined below.

The standard hydrogen electrode (SHE) is chosen as the reference electrode potential. The chemical potential (the free energy per H) of $H^+ + e^-$ is related to that of $\frac{1}{2}H_2(g)$, see eq. 4.1. For an applied potential of U = 0 V relative to the SHE and a partial pressure of 1 bar of H_2 in the gas phase at 298 K and pH = 0, the reaction free energy of eq. 4.1 is equal to the net reaction of eq. 4.3a - 4.3j and eq. 4.4c - 4.4g at an electrode.

The next step is to incorporate the effects of an applied potential in all reactions involving an electron transfer and for the protons the pH. The free energy shift for a reaction involving n electrons is -neU, and hence the change in free energy reads

$$\Delta G = \Delta E + \Delta E_{ZPE} - T\Delta S - neU, \tag{4.10}$$

where the pH value is set to zero. For pH values different from 0, one needs to add on entropy coorections arising from the concentration dependence of free H^+ energy which gives a shift of $G(pH) = -kT \cdot \ln[H^+] = 2.3 \cdot kT \cdot pH \cdot \ln[10]$. All calculations presented in this thesis are for a pH value of 0.

To drive the electrochemical reaction forward, the reaction should be exergonic, *i.e.* the change in free energy for each electrochemical step described in eq. 4.3a - 4.3j and eq. 4.4c - 4.4g has to be negative. From eq. 4.10, it is evident

that the applied potential can be tuned such that the reaction steps involving a proton transfer can be made exergonic. The specific applied potential that ensures this criteria for all proton transfer reaction in e.q. electrochemical ammonia formation is denoted the "onset" potential. As an example, the potential for making the reaction step 4.3g exergonic is to be determined. The reaction free energy is calculated in the following way:

$$\begin{aligned} \Delta G_{dis,2} &= \Delta G_{NH_2^*} - \Delta G_{NH^*} \\ &= \Delta E_{NH_2} + E_{ZPE,NH_2} - T\Delta S_{NH_2} - eU \\ &- (\Delta E_{NH} + E_{ZPE,NH} - T\Delta S_{NH} - 2eU). \end{aligned} \tag{4.11}$$

The next step is to apply a potential such that this reaction step has negative free energy change. This is accomplished when $\Delta G_{dis,2} = 0$.

$$\begin{aligned} U &= (\Delta E_{NH} + E_{ZPE,NH} - T\Delta S_{NH}) \\ &- (\Delta E_{NH_2} + E_{ZPE,NH_2} - T\Delta S_{NH_2}). \end{aligned} \tag{4.12}$$

Applying the potential U ensures that the reaction occurs spontaneously, as long as the protonation barrier is low.

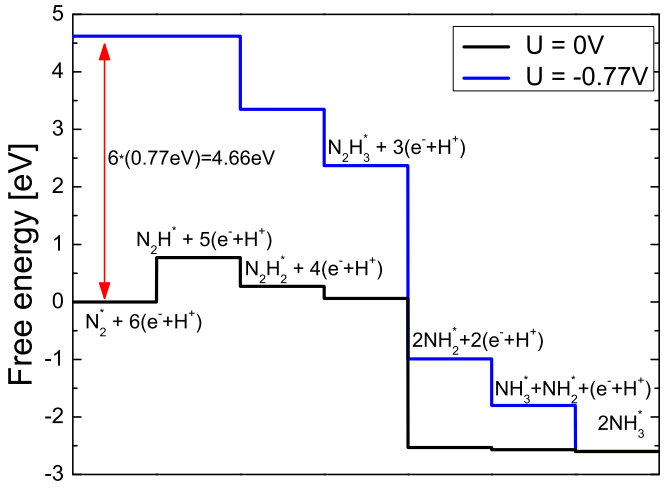

Figure 4.3: *Free energy diagram for the associative mechanism on a Ru M12 nanocluster with and without applied potential. The diagram shows that the production of ammonia on the ruthenium surface can be facilitated at onset potentials of -0.77 V.*

Figure 4.3 shows the free energy diagram for production of ammonia through the associative process on a Ru nanoparticle (see section 6 for more info on this study). The black line is the free energy without an applied potential. The main issue for the reaction on the ruthenium surface is the first protonation, which is an endothermic reaction of 0.77 eV. The blue line shows the new free energy landscape at an applied potential of -0.77 V, where the free energy change for the first protonation step now is 0.0 eV. The electrochemical production of ammonia through the associative mechanism therefore require, an onset potential of -0.77 V. Apart from the energy loss related to the over potential needed to drive an reaction forwards, production of undesired products from the protons and electrons gives rise to a Faradaic loss.

Chapter 5

Brønsted-Evans-Polanyi relations for (de)hydrogenation reactions

This chapter is based on the included Paper A and the chapter includes additional information to what is presented in the paper.

5.1 Introduction

Linear energy relations have proven useful in simplifying the theoretical analysis of a number of catalytic reactions, thereby helping to establish an improved understanding of their underlying trends [42, 108, 109]. The linear energy relations in question are especially the so-called Brønsted-Evans-Polanyi (BEP) relations [31, 95–97, 110–115] describing correlations between transition states and reaction energies, the adsorbate scaling relations [91] describing correlations between the adsorption energies of adsorbed reaction intermediates containing hydrogen with respect to either N, O or C. The relations for carbon can be found in paper A. More generalized, the BEP relations can be viewed as resulting from a scaling relation between reaction intermediates and transition states. By combining transition state scaling relations and adsorbate scaling relations the number of individual parameters that need to be determined in order to describe the energetic trends underlying the kinetics of a complex catalytic reaction can be significantly reduced and often limited to only one or very few descriptors. Good descriptors are typically adsorption energies of some of the key reactive intermediates, or combinations of adsorption energies [34, 116–123].

In the present chapter, I will present an analysis of the transition state energies for 249 dehydrogenation reactions determined by the usage of DFT of small hydrogen containing molecules over mostly close-packed and stepped surfaces, as well as, some over nanoparticles, all surfaces consist of transition metals. Linear energy correlations are observed for the transition state structures leading to transition state scaling relations for all the investigated reactions. Upon implementing a suitable choice of reference systems all the transition state scaling relations form a universality class [97, 111] in which only one single descriptor

determines the transition state for every reaction over all types of surfaces and nanoclusters.

5.2 Computational detail

The calculations were carried out using the DACAPO plane wave Density Functional Theory code [124]. Exchange-correlation effects were described using the RPBE functional [44] with an energy cutoff of 340 eV or more. The ionic cores were described by Vanderbilt ultrasoft pseudopotentials [125]. A slab model with three (or in some cases four) close-packed atomic-layers was chosen to represent the transition metal surfaces describing the close-packed and stepped surfaces. At least one (in some cases two) top layer was fully relaxed and the rest of the metal layers were held at fixed positions. The size of a surface supercell was 2×2 for the close-packed surfaces, and supercell sizes of 1×2, 2×2, and 2×3 were used for the stepped surfaces depending on the size of the adsorbed molecules. The Brillouin zones were sampled using Monkhorst-Pack [81] k-point meshes of $4 \times 4 \times 1$ points or denser. For the M12 nanoparticles, all the 12 atoms were fixed, while the adsorbates were allowed to relax. The M12 nanoparticles was fixed in a planar structure identical to the geometry used in a recent study on CO oxidation [119]. The calculations on the M12 nanoparticles were carried out using only the gamma-point. The transition state energies were calculated using either a bond stretching method [118] or the nudged elastic band method which can be combined with the climbing image method to precisely determine the transition state [72]. Several pathways were tested for each reaction step and in this paper we only report the first order saddle points corresponding to the lowest barrier. Four examples of dehydrogenation transition states for NH_3, H_2O on both closed-packed and stepped surfaces are presented in Fig. 5.1 and Fig. 5.2, respectively.

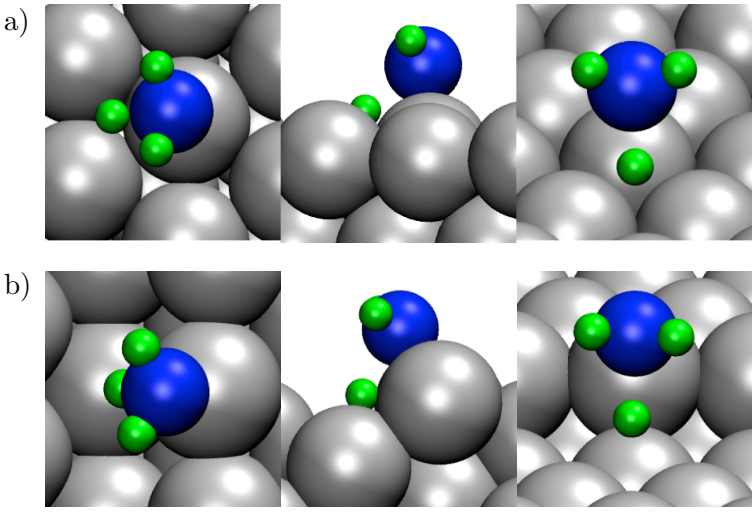

Figure 5.1: *The first dehydrogenation of ammonia on a fcc(111) a) and on a fcc(211) b) surface.*

The maximum coverage on the active sites was a half. The convergence

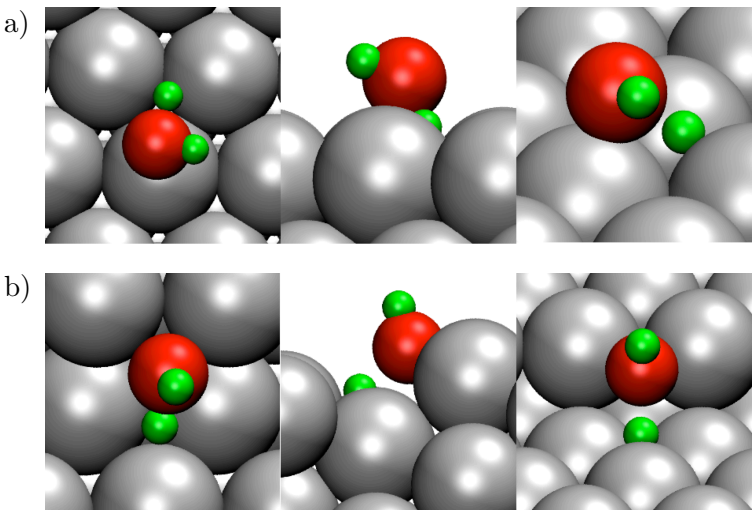

Figure 5.2: *The first dehydrogenation of water on a fcc(111) a) and on a fcc(211) b) surface.*

with respect to, number of layers, cutoff energy, and k-point sampling has been studied elsewhere [126] and I refer to the previous work for a more detailed evaluation of the accuracy of the data presented here.

5.3 Defining transition state and Brønsted-Evans-Polanyi relations

A diagram explaining the reference energy levels used in the transition state scaling relations and in the Brønsted-Evans-Polanyi (BEP) relations for the dehydrogenation/hydrogenation processes is presented in Fig. 5.3. The transition state scaling relations are based on the transition state energy, E_{ts}, and the final state energy, E_{diss}, with respect to the gas phase species [127] CH_4, NH_3, H_2O and H_2, see Fig. 5.3a. Whereas, the BEP relation is based on the reaction energy, ΔE_{diss}, which is the energy difference between the initial and the final state, while the activation barrier, ΔE^a_{diss}, is the energy based on the difference in energy between the initial state and the transition state. This can be seen in Fig. 5.3b.

5.4 Transition state scaling relations

Fig. 5.4 shows a universal transition state (TS) scaling relation for a series of dehydrogenation reactions over a wide range of transition metal surfaces, such as close-packed and stepped surfaces and nanoparticles. The fitted data for the transition state scaling relations for all the dehydrogenation reactions are presented in Table 5.1. Here the data have been arranged in categories of individual, classes, groups and overall. The individual fit is based on only one type of reaction on one surface type, the class is based on a specific reaction on all the types of surfaces, the grouped data are for all data containing either

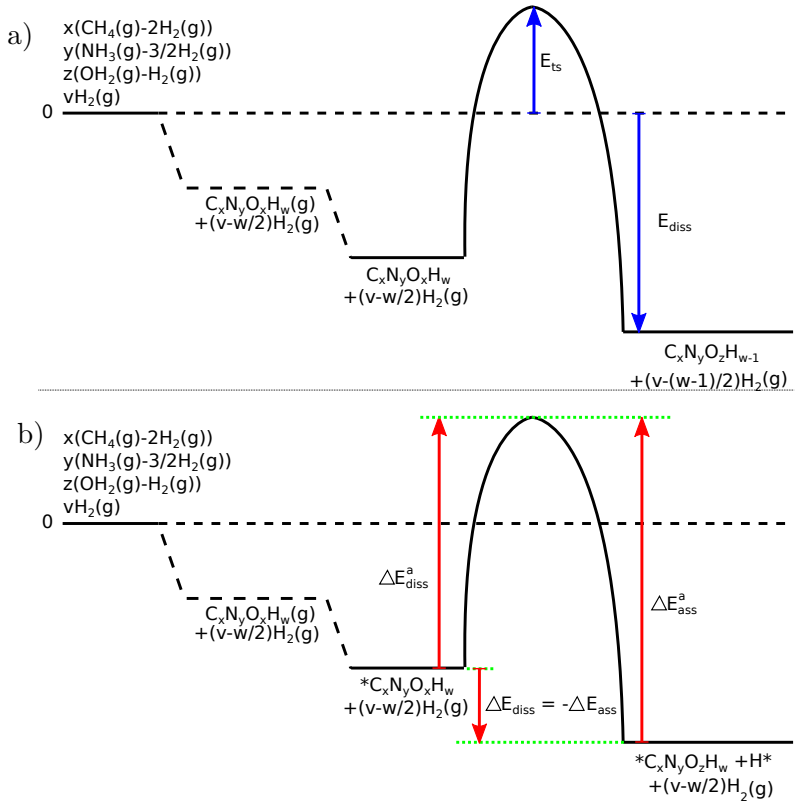

Figure 5.3: *The definition of energies used in the analysis of the hydrogenation/dehydrogenation processes. All energies are with respect to the gas-phase CH_4, NH_3, H_2O, and H_2. Top-view. a) The transition state (TS) scaling relation are based upon the energies given by the two blue arrows denoted as E^{ts} for the transition state energy and E_{diss} for the final state energy. Bottom-view. b) The Brønsted-Evans-Polanyi (BEP) relations use another reference energy. The BEP relations are based upon the activation barrier $\Delta E^a_{diss/ass}$ and the reaction energy $\Delta E_{diss/ass}$ as defined in the bottom panel and presented with red arrows.*

nitrogen, carbon or oxygen, and lastly the overall fit is based on all reactions on all types of surfaces.

The mean absolute error (MAE) of the fitted line in Fig. 5.4 is 0.28 eV. The correlation is certainly not perfect, and compared to the so-called chemical accuracy which is typically defined as 1 kcal mole^{-1} or approximately 40 meV, the error on a prediction based on using the linear relation shown in Fig. 5.4 will typically be one order of magnitude larger. The prediction error, however, has to be seen in the light of how well a typical GGA exchange-correlation functional can describe the reaction and transition state energies. The error in currently employed exchange-correlation functionals could easily be of the same size as the error from predictions based on the transition state scaling relations. The errors in the presented relations are certainly small enough to rapidly produce a first rough estimation of activation barriers for hydrogenation/dehydrogenation reactions. The universal TS scaling relation relates the energies of transition states with final states of dehydrogenation reactions [115]. Such correlation originates from the geometrical similarity of the structures of transition states

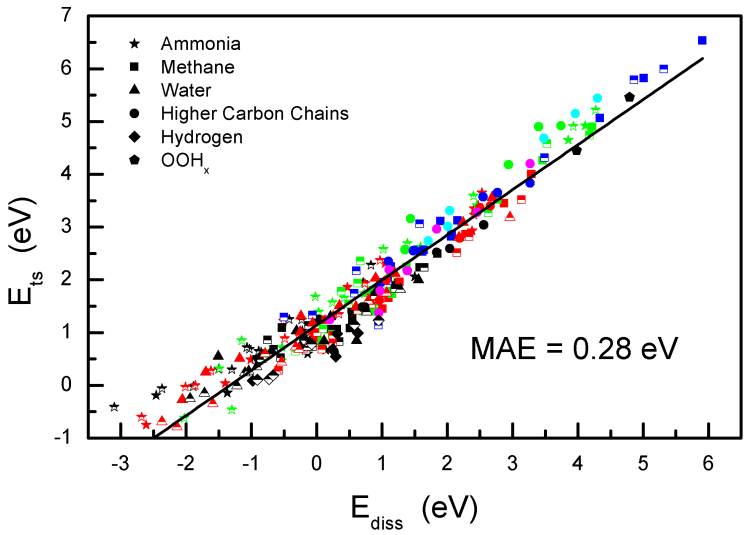

Figure 5.4: *Transition state energies plotted against dissociation energies with respect to energies of gas-phase CH_4, H_2O, NH_3, and H_2. The fully filled symbols refer to dissociation over close-packed surfaces, and the half-filled symbols refer to dissociation over stepped surfaces and OOH_x species have been dissociated on a M12 nanocluster. The colors represent the different hydrogen content in the molecules, where black is the first dehydrogenation step, red is the second step, green is the third step, and blue is the fourth dehydrogenation step.*

and final states [97].

Fig. 5.4 collects different types of dehydrogenation reactions on transition metal surfaces and clusters. The deviation of the points comes predominantly from the difference of the structures of the reactions. As expected from Table 5.1, the MAE becomes smaller when we look into a certain reaction or a series of similar reactions, since the structures are more similar to each other. The MAE is typically smaller than 0.15 eV for an individual reaction over a given geometry of an active surface site, as evidence in Table 5.1 show. When looking at several reactions simultaneously or several surface geometries, the uncertainty of a prediction made from their common linear regression fit will generally increase, but in all cases stays below 0.3 eV. It is therefore useful to see Table 5.1 as a hierarchy of accuracy that allows treating a particular reaction more accurately if it resembles one of the specifically presented reactions, whereas the overall universal TS scaling can be used as a first approach for a random hydrogen bond breaking reaction that has not been specifically treated in this study.

Table 5.1: The fitted parameters of the transition state scaling relations. TS scaling relations for C containing can be seen in paper A.

Reaction	Surface	Slope	Constant [eV]	MAE [eV]
H_2O + 2* → OH*+H*	Close packed	0.47±0.10	0.99±0.07	0.20
	Step	0.77±0.02	0.95±0.04	0.17
	All	0.58±0.05	0.94±0.04	0.16
OH* + * → O*+H*	Close packed	0.75±0.03	1.32±0.04	0.12
	Step	0.63±0.03	0.92±0.03	0.21
	All	0.78±0.03	1.13±0.05	0.20
Water group	All	0.74±0.03	1.06±0.04	0.20
NH_3* + *→ NH_2*+H*	Close packed	0.57±0.09	0.95±0.11	0.24
	Step	0.69±0.05	1.45±0.07	0.14
	All	0.59±0.06	1.19±0.09	0.23
NH_2* + *→ NH*+H*	Close packed	0.81±0.03	1.26±0.05	0.15
	Step	0.78±0.04	1.41±0.05	0.16
	All	0.79±0.03	1.32±0.04	0.16
NH* + *→ N*+H*	Close packed	0.92±0.04	1.09±0.08	0.12
	Step	0.91±0.04	1.41±0.09	0.17
	All	0.87±0.03	1.34±0.07	0.19
Ammonia group	All	0.82±0.02	1.33±0.04	0.24
H_2(g) + 2*→ 2H*	Close packed	0.67±0.06	0.69±0.04	0.08
	Step	0.54±0.14	0.60±0.08	0.11
Hydrogen group	All	0.61±0.07	0.65±0.04	0.10
Universal	All	0.86±0.01	1.14±0.02	0.28

5.5 Brønsted-Evans-Polanyi scaling relations

Fig. 5.5 shows the BEP relations of the whole set of dehydrogenation reactions. The MAE of 0.27 eV is close to that of the above-discussed universal TS scaling relation. The practical performance of these two relations with respect to estimation of activation energies should be very similar, based on the fact that their MAEs are very close.

Although the universal BEP relation in Fig. 5.5 may at a first glance look less presentable than the universal TS scaling relation, we would like to emphasize several merits of it. The first merit of BEP relations is of course the clear trend reflected by the relations. Since activation energies and reaction energies are typical experimentally measured properties for the analysis of catalytic reactions, rather than the transition state total energies and final state total energies with respect to a gas phase reference it may also be easier to correlate theory and experiments using the BEP relations. The TS scaling relations are (in the present study) based on the structural similarities of the transition states and the final states of a reaction. Such direct similarity between states generally only holds for a limited range of surface reactivity. On the late transition metals there will be a tendency towards having late transition states, and over the early transition metals the transition states will also be earlier. The TS scaling relations (in the form presented above) will thus have a relatively larger MAE when applied to reactions over early transition metals. Therefore it makes more sense to use

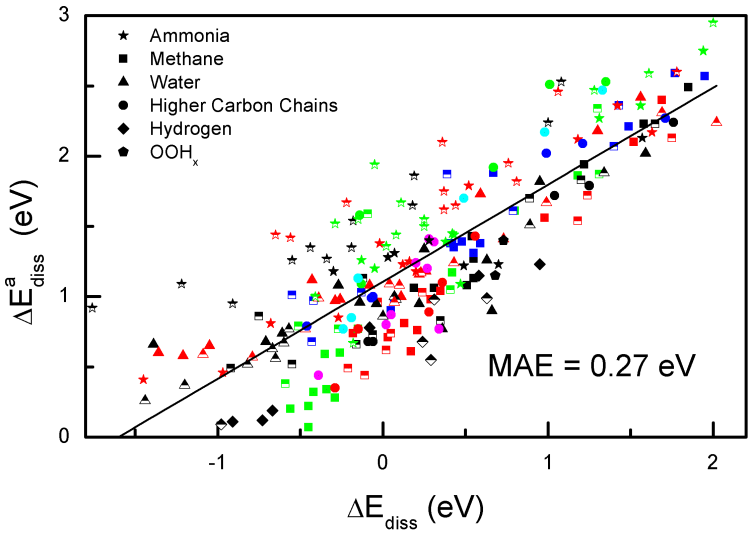

Figure 5.5: *Activation energies, ΔE^a_{diss}, plotted against reaction energies, $\Delta_{E_{diss}}$, of the dehydrogenation reactions. The fully filled symbols refer to data on close-packed surfaces, and the half filled symbols mean the data on step surfaces. The colors represent the different hydrogen content in the molecules, where black is the first dehydrogenation step, red is the second step, green is the third step and blue is the fourth dehydrogenation step.*

the TS scaling relations in the presented form for reactions over surfaces of a rather similar reactivity. The BEP relations correlate the activation barrier with contributions from both initial and final states. Therefore the BEP relations tend to be valid for the catalytic reactions in a larger window of variation of the surface reactivity. The shift in similarity of the transition state structures with initial and final states thus gives rise to a slightly v-shaped distribution of errors in Fig. 5.4, whereas the noise distribution is more homogeneous in Fig. 5.5.

The fitted parameters of separate BEP relations of the dehydrogenation reactions are listed in Table 5.2. It is found that the MAE becomes gradually smaller from the whole set of data compared to similar groups of reactions and one reaction. The reason is that the scattering caused by the difference of geometric structures has to be to a large degree eliminated when only focusing on similar reactions. Hence, using parameters for a certain reaction will yield high accuracy for that or very similar reactions. The parameters for grouped reactions and the universal relation are also useful for fast calculations to aquire preliminary and rough trends. This becomes useful when not all parameters are available or in cases where the demand for accuracy is less strict.

Table 5.2: The fitted parameters of the BEP relations. The BEP relations for C containing adsorbates can be seen in paper A.

Reaction	Surface	Slope	Constant [eV]	MAE [eV]
$H_2O + 2^* \rightarrow OH^*+H^*$	Close packed	0.44±0.10	1.04±0.07	0.19
	Step	0.57±0.03	1.00±0.02	0.06
	All	0.51±0.05	1.01±0.04	0.14
$OH^* + ^* \rightarrow O^*+H^*$	Close packed	0.62±0.06	1.23±0.05	0.16
	Step	0.59±0.04	1.08±0.03	0.09
	All	0.59±0.03	1.15±0.03	0.17
Water group	All	0.57±0.03	1.09±0.03	0.15
$NH_3^* + ^* \rightarrow NH_2^*+H^*$	Close packed	0.46±0.03	1.21±0.09	0.14
	Step	0.57±0.06	1.65±0.05	0.13
	All	0.42±0.08	1.47±0.06	0.20
$NH_2^* + ^* \rightarrow NH^*+H^*$	Close packed	0.68±0.05	1.23±0.05	0.14
	Step	0.57±0.08	1.66±0.08	0.19
	All	0.68±0.06	1.41±0.06	0.21
$NH^* + ^* \rightarrow N^*+H^*$	Close packed	0.79±0.09	1.13±0.09	0.11
	Step	0.74±0.11	1.45±0.09	0.19
	All	0.72±0.08	1.35±0.07	0.19
Ammonia group	All	0.61±0.04	1.43±0.04	0.23
$H_2(g) + 2^* \rightarrow 2H^*$	Close packed	0.67±0.06	0.69±0.04	0.08
	Step	0.54±0.14	0.60±0.08	0.11
Hydrogen group	All	0.61±0.07	0.65±0.04	0.10
Universal	All	0.69±0.03	1.11±0.02	0.27

5.6 Scaling relations

According to the scaling relations, the binding energies of a series of hydrogen-containing molecules are linearly correlated with the binding energies of their central atoms [128]. Fig. 5.6 shows that the linear relations are also valid for the correlation of the transition state energies for hydrogenation/dehydrogenation reactions and binding energies of the central atoms. Furthermore, Fig. 5.7 shows that the adsorption energies of hydrogen scale approximately with the adsorption energies of N and O. The linear TS scaling relations and the BEP relations are therefore both manifestations of the scaling relation between reaction intermediates and transition states with the adsorption energies of the central atoms (those atoms in contact with the surface). Because the transition state for dehydrogenation reactions is very similar over close-packed and stepped surfaces or a nanoparticle, there is no major geometrical effect for the single TS scaling relation and the BEP relation for all treated hydrogenation/dehydrogenation steps (all points fall on one line in Fig. 5.5). For a single reaction, however, there can be a significant electronic effect going from a close-packed surface to a more under-coordinated surface, such as a step surfaces or a surface on a nanocluster. This is a particular feature of hydrogenation/dehydrogenation reactions and somewhat different from many other bond-breaking reactions on transition metal surfaces, where steps are typically many orders of magnitude more reactive than the close-packed surfaces [112, 129].

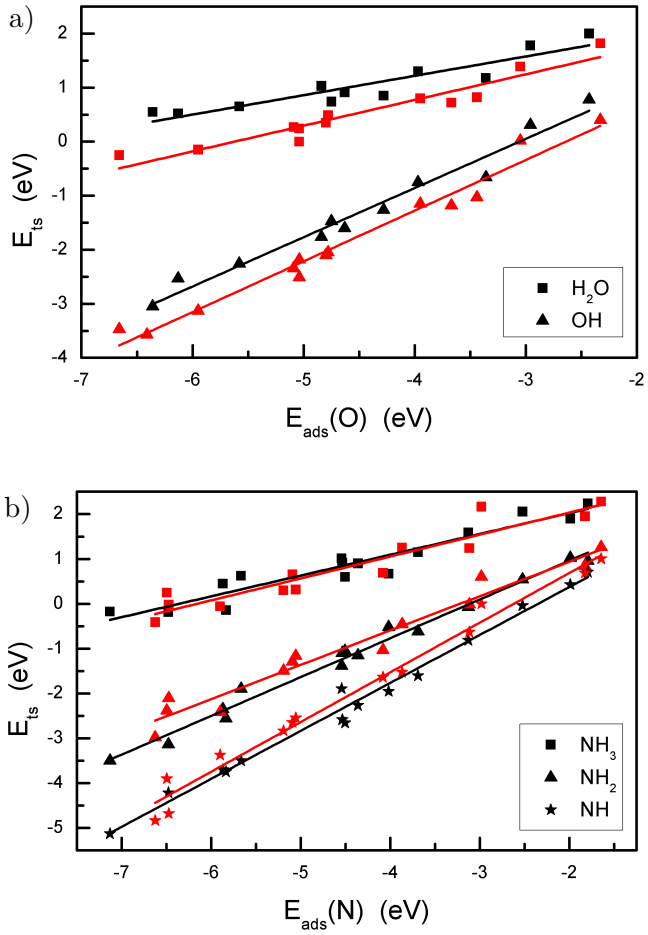

Figure 5.6: *The transition state energies of dehydrogenation reactions plotted against the adsorption energies of (a) O and (b) N with respect to their gas-phase energies. The black and red colors indicate the results on close-packed and stepped surfaces respectively.*

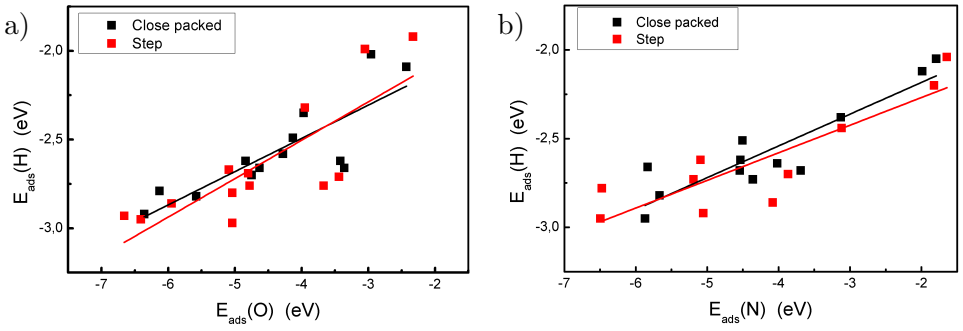

Figure 5.7: *The adsorption energies of H plotted against the adsorption energies of (a) O and (b) N with respect to their gas-phase energies.*

If we now more generally consider a transition state scaling relation to represent a general correlation between the energy of the transition state and some combination of relevant adsorption energies, then the BEP relation is one such

particular choice of linear combination of the relevant adsorption energies.

5.7 Conclusion

In this section, a universal transition state scaling relation for dehydrogenation reactions over close-packed and stepped surfaces as well as nanoparticles of transition metals have been presented. One simple relation is demonstrated to cover a very broad class of hydrogenation/dehydrogenation surface chemistry over transition metals, since all of the investigated reactions, metals and surface geometries can be reasonably well approximated by one universal linear transition state scaling relation. This holds promise that in the future the search for new hydrogenation catalysts may be facilitated by the fact that a first rough initial screening can be carried out based on this general linear energy relation without the need for performing full DFT calculations. Together with the adsorbate scaling relations for various reaction intermediates, the universal BEP relation for (de)hydrogenation reactions can become a tool with predictive power and give a fast and semi-accurate first-hand knowledge for a number of catalytic reactions, which can then subsequently be analyzed in greater detail.

Chapter 6

The effect of under-coordination for ammonia synthesis: A study of M12 nanoclusters

This chapter is based on the included Paper B and the chapter includes additional information to what is presented in the paper.

6.1 Introduction

For electrochemical production of ammonia the main issue is the competing hydrogen evolution that decreases the Faradaic effeciency of the ammonia production. In this chapter, I will present a model system study of the M12 nanocluster, that, with its extreme under-coordination, should explore the discrepancy between the hydrogen evolution insensitivity to under-coordination [39] and the under-coordination sensitivity for ammonia production [25, 37, 38]. The study has focused on most transition metals to gain insight into trends underlining electrochemical ammonia formation at highly under-coordinated reaction sites. These trends will be compared to calculations performed on stepped fcc(211) surfaces.

6.2 Model system

6.2.1 M12 nanocluster

The model system investigated in this chapter is the M12 nanocluster. It has previously served as a model system for under-coordination for CO oxidation [40]. The model system is used as a probe for the most possibly under-coordinated active site. The nanocluster contains 12 metal atoms, where the atoms are positioned in two layers, with six atoms in each layer. Each layer follows the fcc close-packed surface structure creating a triangle, see Fig. 6.1a. The layers are

placed above each other, following the normal close-packed fcc surface, see Fig. 6.1.

For the M12 nanocluster two lattice constants were used for each of the investigated metals. The first lattice constant was determined from calculations of the bulk lattice constants in the fcc structure (denoted fixed M12). The second lattice constant was determined by allowing the M12 nanocluster to relax into a lattice constant where the lowest energy configuration is obtained (denoted relaxed M12). The obtained lattice constants are presented in table 6.1. For both M12 nanoclusters, the fixed and the relaxed, the structure of the nanocluster was kept fixed during all calculations.

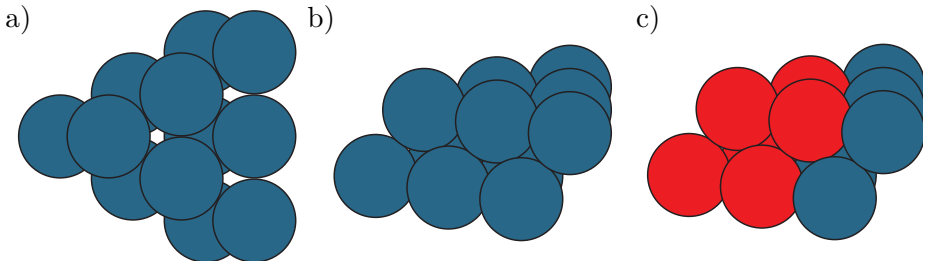

Figure 6.1: *a: The M12 nanocluster seen from above. The close-packed structure is shown and the layers are arranged as two fcc close-packed layers would be in a normal fcc structure. b: The M12 nanocluster seen from the side. c: The red atoms are the ones where the intermediates are allowed to bond to.*

Table 6.1: The lattice constants used in this study for M12 nanocluster (fixed/relaxed) and for the fcc(211) stepped surface the bulk lattice constants were used.

	Relaxed M12	Fixed M12
Metal	Lat. const. [Å]	Lat. const. [Å]
Ag	4.06	4.24
Au	4	4.22
Co	3.35	3.57
Cu	3.52	3.7
Fe	3.5	3.54
Mo	3.66	4.04
Nb	3.84	4.24
Ni	3.37	3.57
Pd	3.81	3.99
Pt	3.78	4.00
Rh	3.64	3.88
Ru	3.58	3.86
Sc	4.34	4.68
Ti	3.8	4.14
V	3.52	3.9
W	3.72	4.08

Fixing the structure of the M12 nanocluster will not replicate the structural deformation that occurs to catalysts surfaces during a catalytic cycle. However, due to the nature of the model system, adsorption of atoms or molecules to the surfaces will make huge deformations and a determination of adsorption energies will be very difficult. Furthermore, the support layer that helps nanoparticles to hold its overall shape and decrease sintering effects have not been included in the study. The influence of a support can be a whole study in itself. The aim of this study was focused on capturing trends for electrochemical production of ammonia, and not on structural effects on working nanoparticle catalysts.

In this study, the analysis was limited to the adsorption sites indicated by the atoms marked with red in Fig. 6.1c for the reaction intermediates, presented in eq. 4.3c-4.3h and 4.4c-4.4g. The red marked sites are chosen because they are highly under-coordinated and have other features than those of the back side of the clusters which resembles a step closer, but lack the stabilizing terraces and the red marked sites have been analyzed in greater detail in ref. [36].

6.2.2 Step surfaces

Since the computational framework for this work was chosen to be GPAW, a fairly new DFT implementation, not that many calculations of adsorption energies of the ammonia synthesis reaction intermediates had been performed. The fcc(211) surface was therefore picked as a reference system and calculations of the reaction intermediates was performed on the surface. We have chosen only to use the fcc framework for all the stepped surfaces, because it gives a uniform investigation and hint to trends across the investigated transition metals. This ensured that the differences in adsorption energies between the under-coordination of the M12 nanocluster and the fcc(211) step surface could be extracted properly.

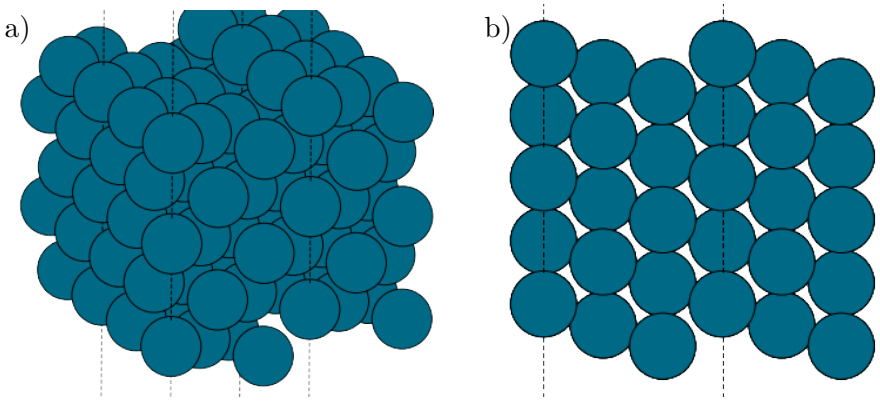

Figure 6.2: *a: The step fcc(211) surface seen above and from the side. b: The step fcc(211) surface seen directly from the side. In these pictures there are three atoms between each step and a five layer slab has been used. There are 30 metal atoms in the slab prior to adding any adsorbates.*

The fcc(211) surface is a stepped surface with three atoms between each step, see fig. 6.2. The dashed lines on the figures confine the 2x3 unitcell used in this study. It has high concentration of steps on the surface and has in many studies been used to examine the effect of undercoordination [25, 36–38]. One

can argue that this step surface has a step density that is too high, and hence the terrace sites are not representative of sites on a more flat surface. This is not a very important issue in theoretical studies, since terrace sites can easily be simulated using close-packed surfaces. Furthermore, increasing the number of atoms between each step from three to four would also increase the number of atoms in each calculation by approximately 30 %, thereby significantly increasing the computational time. But the change in reactivity between step surfaces with high or low concentrations of step sites are extremely minor.

The step fcc(211) surface does not capture the two well-known α and β step sites [130]. These two sites have been shown to be key reaction sites that has been crucial in understanding the reactivity of the Ru hcp step surface [25,131]. In this study, focus has been on capturing the overall trends for the step surfaces, rather than studying specific surface phenomena.

6.3 Computational details

The calculations were carried out with DFT [50,51] using the RPBE exchange correlation functional [44] in the projector augmented wave method [69,132] as implemented in the `GPAW` code [45,46,68]. A grid of (3,3) for the finite difference stencils have been used together with a grid spacing of 0.18 Å, at least 20 free bands above the Fermi level and a Monkhorst-Pack [81] k-point sampling of 2×2×2. A 7 Å vacuum layer around the nanocluster has been applied. In solving the electronic density self-consistently, the convergence criteria have been chosen such that the changes in energy between each iteration were $< 10^{-5}$ eV and density was 0.0001 electrons pr. valence electron and for most systems chosen orders of magnitude lower. Spin polarized calculations were also performed for metals that usually have a magnetic moment, such as Fe, Ni and Co although the magnetic moment could depend on the fixed geometry. In all calculations a Fermi smearing of 0.0001 eV have been used. The atomic simulation environment `ASE` [47] was used to set up the atomic structure of these systems. All relaxations of the adsorbates (N, H, NH, etc.) sitting on the bulk M12 nanocluster were carried out using the BFGS optimizer within `ASE`.

For the reference calculations on the fcc(211) stepped surface, a slab with five layers was utilized and in the direction following the edge of the step it was repeated once such that each layer consisted of 3 x 2 atoms. Of the five layers that were employed, the top two were allowed to relax and a vacuum of 7 Å on both sides of the slab was used. The utilized computational criteria only differ from the clusters in that a Monkhorst-Pack k-point sampling of 4×4×1 was used, and the Fermi smearing was 0.0001 eV.

6.4 Results and discussion

In this section, I will present the adsorption sites of the reaction intermediates and the corresponding adsorption energies defined by eq. 4.8 plotted as linear scaling relations for the studied geometric structures. With these tools, the

construction of volcano plots showing the onset potential for each of the reaction mechanisms for electrochemical N_2 fixation is possible.

6.4.1 Applying the d-band model

As stated in chapter 3 the d-band center is an important asset when describing and understanding the reactivity of surfaces. It is expected that the d-band for a metal surface atom should change appearance when the surface composition is varied. I will present two examples of how the extreme under-coordination of the model system investigated in this chapter has changed form and position in comparison to less under-coordinated surfaces. First, a comparison of the d-band appearance of rhodium for the following structures/surfaces: a fcc bulk structure, a close-packed fcc(111) surface, a stepped fcc(211) surface and the fixed M12 nanocluster (with the bulk lattice constant). The coordination number for these structures are 12, 9, 7 and 3, respectively.

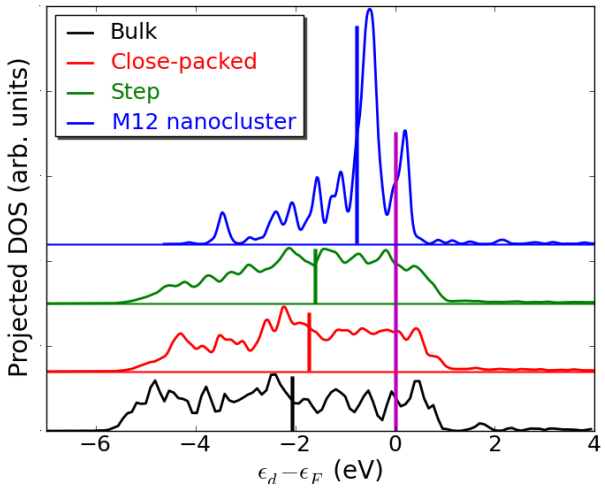

Figure 6.3: *The d-band for Rh in bulk, as atom in the close-packed fcc(111) surface, as step atom on the stepped fcc(211) surface and as atom on the M12 nanocluster. The Fermi level is marked with the purple vertical line. The vertical line for each structure type illustrates the position of the d-band center.*

The d-band is presented in Fig. 6.3 for four rhodium surfaces. The composition of the d-band have the same form for bulk structure, close packed and stepped surfaces, where the d-band are smeared out with fewer peaks. In contrast, the d-band for the M12 atom is very localized around fewer peaks. The reason is that for bulk structures, close packed and stepped surface they have plenty of neighboring metal atoms, resulting in an overlap of the electrons and a smearing of energies. The surface atom on the M12 nanocluster has only three neighbors, and the neighbor atoms also have very few neighbors (5, 7, and 7 respectively), which result in a low overlap between electrons, resulting in very localized bands.

It is also clear from the figure that the d-band narrows as the studied metal atom is getting more under-coordinated. The result is thus a shift for the band,

such that it can sustain the filling degree of the d-band. According to the d-band model, a higher lying d-band center should result in a more reactive surface. I can conclude, that M12 nanoclusters indeed are more reactive than the other three surfaces and we should expect stronger adsorption of adsorbates on the surface.

Fig. 6.4 shows the d-band center of the fixed and relaxed M12 nanocluster for all studied metals. For the noble metals the d-band are very localized and deep-lying, while as the metals become more reactive (the adsorption of N is used to order the metals) the band moves up and the width increases. There are small shifts between the d-bands for fixed M12 nanoclusters and relaxed M12 nanoclusters. The width of the d-band for relaxed M12 nanoclusters increases

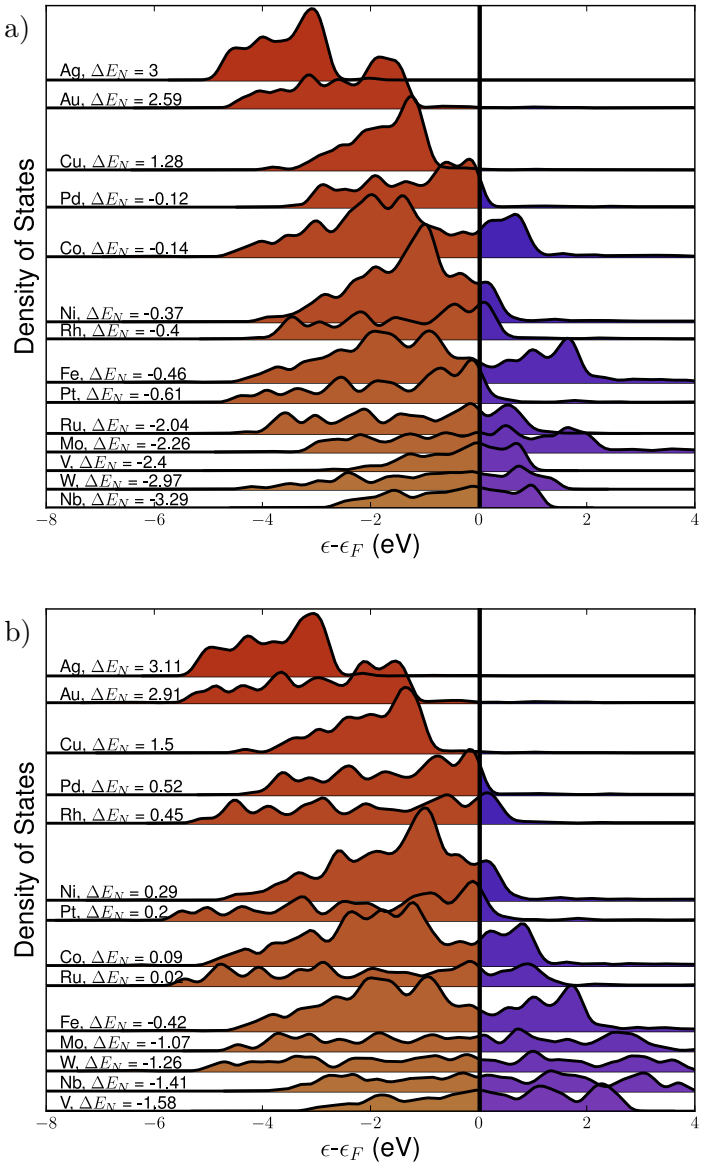

Figure 6.4: *The d-band of the fixed and relaxed M12 nanoclusters. a) the fixed M12 nanoclusters and b) the relaxed nanoclusters.*

compared to the width of fixed M12 nanoclusters, which can visually be seen on Fig. 6.4, while the position of the d-band centers are moving down for all metals (except W and Nb), see table C.2 in appendix C. This is well described as an stress/strain [133] effect caused by the difference in lattice constant between the two M12 model systems. The reason is less overlap between atoms for the fixed M12 nanocluster, and leads to a narrowing of the d-band. To ensure the same filling degree the d-bands have to moves up. In total, this should result in less reactivity of relaxed M12 nanoclusters compared to fixed M12 nanoclusters.

The d-bands are calculated using the projected density of states method which is described in section 2.5.4. To ensure that the d-band was described as accurately as DFT can, knowing that DFT has it limitations due to being a ground state theory and therefore only should be valid for ground state properties, very high amount of bands above the Fermi level was employed in the setup. For the spin polarized calculations, both the bonding and the antibonding states have been taken into account.

6.4.2 Adsorption sites

The adsorption of the studied reaction intermediates on the ruthenium M12 nanocluster will be used to illustrate the adsorption sites and this metal resembles the characteristics of all the metals studied here. Among the studied metals, from the very reactive metals such as Sc, Ti, and Nb to the very noble metals such as Au, Ag, and Cu, there are small variations in the adsorption sites. However, the M12 nanocluster have many similar types of adsorption sites, which can be divided into the usual adsorption-site subgroups such as hollow, bridge, and on-top. The adsorption sites in a subgroup will be slightly geometrically different, see Fig. 6.1 where e.g. there are three different hollow sites on the red marked atoms, and for each of the metals the specific electronic properties will be different. This will lead to different sites being preferred for the different metals. But the type of sites are close to identical throughout the investigated metals across all reaction intermediates, with the only exception being N_2 (this will be discussed in greater details later). In figure 6.5, the adsorption sites on ruthenium M12 nanocluster can be seen.

In fig. 6.5(1) the adsorption site for N_2 is shown. For the reactive metals, the nitrogen molecule prefer to bind to the surface in a di-sigma bond. Here, the nitrogen atoms are bonded to two different metal atoms on the surface and among the studied reactive metals the most stable sites were edges. For the more noble metals bonding of the N_2 molecule vertically to the surface was preferred. Here, one atom was attached to the surface and the other nitrogen atom is not in contact with the surface and acting as an antenna. The difference in adsorption energy between these two types of bonds are on the order of 0.1 to 0.3 eV. It should be noted that for the very reactive metals, the N_2 molecule had very few stable adsorption configurations since the splitting of the N-N bond and creation of two N^* on the surface is exothermic. This is in good agreement with the literature [134], where the barrier for N_2 dissociation has been shown to be much lower on reactive metals compared to noble metals and thus obeying the BEP relations.

The nitrogen adatom adsorbs in a hollow site. For hydrogen, the H_2 molecule

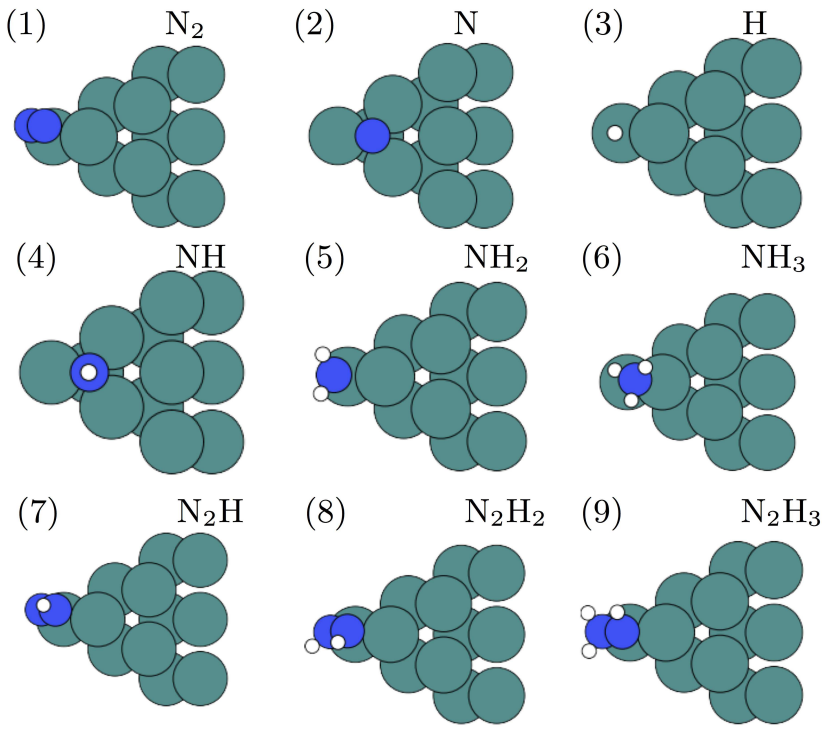

Figure 6.5: *The most stable adsorption sites for the reaction intermediates of both the dissociative and associative mechanism on the ruthenium M12 nanocluster. The dark blue atoms are nitrogen, the small atoms are hydrogen and the light atoms are ruthenium. The adsorption sites presented for the adsorbates on the Ru M12 nanocluster are only representative of the adsorption site type (hollow, bridge, ontop) and do not describe the actual bonding site that are the most stable for the other metals, which means a N atom could bind more strongly to another hollow site on a different metal studied in this work.*

was very rarely stable on the surface and would split into two hydrogen adatoms on the surface. The bonding site of the hydrogen adatom is on figure 6.5(3) shown to be a bridge site, but the difference in adsorption energy between the different types of adsorption sites are very small. For NH, NH_2 and NH_3 they bind to hollow, bridge and ontop sites respectively, see fig. 6.5(4-6).

The N_2H_x species on the M12 nanoclusters prefer to bind to a bridge site, where each N atom is bound to different metal atoms, similarly to a di-sigma bond. The configuration changes slightly depending on the number of hydrogen atoms in the surface species. Looking carefully at the figures of the N_2H_x, on fig.

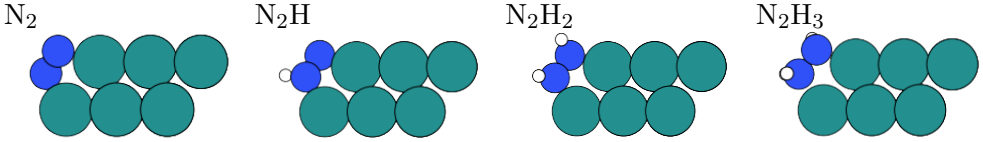

Figure 6.6: *The bonding sites for molecules with a N-N backbone on the M12 nanocluster. The change in internal bonding and the bonding length to the surface are illustrated. The details visualized here, is decribed in greater details in Table 6.2.*

6.6, it is possible to see an increase in the internal bonding length as the number of hydrogen is increased and that one of the nitrogen atoms is further away from the metal atom than the other nitrogen atom. This represent the internal weakening of the N-N bond and is a key factor in the associative mechanism. A weaker bond between the metal and one of the nitrogen atoms is observed, when more hydrogen atoms are present. In most cases, the molecules (N_2H_x) are therefore mostly bound through only one of the nitrogen atoms. Again, the

Table 6.2: The length of various bonds for gas-phase and adsorbed molecules with a N-N backbone. The adsorbed molecule configuration be seen in fig. 6.6. The influence on the N-N bond length is caused by the interactions with the metal *d*-band, as well as the with hydrogenation of the N-N backbone.

	M12 nanocluster				
Bonding	N_2(g)	N_2^*	N_2H^*	$N_2H_2^*$	$N_2H_3^*$
N-N [Å]	1.107	1.187	1.275	1.36	1.467
N^{up}-surface [Å]		2.073	1.945	2.008	2.037
N^{lo}-surface [Å]		1.994	1.989	1.996	2.131
N-H [Å]			1.036	1.034	1.029
N-H [Å]				1.030	1.028
N-H [Å]					1.028

Ru surface is used to show these details in internal N-N bond length, N-H bond length and the N to metal bond length, see table 6.2.

The reaction intermediate N_2H_4 has not shown to be stable on any of the studied metals. The internal N-N bond strength is by the successive protonations weakened to an extent, where it is more favorable to split the molecule into two smaller molecules.

6.4.3 Scaling relations

In section 3.5, it was showed that there exist a linear correlation between the adsorption energies of the reaction intermediates for ammonia formation and the adsorption energy of nitrogen. These relations for the M12 nanocluster will be presented in this section.

In fig. 6.7 the adsorption energy for NH, NH_2 and NH_3 is plotted as a function of the adsorption energy of N adatoms on the relaxed M12 nanocluster. The obtained data confirms that there is linear relations, such as described in eq. 3.4, for all NH_x species on this very under-coordinated structure. The slopes match to a large extent the predicted slopes calculated by eq. 3.5, that relates the slope and valency of N. For NH, NH_2, and NH_3 the slopes are 0.72, 0.46, and 0.05. For both the fixed M12 and the relaxed M12 nanoclusters the trend for the slope is the same, see Fig. 6.8a-c. It is worth noting that the scaling relation holds true for both lattice constants used for the M12 nanoclusters. The only difference between the two types M12 nanoclusters are an electronic effect that shifts the binding energy of a metal with a bulk lattice constant along the line to the adsorption energy of the same metal with a relaxed lattice constant. The adsorption energies of the reaction species show that the M12 nanocluster with the bulk lattice constant is more reactive than the relaxed M12 nanocluster.

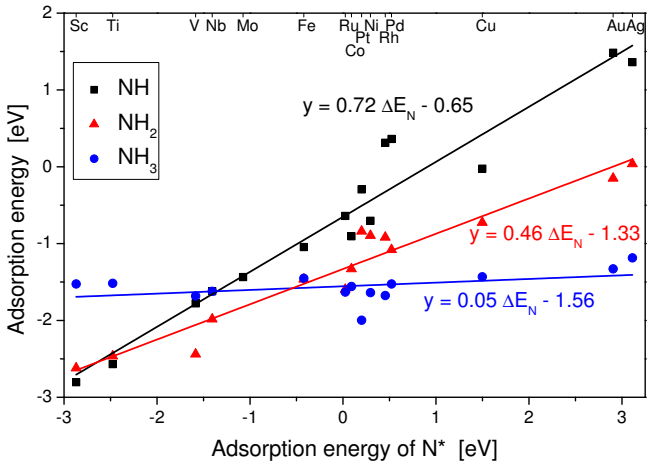

Figure 6.7: *The scaling relations for NH_x species on the relaxed M12 nanoclusters consisting of transition metals.*

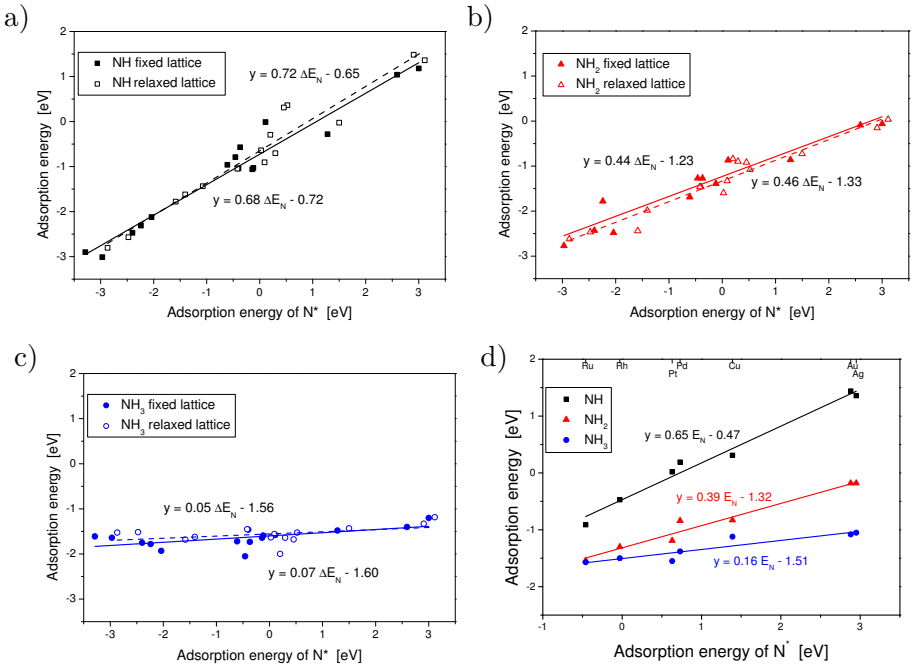

Figure 6.8: *Scaling relations, a) of the NH adsorbate, b) of the NH_2 adsorbate, and c) of the NH_3 adsorbate for both the fixed and relaxed M12. d) Scaling relations of the NH_x adsorbates on the stepped fcc(211) surface.*

This is to be expected due to the effects of stress and strain that has been shown previously by Nørskov *et al* [135]. The fitted values of the slopes are in good agreement with what we would have expected from results obtained in earlier studies of the scaling relations for these species on close-packed and stepped surfaces. We can not directly compare these calculated scaling relations with the previously described relations of NH_x species, since the underlying computational *ab initio* codes are different. Therefore, reference calculations of similar relations for a lower number of stepped fcc(211) surfaces have been

carried out, see Fig. 6.8d, and the slopes α(x) and the constants κ(x) are presented in table 6.3. The variations in the constants between the two systems are very small and close to the uncertainty of DFT calculations. It is therefore not possible to define a conclusive geometrical effect, of -0.05 eV to -0.25 eV, when going from the stepped fcc(211) surface to this highly under-coordinated surface. However, the electronic effect (which is the movement down along the line) is somewhat more noticeable, in the order of 0.1-0.6 eV for the bulk M12 nanoclusters. For the relaxed M12 nanoclusters the electronic effect is small. Comparing these effects with the previous obtained shifts between close-packed and stepped surfaces the geometrical effect observed here is minor [128, 129]. The fixation of the metals in the M12 structure will, however, influence the calculated adsorption energies and hence effect the determined scaling relations. Structures with or without adsorbates would all have had lower energy, if the structure were allowed to relax fully but this study is focused on determining trends in such under-coordinated structures. Calculations with completely free metal atoms will be difficult to systematically examine in this specific case, with a model system that is far from known geometrical stable structures.

Table 6.3: The energy scaling relations for all reaction intermediates for ammonia synthesis on the M12 nanocluster for both relaxed and bulk lattice constants structures and comparing them to the fcc(211) stepped surface. The energy relations are with respect to an adsorbed N. It has to be noted that the number of metals for the stepped surface is not as large as for the M12 nanocluster study.

	fcc(211)		M12 relax		M12 fixed	
Adsorbate	α(y,x)	κ (eV)	α(y,x)	κ (eV)	α(y,x)	κ (eV)
N_2	0.31	-0.47	0.26	-0.60	0.46	-0.63
H	0.23	-0.49	0.2	-0.48	0.17	-0.52
NH	0.65	-0.47	0.72	-0.65	0.68	-0.72
NH_2	0.39	-1.32	0.46	-1.33	0.44	-1.23
NH_3	0.16	-1.51	0.05	-1.56	0.07	-1.60
N_2H	0.57	0.21	0.77	0.05	0.81	0.01
N_2H_2	0.54	0.01	0.66	-0.15	0.68	-0.19
N_2H_3	0.46	-0.25	0.50	-0.28	0.44	-0.30

In fig. 6.9, the scaling relations for the adsorption energy of a N_2 molecule and a H adatom are plotted against the adsorption energy of N adatoms. The slope for the adsorption energies of 0.2 for H adatoms lies close to what previously has been documented in literature [37]. The scaling relation for a H adatom is systematic and there is only a minor electronic effect between the bulk M12 and the relaxed M12 nanocluster, see Fig. 6.10a. The shift between the M12 nanocluster calculations and the fcc(211) stepped calculations for H are again minor and there is no signs of a noticeable geometric effect, see Fig. 6.10c.

However, for the N_2 scaling relation there is a significant variation in the slope for the fixed M12 nanocluster, compared to the two other relations. The relaxed M12 nanocluster has a slope of 0.26, while the fixed M12 nanocluster has a slope of 0.46, see Fig. 6.10b. The values for the relaxed M12 corresponds very well to the reference calculations on the fcc(211) stepped surface, see Fig.

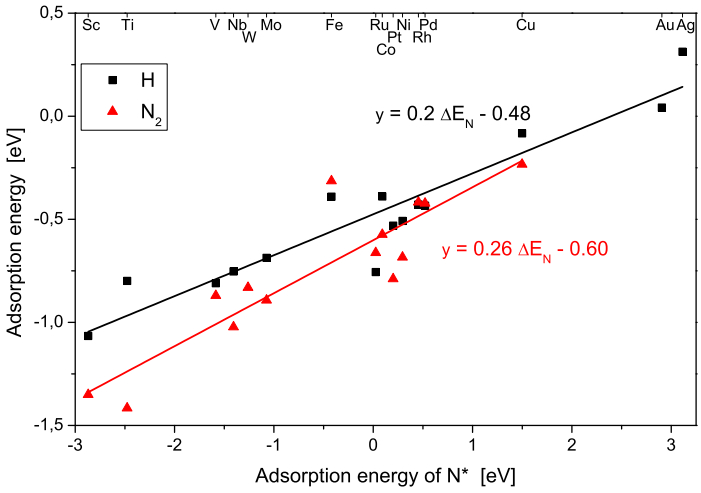

Figure 6.9: The scaling relations for N_2 and H species on the relaxed M12 nanoclusters. The adsorption positions are chosen as the most stable ones.

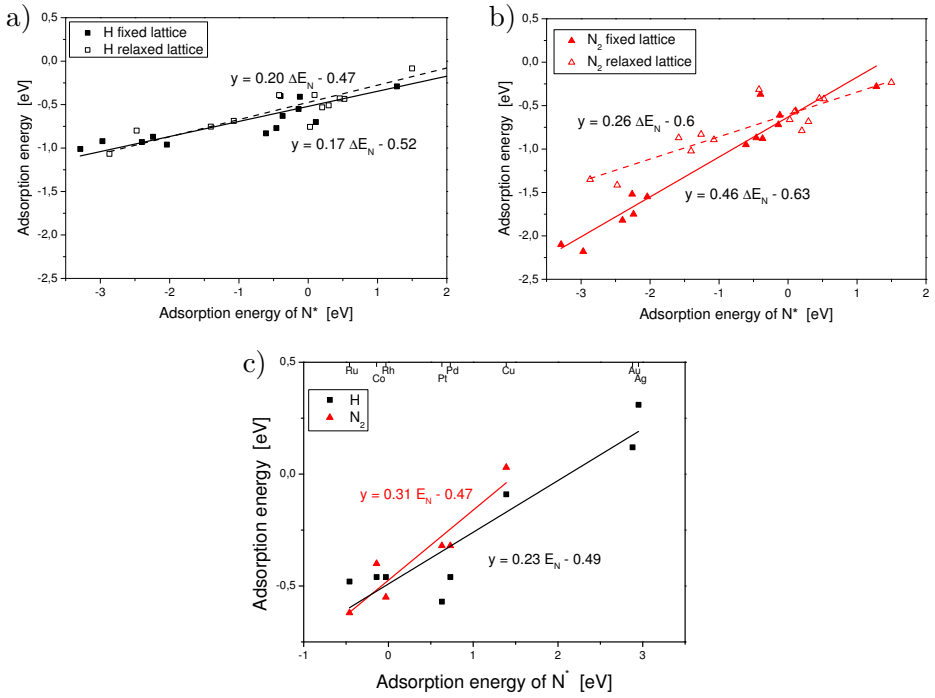

Figure 6.10: *a: The scaling relation of H on both the fixed and relaxed M12. b: The scaling relation of N_2 on both the fixed and relaxed M12. c: The scaling relations for N_2 and H on the stepped fcc(211) surface.*

6.10c, which has a slope of 0.31; and the reported slope for N_2 scaling relation is 0.3 from literature for both stepped and close-packed surfaces [128].

The variation in the adsorption energy of N_2 between the fixed M12 and relaxed M12 nanocluster originates from a combination of an electronic effect from the relaxation of the lattice constant, causing a shift along the scaling relation line, and a geometric effect caused by different adsorption geometries for

the reactive metals compared to the noble metals. For the reactive metals, the adsorption sites are di-sigma bonded while for the more noble metals N_2 is adsorbed as an antenna on the surface, which could explain the big change observed specifically for the reactive metals. This difference in adsorption geometry can influence the strength of the adsorption when changing the overall reactivity of the nanocluster going from one M12 lattice constant to another. For the other reaction intermediates studied in this work and N_2 on the noble metals, one nitrogen atom is mainly bound to the surface, while for N_2 on the reactive metals, both nitrogen atoms are adsorbed to the surface. The adsorption sites for the adsorbed N_2 molecule is different on the stepped fcc(211) surface where the N_2 molecule is bonded to the edge and terrace at the same time [34, 36, 37].

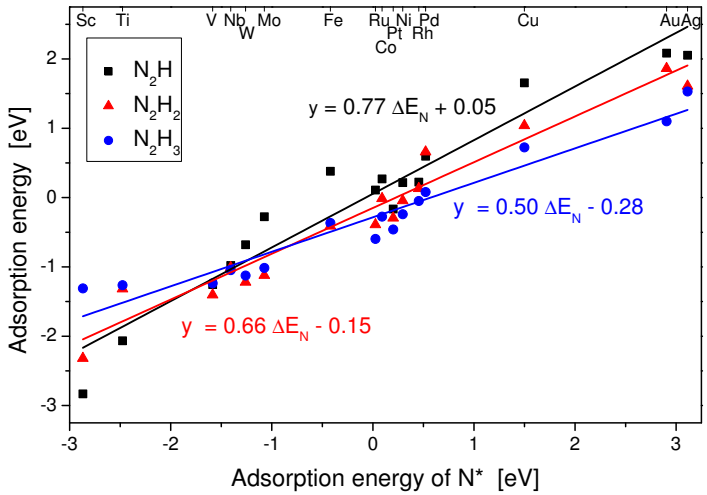

Figure 6.11: *The scaling relations for N_2H_x species on the relaxed M12 nanoclusters. The adsorption positions are chosen as the most stable ones.*

On fig. 6.11, the linear scaling relations for the N_2H_x adsorbates on the relaxed M12 nanocluster are shown. In the plot only the adsorption energies calculated for the N_2H, N_2H_2, and N_2H_3 adsorbates are included, since adsorbates containing more hydrogen spontaneously split into two molecules, ranging over NH, NH_2, NH_3 to NH_3(g). The slopes for the adsorbates are 0.77, 0.66 and 0.50 for N_2H, N_2H_2 and N_2H_3 respectively. The slopes for N_2H and N_2H_2 species are different than those of the stepped fcc(211) surface reference system, see Fig. 6.12a. These relations again present a change in the mechanics for the associative mechanism for the under-coordinated reaction sites. To compare with the substantial effect between the bulk M12 and relaxed M12 nanocluster observed for N_2, there is no change between the two systems, see Fig. 6.12b-d, indicating that the electronic effect on N_2 is higher because the N_2 is bonded in two sites, whereas the N_2H_x species are bonded mostly to one metal through one of the nitrogen atoms and the other nitrogen atom has an increased distance to the nearly metal atom.

The simple underlying argument for scaling relations for NH_x species does not hold for more complicated molecules, such as the N_2H_x molecules considered in this work and presented in Fig. 6.11 and Fig. 6.12. The internal bonding of orbitals in the N-N backbone will make a derivation similar to the one carried

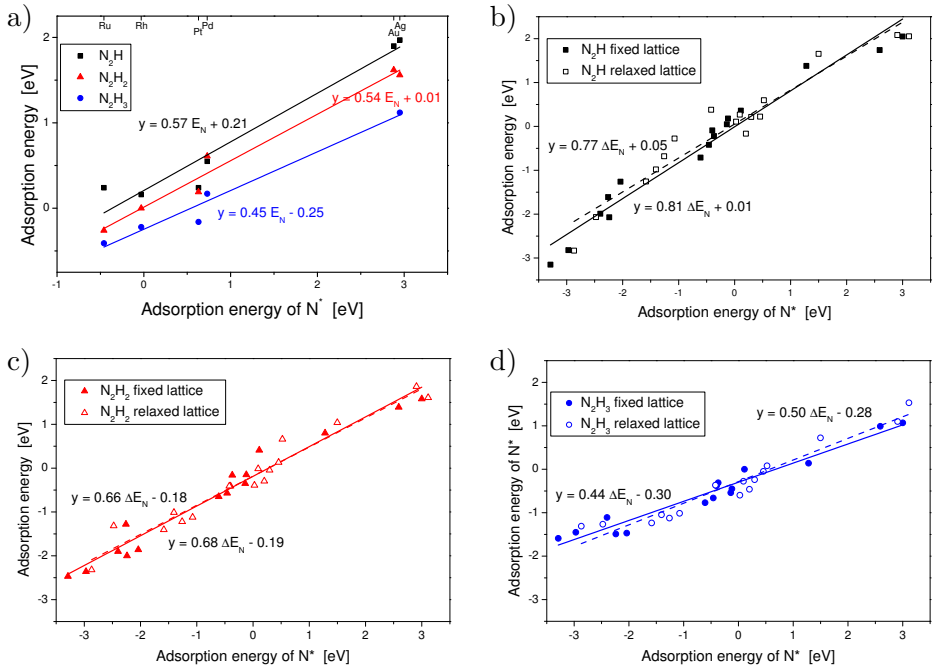

Figure 6.12: *a: Scaling relations of the N_2H_x on the stepped fcc(211) surface. b-d: Scaling relations for the fixed and relaxed M12 nanocluster: of N_2H on a), of N_2H_2 on b), and of N_2H_3 on c).*

out for NH_x species much more complicated and may depend more strongly on the local adsorption environment; i.e. whether both backbone atoms binds to the surface or only one, and how the hydrogen atoms bind to one or both backbone atoms and how this affect the bonding.

6.5 Volcano Plots

Using the relations presented in the previous section and the tools described in chapter 4, it is possible to create plots visualizing the onset potential for electrochemical nitrogen fixation. This method was introduced in ref. [105] for the electrolysis of water on oxide surfaces.

In this analysis, the reaction free energy can be used directly as a simple measure of electrocatalytic activity. The reaction free energy for each elementary step can be expressed as functions of the applied bias U and the adsorption energy ΔE_N or the reaction free energy ΔG_N of the nitrogen adatom (N*). This is possible because the linear scaling relations combined with the approximation that the free energy corrections calculated on the Ru M12 nanocluster, presented in section 2.6, describe all important trends for the electrocatalytic activity. All protonation steps for both the *dissociative* and *associative* mechanisms include a removal of a proton and a electron from the surrounding electrolyte and a addition of a hydrogen to the adsorbed molecule. A dependency on the applied potential will therefore be a direct result of this framework. In the following, the method to determine the onset potential as a function of the free energy of

an adsorbed nitrogen adatom will be illustrated.

The free energy of a basic protonation reaction where both reaction intermediates (initial and final state) are bonded to the surface, e.g. eq. 4.3d, can be described solely by the reactants taking active part in the electron transfer. The result is a simplification of the reaction described in eq. 4.3d to the following reaction:

$$\begin{aligned} \mathrm{NH^* + 2(H^+ + e^-)} &\rightleftharpoons \mathrm{NH_2^* + (H^+ + e^-)}, \\ \Delta \mathrm{G_{dis,2}} &= \Delta \mathrm{G_{NH_2^*}} - \Delta \mathrm{G_{NH^*}}, \end{aligned} \tag{6.1}$$

which describes the change in free energy of the reaction as defined in eq. 4.10. Inserting the general expression for the scaling relations formulated in eq. 3.4 for each adsorbed reaction intermediate into the equation above, the change in free energy for this part reaction is given as a function of the nitrogen binding energy, $\Delta \mathrm{E_N}$, and the applied potential, U.

$$\begin{aligned} \Delta \mathrm{G_{dis,2}} &= \Delta \mathrm{G_{NH_2^*}} - \Delta \mathrm{G_{NH^*}} \\ &= \alpha_{\mathrm{NH_2}} \Delta \mathrm{E_N} + \kappa_{\mathrm{NH_2}} + \mathrm{E_{ZPE,NH_2}} - \mathrm{T}\Delta \mathrm{S_{NH_2}} - \mathrm{eU} \\ &- (\alpha_{\mathrm{NH}} \Delta \mathrm{E_N} + \kappa_{\mathrm{NH}} + \mathrm{E_{ZPE,NH}} - \mathrm{T}\Delta \mathrm{S_{NH}} - 2\mathrm{eU}) \\ &= (\alpha_{\mathrm{NH_2}} - \alpha_{\mathrm{NH}}) \Delta \mathrm{E_N} + \mathrm{eU} \\ &+ (\kappa_{\mathrm{NH_2}} + \mathrm{E_{ZPE,NH_2}} - \mathrm{T}\Delta \mathrm{S_{NH_2}}) \\ &- (\kappa_{\mathrm{NH}} + \mathrm{E_{ZPE,NH}} - \mathrm{T}\Delta \mathrm{S_{NH}}) \end{aligned} \tag{6.2}$$

Inserting the derived numbers from the scaling relations presented in table 6.3 and the calculated free energy corrections from table 2.1 into eq. 6.2 and subsequently converting $\Delta \mathrm{E_N}$ to $\Delta \mathrm{G_N}$ yields:

$$\begin{aligned} \Delta \mathrm{G_{dis,2}} &= -0.26 \Delta \mathrm{E_N} - 0.34\mathrm{eV} + \mathrm{eU} \\ &= -0.26(\Delta \mathrm{G_N} - 0.23\mathrm{eV}) - 0.34\mathrm{eV} + \mathrm{eU} \\ &= -0.26 \Delta \mathrm{G_N} - 0.28\mathrm{eV} + \mathrm{eU}, \end{aligned} \tag{6.3}$$

where the 0.23 eV is the calculated change in energy going from adsorption energy to reaction free energy for an adsorbed nitrogen adatom. The next step that must be taken is to apply a potential such that each forward reaction has negative free energy change and the onset potential is defined when $\Delta \mathrm{G_{dis,2}} = 0$. This ensures that the reaction occurs spontaneously, as long as the protonation barrier is low. Applying this constraint to eq. 6.3, the minimum onset potential needed to drive this specific reaction is given by:

$$\mathrm{U} = 0.26/\mathrm{e}\ \Delta \mathrm{G_N} + 0.28\ \mathrm{V} \tag{6.4}$$

where e is the elementary charge.

This procedure can be done for all pure protonation steps and plotting the obtained expressions in one plot will form a volcano describing the necessary onset potential which makes each part reaction exothermic. Fig. 6.13 shows both the associative and dissociative process. The associative process is purely electrochemical, whereas the dissociative process involves the non-electrochemical (thermal) step, i.e. the splitting of the N-N bond, which has to be dealt with separately as outlined below.

The volcano for the associative mechanism can be understood utilizing the method behind eq. 6.2, 6.3 and 6.4, and the limiting reactions are the plotted two solid lines in fig. 6.13 forming a volcano. These part reactions are the ones that limits the associative electrochemical ammonia synthesis. The reactions are the protonations of N_2 (see 4.4b) and the protonation of NH_2 (see 4.4f). The two solid lines form a volcano, where the lowest onset potential for driving the associative ammonia synthesis electrochemically is close to U = -0.45 V. None of the investigated metals are, however, at the optimal reaction free energy of a nitrogen adatom at -0.5 eV. The closest metals are divided in two groups, one consisting of the more reactive metals Mo, V and Nb and the other group consisting of Fe, Ru, Pt and Co, where Mo is the closest metal while Fe and Nb are the equally close to the optimum. Here Ru and Fe are already well known good heterogenous catalyst materials for the Haber-Bosch process and are unfortunately even better hydrogen evolution reaction (HER) catalysts. Finding that the optimum for the associative mechanism lies between Mo and Fe fits very well with the active site in the enzyme Nitrogenase which is the Iron Molybdenum cofactor [10]. Employing this methodology, effects such as coverage dependence, and the dissociation of N_2 or desorption of NH_3 in particular are not included and will have an effect on the predicted efficiency. However, this analysis suggest that alloy particles with free energies of -0.5 eV for adsorbed N adatoms should be good catalysts for the associative mechanism.

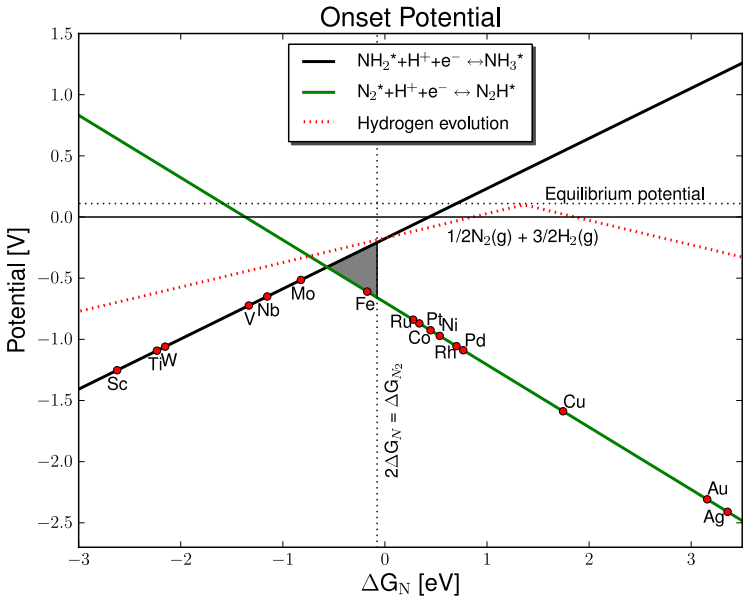

Figure 6.13: *Volcano plot of the associative and dissociative mechanism with the free energy ΔG_{N*} as a descriptor. The competing reaction of creating hydrogen on the surface is also shown as the dotted red lines. The two solid lines indicate the limiting potential for the associative mechanism. For the dissociative mechanism the gray area is added as a potential area for where it could be more favorable to go through the dissociative mechanism. The effeciency in this area is dependent on the dissociation of the N_2 molecule on the surface. At the top of the gray area the dissociative mechanism will be comparable to HER.*

The framework utilized above does not describe the main challenges of the electrochemical dissociative mechanism, because it lacks the description of the dissociation of N_2 at the surface. Furthermore, this description of the electrochemical process will not form both of the two legs to create a volcano (in this case the so-called right leg), see fig. 6.13. Here, the solid black line is the electrochemical limiting reaction for the dissociative mechanism. The reason for this behavior is the scaling relations and that the slopes depend on the number of hydrogen vacancies in the adsorbed molecule. The lines describing the necessary onset potential for the dissociative mechanisms will therefore have slopes with the same sign and almost the same size. The consequence of this behavior will be that the limitations to the electrochemical reaction will only be described for the reactive metals and lack for the noble metals, because they cannot break the N-N bond. This description suggest that the electrochemical nitrogen fixation efficiency will be perfect over the noble metals. However, this picture is not correct, since the main hindrance for the noble metals is the N_2 dissociation. The dissociation of N_2 is not affected by the potential and is normally seen as a heterogenous reaction step and will have activation barriers that is much higher for noble metals than for reactive metals described by the Brøndsted-Evans-Polanyi lines [134]. For the good dissociation catalysts (the reactive metals) the hydrogen evolution reaction are preferred compared to ammonia production. This is the reason why a shift of the volcano utilizing the structure (in)sensitivity to enhance the ammonia production with respect to HER is interesting.

Another method is therefore needed to describe the limitations for the dissociative mechanism on the right leg. Three requirements that should be satisfied for the dissociation of N_2 to be possible on the surfaces are:

1: It should be preferred to have a nitrogen molecule bonded to the surface. The free energy of N_2^* should hence be negative. This break-point are located at $\Delta G_N = 0.03$ eV.

2: The reaction free energy of $N_2(g)$ to $2N^*$ should be negative and hence exergonic. This corresponds to $\Delta G_N = 0$ eV and should describe the shift from having nitrogen on the surface to having problems bonding the nitrogen at all.

3: The gain in reaction free energy for the dissociation reaction of N_2^* to $2N^*$ on the surface should be negative and hence have a more stable end configuration. Using the linear scaling relations and free energy corrections the break-point for where the gain is zero can be calculated. This occur at the reaction free energy of nitrogen adatoms at -0.08 eV.

The most conservative limit have been implemented as a horizontal line on fig. 6.13. Together with the line defining the limiting onset potentials, this limit adds a triangle to the existing associative volcano and this triangle is marked with gray.

These three possible ways of looking at the limiting step for the dissociative mechanism gives an estimate of the upper and lower bounds for when the dissociative mechanism will be limited by the dissociation. Including one of the other proposed limitations only shift the top of the volcano by 0.11 eV on the x-axis and only have a minor change in the onset bias. The added triangle only marks a potential increase in electrocatalytic activity and is to some degree uncertain. Here it is worth to note that in the gray marked area the vertical line is the best case scenario, while the two lines (filled black and green) describing associative

mechanism are the worst case scenario.

By comparing the onset potential for ammonia and hydrogen production it is possible to see that it is only at the very top of the NH_3 production volcano that there is a possibility of ammonia production requiring a lower onset potential than hydrogen production. As it seems from this volcano it would still be marginally preferred to create hydrogen. However, there will be effects not included in this analysis that will have an effect in the efficiency of the catalyst and on the competition between ammonia and hydrogen production such as coverage, adsorbate-adsorbate effects and the surrounding electrolyte affecting the equilibriums. Furthermore, the fixed geometry used in this study could also influence the results. But it is important to see this study as a trend study to understand to some degree how under-coordinated reactive sites can act as ammonia catalysts.

The volcano plot in fig. 6.13 shows the potential determining steps of both the dissociative and associative mechanism when using the free energy corrections calculated for the adsorbed reaction intermediates within the harmonic approximation. Leaving out the free energy corrections would yield a minor shift for the top of the volcano where the free energy for an adsorbed nitrogen adatom moves from -0.5 eV to -0.6 eV while the onset potential moves up with 0.4 eV. The potential determining step remains the same for the new volcano and the overall trend is the same, however NH_3 would be favored compared to HER. The fact that the top of the volcano is positioned close to the same free energy of adsorbed nitrogen adatom indicates that the overall trends for these very under-coordinated reaction sites are to a large degree independent on the calculated free energy corrections.

6.6 Conclusion

A theoretical analysis of the highly under-coordinated reaction sites for electrochemical formation of ammonia on pure transition metal electrodes indicates that the associative mechanism could yield ammonia at an onset potential around -0.6 to -0.45 V with respect to SHE. Here, the hydrogen reaction will be a competing reaction and have a slightly lower onset potential and hence should be preferred. The most promising candidate for electrochemical ammonia production through the associative mechanism is Mo but closely followed by Fe. Alloy materials with reactivities between that of Mo, Fe and Ru could also be candidates, especially if they can hinder the HER and still be good catalysts for NH_3 production. However, even at these very under-coordinated structures there is still a gap between HER and electrochemical ammonia production in terms of onset potential for the potential determining steps. Though this problem could potentially be solved by further utilizing the structure (in)sensitivity, this remains the main challenge for the electrochemical ammonia production.

For the dissociative mechanism a proposed onset potential of -0.5 to -0.1 volts could be obtained with a preferred ammonia production over HER for the potential determining steps. However, for the dissociative mechanism N_2 dissociation barrier for splitting the N_2 molecule has not been included since this would require a purely thermally activated Langmuir-type mechanism for

one elementary step combined with the electrochemical onset potential. Instead an estimate of the equilibrium of having N adatoms compared to N_2 molecules on the surface has been established and this will hence act as a cut-off for the noble metals and describe to some extent the limitations for these metals for the dissociation of a nitrogen molecule on the surface. The cutoff could vary depending on the detailed treatment from a free energy of N adatoms of -0.08 eV to 0.03 eV, which gives an overall uncertainty of approximately 0.1 V in onset potential for the potential determining steps.

Chapter 7

Molybdenum nanoclusters for ammonia production

This chapter is based on the included Paper C and the chapter includes additional information to what is presented in the paper.

7.1 Introduction

In chapter 6 molybdenum nanoclusters was identified as a primary candidate for electrochemical production of NH_3 via the associative mechanism [107] and it has been shown that at potentials relevant for NH_3 production, nitrogen will adsorb preferentially over hydrogen [37] at molybdenum surfaces, thereby minimizing the traditional Faradaic losses due to the competing hydrogen evolution [39]. These findings render Mo nanoclusters as a prime candidate for electrochemical ammonia production. In this section, a thorough study of the molybdenum nanoclusters for electrochemical production of ammonia will be presented.

7.2 Computational details

7.2.1 DFT calculations

The calculations were carried out with density functional theory (DFT) calculations [50, 51] using the RPBE exchange correlation functional [44] along with the projector augmented wave method [69, 132] as implemented in the GPAW code [45, 46, 68]. A grid of (3,3) for the finite difference stencils have been used together with a grid spacing of 0.18 Å, at least 20 free bands above the Fermi level and a Monkhorst-Pack [81] k-point sampling of 2×2×2. A 7 Å vacuum layer around the nanocluster has been applied. When solving the electronic density self-consistently, the convergence criteria have been chosen such that the changes were $\leq 10^{-5}$ eV for the energy and 10^{-4} electrons per valence electron for the density. In all calculations, a Fermi smearing of 10^{-4} eV has been used. The atomic simulation environment ASE [47] was used to set up the atomic struc-

ture of these systems. All structural (and atomic) relaxations of the adsorbates (N, H, NH, etc.) attached on the Mo_{13} nanocluster were carried out using the BFGS and FIRE [67] optimizers within ASE. In the determination of transition states and activation barriers the nudged elastic band (NEB) method [71,72,136] has been used with a spring constant of 1 eV/Å^2. To precisely determine the transition state configuration and the corresponding minimum energy pathway between initial and final states, the climbing image method [136] was used as the final step in the NEB calculations.

7.2.2 Study approach

In this study, there are a number of aspects of using the Mo_{13} nanocluster as catalyst for electrochemical ammonia production that will be investigated [137–139]. The relative stability of adsorbates on the surface, where the Gibbs free energy, eq. 2.20, is used to determine which adsorbates will be prefered. Gibbs free energy do not describe the adsorption strength of hydrogen atoms, as there is a potential applied. Therefore, eq. 4.10 will be used to describe the effects of an applied potential on the hydrogen bond strength.

Two pathways of electrochemical ammonia formation will be investigated. The first is the protonation of a nitrogen molecule adsorbed on the surface through the associative Heyrovski mechanism described in eq. 4.4a-4.4g. The second pathway is the direct protonation of adsorbed nitrogen adatoms on the surface, see eq. 4.3c to eq. 4.3e for a description.

To describe the electrochemical efficiency of the molybdenum nanocluster for ammonia production, the method described in section 4.3.1 will be used to determine the onset potential for each reaction step, such that the protonation is exergonic, and the overall onset potential for the whole reaction can be determined.

7.3 Model system

The system of interest is the cuboctahedral molybdenum particle containing 13 atoms. The clean molybdenum structure is shown in Fig. 7.1a. It has a molybdenum atom at the center and a shell of 12 molybdenum atoms around the center atom. The particle was allowed to relax in order to find the optimum structure and the nanocluster is through the whole study allowed to relax in all directions. The Mo_{13} particle is of particular interest because it is highly undercoordinated and has a feasible size to allow for a thorough study, including coverage and poisoning effects. The coverages of nitrogen, hydrogen and oxygen have been investigated, as well as the poisoning/adsorption of these molecules at the particle with a coverage of one of the other studied adsorbates.

7.3.1 The $Mo_{13}N_x$ cluster

There are two relevant adsorption sites on the molybdenum particle surface. The first adsorption site is the three-fold hollow site, marked with 1 on Fig. 7.1a, where the adsorbate has three nearest metal neighbors. The second adsorption site is a four-fold hollow site, marked with 2 on Fig. 7.1a, where the adsorbate

have four metal atoms as neighbors. Filling of the nitrogen skin are visualized on Fig. 7.1b) (half-filled skin) and 7.1c) (filled skin).

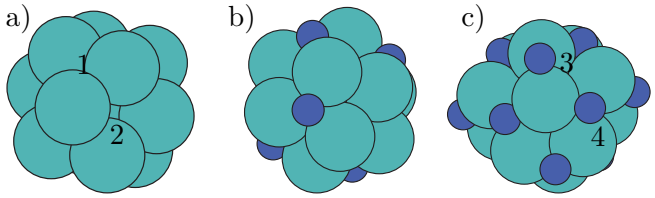

Figure 7.1: *a) The clean Mo_{13} nanocluster. b) the $Mo_{13}N_7$ nanocluster after adsorption of seven nitrogen atoms (the dark atoms). c) the $Mo_{13}N_{14}$ with a filled nitrogen skin. The clean cuboctahedral nanoparticle, a), has two special adsorption sites, where the three-fold hollow is marked with 1 and the four-fold hollow site is marked with 2. In the filled nitrogen skin, the four-fold hollow adsorption sites have changed into a bridge site and is now marked 3 on c), while the geometry is kept for the adsorbed nitrogen atoms in the original three-fold hollow sites (marked with 4).*

In the case of an almost filled nitrogen skin, one adsorption site continues to exist, while the other adsorption site transforms in a new site. The bonding site left unchanged is the three-fold hollow site, marked with 3 in Fig. 7.1c of the restructured nanocluster. The other new adsorption sites is a bridge site, marked 4 in Fig. 7.1c, which originates from a restructuring of the nanocluster. In the process of filling the nitrogen skin, the adsorption sites change from a four-fold hollow site to a bridge site; the change will be discussed further in a later section.

7.4 Ammonia formation

7.4.1 Stability of the nitrogen skin

The energetics of the nitrogen and hydrogen skins

In the investigation of the nitrogen coverage on the cuboctahedral structure, the first sites of interest for nitrogen adsorption are the three-fold hollow sites, marked with 1 in Fig. 7.1a. These sites are known to adsorb nitrogen most strongly [34, 107].

The addition of nitrogen adatoms to the molybdenum nanoparticle has been carried out adding the nitrogen adatoms to three-fold hollow sites. The first additions of nitrogen adatoms the particle changes shape to optimize the adsorption of nitrogen adatoms. For the fifth nitrogen addition, the adsorption in the three-fold hollow site again follow the cuboctahedral shape. The adsorption free energies of the first eight nitrogen atoms are shown in Fig. 7.2, (dark filled line), where 0 is the free energy of the clean Mo_{13} nanocluster and the respective number of $1/2N_2$ in gas phase. The graph shows that the adsorption free energies are strongest for the first additions and the adsorption energies are reduced as more nitrogen are added to the surface. The average binding energy for the nitrogen adatoms is presented with a dotted dark line in Fig. 7.2. The higher the nitrogen coverage, the smaller the structural changes.

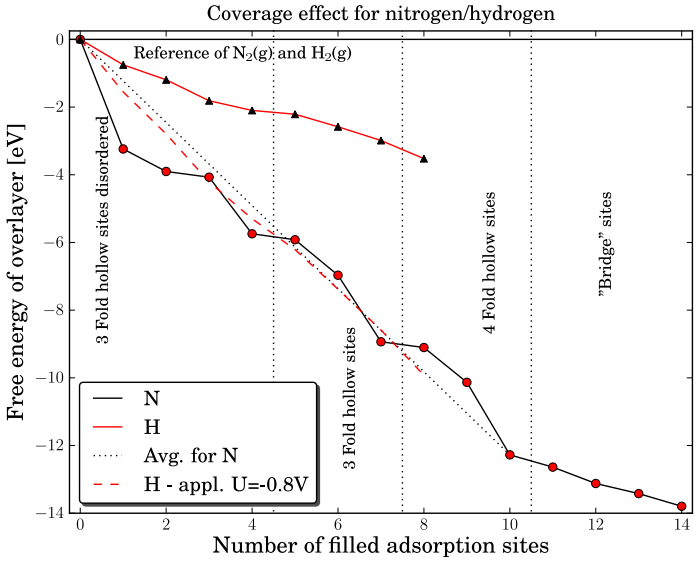

Figure 7.2: *The free energy for covering the Mo_{13} cuboctahedral nanoparticle with either nitrogen or hydrogen. The black line shows the filling of the nitrogen skin and the black dotted line shows the average free energy of binding the ten first nitrogen to the surface. The red line shows the free energy of adsorbing hydrogen, while the dashed red line shows the free energy of adsorbed hydrogen with an applied potential of -0.8 V.*

The adsorption of the tenth nitrogen, which is the second adsorption at a four-fold hollow site, rearranges the nanocluster. The six four-fold hollow sites that are on the nanoparticle are changed into six bridge sites due to a big restructuring of the nanocluster. The nanocluster is along one axis tightened and elongated along the two other axes. An example of the newly created bridge site can be seen on Fig. 7.1c, marked with a 4. The restructuring increase the adsorption free energy for each nitrogen adatom adsorbed at the nanocluster compared to the adsorption in the four-fold hollow. The adsorption free energy for nitrogen adatoms at the four-fold hollow sites and the bridge sites are lower than the average adsorption energy at the three fold sites. This is a combination of change in adsorption sites and filling of the nitrogen skin resulting in a repulsive force between the nitrogen atoms.

The adsorption of hydrogen on the cuboctahedral molybdenum nanoparticle is carried out by adding hydrogen to the three fold hollow sites. In Fig. 7.2, the adsorption free energy of hydrogen is plotted with a pale red color and forms almost a straight line. There is no observed restructuring of the nanocluster.

Fig. 7.3 shows the evolution of the d-band of the molybdenum nanocluster as the coverage of either nitrogen or hydrogen increases. It is clear that there is a distinction between the adsorption of hydrogen and nitrogen. The nitrogen adsorption significantly changes the d-band position and width, while the influence of hydrogen is minor. This should result in a decrease of the nitride covered molybdenum nanocluster, as the nitrogen increase, while minor or no effects should be expected for the hydrogen covered molybdenum nanocluster.

For the nitrogen coverage, the d-band center shifts down together with an increase in the width of the d-band. This explains the observed saturation of

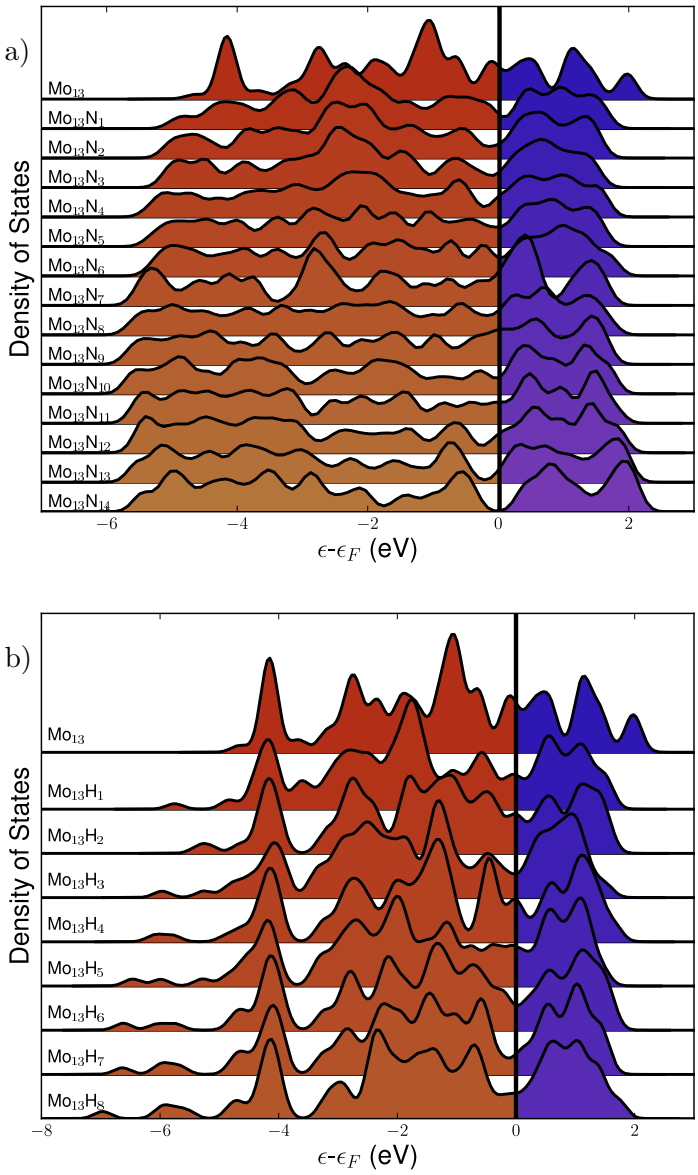

Figure 7.3: *The evolution of the d-band as the coverage of nitrogen and hydrogen increases on the The $Mo_{13}Y_x$ ($Y = \{N, H\}$) nanocluster. a) Nitrogen and b) hydrogen.*

the surface and overall decreasing adsorption energy that is observed at higher coverages. For the adsorption energy of nitrogen and the d-band center, a correlation cannot be extracted from the data, due to what seems to be noise on the adsorption energy, see Fig. C.1, and visually it seems to be geometrical changes of the nanocluster that is the reason to the fluctuations. If instead, the total adsorption energy of the nitrogen skin is correlated with the d-band center a clear correlation is the outcome, see Fig. C.2 in appendix C. The local restructuring affects each individual nitrogen adsorption energy, but the d-band depicts the overall adsorption energy phenomena.

The influence of hydrogen on the d-band is minor, where only small peaks of

d-electrons densities is arising at -6 eV and -7 eV. The peak at 4 eV is constant and do not move as the hydrogen coverage increases, while the band at -3 eV to 0 eV seems to narrow slightly. Again, no correlation between the adsorption energy of hydrogen and the d-band center is noticed, see Fig. C.1, but just as for nitrogen the total adsorption energy and d-band correlates.

The adsorption energies of H are much lower than the similar ones for nitrogen, and at the same time, the structural rearrangements of the nanocluster are not seen as hydrogen are added to the surface and is thus expected due to the smaller size of hydrogen.

The nitrogen skin under reaction conditions

With respect to coverage, the competition between nitrogen (dark filled line) and hydrogen (the light dashed line) at an applied potential of -0.8 V in Fig. 7.2 shows that nitrogen will be preferred on the surface with overpotential as high as -0.8 V with respect to the SHE. Overpotential of up to -0.8 V have previously been shown to be sufficient for the production of ammonia on a Mo model system surface [107], and for more detail see Fig. 6.13 in chapter 6.

The results for molybdenum nanocluster covered with either nitrogen or hydrogen shows that it is indeed interesting to investigate the production of ammonia on this nitrogen skinned molybdenum particles because the particle should preferentially have nitrogen on the surface under reaction conditions. The stronger nitrogen bonds relative to hydrogen should subsequently result in reduced Faradaic losses due to lower hydrogen evolution on the molybdenum nanocluster under reaction conditions for electrochemical ammonia production. The next step is to determine the electrochemical properties of the $Mo_{13}N_x$ nanoparticle with respect to the direct protonation of nitrogen adatoms or the associative pathway from an adsorbed N_2 molecule at nitrogen vacancy sites.

7.4.2 High nitrogen coverage

Direct protonation of the nitrogen skin

My calculations show that a nitrogen skin is stable with respect to a hydrogen skin. The first thing to investigate in the determination of the electrocatalytic properties of the molybdenum nanocluster is thus the direct protonation of the nitrogen skin. The filled skin has two nitrogen adsorption sites, the three-fold hollow site and the bridge site.

Calculations performed on the filled skin are shown in Fig. 7.4a where the onset potential is the potential required to make each reaction step exergonic. The figure shows that the onset potential is close to -0.5 V for ammonia production with respect to SHE for both nitrogen adsorption sites. The geometry of the reaction intermediates for each of the reaction pathways is presented in Fig. 7.4a. The geometries of NH are either a bridge site or a three-fold hollow site. For both NH_2 species the adsorption site is a bridge site, where the positioning of the NH_2 adsorbate in the three-fold hollow pathway has been moved from the three-fold hollow site to a bridge site during the relaxation of the system. The most stable adsorption site of NH_3 for both studied reaction pathways are top sites. These observations of the adsorption geometries are in

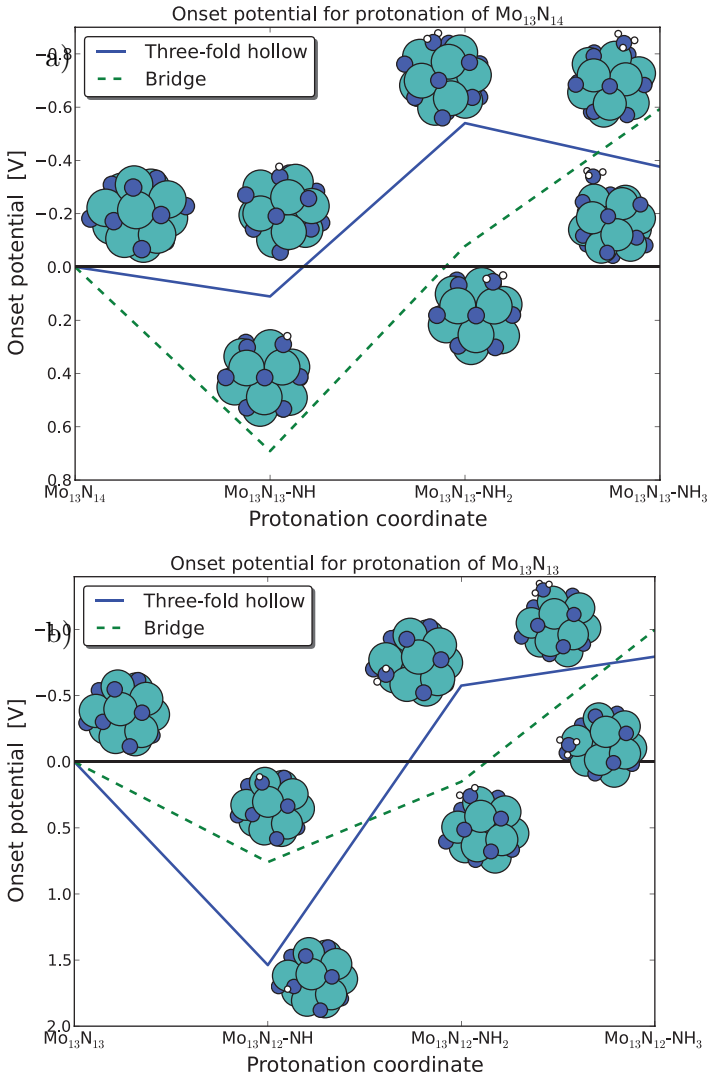

Figure 7.4: *a) The onset potential for each protonation reaction of a nitrogen adatom originating from the $Mo_{13}N_{14}$ nanocluster structure. The onset potential for the three-fold site, dark filled line, and the bridge site, light dashed line, are close to -0.5 V. b) The onset potential for the protonation of a nitrogen adatom on the $Mo_{13}N_{13}$ nanocluster structure. For the bridge site, the light dashed line, the onset potential is -1 V and for the three-fold site, the dark filled line, the onset potential is -0.8 V.*

good agreement with observed geometries for NH_x adsorption structures presented in literature [34,37,107,128] and even at these large coverages of nitrogen the flexibility of the system is large enough to accommodate such structural changes.

For the $Mo_{13}N_{13}$ nanocluster same calculations have been performed. Fig. 7.4b shows that for the nitrogen adatoms adsorbed at the bridge site, the light dashed line, require an onset potential of -1 V and for the three-fold hollow site, the dark filled line, require an onset potential of -0.75 V. The geometries of the reaction intermediates for both calculated pathways have same trend as

presented above for the $Mo_{13}N_{14}$ nanocluster.

Further direct protonation of the $Mo_{13}N_x$ nanoclusters, similar onset potentials for reduction of the nitrogen skin as presented earlier. For structures with high nitrogen coverage, the onset potentials are on the order of -0.6 V to -0.8 V. These calculations indicate that the nitrogen skin can be protonated to form ammonia and subsequently create a nitrogen vacancy site at the surface.

The created vacancy site, and when enough is created (2-4 missing N adatoms), the nanocluster can adsorb nitrogen molecules. The $Mo_{13}N_{12}$-N_2 is the system with the highest nitrogen coverage that can adsorb a nitrogen molecule in a nitrogen vacancy site. The nitrogen molecule has two possible adsorption sites, one is a three-fold hollow site and the other is a bridge site. The vacancy site barely adsorbs the N_2 molecule; the reaction free energy for adsorption is -0.07 eV with the three-fold hollow site as the most stable one. When a $Mo_{13}N_x$ nanocluster adsorbs a nitrogen molecule, there are two pathways for the further process. The nitrogen molecule can either go through the associative mechanism and create ammonia directly or dissociate into two nitrogen adatoms and hence regenerate the nitrogen skin. The dissociation of N_2 molecule will be discussed first.

N_2 dissociation

One way of regenerating the nitrogen skin is by adsorption and dissociation of N_2 molecules into two N adatoms on the surface filling up two vacancy sites. Here, we investigate the partially reduced $Mo_{13}N_{10}$ cluster that display a very stable final configurations for the adsorbed N adatoms.

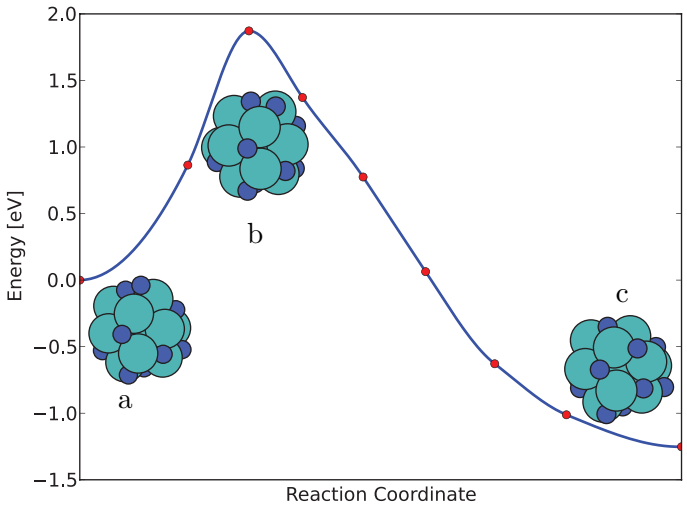

Figure 7.5: *Dissociation of N_2 on the $Mo_{13}N_{10}$ nanocluster calculated using the nudged elastic band method. The initial state of adsorbed N_2, marked with a, the transition state is marked with b and the final state is marked with c.*

The minimum energy path for the N_2 dissociation on the $Mo_{13}N_{10}$ can be seen in Fig. 7.5. Here, the initial and final state configuration together with the transition state is shown. The barrier for splitting of N_2 is found to be 1.72 eV,

indicating that splitting of N_2 is not possible on an almost filled nitrogen skin on the molybdenum particle.

The associative mechanism

The direct protonation of N_2 admolecules has been thoroughly investigated on the molybdenum cluster with an almost filled nitrogen skin. Two adsorbed nitrogen molecules were both studied at two nitrogen coverages. The higher nitrogen coverage ($Mo_{13}N_{12}$) is presented first, while the lower nitrogen coverage case ($Mo_{13}N_{10}$) will be presented second.

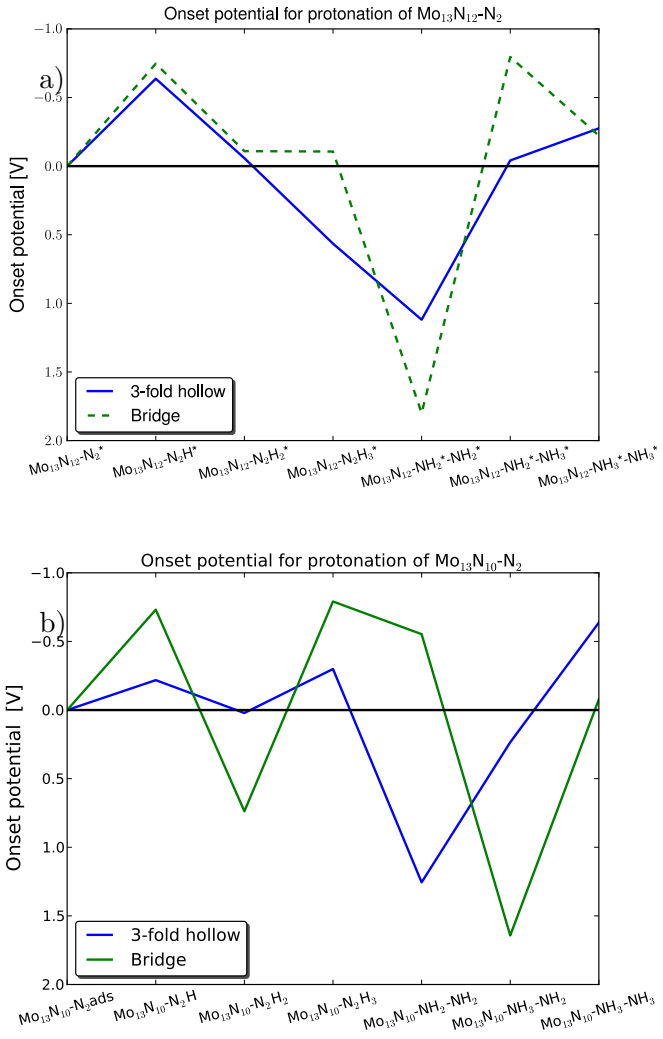

Figure 7.6: *a) Onset potentials for all reaction steps for protonation of an adsorbed nitrogen molecule via the associative mechanism on the $Mo_{13}N_{12}$ nanocluster. For the bridge site, the light dashed line, the onset potential is -0.75 V and for the three-fold site, the dark filled line, the onset potential is -0.6 V. b) The onset potential for the protonation of a nitrogen molecule through the associative mechanism on the $Mo_{13}N_{10}$ nanocluster. For the bridge site, the light filled line, the onset potential is -0.8 V and for the three-fold site, the dark filled line, the onset potential is -0.65 V.*

Fig. 7.6a shows the onset potentials for driving the protonation of N_2. For both reduction pathways, the most endergonic reaction step is the first protonation step. Here, the onset potential is around -0.6 V for the nitrogen molecule adsorbed in the three-fold hollow site, the dark filled line, and -0.75 V for the nitrogen molecule adsorbed in the bridge site, the light dashed line. During the fourth protonation of N_2H_3 at the three-fold hollow site, the molecule prefers to dissociate into two NH_2 molecules on the surface. The protonation and splitting of the N-N bond is strongly exergonic, where the reaction free energy of this step is 1 eV downhill. It was possible to find a semi-stable N_2H_4 configuration, but the creation of this reaction intermediate on the surface is 0.9 eV uphill and therefore not a possible reaction intermediate.

The associative mechanism was also examined on a more reduced cluster ($Mo_{13}N_{10}$). The adsorption free energy of the nitrogen molecule is stronger, -1.2 eV, and the onset potentials for the individual reactions step for ammonia formation are presented in Fig. 7.6b, where an onset potential of -0.6 V is the observed best case at high nitrogen coverages.

With onset potentials of less than -0.8 V for all protonation processes, both the direct protonation of surface nitrogen and the associative pathways for N_2, shows that the protonation of nitrogen adatoms and admolecules into ammonia is possible.

7.4.3 The hydrogen competition

With an adsorption energy of -0.06 eV for N_2, in the case $Mo_{13}N_{12}$ and a corresponding adsorption energy of hydrogen adatoms at -0.65 eV, the hydrogen adatoms will preferential bind to the nitrogen vacancy sites. Lower nitrogen coverage increases the adsorption energy of nitrogen molecules. It increase from -0.06 eV to -2.56 eV at the clean molybdenum particle, while the corresponding adsorption energies of hydrogen is almost constant, rising from -0.66 eV to -0.74 eV. The adsorption energies can be seen in table 7.1.

System	ΔG_{N_2} [eV]	ΔG_H [eV]	ΔG_H [eV] (U = -0.6V)
$Mo_{13}N_{12}$	-0.06	-0.66	-1.26
$Mo_{13}N_{11}$	-0.43	-0.71	-1.31
$Mo_{13}N_{10}$	-1.2	-0.73	-1.33
$Mo_{13}N_9$	-1.13	-0.59	-1.19
Mo_{13}	-2.56	-0.74	- 1.34

Table 7.1: *The most stable adsorption energies of nitrogen molecules and hydrogen adatoms at different nitrogen coverages. The last column presents the binding energy of hydrogen at an applied potential of -0.6 V, which is potential at what ammonia creation is possible.*

The pathways studied at the high nitrogen coverage show that the hydrogenation of the nitrogen adatoms and admolecules is possible at reasonable overpotentials, but the dissociation is an issue with a huge activation barrier. This will lead to formation of ammonia from adsorbed nitrogen, but the nitrogen skin will be reduced under reaction conditions because the dissociation will not lead

to a regeneration of the nitrogen skin. Furthermore, the adsorption of nitrogen molecules with respect to hydrogen adatoms is not preferential at high nitrogen coverage.

At the coverage of ten nitrogen atoms, N_2 binds with -1.2 eV. Assuming that the hydrogen adsorption energy are constant at θG_H = -0.73 eV, then Fig. 2 in ESI show that the driving potential for electrochemical ammonia production is -0.6 V. At this potential, the formation of H on the surface will have a reaction free energy of -1.33 eV, while the protonation of N_2 will have a reaction free energy of -0.4 eV. It is therefore assumed that H will cover the unoccupied nitrogen vacancy sites. When all of the sites are filled, the protonation of N2 will proceed because the formation of H2(g) will be 0.13 eV uphill and at the potential required for electrochemical ammonia production all reaction steps for ammonia production will have reaction free energies that are 0 (potential limiting step) or exergonic.

In the discussion of the preferential reactions on the Mo13N10 nanocluster, we have assumed that the adsorbate adsorbate interactions can be neglected. This is an important assumption, especially knowing that the adsorption energies will be affected at higher coverage []. For hydrogen evolution, it will for the $Mo_{13}N_{10}$ nanocluster have the consequence that the free energy barrier for producing gas phase hydrogen molecules will be lower.

Overall, this will lead to reduction of the nitrogen skin and hydrogen adsorption at high nitrogen coverage. On the other hand, adsorption energies at low nitrogen coverage show that nitrogen will be preferred over hydrogen at these conditions.

7.4.4 Low nitrogen coverage

From the study of the N_2 dissociation, the direct protonation of the nitrogen skin, the protonation of N_2 and the competing adsorption of hydrogen, we find that the skin will most likely not be completely filled with nitrogen. Even at low nitrogen coverages the onset potential for the direct protonation is still less than -0.6 V, see Fig. 7.7. Nitrogen adatoms on the surface for any given nitrogen coverage will be protonated into ammonia at potentials lower than -0.6 V. In the following, the dissociation and reduction of N_2 molecules are carried out on a clean molybdenum surface with either N_2 or two N adatoms adsorbed.

As see in table 7.1, N_2 adsorbs with 2.56 eV while two nitrogen atoms adsorb with 3.9 eV. In comparison the hydrogen binding energy is only -0.74 eV and with an applied potential of -0.8 V the hydrogen is bonded -1.54 eV and hence still weaker than N_2.

N_2 dissociation

The dissociation of nitrogen molecules is a crucial reaction step. The free energy of the N_2 and 2N on the surface gives rise to a very exothermic splitting of N_2. According to the Brøndsted-Evans-Polanyi [112] relations one would expect a lower activation barrier. This is not the case, the activation barrier for this system is still around 1.8 eV, see Fig. 7.8, and will be rate limiting at room temperature.

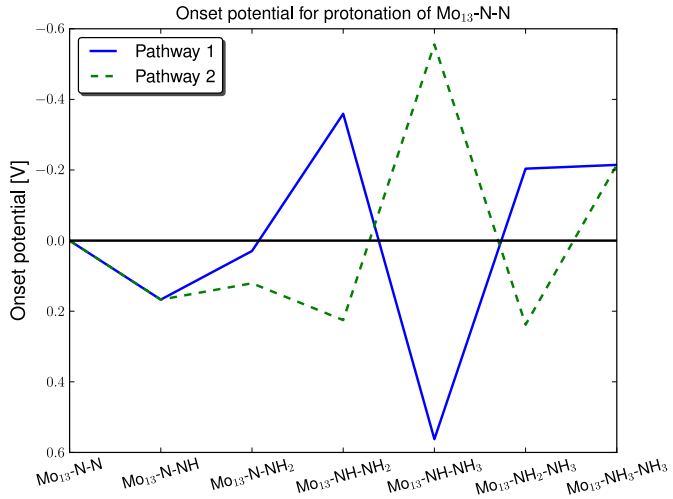

Figure 7.7: *The potential for protonation of the last two nitrogen adatoms on the Mo_{13} nanocluster.*

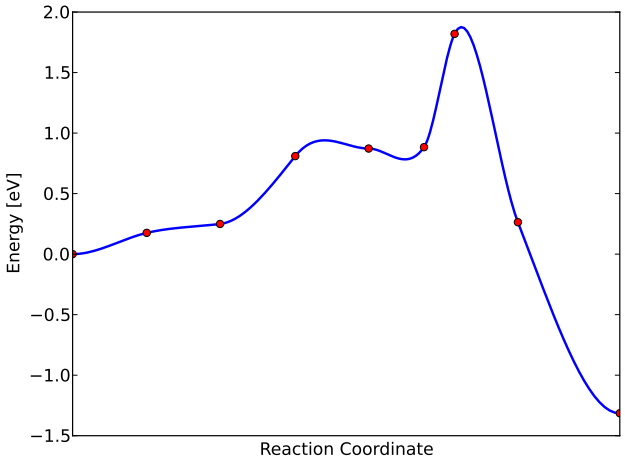

Figure 7.8: *The activation barrier for splitting N_2 on the clean molybdenum particle determined using NEB calculations. The barrier is 1.8 eV and dissociation of N_2 on the clean molybdenum will not happen at room temperatures.*

It is therefore not expected from these results, that a regeneration or creation of a nitrogen skin from dissociation N_2 molecules will occur at the present conditions on a molybdenum nanocluster.

Associative mechanism

Two routes for the associative pathways are presented in Fig. 7.9. The first route is pathway 1, which is a process where first one of the nitrogen atoms is directly protonated until ammonia is formed and then the protonation will continue with the second nitrogen atom until formation of ammonia is yet again

achieved. This results in a splitting of the nitrogen bond at the third addition of a hydrogen atom. The second part of the first route is protonation of the second nitrogen atom. The crucial step is the last protonation of the NH_2 to NH_3, where an onset potential of -0.6 V is required. This route presents a pathway

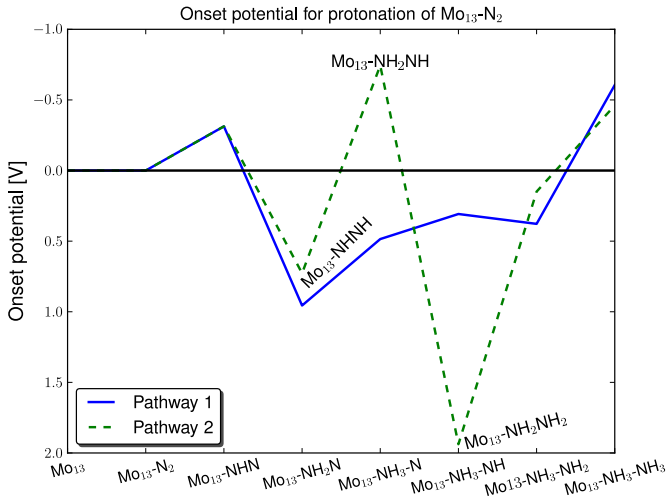

Figure 7.9: *The potential for protonation of the N_2 molecule on a 'clean' Mo_{13} nanocluster.*

for formation of the nitrogen skin, but the onset potentials for the nitrogen adatom (4^{th} and 5^{th} protonation coordinate) is positive and hence should occur instantaneously at reaction conditions and therefore a nitrogen build up on the surface is most likely not happening.

The second route is going through NH-N, NH-NH and NH_2-NH and then breaking of the N-N bond where NH and NH_3 are formed on the surface. The issues for this route are both the formation of NH_2-NH and the formation of NH_3. These steps require an onset potential of -0.7 V and -0.45 V, respectively. The graph shows that the fourth protonation step, where the N-N breaking occurs, is very exergonic.

7.4.5 Desorption of ammonia

One issue that has not been (and can not be) illustrated with the use of the onset potential for the presented pathways of ammonia formation is desorption of ammonia from the surface. In this study the very reactive metal molybdenum is being studied and according to literature and the Sabatier principle the best catalysts are the ones that have just the right reactivity. Too reactive metals have issue of getting products off the surface and too weak metals will have issues in the formation of the products.

Two nitrogen coverages have been chosen to illustrate desorption of ammonia from the molybdenum nanocluster. One case is the high coverage of nitrogen (the $Mo_{13}N_{10}$ cluster) and the other case a low coverage of nitrogen (the Mo_{13} cluster). In both cases the molybdenum nanoclusters have two ammonia molecules adsorbed. The different ways of desorbing the two ammonia molecules

were studied. The reference system for calculating the desorption energy of ammonia is the free ammonia particle and the respective ammonia molecule(s) in gas phase.

In the case of high nitrogen coverage the energy for desorption of ammonia from the surface is as low as 0.38 eV and in the worst-case scenario it is 0.51 eV. These desorption barriers will not be a major issue under ambient reaction conditions. Desorption of ammonia will be slightly hindered, but not that it will lower the activity of the catalyst by many orders of magnitude.

In the other case, the low nitrogen coverage, the values of the desorption energy of ammonia are in the best case 0.16 eV and in the worst case 0.40 eV. These are low thermodynamic barriers for desorption of ammonia from the surface. These calculations indicate that the electrochemical production of ammonia should not be thermally hindered.

7.5 Conclusions

My theoretical study of the nitrogen covered molybdenum nanoparticle at ambient temperature and pressure indicate that these particles have potential for creating ammonia with low onset potential both at low and high nitrogen coverage. Faradaic losses due to the competing HER are reduced compared to other model systems presented in the literature. On the molybdenum nanoparticles nitrogen should be favored on the surface with applied potentials as high as -0.8 V.

At high nitrogen coverage, the pathways for creating ammonia are both the direct protonation of the nitrogen adatoms from the nitrogen coverage on the molybdenum nanoparticle and the protonation of an adsorbed nitrogen molecule adsorbed in the created nitrogen vacancy. The required onset potentials for both reaction pathways are on the order of -0.7 V to -0.5 V. The competition between hydrogen adatoms and nitrogen admolecules will be an issue at high nitrogen coverage, where hydrogen is preferred.

At low nitrogen coverage, the associative mechanism should require onset potentials of -0.6 V. Nitrogen admolecules are preferred at these conditions compared to hydrogen adatoms.

The dissociation of nitrogen at both low and high nitrogen coverage have very high activation barriers of around 1.8 eV, effectively blocking the dissociative mechanism at ambient conditions.

Desorption energies of ammonia from the surface is varying from 0.1 eV to 0.5 eV. These desorption barriers should not make the ammonia production on the molybdenum thermally hindered at ambient conditions and room temperature.

The study of the molybdenum nanocluster show that the molybdenum nanoclusters are promising electro-catalyst for ammonia production.

Chapter 8

The role of oxygen on molybdenum nanocluster for electro-catalytic ammonia production

This chapter is based on the included Paper D and the chapter includes additional information to what is presented in the paper.

8.1 Introduction

Molybdenum nanocluster [107] have been identified as a prime candidate for electrochemical ammonia production with seemingly low Faradaic losses to hydrogen evolution in the previous chapter. To produce ammonia electrochemically one can either use a liquid or a solid electrolyte. Many of these electrolytes will require wet conditions and it will lead to water being present. It will give rise to oxygen adsorption on the surface and the oxygen atoms will occupy important surfaces sites. The adsorbed oxygen can either decrease or totally hinder other chemical reactions taking place at that site. Oxygen poisoning of the surface is indeed a main inhibitor for ammonia production [140, 141]. In this chapter the presence of oxygen in the form of water on the molybdenum nanocluster will be investigated to understand the implications oxygen has on the catalytic properties for electrochemical ammonia production. In addition, the blocking of active sites by oxygen has been explored, together with a determination of reduction pathways to fully reduce the adsorbed oxygen atoms into water.

The basis for this continued study of the molybdenum nanocluster is the same computational settings as used in the previous chapter. To describe the electrochemical efficiency of the molybdenum nanocluster for reduction of oxygen and ammonia production, the method described in section 4.3.1 will be used to determine the onset potential for each reaction step, such that the protonation is exergonic, and the overall onset potential for the whole reaction can be

determined.

8.2 Results

8.2.1 Oxygen adsorbed in nitrogen vacancies

In the previous chapter, I showed that at a partially reduced nitrogen covered molybdenum nanocluster, N_2 adsorption is preferred over H in the nitrogen vacancy sites at lower nitrogen coverages at the potential of U= -0.6 V needed for electrochemical ammonia production through the associative mechanism. Adsorption of oxygen atoms are presented in Fig. 8.1, where they have been adsorbed at the vacant bridge site.

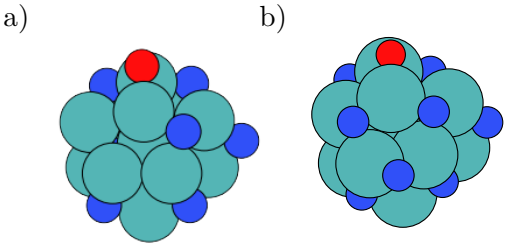

Figure 8.1: *a) Adsorption of oxygen at a nitrogen vacancy site on $Mo_{13}N_{10}$, and b) Adsorption of oxygen at a nitrogen vacancy site on $Mo_{13}N_{12}$. Oxygen is adsorbed in the bridge site in both cases.*

The free energies for adsorbing oxygen are shown in table 8.1, where the energies for nitrogen and hydrogen are also listed. The table shows that oxygen will be the preferred adsorbate, with much higher adsorption energies of -1.58 eV increasing to -2.15 eV. It is evident that if water is present, the vacancy sites will be filled with oxygen and hence blocks the active sites. This will block nitrogen molecules from adsorbing to this site and stop the electrochemical formation of ammonia from this site.

Table 8.1: Stability of nitrogen, hydrogen and oxygen with (U = -0.6 V) and without an applied potential at nitrogen vacancy sites on the $Mo_{13}N_x$ nanocluster. The potential required to produce ammonia electrochemically at partially nitrogen covered molybdenum nanoclusters was shown to be U = -0.6 V [142]. The energies are given with respect to H_2O(g), H_2(g) and N_2(g).

	ΔG_{N_2} [eV]	ΔG_H [eV]	ΔG_H [eV] (U = -0.6V)	ΔG_O [eV]	ΔG_O [eV] (U = -0.6V)
$Mo_{13}N_{12}$	-0.06	-0.66	-1.26	-1.58	-0.38
$Mo_{13}N_{11}$	-0.43	-0.71	-1.31	-2.24	-1.24
$Mo_{13}N_{10}$	-1.2	-0.73	-1.33	-2.33	-1.13
$Mo_{13}N_9$	-1.13	-0.59	-1.19	-2.15	-0.95

However, another reference can be used for the adsorption free energy of O. Protons and electrons can be used instead of H_2(g) together with gas phase water. This will model the relative stability of oxygen in an electrochemical cell

during operating conditions where the applied potential will influence stability of O. The relative shift in stability between the two methods is - 2 · U. In the specific case with an applied potential of -0.6 V, oxygen will be 1.2 eV less stable if the proton and electron reference is used. This is shown in table 8.1, where the stability of O changes such that it comparable to either nitrogen or hydrogen.

To free the active sites for N_2 adsorption and subsequent electrochemical ammonia production, oxygen needs to be removed from the surface sites. One way of re-activating the molybdenum nanocluster for electrochemical ammonia production is to reduce the oxygen electrochemically. The reduction of oxygen will form water, which will be less strongly bound to the active site and make it possible to bind N_2 preferentially.

In the case of oxygen adsorption on the more nitrogen rich molybdenum nanoclusters, table 8.2 shows the required potentials for the two-proton transfer steps in the reduction of oxygen.

The potentials range from -1.28 to -1.62 V for the second protonation step. The second protonation steps, the formation of H_2O, are hindered by the adsorbed nitrogen atoms that is present around the adsorption site of O, OH and H_2O at the surrounding three fold hollow sites. The required high potential will limit the removal of oxygen from the partially nitrogen covered molybdenum surface and oxygen will therefore constitute a very strong blocking of the active sites and subsequently limit the ammonia production rate through the associative mechanism on the nitrogen covered molybdenum nanoclusters.

Table 8.2: Reduction of oxygen adsorbed on the $Mo_{13}N_x$ nanocluster.

	$U_{O\rightarrow OH}$ [V]	$U_{OH\rightarrow H_2O}$ [V]
$Mo_{13}N_{12}O$	-0.35	-1.62
$Mo_{13}N_{11}O$	-0.97	-1.25
$Mo_{13}N_{10}O$	-1.18	-1.28
$Mo_{13}N_9O$	-0.72	-1.41

Direct reduction of the residual nitrogen skin will, however, still be possible and the potential will not be influenced by the presence of oxygen and the nitrogen skin will be reduced electrochemically at -0.6 V as shown in chapter 7 or in ref. [142] for a water free environment.

8.2.2 An oxygen skin

In the previous chapter, I showed that the electrochemical production of ammonia will not only occur on nitrogen covered molybdenum clusters, but could also take place at very low or no nitrogen coverage. A clean molybdenum nanocluster in contact with nitrogen, hydrogen and water will preferentially adsorb oxygen on the surface, see Fig. 8.2. The figure shows the total adsorption free energies of oxygen, nitrogen and hydrogen as the coverage evolves and until saturation of oxygen and nitrogen is obtained on the surface. The oxygen skin is approximate 1-2 eV more energetically favored than a nitrogen skin at low coverages. At higher coverages, the oxygen skin becomes even more energetically favored. The consequence is that oxygen will be preferred on the surface compared to nitrogen and hydrogen. If water is present, the surface is expected to have an

oxygen coverage. However, if we use the reference of protons and electrons, the dashed blue line on Fig. 8.2 show that the potential have destabilized the oxygen atoms such that a overlayer of oxygen arising from electro chemical splitting of water should not be expected.

A cyclic pattern is seen in the binding energy for both nitrogen and oxygen adatoms, corresponding roughly to 10 electrons. Fig. 8.2 shows the d-band of the molybdenum nanocluster as the oxygen coverage increases and it is observed that the d-band broadens and the energetically lower lying d-orbitals are filled.

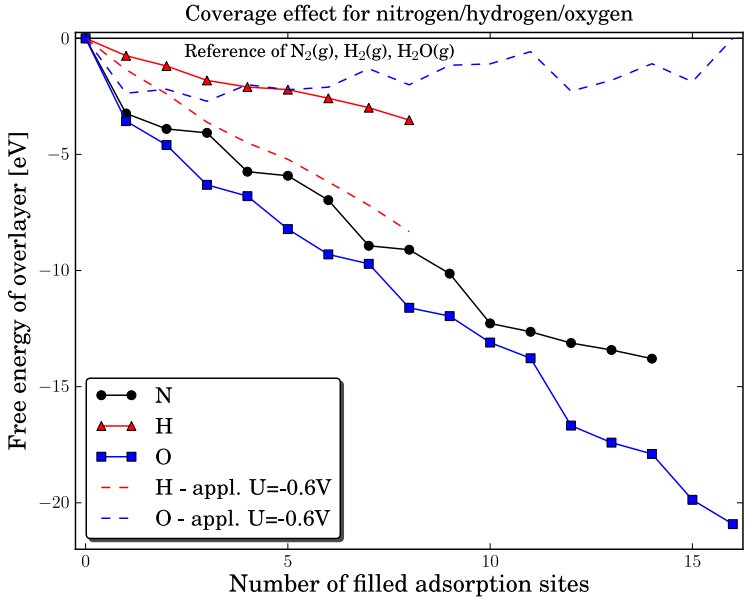

Figure 8.2: *The total free energy for covering the Mo_{13} nanocluster with either nitrogen, hydrogen or oxygen. The filled dark line shows the filling of the nitrogen skin, while the filled blue line shows the evolution of oxygen coverage. The red line shows the adsorption of hydrogen, while the dashed red line shows the adsorption of hydrogen and the dashed blue line shows the adsorption of oxygen (proton and electron reference) at an external applied potential of -0.6 V, which is the potential needed for electrochemically ammonia production previously determined for the clean and nitrogen covered molybdenum nanocluster [142].*

The preferred adsorption sites for oxygen atoms are the three fold hollow sites, see Fig. 8.3a. When all the three fold sites are filled, the oxygen atoms will adsorb in the four fold hollow sites, see Fig. 8.3c. After additional adsorption of a few oxygen atoms the surface has greatly distorted. The restructuring allows a higher filling of oxygen on the surface, see Fig. 8.3d. The maximum filling of the surface increases to 16 oxygen atoms and further additions of oxygen atoms are energetically un-favored. At a near full overlayer, the binding of oxygen are asymmetric where oxygen now binds in a mix of a three fold hollow site and a bridge site.

Fig. 8.4 shows the evolution of the d-band of the molybdenum nanocluster as the coverage of oxygen increases. The oxygen skin formation significantly changes the d-band position and width, where the d-band center shifts down together with an increase in the width. The molybdenum atoms seems to become

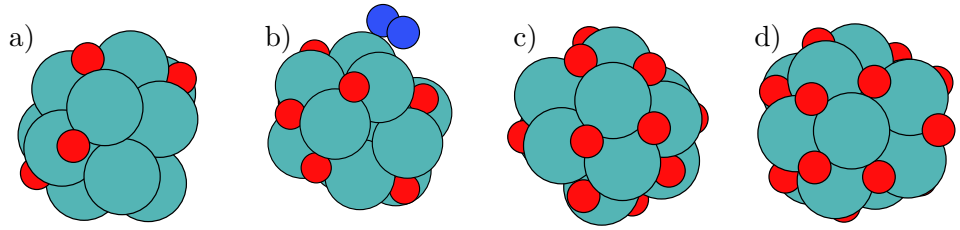

Figure 8.3: *a) The $Mo_{13}O_6$ nanocluster, b) the $Mo_{13}O_9$ nanocluster with N_2 adsorbed, c) the $Mo_{13}O_{12}$ with an almost filled oxygen skin, d) the $Mo_{13}O_{16}$ with a filled oxygen skin. At the the $Mo_{13}O_{16}$, the oxygen adsorption sites are a mix of three fold hollow sites and bridge sites.*

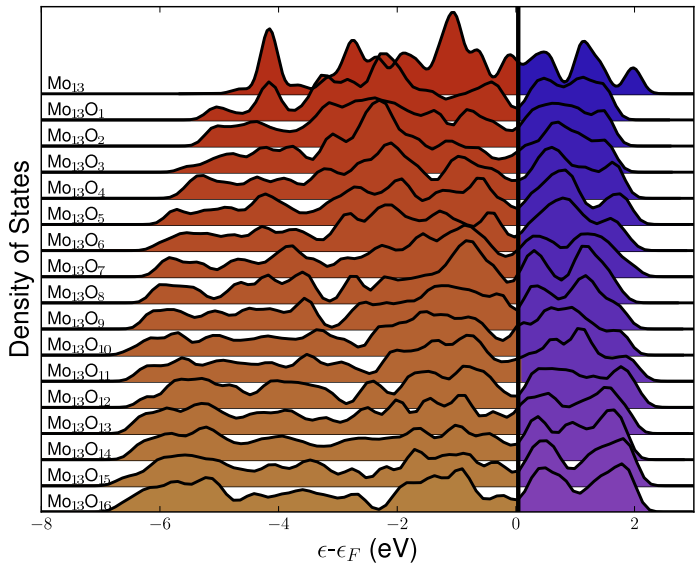

Figure 8.4: *The evolution of the d-band as the coverage of oxygen increases on the The $Mo_{13}O_x$ nanocluster.*

more bulk like, see Fig. 6.3 for the d-band structure of bulk molybdenum. This explains the observed saturation of the surface and overall decreasing in adsorption energy that is observed at higher coverages. As for the hydrogen and nitrogen in the previous chapter, no correlation can be extracted between the adsorption energy of oxygen and the d-band position, see Fig. C.1. Instead, again the total adsorption energy of the oxygen skin correlates with the d-band center , see Fig. C.2 in appendix C.

8.2.3 Reduction of the oxygen overlayer

At the fully oxygen covered molybdenum nanocluster, nitrogen molecules cannot adsorb to the surface. Therefore, a full oxygen skin eliminates electrochemical ammonia production. It is therefore necessary to reduce the surface, in order to create active sites for nitrogen adsorption. To fully investigate the reduction of oxygen on a partially or fully oxygen covered molybdenum nanocluster, the

reduction of all adsorbed oxygen atoms should, in principle, be analysed. This is, however, not computationally feasible and instead up to three representative adsorbed oxygen atoms are reduced at each investigated oxygen coverage. Each of the chosen oxygen atoms represents an unique oxygen adsorption position and the coverage ranges from 16 oxygen atoms to only one oxygen atom. The

Table 8.3: Reduction of an oxygen overlayer on molybdenum nanoparticles where multiple adsorbed oxygen atoms have been reduced at each coverage. This is done to probe the reduction of all the unique adsorption sites at each coverage.

	$U_{O\rightarrow OH}$ [V]	$U_{OH\rightarrow H_2O}$ [V]
$Mo_{13}O_{16}$	-0.49	-0.44
$Mo_{13}O_{14}$	0.04	-0.47
$Mo_{13}O_{12}$	-0.64	-0.66
$Mo_{13}O_{9}$	-0.27	-0.67
$Mo_{13}O_{6}$	-0.29	-0.24
$Mo_{13}O_{2}$	-0.44	-0.31
$Mo_{13}O$	-0.67	-0.72

potentials for the two proton transfer processes are presented in Table 8.3. For other proton transfer processes (not shown), the local geometries around the adsorption site can hinder both protonation steps, but most often the second protonation is hindered. One such hindrance can be the movements from the adsorption site of the OH species to an on top site, where the H_2O specie is energetically most stable. Such movement requires a restructuring of the local environment, and hence the protonation step can become energetically very endothermic. The largest variation is therefore seen for the second protonation step. For the presented reduction steps of OH, the required potentials are in the range of -0.2 to -0.7 V. The formation of OH from O will require a negative potential to stabilize the OH specie compared to the O atom, and in most cases the potential required are in the range of -0.3 V to -0.7 V.

For most of the studied coverages, the reaction free energies for desorption of H_2O off the surface are either low or exergonic. In general, desorption energies are lower than 0.4 eV, but for a single adsorbed oxygen atom, it is as high as 1.2 eV. Water should therefore desorb thermally from the surface, except at very low oxygen coverages.

The study of oxygen reduction produces adsorption energies for O, OH, H_2O at different coverages. No apparent correlation is found between the adsorption energies of E_O, E_{OH} and E_{H_2O}, see Fig. D.1 and Fig. D.2 in appendix D, in contrast to what has previously been observed on metal surfaces, where scaling relations are applicable for OH species on close-packed and stepped surfaces for low coverages [128]. The close packed and stepped surfaces typically have less restructuring during the adsorption of O, OH and H_2O.

On the molybdenum nanocluster surface, larger local restructuring takes place when either O is added or removed and when either O or OH is protonated. The restructuring of the molybdenum cluster involves all atoms in the nanocluster. This is an effect of the small size of the nanocluster, where the local impact from an adsorption or a reduction step influences the whole nanocluster.

The lowest required potential for water formation at the different coverages is in the range of -0.3 V to -0.7 V. These values are lower than the required potential needed to form ammonia on the molybdenum nanocluster [142]. Overall, it seems that it is possible to reduce oxygen of the surface at moderate potential of -0.72 V.

The potential required for reduction of a surface oxygen atom indicates that the nanoclusters can be reactivated after exposure to air or water from the electrolyte or the fabrication process.

8.2.4 Formation of ammonia at relative high oxygen coverage

Nitrogen molecules are not able to adsorb to neither an oxygen vacancy site nor ontop of an oxygen atom at high oxygen coverages. Once the oxygen skin has been partially reduced, the nitrogen molecules adsorb onto the surface at the oxygen vacancy sites, see Fig. 8.3b. The adsorption of nitrogen become stable at a coverage of less than 10 oxygen atoms, see Table 8.5. The adsorption energies of N_2 are varying from -1.0 eV to -1.8 eV depending on the oxygen coverage. The corresponding hydrogen adsorption energies are lower, ranging from -0.65 eV to -0.86 eV, and nitrogen molecules are therefore preferred over hydrogen on the surface at zero applied potential. At an applied potential of -0.6 V, which is the potential shown to electrochemically produce ammonia on the clean molybdenum nanocluster, the reaction free energy of adsorbing either a hydrogen atom (coming from H^+ and e) or a nitrogen molecule will at certain coverages be in favor of H ($Mo_{13}O_8$ and $Mo_{13}O_6$) and others of N_2 ($Mo_{13}O_9$ and $Mo_{13}O_7$).

Table 8.4: The adsorption free energies of nitrogen and hydrogen with and without an applied potential on a partly oxygen covered Mo_{13} nanocluster.

	ΔG_{N_2} [eV]	ΔG_H [eV]	ΔG_H [eV] (U = -0.6 V)
$Mo_{13}O_{12}$	No binding	-0.23	0.43
$Mo_{13}O_{10}$	0.33	-0.84	-1.44
$Mo_{13}O_9$	-1.82	-0.72	-1.32
$Mo_{13}O_8$	-1.02	-0.75	-1.35
$Mo_{13}O_7$	-1.77	-0.86	-1.46
$Mo_{13}O_6$	-0.93	-0.65	-1.25

For nitrogen molecules adsorbed at a vacancy site on either $Mo_{13}O_9$ or $Mo_{13}O_6$, the potential for driving the electrochemical production of ammonia can be determined. These nanoclusters were selected to describe the two regimes with strong and weak N_2 adsorption compared to hydrogen adsorption, respectively. On the $Mo_{13}O_9$ nanocluster, N_2 is bound most strongly at an applied potential of -0.6 V, while hydrogen is bound stronger on the $Mo_{13}O_6$ nanocluster. Investigations of the associative pathway on the $Mo_{13}O_9$ nanocluster, shows the first protonation step to require an onset potential of -0.7 V. The onset potentials are shown in Fig. 8.5 for the following electrochemical reaction steps:

For nitrogen molecules adsorbed at a vacancy site on either $Mo_{13}O_9$ or $Mo_{13}O_6$, the potential for driving the electrochemical production of ammonia

can be determined. These nanoclusters were selected to describe the two regimes with strong and weak N_2 adsorption compared to hydrogen adsorption, respectively. On the $Mo_{13}O_9$ nanocluster, N_2 is bound most strongly at an applied potential of -0.6 V, while hydrogen is bound stronger on the $Mo_{13}O_6$ nanocluster. Investigations of the associative pathway on the $Mo_{13}O_9$ nanocluster, shows the first protonation step to require an onset potential of -0.7 V. The onset potentials are shown in Fig. 8.5 for the following electrochemical reaction steps:

$$\begin{aligned}
\mathrm{NN}^* + 6(\mathrm{e}^- + \mathrm{H}^+) &\rightarrow \\
\mathrm{NHN} * + 5(\mathrm{e}^- + \mathrm{H}^+) &\rightarrow \\
\mathrm{NH_2N}^* + 4(\mathrm{e}^- + \mathrm{H}^+) &\rightarrow \\
\mathrm{NH_3^*} + \mathrm{N}^* + 3(\mathrm{e}^- + \mathrm{H}^+) &\rightarrow \\
\mathrm{NH_3^*} + \mathrm{NH}^* + 2(\mathrm{e}^- + \mathrm{H}^+) &\rightarrow \\
\mathrm{NH_3^*} + \mathrm{NH_2^*} + (\mathrm{e}^- + \mathrm{H}^+) &\rightarrow \\
\mathrm{NH_3^*} + \mathrm{NH_3^*} &
\end{aligned}$$

The x-axis show the adsorbed reaction intermediate for each protonation step and NH_2N denotes a doubly protonated nitrogen molecule with the N-N backbone intact, while NH_3-NH denotes NH_3 and NH adsorbed on the surface. Five pathways were studied, and all of had the first initial protonation step to be the potential limiting step with identical required onset potentials.

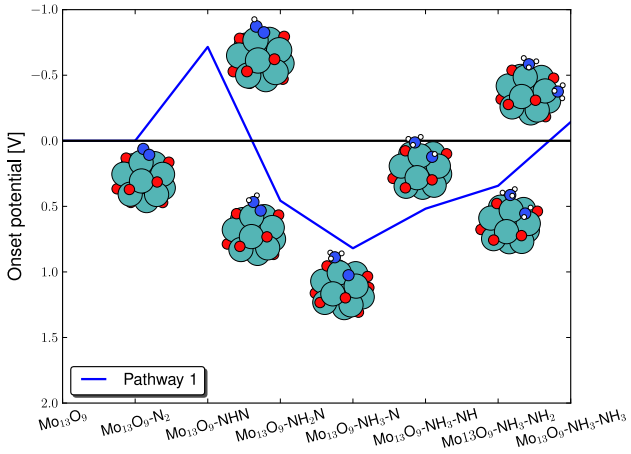

Figure 8.5: *Diagram of the required applied potential to make each reaction step exergonic for electrochemical ammonia production on the $Mo_{13}O_9$ through the associative mechanism. For all five studied reaction pathways, the highest required potential is -0.7 V for the first protonation step.*

For a more reduced oxygen skin, e.g. the $Mo_{13}O_6$ nanocluster, the energetics of the electrochemical production of ammonia are much more diverse. Here, two routes are very favorably, demanding only potentials of around -0.45 V, to drive the electrochemical production of ammonia, see Fig. 8.6. The routes not shown require potentials of -0.85 V to -1.3 V. The reaction intermediates for the preferred ammonia formation route have been used as the bottom x-axis. The blue

filled line on Fig. 8.6 shows that the rate-limiting step is the last protonation; while for the alternative route, marked with the green dashed line and the corresponding reaction intermediates have been used as the top x-axis in Fig. 8.6, the rate-limiting steps are found to be both the third and the last protonation step. The limiting step for this reaction path is the formation of the NH_2-NH intermediate on the surface. The reaction is then followed by a very exergonic reaction step, where the N-N bond breaks. In both pathways, the N-N bond breaking in the associative process is very exergonic and no apparent activation barrier is observed for the N-N cleavage at either the third or fourth protonation step. The onset potential presented here for electrochemical ammonia production is similar to those obtained in previous studies on both clean and nitrogen covered molybdenum nanoclusters presented in chapter 7 and published in paper [142].

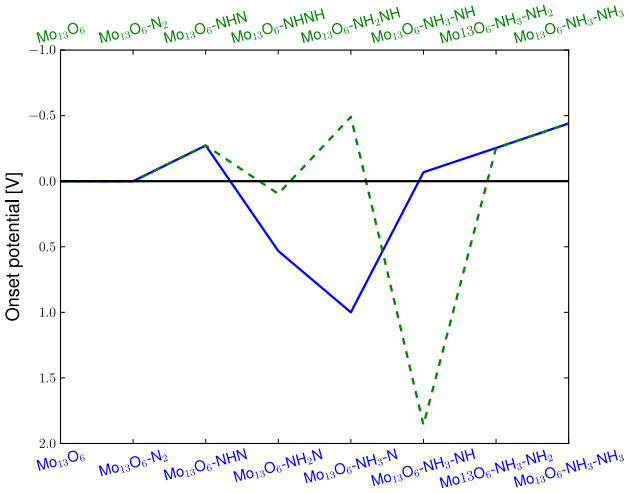

Figure 8.6: *Diagram of the required applied potential to make each reaction step exergonic for electrochemical ammonia production on the $Mo_{13}O_6$ through the associative mechanism. The limiting reaction is the last protonation to form the second ammonia on the surface requiring a potential of -0.45 V to become exergonic.*

Instead of protonating the adsorbed nitrogen molecule, the potential could drive the reduction of oxygen. In Table 8.5, the potentials for driving the oxygen reduction processes are presented. Here, a potential of -0.77 V is required for the high oxygen coverage case, while the last reduction step for the lower oxygen coverage requires significantly larger potentials, i.e. -1.3 V to -1.75 V, to make the reaction exergonic. H_2O is found to be unstable on $Mo_{13}O_6$, while $Mo_{13}O_9$ has a stable adsorption of water.

Table 8.5: The required potentials for reducing oxygen at two oxygen coverages when nitrogen molecules are present on the partly covered oxygen surfaces.

	$U_{O\rightarrow OH}$ [V]	$U_{OH\rightarrow H_2O}$ [V]
$Mo_{13}O_9$-N_2	-0.53	-0.77
$Mo_{13}O_6$-N_2	-0.26	-1.30

8.2.5 Competing reaction mechanisms

A procedure to determine the possible reaction pathways on the $Mo_{13}O_9$ nanocluster with N_2 adsorbed with an applied potential U = -0.7 V, such that electrochemical ammonia production is exergonic, is presented. Three possible mechanisms must be considered: the reduction of N_2 to ammonia, hydrogen adsorption and evolution, and last the reduction of oxygen and subsequently formation of water. Here, we assume that the adsorption of H with N_2 present on the surface will be equal to adsorption of H on a surface without N_2 present.

The reaction free energies of forming H, OH, and N_2H at U = -0.7 V are: $\Delta G_{N_2*+(H^+ + e^-)\rightarrow N_2H*} = 0$ eV, $\Delta G_{(H^+ + e^-)\rightarrow H*} = -1.42$ eV, $\Delta G_{O*+(H^+ + e^-)\rightarrow OH*} = -0.17$ eV, respectively. The reaction step with the lowest reaction free energy is hydrogen adsorption on the surface. For adsorbed hydrogen, the next step will be formation of H_2(g) with a reaction free energies of $\Delta G_{H*+(H^+ + e^-)\rightarrow H_2(g)} = 0.02$ eV. The next reaction to occur on the surface will therefore be the reduction O to OH at -0.17 V. For this reaction intermediate, the next reaction will produce H_2O with a reaction free energies of $\Delta G_{OH*+(H^+ + e^-)\rightarrow H_2O*} = 0.08$ eV. Small energy differences between the next protonation, but N_2H will be formed on the surface.

The subsequent reaction intermediates for ammonia formation are exergonic at U = -0.7 V. The initial production of an overlayer of H is followed by reduction of O into OH, until the electrochemical reduction of N_2 becomes possible. When the ammonia molecules have desorbed from the surface, adsorption of N_2 is 0.4 eV more stable than H, which would make the adsorption of nitrogen at a vacancy site energetically favorable. At higher pH-values this difference would increase in favour of N_2 adsorption, as given by eq. 4.10. Because of the very small difference between the formation of N_2H, H_2O and H_2(g) a Faradaic loss due to hydrogen evolution should be expected and a reduction of the oxygen skin on the surface would also be expected at this oxygen coverage and potential.

For the $Mo_{13}O_6$ nanocluster with N_2 adsorbed at an applied potential of U = -0.45 V, the preferred mechanism is the following. First hydrogen is bound to the surface, then O is reduced to OH and then finally the reduction of N_2 can take place. Here, the reaction free energy for production of gas phase hydrogen is $\Delta G_{H*+(H^+ + e^-)\rightarrow H_2(g)} = 0.20$ eV and for water formation is $\Delta G_{OH+(H^+ + e^-)\rightarrow H_2O*} = 0.59$ eV, while ΔG for all electrochemical reaction steps for ammonia production, see Fig. 8.6, are zero or lower as in the previous example on the $Mo_{13}O_9$ nanocluster.

In the discussion of the preferential reactions on the $Mo_{13}O_9$ and $Mo_{13}O_6$ nanoclusters, adsorbate-adsorbate interactions are not included due to the large computational cost associated with a comprehensive investigation. This is a potentially significant assumption, since the adsorption energies may decrease with higher coverage [83]. For hydrogen evolution on the $Mo_{13}O_6$ nanocluster, this could have the consequence that the free energy barrier for producing gas phase hydrogen molecules is lowered.

The results for ammonia production on a partially oxidized molybdenum nanocluster indicates that the formation of ammonia on the molybdenum nanocluster is possible at a low onset potential, but with a low Faradaic efficiency due to the parasitic formation of both adsorbed H or OH on $Mo_{13}O_9$ and $Mo_{13}O_6$.

Adsorption of nitrogen seems to hinder the further reduction of OH at lower oxygen coverages. This indicates that the nanocluster should be fully reduced, i.e. no oxygen present on the surface, before nitrogen is able to reach the catalyst surface. Small amounts of oxygen in the form of water may however be present in the electrochemical cell, e.g. from the solid proton conduction electrolyte, without limiting the electrochemical production of ammonia does not seem to be limited at low oxygen coverages.

8.3 Conclusions

Density functional theory calculations have been employed to investigate the adsorption and reduction of oxygen on molybdenum nanoclusters. The computational hydrogen electrode was used to determine potentials for reduction of nitrogen and oxygen and the hydrogen evolution reaction.

First, a partially nitrogen covered molybdenum nanocluster was exposed to oxygen and the adsorption of oxygen atoms was shown to be stronger than both hydrogen atoms and nitrogen molecules. The consequence is that the presence of water will lead to preferential oxygen adsorption at the nitrogen vacancy sites. The reduction of the oxygen atoms at the nitrogen rich molybdenum nanocluster was studied, and the potentials more negative than -1.25 V. The main challenge is the second protonation step, where the reaction step is very dependent on the local environment. The oxygen atom will bind to the vacancy site blocking the adsorption of nitrogen molecules and thereby greatly reduce the efficiency of the nitrogen rich molybdenum nanocluster as an electro catalyst for ammonia production through the associative mechanism. A direct reduction of the nitrogen skin will, however, still be possible at -0.6 V.

A clean molybdenum nanocluster in contact with oxygen, hydrogen and nitrogen will preferentially form an oxygen skin. Nitrogen adsorption on an oxygen covered molybdenum nanocluster is impossible, and therefore the reduction of an oxygen overlayer was studied. It was found that the reduction requires potentials of -0.29 V to -0.72 V to successfully produce water from adsorbed oxygen atoms. The desorption of water has low free energy barriers. With oxygen coverage of nine or less oxygen atoms, adsorption of nitrogen and hydrogen becomes possible. The electrochemical production of ammonia for adsorbed nitrogen molecules at partial oxygen coverage will only require potentials of -0.45 V to -0.7 V to make the reaction exergonic. These onset potentials are similar to values reported in earlier studies of electrochemical ammonia production on molybdenum nanocluster with or without a nitrogen skin. At the potentials needed to make the ammonia production exergonic, hydrogen is found to be present on the surface, and a reduction of oxygen to OH is observed, before electrochemical production of ammonia is possible.

Chapter 9

Outlook

In this thesis we have developed a universal transition state scaling relation for a large number of (de)hydrogenation reactions over close-packed and stepped surfaces as well as nanoparticles of transition metals. This is a great tool that can be utilized in future studies of (de)hydrogenation reactions, where one can apply the relations to simplify the complexity of the reaction. Hopefully, the relations can be used to construct new catalysts, that is better, cheaper or have better desired properties.

The volcano plots constructed on the basis of the scaling relations obtained on very under-coordinated reaction sites on the M12 nanocluster model system have proposed molybdenum as a new material for electrochemical ammonia production. The molybdenum nanocluster should require an onset potential of -0.55 V for electrochemical ammonia production. The competing hydrogen evolution is preferred for Mo with a lower required potential, whereas the adsorption strength of hydrogen atoms and nitrogen molecules at reaction conditions (U = -0.55 V) are identical. On the basis of this investigation, one could search for M12 alloys that have an adsorption free energy for nitrogen atoms of approximately -0.6 eV. These alloys could potentially be good candidates for electrochemical ammonia production. However, the stability of alloy materials are a much more difficult task to achieve for a catalyst under electrochemical reaction conditions.

On the basis of the findings in the M12 nanocluster study, the properties of a cuboctahedral molybdenum nanoclusters consisting of 13 atoms for electrochemical ammonia production where extensively studied using DFT. The properties of the catalyst were in good agreement with expected properties for onset potential and hydrogen competition. The nanocluster should preferentially bind nitrogen at applied potentials of -0.8 V and lower. The potentials required for electrochemical ammonia production are around -0.6 V for various pathways and nitrogen coverages.

The good results for the Mo nanocluster initiated a study of oxygen on the molybdenum surface. This study shows that the main inhibitor for catalytic activity of the molybdenum nanocluster is the presence of water and hence oxygen. The adsorption is stronger for oxygen than for nitrogen. The required potential to reduce oxygen off the surface should be around -0.67 V and thus

oxygen poisoning should not be a problem at this potential. Preparation of the molybdenum nanoclusters do not need to be away from either air or water, because the calculations present suitable pathways for reducing the oxygen off the surface. With a partly coverage of oxygen, nitrogen can adsorb and electrochemical production of ammonia is possible with potentials lower than -0.7 V.

The thesis have shown that it is possible to reduce the complexity of chemical reactions using scaling relations, BEP relations and the computational hydrogen electrode approach. In the M12 nanocluster study the dissociative mechanism was studied, and I had to implement an arbitrary cut-off enabling us to describe the reaction pathway. But it does not give a real picture of the limitations for N_2 dissociation. I claim that we need to bridge the gap even further between modelling electrochemistry with the use of the computational hydrogen electrode approach and the microkinetic modelling of heterogeneous reactions employing transition state theory. I will use the decomposition of ammonia as an example of some the difficulties we face, when lacking the knowledge of the interplay between the two domains.

Ammonia decomposition

One way of using ammonia as a fuel, would be to decompose ammonia on a M12 nanocluster catalyst at the cathode in a electrochemical cell. Ammonia dehydrogenate until N_2 is formed while protons and electrons are produced. The protons will diffuse through the electrolyte while the electrons run through the circuit (potentially driving an engine) and at the anode the electrons and protons recombine into hydrogen or react with oxygen to form water, see Fig. 4.1. In this study, the focus will only be on the reaction steps taking place at the cathode side and the scaling relations presented in chapter 6 will be used.

First, lets us start by only applying the computational hydrogen electrode, and assume that all reactions will be a proton transfer process. This will be an assumption, because the N-N recombination will be a heterogeneous reaction step and I will later come back to discuss this assumption. The reactions 4.4a - 4.4g will be reversed and a few additional reactions will be added, such that all possible pathways are included. Especially, possible reaction steps have been added for the N-N recombination and these involves recombination of NH_x species in different combinations. This opens for other pathways than the traditional N + N recombination step. However, reactions creating N_2H_4 or N_2H_5 species have been omitted, due to the fact that no observed stable configurations

were found on the M12 nanoclusters. The studied reactions are shown next:

$$\mathrm{NH_3}* \rightleftharpoons \mathrm{NH_2}* + (\mathrm{H^+} + \mathrm{e^-}) \tag{9.1a}$$
$$\mathrm{NH_2}* \rightleftharpoons \mathrm{NH}* + (\mathrm{H^+} + \mathrm{e^-}) \tag{9.1b}$$
$$\mathrm{NH}* \rightleftharpoons \mathrm{N}* + (\mathrm{H^+} + \mathrm{e^-}) \tag{9.1c}$$
$$\mathrm{NH_3}* + \mathrm{NH}* \rightleftharpoons \mathrm{N_2H_3}* + (\mathrm{H^+} + \mathrm{e^-}) \tag{9.1d}$$
$$\mathrm{NH_2}* + \mathrm{NH_2}* \rightleftharpoons \mathrm{N_2H_3}* + (\mathrm{H^+} + \mathrm{e^-}) \tag{9.1e}$$
$$\mathrm{NH_2}* + \mathrm{NH}* \rightleftharpoons \mathrm{N_2H_2}* + (\mathrm{H^+} + \mathrm{e^-}) \tag{9.1f}$$
$$\mathrm{NH_2}* + \mathrm{N}* \rightleftharpoons \mathrm{N_2H}* + (\mathrm{H^+} + \mathrm{e^-}) \tag{9.1g}$$
$$\mathrm{NH}* + \mathrm{NH}* \rightleftharpoons \mathrm{N_2H}* + (\mathrm{H^+} + \mathrm{e^-}) \tag{9.1h}$$
$$\mathrm{NH}* + \mathrm{N}* \rightleftharpoons \mathrm{N_2}* + (\mathrm{H^+} + \mathrm{e^-}) \tag{9.1i}$$
$$\mathrm{N_2H_3}* \rightleftharpoons \mathrm{N_2H_2}* + (\mathrm{H^+} + \mathrm{e^-}) \tag{9.1j}$$
$$\mathrm{N_2H_2}* \rightleftharpoons \mathrm{N_2H}* + (\mathrm{H^+} + \mathrm{e^-}) \tag{9.1k}$$
$$\mathrm{N_2H}* \rightleftharpoons \mathrm{N_2}* + (\mathrm{H^+} + \mathrm{e^-}) \tag{9.1l}$$

The presented reactions can in many different pathways form $\mathrm{N_2}$, where the most promising pathway is through the reactions 9.1a, 9.1b, 9.1c, and 9.1i. The resulting volcano plot is shown in Fig. 9.1 and illuminates the potential required to make each of the reaction steps exergonic. As opposed to the volcano plots

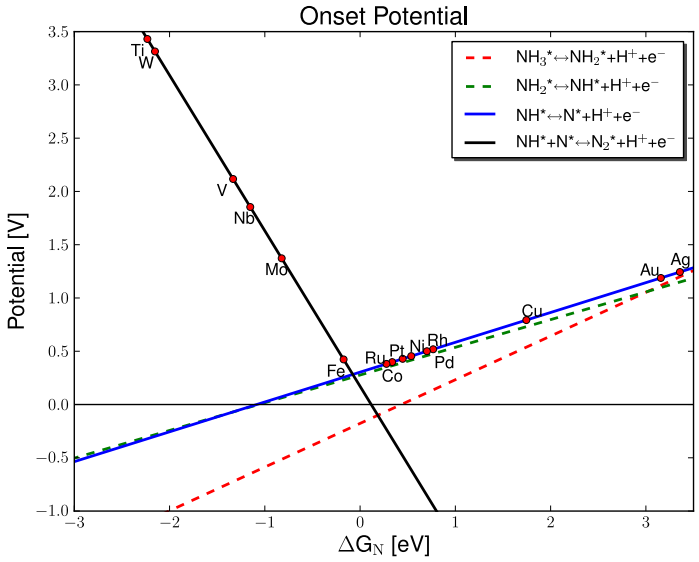

Figure 9.1: *Volcano plot for the electrochemical decomposition of ammonia.*

presented in chapter 6 for the electrochemical ammonia production, the rate limiting reaction steps for the ammonia decomposition are now the top lying lines. For ammonia decomposition, it is the reduction of NH into $\mathrm{N} + \mathrm{e^-} + \mathrm{H^+}$ that is the limiting reaction for the noble metals. For the reactive metals it is the N-N bond formation reaction 9.1i.The potential for reduction of NH is slowly increasing as the metals become more noble, whereas the N-N backbone recombination is represented by a steep line that acts as a very sharp cut off for the more reactive metals. At the top of the volcano potentials of only 0.3 V is

required to decompose ammonia. The metals Fe, Ru, Co, Pt, Pd, Rh, and Ni are capable of ammonia decomposition employing potentials lower than 0.5 V.

In this description, I have circumvented the heterogeneous reaction step of N + N recombination. From the volcano plot, it seem that this recombination is easy, but that is not the case. Therefore, the assumption made for the N + N recombination reaction has to be revised and the activation barriers need to be included in the analysis.

Estimating the activation barrier for N_x-N_y formation

One way to gain insight in the N-N backbone recombination reactions, is to use the activation barriers for the reactions 9.2 instead of the reaction free energy of the reactions 9.1. There are six possible N-N recombination reactions.

$$NH_3* + N* \rightleftharpoons N_2H_3* \tag{9.2a}$$
$$NH_2* + NH* \rightleftharpoons N_2H_3* \tag{9.2b}$$
$$NH_2* + N* \rightleftharpoons N_2H_2* \tag{9.2c}$$
$$NH* + NH* \rightleftharpoons N_2H_2* \tag{9.2d}$$
$$NH* + N* \rightleftharpoons N_2H* \tag{9.2e}$$
$$N* + N* \rightleftharpoons N_2*. \tag{9.2f}$$

In the article by Wang et *al* [112] TS relations was presented for splitting of N-O, N-N, O-O, C-C, C-O and C-N over fcc(211) surfaces. Like the TS and BEP relations presented in chapter 5, the relations show a general trend for many backbone cleavage reactions. The relations presented in the paper can be used to give a fast and dirty indication of the recombination reactions shown in eq. 9.2. In the modification of the TS relation to fit to this work, I have used the general values for the slope (0.84) and constant (1.92 eV), where both N_2 dissociation is considered, together with other dissociation reactions involving hydrogen containing species. The TS relation is dependent on the dissociative energy of the reaction, E_{diss}, and this can be expressed in terms of the linear scaling relations calculated previously on the M12 nanocluster.

The activation barrier estimations for the recombination of the N-N backbone are presented for all considered reactions in Fig. 9.2. The differences in slope and constant between the plotted recombination reactions originates from the scaling relations describing the adsorption energy of the reaction intermediates. The best pathway for most metals is the recombination reaction 9.2f. The very noble metals Au and Ag have moderate activation barriers for this process, around 0.8 eV, while the more reactive metals have activation barriers ranging from 1.5 eV to 2.5 eV.

We now know that electrochemical decomposition of ammonia should be possible with low onset potentials, but with one major assumption for the key reaction step. On the other hand, the key reaction step seems to have a very high activation barrier. But it is erroneous to directly compare the two properties. The key to solve this, would be to model the reaction step

$$N + NH \rightarrow N_2 + e^- + H^+ \tag{9.3}$$

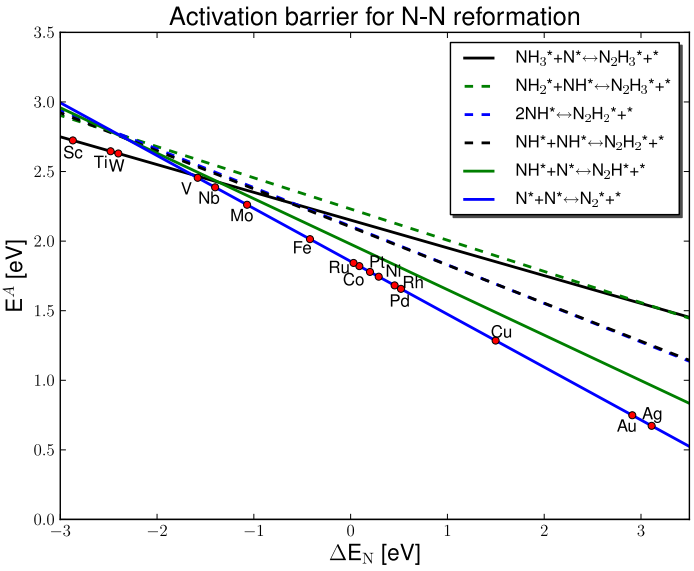

Figure 9.2: *Estimations of activation barriers for N-N backbone recombination.*

where we include the effects of an applied potential along the reaction coordinate. But this is no simple task.

Concluding remarks

What has come out of this short section on ammonia decomposition, is that the use of the computational hydrogen electrode approach can cover many important reactions, but faces the limitations of the approach in others. The electrochemical decomposition of NH_3 is an example of the limitations that arises when we as theoreticians want to investigate a reaction that is not entirely electrochemical, but also have heterogeneous reaction steps. We cannot describe the full picture with either methods, and have to circumvent the problematic reactions as I also did for the dissociative mechanism in chapter 6. The efficiency of a pure heterogeneous catalyst can be obtained by the use of mikrokinetic modelling, and the efficiency of the electro-catalyst can be estimated using the computational standard hydrogen electrode approach. But, as this case highlights, a combination of these two methods would be much desired to increase the insight we can gain from first principle calculations.

Bibliography

[1] THE DANISH GOVERNMENT 2011. *Energy Strategy 2050 - from coal, oil and gas to green energy.* 2011.

[2] V. Smil. Detonator of the population explosion. *Nature*, 400(415), 1999.

[3] V. Smil. Enriching the earth: Fritz Haber, Carl Bosch, and the Transformation of World Food Production. *Massachusetts Institute of Technology*, 2001.

[4] A. Klerke, C. H. Christensen, J. K. Nørskov, and T. Vegge. Ammonia for hydrogen storage: challenges and opportunities. *Journal of Materials Chemistry*, 18(20):2304–2310, 2008.

[5] R. Lan, J.T.S. Irvine, and S. Tao. Ammonia and related chemicals as potential indirect hydrogen storage materials. *Internaltional Journal of Hydrogen Energy*, 37:1482–1494, 2012.

[6] D. R. Lide. *CRC Handbook of Chemistry and Physics.* CRC Press, 90th edition, 2009.

[7] F. Haber and G. van Oordt. Über die Bildung von Ammoniak aus den Elementen. *Zeitschrift für anorganische Chemie*, 47:42–44, 1905.

[8] A. Nielsen. Ammonia: Catalysis and manufacture. *Springer-Verlag*, 1995.

[9] L. Stryer. *Biochemistry, 4th ed.* W.H. Freeman, New York, 4th edition, 1995.

[10] B. Hinnemann and J. K. Nørskov. Modeling a central ligand in the nitrogenase femo cofactor. *Journal of the American Chemical Society*, 125:1466–1467, 2003.

[11] G. Ertl, Z. Paal, and S. B. Lee. Structure sensitivity in the iron single-crystal catalyzed synthesis of ammonia. *Applied Surface Science*, 8:231–249, 1981.

[12] G. Ertl, M. Weiss, and S. B. Lee. Role of potassium in the catalytic synthesis of ammonia. *Chemical Physics Letters*, 60:391–394, 1979.

[13] N. D. Spencer, R. C. Schoonmaker, and G. A. Somorjai. Structure sensitivity in the iron single-crystal catalyzed synthesis of ammonia. *Nature*, 294:643–644, 1981.

[14] G. Ertl, S. B. Lee, and M. Weiss. Kinetics of nitrogen adsorption on fe (111). *Surface Science*, 114:515–526, 1982.

[15] G. Ertl, S. B. Lee, and M. Weiss. Adsorption of nitrogen on potassium promoted fe (111) and (100) surfaces. *Surface Science*, 114:527–545, 1982.

[16] N. D. Spencer, R. C. Schoonmaker, and G. A. Somorjai. Iron single crystals as ammonia synthesis catalysts: Effect of surface-structure on catalyst activity. *Journal of Catalysis*, 74:129–135, 1982.

[17] G. Ertl. Primary steps in catalytic synthesis of ammonia. *Journal of Vacuum Science & Technology A-Vacuum Surfaces and Films*, 1:1247–1253, 1983.

[18] L. Volpe and M. Boudart. Ammonia synthesis on molybdenum nitride. *Journal of Physical Chemistry*, 90:4874–4877, 1986.

[19] D. R. Strongin, J. Carrazza, S. R. Bare, and G. A. Somorjai. The importance of C7 sites and surface-roughness in the ammonia synthesis reaction over iron. *Journal of Catalysis*, 103:213–215, 1987.

[20] D. R. Strongin and G. A. Somorjai. The effects of potassium on ammonia synthesis over iron single-crystal surfaces. *Journal of Catalysis*, 109:51–60, 1988.

[21] J. A. Dumesic and A. A. Trevino. Kinetic simulation of ammonia synthesis catalysis. *Journal of Catalysis*, 116:119–129, 1989.

[22] L. M. Aparicio and J. A. Dumesic. Ammonia synthesis kinetics: surface chemistry, rate expressions, and kinetic analysis. *Journal of Materials Chemistry*, 18:2304–2310, 2008.

[23] M. Boudart. Ammonia synthesis: The bellwether reaction in heterogeneous catalysis. *Topics in Catalysis*, 1:405–414, 1994.

[24] G. Marnellos and M. Stoukides. Ammonia synthesis at atmospheric pressure. *Journal of Materials Chemistry*, 282:98–100, 1988.

[25] S. Dahl, A. Logadottir, R.C. Egeberg, J.H. Larsen, I. Chorkendorff, E. Törnqvist, and J.K. Nørskov. Role of steps in N2 activation on Ru(0001). *Physical Review Letters*, 83:1814–1817, 1999.

[26] S. Dahl, E. Törnqvist, and I. Chorkendorff. Dissociative adsorption of N2 on Ru(0001): A surface reaction totally dominated by steps. *Journal of Catalysis*, 192:381–390, 2000.

[27] S. Dahl, J. Sehested, C. J. H. Jacobsen, E. Törnqvist, and I. Chorkendorff. Surface science based microkinetic analysis of ammonia synthesis over ruthenium catalysts. *Journal of Catalysis*, 192:391–399, 2000.

[28] T. Murakami, T. Nishikiori, T. Nohira, and Y. Ito. Electrolytic synthesis of ammonia in molten salts under atmospheric pressure. *Journal of the American Chemical Society*, 125:334–335, 2003.

[29] R. Kojima and K. Aika. Molybdenum nitride and carbide catalysts for ammonia synthesis. *Applied Catalysis A: General*, 219:141–147, 2001.

[30] T. H. Rod, A. Logadottir, and J. K. Nørskov. Ammonia synthesis at low temperatures. *Journal of Chemical Physics*, 112:5343–5347, 2000.

[31] A. Logadottir, T. H. Rod, J. K. Nørskov, B. Hammer, S. Dahl, and C. J. H. Jacobsen. The Brønsted-Evans-Polanyi Relation and the Volcano Plot for Ammonia Synthesis over Transition Metal Catalysts. *Journal of Catalysis*, 197(2):229–231, 2001.

[32] A. Logadottir and J. K. Nørskov. Ammonia synthesis over a ru (0001) surface studied by density functional calculations. *Journal of Catalysis*, 220:273–279, 2003.

[33] A. Hellman, K. Honkala, I. N. Remediakis, A. Logadottir, A. Carlsson, S. Dahl, C. H. Christensen, and J. K. Nørskov. Ammonia synthesis and decomposition on a ru-based catalyst modeled by first-principles. *Surface Science*, 603:1731–1739, 2009.

[34] A. Hellman, E. J. Baerends, M. Biczysko, T. Bligaard, C. H. Christensen, D. C. Clary, S. Dahl, R. van Harrevelt, K. Honkala, H. Jónsson, G. J. Kroes, M. Luppi, U. Manthe, J. K. Nørskov, R. A. Olsen, J. Rossmeisl, E. Skulason, C. S. Tautermann, A. J. C. Varandas, and J. K. Vincent. Predicting catalysis: Understanding ammonia synthesis from first- principles calculations. *Journal of Physical Chemistry B*, 110:17719–17735, 2006.

[35] T. Song and P. Hu. Insight into the adsorption competition and the relationship between dissociation and association reactions in ammonia synthesis. *Journal of Chemical Physics*, 127:234706, 2007.

[36] K. Honkala, A. Hellman, I. N. Remediakis, A. Logadottir, A. Carlsson, S. Dahl, C. H. Christensen, and J. K. Nørskov. Ammonia synthesis from first-principles calculations. *Science*, 307:555–558, 2005.

[37] E. Skúlason, T. Bligaard, S. Gudmundsdottir, F. Studt, J. Rossmeisl, F. Abild-Pedersen, T. Vegge, H. Jónsson, and J.K. Nørskov. A theoretical evaluation of possible transition metal electro-catalysts for N2 reduction. *Phys. Chem. Chem. Phys.*, 14:1235–1245, 2012.

[38] C.J.H Jacobsen, S. Dahl, P.L. Hansen, E. Törnqvist, L. Jensen, H. Tøpsoe, D.V. Prip, P.B. Moenshaug, and I. Chorkendorff. Structure sensitivity of supported ruthenium catalysts for ammonia synthesis. *Journal of Molecular Canalysis A-Chemical*, 163:19–26, 2000.

[39] R. Gomez, A. Fernandez-Vega, J. M. Feliu, and A. Aldaz. Hydrogen evolution on platinum single crystal surfaces: effects of irreversibly adsorbed bismuth and antimony on hydrogen adsorption and evolution on platinum (100). *The Journal of Physical Chemistry*, 97(18):4769–4776, 1993.

[40] T. Jiang, D.J. Mowbray, S. Dobrin, H. Falsig, B. Hvolbæk, T. Bligaard, and J.K. Nørskov. Trends in co oxidation rates for metal nanoparticles and close-packed, stepped, and kinked surfaces. *Journal of Physical Chemistry C*, 113(10548), 2009.

[41] W. Kohn. Nobel lecture: Electronic structure of matter-wave functions and density functionals. *Review of Modern Physics*, 71(5):1253–1266, 1999.

[42] J.K. Nørskov, T. Bligaard, J. Rossmeisl, and C.H. Christensen. Towards the computational design of solid catalysts. *Nature Chemistry*, 1:37–46, 2009.

[43] E. Hansen and M. Neurock. First-principles-based monte carlo simulation of ethylene hydrogenation kinetics on pd. *J. Catalysis*, 45:71–129, 2000.

[44] B. Hammer, L.B. Hansen, and J.K. Nørskov. Improved adsorption energetics within density-functional theory using revised Perdew-Burke-Ernzerhof functionals. *Phys. Review*, 59(11):7413–7421, 1999.

[45] J. J. Mortensen, L. B. Hansen, and K. W. Jacobsen. Real-space grid implementation of the projector augmented wave method. *Physical Review B*, 71(33):035109, 2005.

[46] J. Enkovaara et. al. Electronic structure calculations with gpaw: A real-space implementation of the projector augmented-wave method. *Journal of Physics: Condensed Matter*, 22(25):253202, 2010.

[47] The ASE code is available as a part of the CAMPOS software: http://www.camd.dtu.dk/Software.

[48] M. Born and R. Oppenheimer. Zur quantentheorie der molekule. *Annalen der Physik*, 84:457–484, 1927.

[49] C. Eckart. Some studies concerning rotating axes and polyatomic molecules. *Physical Review*, 46:383–387, 1935.

[50] P. Hohenberg and W. Kohn. Inhomogeneous electron gas. *Physical Review*, 136(3B):B864–B871, 1964.

[51] W. Kohn and L. J. Sham. Self-consistent equations including exchange and correlation effects. *Physical Review*, 140(4A):A1133–A1138, 1965.

[52] K. Kobayashi, N. Kurita, H. Kumahora, K. Tago, and K. Ozawa. Nonlocal-density-functional bond-energy calculations of cage-shaped carbon fullerenes: c_{32} and c_{60}. *Phys. Rev. B*, 45:13690–13693, Jun 1992.

[53] J. P. Perdew and Y. Wang. Accurate and simple analytic representation of the electron-gas correlation energy. *Phys. Rev. B*, 45:13244–13249, 1992.

[54] J. H. Perdew, K. Burke, and M. Ernzerhof. Generalized gradient approximation made simple. *Physical Review Letters*, 77(18):3865–3868, 1996.

[55] Y. Zhang and W. Yang. Comment on “generalized gradient approximation made simple”. *Phys. Rev. Lett.*, 80:890–890, 1998.

[56] E.H. Lieb and S. Oxford. Improved lower bound on the indirect coulomb energy. *International Journal of Quantum Chemistry*, 19(3):427–439, 1981.

[57] Miguel A.L. Marques, Micael J.T. Oliveira, and Tobias Burnus. Libxc: A library of exchange and correlation functionals for density functional theory. *Computer Physics Communications*, 183(10):2272 – 2281, 2012.

[58] D.R. Hartree. The wave mechanics of an atom with non-coulombic central field: parts i, ii, iii. *Math. Proc. Cambridge Phil. Soc.*, 24:89–132,426–437, 1928.

[59] V. Fock. Näherungsmethode zur losung des quanten-mechanischen mehrkörperprobleme. *Z. Phys.*, 61:126, 1930.

[60] J. P. Perdew and A. Zunger. Self-interaction correction to density-functional approximations for many-electron systems. *Phys. Rev. B*, 23:5048–5079, May 1981.

[61] V. Anisimov, F. Aryasetiawan, and A. Lichtenstein. First-principles calculations of the electronic structure and spectra of strongly correlated systems: the lda+ u method. *J. Phys.: Condensed Matter*, 9:767, 1997.

[62] H. Hellmann. Einfühung in die quantenchemie. *Franz Deuticke: Leipzig*, page p. 285, 1937.

[63] R. P. Feynmann. Forces in molecules. *Phys. Rev. Lett.*, 56:340–343, 1939.

[64] W. Pauli. Die allgemeinen prinzipien der wellenmechanik. *Handbuch der Physik, Springer: Berlin, 1933; Vol. 23; p. 162.*

[65] D.C. Liu and J. Nocedal. On the limited memory bfgs method for large scale optimization. *J. Mathematical Programming*, 45:503–528, 1989.

[66] M. R. Hestenes and E. Stiefel. Methods of conjugate gradients for solving linear systems. *Journal of Research of the National Bureau of Standards*, 49(6):409–436, 1952.

[67] E. Bitzek, P. Koskinen, F. Gähler, M. Moseler, and P. Gumbsch. Structural relaxation made simple. *Physical Review Letters*, 97(12):170201, 2006.

[68] The GPAW code is available as a part of the CAMPOS software: http://www.camd.dtu.dk/Software.

[69] P. E. Blöchl. Projector Augmented Wave Method. *Physical Review B*, 50(24):17953–17979, 1994.

[70] R. M. Martin, editor. *Electronic Structure - Basic Theory and Practical Methods.* Cambridge, Cambridge, UK, 1st edition, 2004.

[71] H. Jónsson, G. Mills, and K. W. Jacobsen. Nudged elastic band method for finding minimum energy paths of transitions. *Classical and Quantum Dynamics in Condensed Phase Simulations*, edited by B. J. Berne, G. Ciccotti, D. F. Coker (World Scientific, Singapore, 1998):385, 1998.

[72] G. Henkelman and H. Jónsson. Improved tangent estimate in the nudged elastic band method for finding minimum energy paths and saddle points. *J. Chem. Phys.*, 113:9978, 2000.

[73] A. A. Peterson, F. Abild-Pedersen, J. Rossmeisl F. Studt, and J.K Nørskov. How copper catalyzes the electroreduction of carbon dioxide into hydrocarbon fuels. *Energy & Environmentral Science*, 3:1311–1315, 2010.

[74] W.J. Durand, A.A. Peterson, F. Studt, F. Abild-Pedersen, and J.K. Nørskov. Structure effects on the energetics of the electrochemical reduction of {CO2} by copper surfaces. *Surface Science*, 605(1516):1354 – 1359, 2011.

[75] C. Kittel. *Introduction to Solid State Physics*. John Wiley & Sons, inc., Massachusetts, 8th edition, 2005.

[76] R. J. Silbey, R. A. Alberty, and M. G. Bawendi. *Physical Chemistry*. Wiley, 4th edition, 2005.

[77] C. J. Cramer. *Physical Chemistry*. John Wiley & Sons, Ltd., 2nd edition, 2004.

[78] NIST. Nist chemical homepage. http://webbook.nist.gov/.

[79] I. Chorkendorff and J. W. Niemantsverdriet, editors. *Concepts of Modern Catalysis and Kinetics*. Wiley-VCH, 2nd edition, 2007.

[80] J. K. Nørskov, J. Rossmeisl, A. Logadottir, L. Lindqvist, J. R. Kitchin, T. Bligaard, and H. Jónsson. Origin of the overpotential for oxygen reduction at a fuel-cell cathode. *Journal of Physical Chemistry B*, 108(46):17886–17892, 2004.

[81] H.J. Monkhorst and J.D. Pack. Special points for brillouin-zone integrations. *Physical Review B*, 13(12):5188–5192, 1976.

[82] D. J. Chadi and Marvin L. Cohen. Special points in the brillouin zone. *Phys. Rev. B*, 8:5747–5753, 1973.

[83] R.B. Getman and W.F. Schneider. Dft-based coverage-dependent model of pt-catalyzed no oxidation. *ChemCatChem*, 2(11):1450–1460, 2010.

[84] D.M. Newns. Self-consistent model of hydrogen chemisorption. *Physical Review*, 178:1123–&, 1969.

[85] P.W. Anderson. Localized magnetic states in metals. *Physical Review*, 124:41–&, 1961.

[86] P.W. Atkins. *Molecular Quantum Mechanics*. Oxford University Press, Oxford, 1983.

[87] J. K. Nørskov and B. Hammer. Theoretical surface science and catalysis - calculations and concepts. *Adv. Catal.*, 45(71), 2000.

[88] J. K. Nørskov and B. Hammer. Electronic factors determining the reactivity of metal surfaces. *Surface Science*, 343(3):211–220, 1995.

[89] B. Hammer, Y. Morikawa, and J.K. Nørskov. Co chemisorption at metal surfaces and overlayers. *Physical Review Letters*, 76(2141), 1996.

[90] O.K. Andersen, O. Jepson, and D. Glötzel. *Highlights of Condensed Matter Theory LXXXIX*, Corso Soc. Italiana di Fisica, V Bologna:59, April 1985.

[91] F. Abild-Pedersen, J. Greeley, F. Studt, J. Rossmeisl, T.R. Munter, P.G Moses, E. Skúlason, T. Bligaard, and J.K. Nørskov. Towards the computational design of solid catalysts. *Nature Chemistry*, 1:37–46, April 2009.

[92] J.K. Nørskov and N.D. Lang. Effective-medium theory of chemical-binding-application to chemisorption. *Physical Review B*, 21:2131–2136, 1980.

[93] N. Brøndsted. *Chem. Rev.*, 5:231, 1928.

[94] M. G. Evans and M. Polanyi. Inertia and driving force of chemical reactions. *Trans. Faraday Soc.*, 34:11–24, 1938.

[95] V. Pallassana and M. Neurock. Electronic factor governing ethylene hydrogenation and dehydrogenation activity of pseudomorphic pd-ml/re(0 0 0 1), pd-ml/ru(0 0 0 1) pd(1 1 1), and pd-ml/au(1 1 1) surfaces. *J. Catalysis*, 191:301, 2000.

[96] Z.P. Liu and P. Hu. General trends in co dissociation on transition metal surfaces. *Journal of chemical physics*, 114:8244, 2001.

[97] J.K. Nørskov, T. Bligaard, A. Logadottir, S. Bahn, L.B. Hansen, M. Bollinger, H. Bengaard, B. Hammer, Z. Sljivancanin, M. Mavrikakis, Y. Xu, S. Dahl, and C.J.H. Jacobsen. Universality in heterogenous catalysis. *Journal of Catalysis*, 209(2):275–278, 2002.

[98] T. Bligaard, J.K. Nørskov, S. Dahl, J. Matthiesen, C.H. Christensen, and J. Sehested. The Brøndsted-Evans-Polanyi relation and the volcano curve in heterogenous catalysis. *Journal of Catalysis*, (224):206–217, 2004.

[99] IbrahimA. Amar, Rong Lan, ChristopheT.G. Petit, and Shanwen Tao. Solid-state electrochemical synthesis of ammonia: a review. *Journal of Solid State Electrochemistry*, 15(9):1845–1860, 2011.

[100] J. Heyrovski. A theory of overpotential. *Recueil des Travaux Chimiques des Pays-Bas*, 46(8):582–585, 1927.

[101] E. Skúlason. Modeling electro-catalytic reactions using density functional theory calculations. page PhD thesis Technical University of Denmark, 2009.

[102] S. Wang, V. Petzold, V. Tripkovic, J. Kleis, J. G. Howalt, E. Skulason, E. M. Fernandez, B. Hvolbaek, G. Jones, A. Toftelund, H. Falsig, M. Björketun, F. Studt, F. Abild-Pedersen, J. Rossmeisl, J. K.

Nørskov, and T. Bligaard. Universal transition state scaling relations for (de)hydrogenation over transition metals. *Physical Chemistry Chemical Physics*, 13(46):20760–20765, 2011.

[103] S. Kurth, J.P. Perdew, and P. Blaha. Molecular and solid-state tests of density functional approximations: Lsd, ggas, and meta-ggas. *International Journal of Quantum Chemistry*, 75(4-5):889–909, 1999.

[104] J. Rossmeisl, A. Logadottir, and J. K. Nørskov. Electrolysis of water on (oxidized) metal surfaces. *Chem. Phys*, 319:178–184, 2005.

[105] J. Rossmeisl, Z.-W. Qu, G.-J. Kroes, and J.K Nørskov. Electrolysis of water on oxide surfaces. *Journal of Electroanalytical Chemistry*, 607:83–89, 2007.

[106] J.S. Hummelshøj, J. Blomquist, S. Datta, T. Vegge, J. Rossmeisl, K.S Thygesen, A. C. Luntz, K.W. Jacobsen, and J.K. Nørskov. Communications: Elementary oxygen electrode reactions in the aprotic li-air battery. *Journal of Chemical Physics*, 132(7):071101, 2010.

[107] J. G. Howalt, T. Bligaard, J. Rossmeisl, and T. Vegge. Dft based study of transition metal nano-clusters for electrochemical nh_3 production. *Phys. Chem. Chem. Phys.*, 15:7785–7795, 2013.

[108] J.K. Nørskov, F. Abild-Pedersen, F. Studt, and T. Bligaard. Density functional theory in surface chemistry and catalysis. *National Academy of Sciences. Proceedings*, 108(3):937–943, 2011.

[109] M. Neurock. Engineering molecular transformations for sustainable energy conversion. *Industrial & Engineering Chemistry Research*, 49(21):10183–10199, 2010.

[110] M. G. Evans and M. Polanyi. Inertia and driving force of chemical reactions. *Trans. Faraday Soc.*, 34:11–24, 1938.

[111] A. Michaelides, Z.-P. Liu, C. J. Zhang, A. Alavi, D.A. King, and P. Hu. Identification of general linear relationships between activation energies and enthalpy changes for dissociation reactions at surfaces. *Journal of the American Chemical Society*, 125(13):3704–3705, 2003.

[112] S. Wang, B. Temel, J. Shen, G. Jones, L.C. Grabow, F. Studt, T. Bligaard, F. Abild-Pedersen, C.H. Christensen, and J.K. Nørskov. Universal brønsted-evans-polanyi relations for cc, co, cn, no, nn, and oo dissociation reactions. *Catalysis Letters*, 141(3):370–373, 2011.

[113] P. Crawford, B. McAllister, and P. Hu. Insights into the staggered nature of hydrogenation reactivity over the 4d transition metals. *The Journal of Physical Chemistry C*, 113(13):5222–5227, 2009.

[114] J. Cheng, Peijun Hu, P. Ellis, S. French, G. Kelly, and C.M. Lok. A dft study of the chain growth probability in fischer-tropsch synthesis. *Journal of Catalysis*, 257(1):221–228, 2008.

[115] D. Loffreda, F. Delbecq, F. Vigné, and P. Sautet. Fast prediction of selectivity in heterogeneous catalysis from extended brønstedevanspolanyi relations: A theoretical insight. *Angewandte Chemie International Edition*, 48(47):8978–8980, 2009.

[116] Felix Studt, Frank Abild-Pedersen, Thomas Bligaard, Rasmus Zink Sørensen, Claus H. Christensen, and Jens Kehlet Nørskov. Identification of non-precious metal alloy catalysts for selective hydrogenation of acetylene. *Science*, 320(5881):1320–1322, 2008.

[117] M. Andersson, T. B. Pedersen, A. Kustov, K.E. Larsen, J.P. Greeley, T. Johannessen, C.H. Christensen, and J.K. Nørskov. Toward computational screening in heterogeneous catalysis: Pareto-optimal methanation catalysts. *Journal of Catalysis*, 239:501, 2006.

[118] G. Jones, J.G. Jakobsen, S.S. Shim, J. Kleis, M. Andersson, J. Rossmeisl, F. Abild-Pedersen, T. Bligaard, S. Helveg, B. Hinnemann, J.R. Rostrup-Nielsen, I. Chorkendorff, J. Sehested, and J.K. Nørskov. First principles calculations and experimental insight into methane steam reforming over transition metal catalysts. *Journal of Catalysis*, 259(1):147–160, 2008.

[119] J.K. Nørskov, H. Falsig, B.H. Larsen, I.S. Kristensen, T. Jiang, T. Bligaard, and C.H. Christensen. Trends in the catalytic co oxidation activity of nanoparticles. *Angewandte Chemie - International Edition*, 47(26):4835–4839, 2008.

[120] P. Ferrin, D. Simonetti, S. Kandoi, E. Kunkes, J.A. Dumesic, Jens Kehlet Nørskov, and M. Mavrikakis. Modeling ethanol decomposition on transition metals: A combined application of scaling and bronsted-evans-polanyi relations. *Journal of the American Chemical Society*, 131(16):5809–5815, 2009.

[121] Gabor A. Somorjai and Yimin Li. Impact of surface chemistry. *Proceedings of the National Academy of Sciences*, 108(3):917–924, 2011.

[122] N.M.P. Schumacher, A. Boisen, S. Dahl, A.A. Gokhale, S. Kandoi, L.C. Grabow, J.A. Dumesic, M. Mavrikakis, and I. Chorkendorff. Trends in low-temperature watergas shift reactivity on transition metals. *Journal of Catalysis*, 229:265–275, 2005.

[123] J. Cheng and P. Hu. Utilization of the three-dimensional volcano surface to understand the chemistry of multiphase systems in heterogeneous catalysis. *Journal of the American Chemical Society*, 130(33):10868–10869, 2008. PMID: 18651740.

[124] The Dacapo plane wave/pseudopotential DFT code is available as open source software at https://wiki.fysik.dtu.dk/dacapo.

[125] R.D. Meade and D. Vanderbilt. Origins of stress on elemental and chemisorbed semiconductor surfaces. *Phys. Rev. Lett.*, 63:1404–1407, Sep 1989.

[126] M. Andersson and F. Abild-Pedersen. Co adsorption energies on metals with correction for high coordination adsorption sites - a density functional study. *Surface Science*, 601:1747, 2007.

[127] R. Alcalá, M. Mavrikakis, and J.A. Dumesic. {DFT} studies for cleavage of cc and co bonds in surface species derived from ethanol on pt(111). *Journal of Catalysis*, 218(1):178 – 190, 2003.

[128] F. Abild-Petersen, J. Greeley, F. Studt, J. Rossmeisl, T. R. Munter, P.G. Moses, E. Skulason, T. Bligaard, and J. K. Nørskov. Scaling properties of adsorption enemies for hydrogen containing molecules on transition metal surfaces. *Physical Review Letters*, 99:016105–016108, 2007.

[129] J. K. Nørskov, T. Bligaard, B. Hvolbæk, F. Abild-Pedersen, I. Chorkendorff, and C.H. Christensen. The nature of the active site in heterogeneous metal catalysis. *Chem. Soc. Rev.*, 37:2163–2171, 2008.

[130] S.B. Vendelbo, M. Johansson, D. Mowbray, M. P. Andersson, F. Abild-Pedersen, J.H. Nielsen, J.K. Nørskov, and I. Chorkendorff. Self blocking of co dissociation on a stepped ruthenium surface. *Topics in Catalysis*, 53(5-6):357–364, 2010.

[131] T. Zambelli, J. Wintterlin, J. Trost, and G. Ertl. Identification of the "active sites" of a surface-catalyzed reaction. *Science*, 273:1688–1690, 1996.

[132] P. E. Blöchl, C. J. Först, and J. Schimpl. Projector augmented wave method: ab-initio molecular dynamics with full wave functions. *Bulletin of Materials Science*, 26(33):33–41, 2003.

[133] A. Ruban, B. Hammer, P. Stoltze, H.L. Skriver, and J.K. Nørskov. Surface electronic structure and reactivity of transition and noble metals. *J. Mol. Catal.*, A115:421, 1997.

[134] S.G. Wang, B. Temel, J.A. Shen, G. Jones, L.C. Grabow, F. Studt, T. Bligaard, F. Abild-Pedersen, C.H. Christensen, and J.K. Nørskov. Universal Brønsted-Evans-Polanyi Relations for C-C, C-O, C-N, N-O, N-N, and O-O Dissociation Reactions. *Catalysis Letter*, 141, 2011.

[135] M. Mavrikakis, B. Hammer, and J. K. Nørskov. Effect of strain on the reactivity of metal surfaces. *Phys. Rev. Lett.*, 81:2819–2822, Sep 1998.

[136] G. Henkelman, B.P. Uberuaga, and H. Jonsson. A climbing image nudged elastic band method for finding saddle points and minimum energy paths. *J. Chem. Phys.*, 113(22):9901–9904, DEC 8 2000.

[137] A.A. Peterson, L.C. Grabow, T.P. Brennan, B. Shong, C. Ooi, D.M. Wu, C.W. Li, A. Kushwaha, A.J. Medford, F. Mbuga, L. Li, and J.K. Nørskov. Finite-size effects in o and co adsorption for the late transition metals. *Topics in Catalysis*, 55(19-20):1276–1282, 2012.

[138] S. H. Huh, H. K. Kim, and G. H. Lee. Critical cluster size of metallic cr and mo nanoclusters. *Physical Review B*, 62(4):2937–2943, 2000.

[139] T. Vystavel, S. A. Koch, G. Palasantzas, and J. Th. M. De Hosson. In situ transmission electron microscopy studies on structural dynamics of transition metal nanoclusters. *J. Mater. Res.*, 20(7):1785–2943, 2005.

[140] B. Fastrup and H. Nygård Nielsen. On the influence of oxygen on iron catalysts during ammonia synthesis and catalyst characterization. *Catalysis Letters*, 14(2):233–239, 1992.

[141] V.L. Kuchaev, E.N. Shapatina, and A.K. Avetisov. Mechanism of oxygen poisoning of ammonia synthesis catalyst. *Russian Journal of Electrochemistry*, 45(9):983–995, 2009.

[142] Jakob G. Howalt and Tejs Vegge. Electrochemical ammonia production on molybdenum nitride nanoclusters. *Phys. Chem. Chem. Phys.*, pages –, 2013.

Appendix A

Examples of how to ensure computational precision

For calculations using the GPAW code numerous computational parameters can be tuned such that the energy differences due to computational settings are lower than a desired precision. In the following, an illustration of how to determine the right parameters is presented. The illustration contains both tests performed on a stepped surface and on a M12 nanocluster for the NH adsorption energy, see section 6.2 for more information about this particular model systems. Some parameters are computational settings, while others are system dependent. The following parameters were varied: amount of vacuum, number of k-points, and number of slab layers.

K-point sampling

An example of how the k-point sampling can be determined is presented here. An Au stepped surface (fcc 211 3x2 unitcell) with periodic boundary conditions in x- and y-direction and non-periodic in the z-direction. The k-point sampling in the z-direction is therefore set to 1, while k-points in the x- and y-direction have been tested. The adsorption of NH on the Au step surface has been used as primer. Fig. A.1(a) shows the adsorption energy of NH. From the figure, one must expect the ground state to have an adsorption of around 1.5 to 1.53 eV and a oscillating behavior is observed. Using a (4x4x1) k-point sampling mimics the adsorption energy of the much higher(8x8x1) sampling with an error of less than 0.03 eV, while the calculations will be a fourth as demanding than using a k-point sampling of (8x8x1).

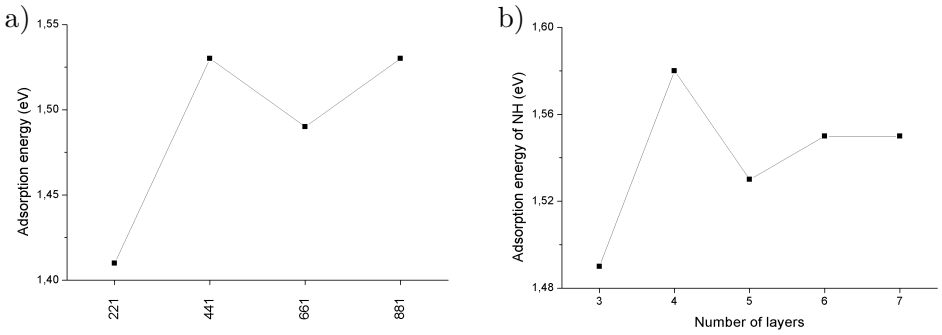

Figure A.1: *a: The adsorption energy of NH for a number of different k-point samplings on a stepped fcc 211 Au surface. It is seen that the variance in the adsorption energy of NH is small when a k-point sampling of (4x4x1) or above is used. b: The adsorption of NH on a stepped Au surface with different number of layers has been carried out. The two top layers are relaxed, while the rest of the layers are fixed. Five layers have been chosen, since the accuracy of the adsorption energy is only 0.02 eV compared to using more layers.*

Layers

In fig. A.1b an example of how to determine the appropriate number of layers. Again the adsorption of a NH species on a stepped Au surface with different number of layers has been carried out. In the calculations, the two top layers are relaxed together with the adsorbate, while the rest of the layers are kept fixed. The adsorption energies can be seen on fig. A.1b and in this case the energy converges towards one unique adsorption energy.

Vacuum

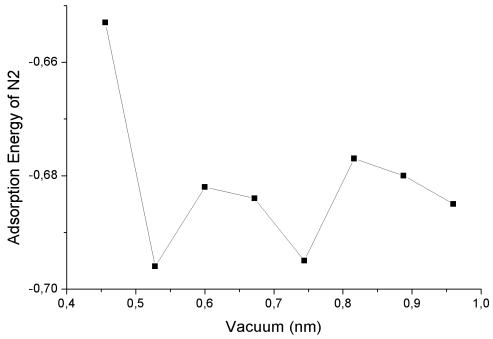

Figure A.2: *On this figure the adsorption energy of N_2 on a Rh M12 nanocluster is plotted against the amount of vacuum used. The differences in the values of the adsorption energy are in the order of 0.02 eV for vacuum sizes larger than 0.54 nm, which is a small error compared to the intrinsic error in DFT.*

In fig. A.2 the adsorption energy of N_2 on the Rh M12 nanocluster for various sizes of the vacuum layers is shown. A uniform convergence is not the case here, and the reason is most likely the consequence of small amounts of egg-box effects arising when enlarging the unit cell.

Appendix B

Newns-Anderson model

The Newns-Anderson model [84, 85] describes the chemisorption of an atom on a surface. In the following an interpretation of the model results will be made to more clearly understand the impact on chemical reactions occurring on surfaces.

Theory behind the Newns-Anderson model

The interactions between a simple adsorbed atom on a metal surface will in the following be derived. Starting from an assumption that the atom has only one valence electron (a crude but important assumption) with an energy of ϵ_a and a corresponding wave function Φ_a. For most surfaces consisting of transition metals it is accurate to assume a continuum of electronic states Φ_k with the resulting energies ϵ_k. In the following derivation the wave function basis is assumed orthogonal and therefore the matrix elements $\int \Phi_a \Phi_k$ will disappear.

The Hamiltonian H describes the interactions between the atom and the surface, and the matrix elements $V_{ak} = \int \Phi_a H \Phi_k$ describe this interaction. The solutions to this eigenvalue problem is assuming that the solution Φ_i will be a linear combination of the separated wave functions of the atom and the surface given by:

$$\Phi_i = c_{ai}\Phi_a + \sum_k c_{ik}\Phi_k$$

This leads to an eigenvalue problem for the system on the following form

$$H\Psi_i = \epsilon_i \Psi_i.$$

Using the assumption taken above the matrix element for this eigenvalue problem will therefore be the following

$$\int \Phi_a H \Phi_a = H_{aa} = \epsilon_a$$
$$\int \Phi_k H \Phi_k = H_{kk} = \epsilon_k$$
$$\int \Phi_k H \Phi_a = H_{ka} = \epsilon_{ka}$$

Secular equations is the solution to the eigenvalue problem,

$$\begin{vmatrix} H_{aa}-\epsilon & V_{a1} & V_{a2} & V_{a3} & \dots & \dots & V_{an} \\ V_{1a} & H_{11}-\epsilon & 0 & 0 & \dots & \dots & 0 \\ V_{2a} & 0 & H_{22}-\epsilon & 0 & \dots & \dots & 0 \\ V_{3a} & 0 & 0 & H_{33}-\epsilon & \dots & \dots & V_{a1} \\ \dots & \dots & \dots & \dots & \dots & \dots & \dots \\ \dots & \dots & \dots & \dots & \dots & \dots & \dots \\ V_{na} & 0 & 0 & 0 & \dots & \dots & H_{nn}-\epsilon \end{vmatrix} = 0$$

The electron orbitals in transition metals are very close and naturally form a continuous band of energy levels and therefore infinitely many states. This makes the exact projection of them all difficult, and instead a projection onto the original atomic level Φ_a of the new states Φ_i is carried out. This simplifies the solving and the development of the adsorbates states of the atom can be determined while the atom gets closer to the surface. The new states are calculated in the following way

$$n_a(\epsilon) = \sum_i \left| \int \Psi_i \Phi_a \right|^2 \delta(\epsilon_i - \epsilon_a), \tag{B.1}$$

where the summation is carried out over all solutions to the wave functions Ψ_i. The introduction of a Green's function, can reformulate equation B.1 to

$$n_a(\epsilon) = \frac{-1}{\pi} \mathrm{Im} \left(\sum_i \frac{\int \Psi_i \Phi_a \int \Phi_a \Psi_i}{\delta(\epsilon - \epsilon_i + i\delta)} \right) |_{\delta \to 0^+}.$$

The Lorenzian function,

$$f(\epsilon) = \frac{\delta}{\pi[(\epsilon - \epsilon_i)^2 + \delta^2]},$$

is used and act as a delta function in the limit of $\delta \to 0^+$, and it can be seen below,

$$\int_{-\infty}^{+\infty} f(\epsilon) d\epsilon = \int_{-\infty}^{+\infty} \frac{\delta}{\pi[(\epsilon - \epsilon_i)^2 + \delta^2]} d\epsilon$$

where the usual definitions of the delta function is and the consequences for the function $f(\epsilon)$ is that $f(\epsilon) = 0$ for $\epsilon \neq \epsilon_i$ and $f(\epsilon) \to \infty$ for $\epsilon = \epsilon_i$. In the following way, is the conversion is performed,

$$\begin{aligned} \mathrm{Im} \sum_i \frac{1}{\delta(\epsilon - \epsilon_i + i\delta)} |_{\delta \to 0^+} &= \mathrm{Im} \left[\frac{\epsilon - \epsilon_i}{(\epsilon - \epsilon_i)^2 + \delta^2} - \frac{i\delta}{(\epsilon - \epsilon_i) + \delta^2} \right] |_{\delta \to 0^+} \\ = \frac{\pi\delta}{\pi[(\epsilon - \epsilon_i)^2 + \delta^2]} |_{\delta \to 0^+} &= \pi\delta(\epsilon - \epsilon_i). \end{aligned} \tag{B.2}$$

Introducing the one-particle Green's function as

$$\mathbf{G}(\epsilon)^{-1} = \sum_i \frac{\int \Psi_i \int \Phi_a}{(\epsilon - \epsilon_i + i\delta)}$$

and rewriting eq. B.1,

$$n_a(\epsilon) = \frac{-1}{\pi}\mathrm{Im}\left(\sum_i \frac{\int \Psi_i\Phi_a \int \Phi_a\Psi_i}{\delta(\epsilon-\epsilon_i+i\delta)}\right)|_{\delta\to 0^+} \equiv \frac{-1}{\pi}\mathrm{Im}[G_{aa}(\epsilon)]. \tag{B.3}$$

The principal definition of the one-particle Green's function, $\mathbf{G}(\epsilon)^{-\mathbf{1}}$, is the inverse matrix to $\epsilon - \mathbf{H} + \mathbf{i}\delta$, as shown below

$$(\epsilon - \mathbf{H} + i\delta)\mathbf{G}(\epsilon)^{-1} = \mathbf{I}.$$

Rewriting the above equation in matrix form result in the following

$$\begin{pmatrix} \epsilon+i\delta-\epsilon_a & -V_{a1} & \dots & V_{a1} \\ -V_{1a} & \epsilon+i\delta-H_{11} & \dots & 0 \\ \dots & \dots & \dots & \dots \\ -V_{na} & 0 & \dots & -\epsilon+i\delta-H_{nn} \end{pmatrix} \begin{pmatrix} G_{aa} & G_{a1} & \dots & G_{an} \\ G_{1a} & G_{11} & \dots & 0 \\ \dots & \dots & \dots & \dots \\ G_{na} & G_{n1} & \dots & G_{nn} \end{pmatrix} = \mathbf{I}$$

From the matrix, two relations involving G_{aa} can be constructed,

$$G_{aa}(\epsilon-\epsilon_a+i\delta) - \sum_k V_{ak}G_{ka} = 1$$
$$-V_{aa}G_{aa} + (\epsilon-\epsilon_k+i\delta)G_{ka} = 0.$$

The solution of the equations for G_{aa} is

$$G_{ka} = \frac{-V_{ka}G_{aa}}{\epsilon-\epsilon_k+i\delta}$$

and it leads to a new expression for G_{aa},

$$\begin{aligned} G_{aa} &= \frac{1}{(\epsilon-\epsilon_k+i\delta) - \sum_k \frac{V_{ak}^2}{(\epsilon-\epsilon_k+i\delta)}} \\ &= [\epsilon-\epsilon_k-\Lambda(\epsilon)+i\Delta(\epsilon)]^{-1} \end{aligned}$$

where

$$\Lambda(\epsilon) = \frac{1}{\pi}\int_{-\infty}^{\infty}\frac{\Delta(x)}{x-\epsilon}dx.$$

and

$$\Delta(\epsilon) = -\mathrm{Im}\left(\sum_k \frac{V_{ak}^2}{(\epsilon-\epsilon_k+i\delta)}\right) \to \pi\sum_k V_{ak}^2\delta(\epsilon-\epsilon_k) \quad \text{for} \quad \delta\to 0^+$$

The first term, $\Lambda(\epsilon)$, is the Kronig-Kramer transformation of $\Delta(\epsilon)$. $\Delta(\epsilon)$ is essentially a hopping matrix element between the metal states 'k' and the adsorbate level 'a' and accounts for the projection of the metal states onto the adsorbate state. Reformulating eq. B.3 gives

$$\begin{aligned} n_a(\epsilon) = \frac{-1}{\pi}\mathrm{G_{aa}} &= \frac{-1}{\pi}\mathrm{Im}\left(\frac{1}{\epsilon-\epsilon_a-\Lambda(\epsilon)+i\Delta(\epsilon)}\right) \\ &= \frac{-1}{\pi}\mathrm{Im}\left(\frac{\epsilon-\epsilon_a-\Lambda(\epsilon)-i\Delta(\epsilon)}{[\epsilon-\epsilon_a-\Lambda(\epsilon)]^2+\Delta(\epsilon)^2}\right) \\ &= \frac{1}{\pi}\frac{\Delta(\epsilon)}{[\epsilon-\epsilon_a-\Lambda(\epsilon)]^2+\Delta(\epsilon)^2} \end{aligned} \tag{B.4}$$

The terms $\Delta(\epsilon)$ and $\Lambda(\epsilon)$ express the interaction between the adsorbate and the metal surface. These terms account for the overlap between the states of the metal and the adsorbate states.

Appendix C

Density of states

C.1 M12

Table C.1: The center and the width of the d-band for the fixed and relaxed M12 nanoclusters.

	Fixed M12 nanocluster		Relaxed M12 nanocluster	
Metal	Center	Width	Center	Width
Ag	-3.56	0.75	-3.71	0.93
Au	-2.41	1.11	-2.72	1.45
Cu	-1.72	0.77	-1.95	0.94
Pd	-1.16	1.11	-1.44	1.44
Co	-1.41	1.51	-1.46	1.69
Ni	-1.23	1.11	-1.40	1.39
Rh	-1.35	1.32	-1.84	1.80
Fe	-0.84	1.74	-0.82	1.83
Pt	-1.45	1.48	-1.84	2.00
Ru	-1.26	1.46	-1.74	2.10
Mo	-0.05	1.67	-0.41	2.24
V	-0.32	0.85	-0.48	2.48
W	-0.81	1.45	0.14	2.00
Nb	-0.47	1.06	0.28	1.55

C.2 Mo_{13}

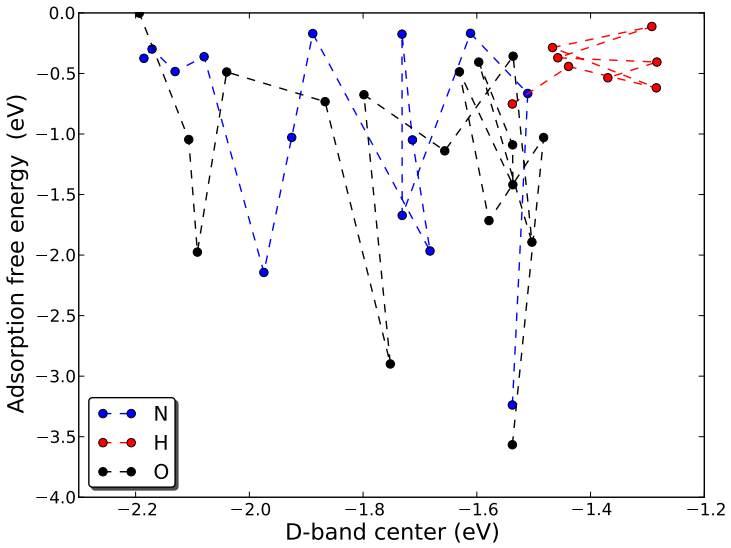

Figure C.1: *The adsorption free energies of N, H, and O plotted against the position of the d-band center of the $Mo_{13}Y_x$ ($Y = \{N, H, O\}$) nanocluster as the coverage of N, H, and O increases.*

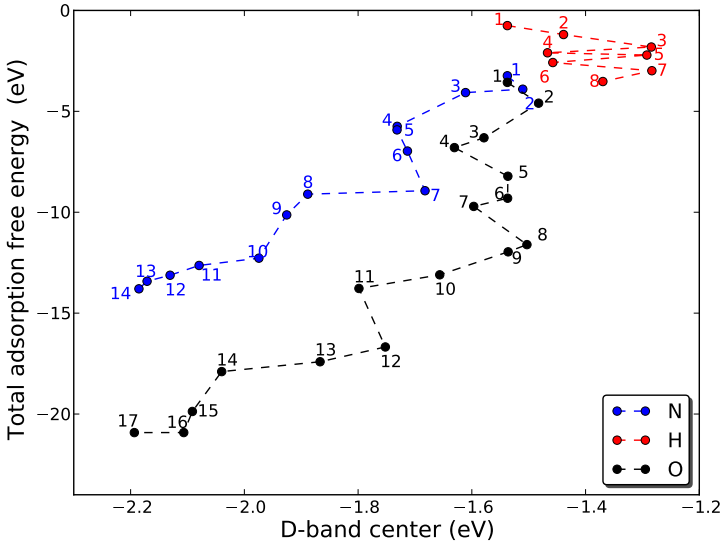

Figure C.2: *The total adsorption free energy of the coverage of either N, H, and O plotted against the position of the d-band center of the $Mo_{13}Y_x$ ($Y = \{N, H, O\}$) nanocluster as the coverage of N, H, and O increases.*

Table C.2: The d-band centers with respect to the Fermi level for all late transition metals for atoms in a bulk, on a close-packed surface, at a step on stepped surfaces and on the M12 nanoclusters.

Adsorbate	Oxygen		Nitrogen		Hydrogen	
Atom no.	Center	Width	Center	Width	Center	Width
0	-1.54	1.79	-1.54	1.79	-1.54	1.79
1	-1.48	1.89	-1.51	1.93	-1.43	1.79
2	-1.58	2.04	-1.61	2.09	-1.28	1.77
3	-1.63	2.14	-1.73	2.22	-1.46	1.78
4	-1.54	2.28	-1.73	2.36	-1.29	1.85
5	-1.54	2.40	-1.71	2.46	-1.45	1.89
6	-1.60	2.51	-1.68	2.58	-1.28	1.91
7	-1.50	2.59	-1.88	2.72	-1.36	1.98
8	-1.54	2.69	-1.92	2.80	-1.37	1.98
9	-1.66	2.82	-1.97	2.92		
10	-1.80	2.91	-2.08	2.99		
11	-1.75	2.98	-2.13	3.06		
12	-1.87	3.09	-2.17	3.14		
13	-2.04	3.22	-2.19	3.22		
14	-2.09	3.30	-2.11	3.30		
15	-2.11	3.41				
16	-2.29	3.51				

Appendix D

OH and H_2O scaling on molybdenum nanoclusters

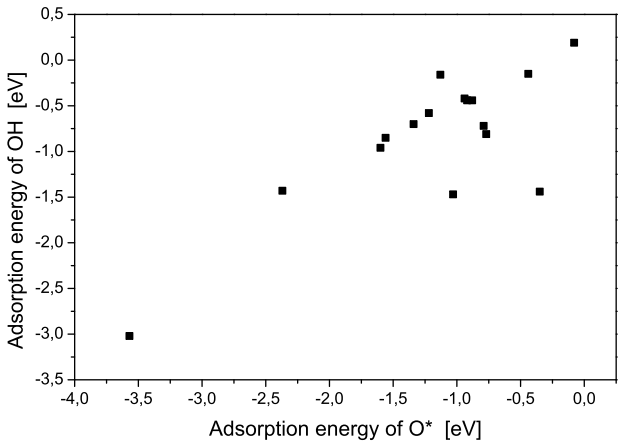

Figure D.1: *The adsorption energy of OH plotted as a function of adsorption energy of O for the oxygen covered molybdenum nanoclusters.*

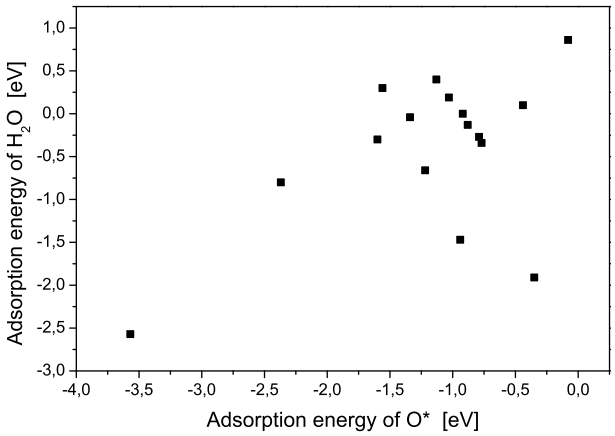

Figure D.2: *The adsorption energy of H_2O plotted as a function of adsorption energy of O for the oxygen covered molybdenum nanoclusters.*

Papers

PCCP

Cite this: *Phys. Chem. Chem. Phys.*, 2011, **13**, 20760–20765

www.rsc.org/pccp

PAPER

Universal transition state scaling relations for (de)hydrogenation over transition metals†

S. Wang,[a] V. Petzold,[a] V. Tripkovic,[a] J. Kleis,[a] J. G. Howalt,[ab] E. Skúlason,[ac] E. M. Fernández,[a] B. Hvolbæk,[a] G. Jones,[a] A. Toftelund,[a] H. Falsig,[a] M. Björketun,[a] F. Studt,[d] F. Abild-Pedersen,[d] J. Rossmeisl,[a] J. K. Nørskov[de] and T. Bligaard*[a]

Received 28th February 2011, Accepted 21st September 2011
DOI: 10.1039/c1cp20547a

We analyse the transition state energies for 249 hydrogenation/dehydrogenation reactions of atoms and simple molecules over close-packed and stepped surfaces and nanoparticles of transition metals using Density Functional Theory. Linear energy scaling relations are observed for the transition state structures leading to transition state scaling relations for all the investigated reactions. With a suitable choice of reference systems the transition state scaling relations form a universality class that can be approximated with one single linear relation describing the entire range of reactions over all types of surfaces and nanoclusters.

1. Introduction

Linear energy relations have proven useful in simplifying the theoretical analysis of a number of catalytic reactions, thereby helping to establish an improved understanding of their underlying trends.[1–3] The linear energy relations in question are especially the so-called Brønsted–Evans–Polanyi (BEP) relations[4–13] describing correlations between transition states and reaction energies, and the adsorbate scaling relations[14] describing correlations between the adsorption energies of adsorbed reaction intermediates containing hydrogen with respect to either C, N, or O. More generalized, the BEP relations can be viewed as resulting from a scaling relation between reaction intermediates and transition states. By combining transition state scaling relations and adsorbate scaling relations the number of individual parameters that needs to be determined in order to describe the energetic trends underlying the kinetics of a complex catalytic reaction can be significantly reduced, and often limited to only one or very few descriptors. Good descriptors are typically adsorption energies of some of the key reactive intermediates, or combinations of these.[15–23]

In the present paper we analyse the transition state energies for 249 dehydrogenation reactions of small hydrogen containing molecules over close-packed and stepped surfaces and nanoparticles of transition metals using Density Functional Theory (DFT). Linear energy correlations are observed for the transition state structures leading to transition state scaling relations for all the investigated reactions. Upon implementing a suitable choice of reference systems all the transition state scaling relations form a universality class[8,9] in which only one single descriptor can be used to determine the transition state for every reaction over all types of surfaces and nanoclusters.

2. Computational method

The calculations were carried out using the DACAPO plane wave Density Functional Theory code.[24] Exchange–correlation effects were described using the RPBE functional[25] with an energy cutoff of 340 eV or more. The ionic cores were described by Vanderbilt ultrasoft pseudopotentials.[26] A slab model with three (or in some cases four) close-packed atomic-layers was chosen to represent the transition metal surfaces describing the close-packed and stepped surfaces. At least one (in some cases two) top layer was fully relaxed and the rest of the metal layers were held at fixed positions. The size of a surface supercell was 2×2 for the close-packed surfaces, and supercell sizes of 1×2, 2×2, and 2×3 were used for the stepped surfaces depending on the size of the adsorbed molecules. The Brillouin zones were sampled using

[a] *Center for Atomic-scale Materials Design, Department of Physics, Building 307, Technical University of Denmark, DK-2800 Kgs. Lyngby, Denmark. E-mail: bligaard@fysik.dtu.dk; Fax: +45 4593 2399; Tel: +45 4525 3179*
[b] *Risø National Laboratory for Sustainable Energy, Materials Research Division, Building 228, Technical University of Denmark, DK-4000 Roskilde, Denmark*
[c] *Science Institute, VR-III, University of Iceland, IS-107 Reykjavik, Iceland*
[d] *SUNCAT Center for Interface Science and Catalysis, SLAC National Accelerator Laboratory, 2575 Sand Hill Road, Menlo Park, California 94025, USA*
[e] *Department of Chemical Engineering, Stanford University, Stanford, CA 94305, USA*

† Electronic supplementary information (ESI) available. See DOI: 10.1039/c1cp20547a

Monkhorst-Pack k-point meshes of 4 × 4 × 1 points or denser.[27] For the M12 nanoparticles, all the 12 atoms were fixed, while the adsorbates were allowed to relax. The M12 cluster was fixed in a planar structure identical to the geometry used in a recent study on CO oxidation.[18] The calculations on the M12 nanoparticles were carried out using only the gamma-point. The transition state energies were calculated using either a bond stretching method[28] or the nudged elastic band method which can be combined with the climbing image method to precisely determine the maximum barrier.[29] Several pathways were tested for each reaction step and in this paper we only report the first order saddle points corresponding to the lowest barrier. The maximum coverage on the active site was one half.

The convergence with respect to, number of layers, cutoff energy, and k-point sampling has been studied elsewhere[30] and we refer to this work for a more detailed evaluation of the accuracy of the data presented in this paper.

3. Results and discussion

A diagram explaining the reference energy levels used in the transition state scaling relations and in the Brønsted–Evans–Polanyi (BEP) relations for the dehydrogenation/hydrogenation processes is presented in Scheme 1. The transition state scaling relations are based on the transition state energy, E_{ts}, and the final state energy E_{diss}, with respect to the gas phase species[31] CH_4, NH_3, H_2O and H_2, see Scheme 1A. Whereas the BEP relation is based on the reaction energy, ΔE_{diss}, which is the energy difference between the initial and the final state, while the activation barrier, ΔE^{a}_{diss}, is the energy based on the difference in energy between the initial state and the transition state. This can be seen in Scheme 1B.

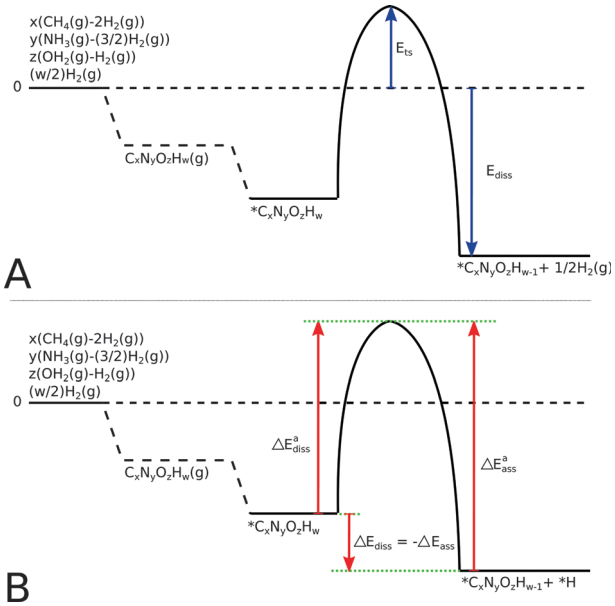

Scheme 1 The definition of energies used in this paper for the hydrogenation/dehydrogenation processes. All energies are with respect to the gas phase molecules of CH_4, NH_3, H_2O, and H_2. Top-view. (A) The transition state (TS) scaling relation are based upon the energies given by the two blue arrows denoted as E_{ts} for the transition state energy and E_{diss} for the final state energy. Bottom-view. (B) The Brønsted–Evans–Polanyi (BEP) relations use another reference energy. The BEP relations are based upon the activation barrier $\Delta E^{a}_{diss/ass}$ and the reaction energy $\Delta E_{diss/ass}$ as defined in the bottom panel.

Fig. 1 shows a universal transition state (TS) scaling relation for a series of dehydrogenation reactions over a wide range of transition metal surfaces, such as close-packed and stepped surfaces and nanoparticles. The fitted data for the transition state scaling relations for all the dehydrogenation reactions are presented in Table 1. Here the data have been arranged in categories of individual, classes, groups and overall. The individual fit is based on only one type of reaction on one surface type, the class is based on a specific reaction on all the types of surfaces, the grouped data are for all data containing either nitrogen, carbon or oxygen, and lastly the overall fit is based on all reactions on all types of surfaces.

The mean absolute error (MAE) of the fitted line in Fig. 1 is 0.28 eV. The correlation is certainly not perfect, and compared to so-called "chemical accuracy" which is typically defined as 1 kcal $mole^{-1}$ or approximately 40 meV, the error on a prediction based on using the linear relation shown in Fig. 1 will have a typical error one order of magnitude larger. The prediction error, however, has to be seen in the light of how well a typical GGA exchange–correlation functional can describe the reaction and transition state energies. The error in currently employed exchange–correlation functionals could easily be of the same size as the error from predictions based on the transition state scaling relations. The errors in the presented relation are certainly small enough to rapidly produce a first rough estimation of activation barriers for hydrogenation/dehydrogenation reactions. The universal TS scaling relation relates the energies of transition states with final states of dehydrogenation reactions.[13] Such correlation originates from the geometrical similarity of the structures of transition states and final states.[8]

Fig. 1 collects different types of dehydrogenation reactions on transition metal surfaces and clusters. The deviation of the

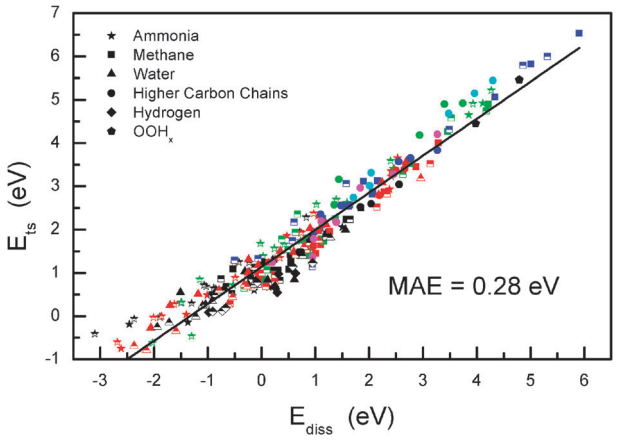

Fig. 1 Transition state energies plotted against dissociation energies with respect to energies of gas-phase CH_4, H_2O, NH_3, and H_2. The fully filled symbols refer to dissociation over close-packed surfaces, and the half-filled symbols refer to dissociation over stepped surfaces and OOH_x species have been dissociated on a M12 nanocluster. The colors represent the different hydrogen content in the molecules, where black is the first dehydrogenation step, red is the second step, green is the third step, and blue is the fourth dehydrogenation step.

Table 1 The fitted parameters of the transition state scaling relations with respect to energies of gas-phase CH_4, H_2O, NH_3, and H_2

Reaction	Surface	Slope	Constant/eV	MAE/eV
$H_2O(g) + 2^* \rightarrow OH^* + H^*$	Close packed	0.47 ± 0.10	0.99 ± 0.07	0.20
	Step	0.77 ± 0.02	0.95 ± 0.04	0.17
	All	0.58 ± 0.05	0.94 ± 0.04	0.16
$OH^* + ^* \rightarrow O^* + H^*$	Close packed	0.75 ± 0.03	1.32 ± 0.04	0.12
	Step	0.63 ± 0.03	0.92 ± 0.03	0.21
	All	0.78 ± 0.03	1.13 ± 0.05	0.20
Water group	All	0.74 ± 0.03	1.06 ± 0.04	0.20
$NH_3^* + ^* \rightarrow NH_2^* + H^*$	Close packed	0.57 ± 0.09	0.95 ± 0.11	0.24
	Step	0.69 ± 0.05	1.45 ± 0.07	0.14
	All	0.59 ± 0.06	1.19 ± 0.09	0.23
$NH_2^* + ^* \rightarrow NH^* + H^*$	Close packed	0.81 ± 0.03	1.26 ± 0.05	0.15
	Step	0.78 ± 0.04	1.41 ± 0.05	0.16
	All	0.79 ± 0.03	1.32 ± 0.04	0.16
$NH^* + ^* \rightarrow N^* + H^*$	Close packed	0.92 ± 0.04	1.09 ± 0.08	0.12
	Step	0.91 ± 0.04	1.41 ± 0.09	0.17
	All	0.87 ± 0.03	1.34 ± 0.07	0.19
Ammonia group	All	0.82 ± 0.02	1.33 ± 0.04	0.24
$CH_4(g) + 2^* \rightarrow CH_3^* + H^*$	Close packed	0.67 ± 0.11	1.04 ± 0.10	0.19
	Step	0.64 ± 0.09	1.01 ± 0.07	0.19
	All	0.67 ± 0.06	1.03 ± 0.05	0.18
$CH_3^* + ^* \rightarrow CH_2^* + H^*$	Close packed	0.92 ± 0.05	0.80 ± 0.08	0.11
	Step	0.86 ± 0.03	0.78 ± 0.05	0.09
	All	0.89 ± 0.03	0.79 ± 0.05	0.11
$CH_2^* + ^* \rightarrow CH^* + H^*$	Close packed	0.94 ± 0.02	1.02 ± 0.07	0.20
	Step	0.88 ± 0.06	1.22 ± 0.11	0.22
	All	0.90 ± 0.04	1.20 ± 0.10	0.27
$CH^* + ^* \rightarrow C^* + H^*$	Close packed	1.00 ± 0.03	0.72 ± 0.06	0.16
	Step	0.88 ± 0.07	1.29 ± 0.17	0.26
	All	0.92 ± 0.04	1.02 ± 0.08	0.23
$C_2H_6(g) + 2^* \rightarrow C_2H_5^* + H^*$	Step	0.85 ± 0.03	0.87 ± 0.05	0.14
$C_2H_5^* + ^* \rightarrow C_2H_4^* + H^*$	Step	0.99 ± 0.10	0.77 ± 0.20	0.11
$C_2H_4^* + ^* \rightarrow C_2H_3^* + H^*$	Step	0.92 ± 0.11	1.57 ± 0.31	0.18
$C_3H_8(g) + 2^* \rightarrow C_3H_7^* + H^*$	Step	0.76 ± 0.06	1.49 ± 0.13	0.08
$C_3H_6^* + ^* \rightarrow C_3H_5^* + H^*$	Step	1.04 ± 0.04	1.03 ± 0.13	0.07
Hydrocarbon group	All	0.95 ± 0.02	0.97 ± 0.04	0.25
$H_2(g) + 2^* \rightarrow 2H^*$	Close packed	0.67 ± 0.06	0.69 ± 0.04	0.08
	Step	0.54 ± 0.14	0.60 ± 0.08	0.11
	All	0.61 ± 0.07	0.65 ± 0.04	0.10
All	All	0.86 ± 0.01	1.14 ± 0.02	0.28

points comes predominantly from the difference of the structures of the reactions. As expected from Table 1, the MAE becomes smaller when we look into a certain reaction or a series of similar reactions, since the structures are more similar to each other. The MAE is typically smaller than 0.15 eV for an individual reaction over a given geometry of an active surface site, as evidenced in Table 1. When looking at several reactions simultaneously or several surface geometries, the uncertainty of a prediction made from their common linear regression fit will generally increase, but in all cases stays below 0.3 eV. It is therefore useful to see Table 1 as a hierarchy of accuracy that allows treating a particular reaction more accurately if it resembles one of the specifically presented reactions, whereas the overall universal TS scaling can be used for a general hydrogen bond breaking reaction which has not been specifically treated in this study.

Fig. 2 shows the BEP relations of the whole set of dehydrogenation reactions. The MAE of 0.27 eV is close to that of the above-discussed universal TS scaling relation. The practical performance of these two relations with respect to estimation of activation energies should be very similar, based on the fact that their MAEs are very close.

Although the universal BEP relation in Fig. 2 may at a first glance look less presentable than the universal TS scaling

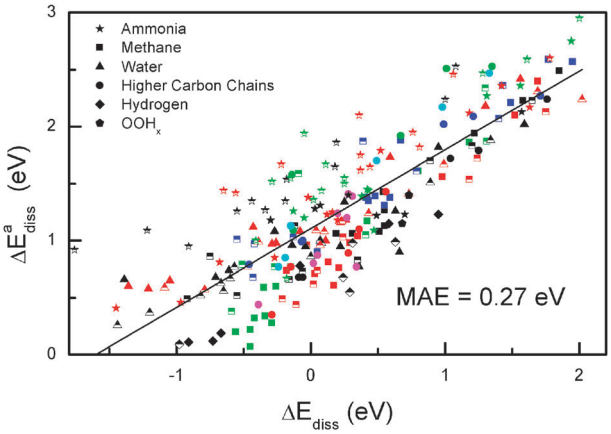

Fig. 2 Activation energies, ΔE^a_{diss}, plotted against reaction energies, ΔE_{diss}, of the dehydrogenation reactions. The fully filled symbols refer to data on close-packed surfaces, and the half filled symbols mean the data on step surfaces. The colors represent the different hydrogen content in the molecules, where black is the first dehydrogenation step, red is the second step, green is the third step and blue is the fourth dehydrogenation step.

relation, we would like to emphasize several merits of it. The first merit of BEP relations is of course the clear trend reflected by the relations. Since activation energies and reaction

energies are typical experimentally measured properties for the analysis of catalytic reactions, rather than the transition state total energies and final state total energies with respect to a gas phase reference it may also be easier to correlate theory and experiments using the BEP relations. The TS scaling relations are (in the present study) based on the structural similarities of the transition states and the final states of a reaction. Such direct similarity between states generally only holds for a limited range of surface reactivity. On the late transition metals there will be a tendency towards having late transition states, and over the early transition metals the transition states will also be earlier. The TS scaling relations (in the form presented above) will thus have a relatively larger MAE when applied to reactions over early transition metals. Therefore it makes more sense to use the TS scaling relations in the presented form for reactions over surfaces of a rather similar reactivity. The BEP relations correlate the activation barrier with contributions from both initial and final states. Therefore the BEP relations tend to be valid for the catalytic reactions in a larger window of variation of the surface reactivity. The shift in similarity of the transition state structures with initial and final states thus gives rise to a slightly v-shaped distribution of errors in Fig. 1, whereas the noise distribution is more homogeneous in Fig. 2.

The fitted parameters of separate BEP relations of the dehydrogenation reactions are listed in Table 2. It is found that the MAE becomes gradually smaller from the whole set of data to similar groups of reactions and one reaction. The reason is that the scattering caused by the difference of geometric structures has been eliminated to a large degree when only focusing on similar reactions. Hence, using parameters for a certain reaction will yield high accuracy for that or very similar reactions. The parameters for grouped reactions and the universal relation are also useful for fast calculations for preliminary and rough trends. This becomes useful when not all parameters are available or in cases where the demand for accuracy is less strict.

According to the scaling relations, the binding energies of a series of hydrogen-containing molecules are linearly correlated with the binding energies of their central atoms.[14] Fig. 3 shows that the linear relations are also valid for the correlation of the transition state energies for hydrogenation/dehydrogenation reactions and binding energies of the central atoms. Furthermore, Fig. 4 shows that the adsorption energies of hydrogen scale approximately with the adsorption energies of C, N, and O. The scatter increases as one moves from C to O. The linear TS scaling relations and the BEP relations are therefore both manifestations of the scaling relation between reaction intermediates and transition states with the adsorption energies of the central

Table 2 The fitted parameters of BEP relations

Reaction	Surface	Slope	Constant/eV	MAE/eV
$H_2O(g) + 2^* \rightarrow OH^* + H^*$	Close packed	0.44 ± 0.10	1.04 ± 0.07	0.19
	Step	0.57 ± 0.03	1.00 ± 0.02	0.06
	All	0.51 ± 0.05	1.01 ± 0.04	0.14
$OH^* + ^* \rightarrow O^* + H^*$	Close packed	0.62 ± 0.06	1.23 ± 0.05	0.16
	Step	0.59 ± 0.04	1.08 ± 0.03	0.09
	All	0.59 ± 0.04	1.15 ± 0.03	0.17
Water group	All	0.57 ± 0.03	1.09 ± 0.03	0.15
$NH_3^* + ^* \rightarrow NH_2^* + H^*$	Close packed	0.46 ± 0.13	1.21 ± 0.09	0.14
	Step	0.57 ± 0.06	1.65 ± 0.05	0.13
	All	0.42 ± 0.08	1.47 ± 0.06	0.20
$NH_2^* + ^* \rightarrow NH^* + H^*$	Close packed	0.68 ± 0.05	1.23 ± 0.05	0.14
	Step	0.57 ± 0.08	1.66 ± 0.08	0.19
	All	0.68 ± 0.06	1.41 ± 0.06	0.21
$NH^* + ^* \rightarrow N^* + H^*$	Close packed	0.79 ± 0.09	1.13 ± 0.09	0.11
	Step	0.74 ± 0.11	1.45 ± 0.09	0.19
	All	0.72 ± 0.08	1.35 ± 0.07	0.19
Ammonia group	All	0.61 ± 0.04	1.43 ± 0.04	0.23
$CH_4(g) + 2^* \rightarrow CH_3^* + H^*$	Close packed	0.92 ± 0.07	0.77 ± 0.07	0.07
	Step	0.66 ± 0.10	1.00 ± 0.08	0.18
	All	0.72 ± 0.06	0.96 ± 0.06	0.16
$CH_3^* + ^* \rightarrow CH_2^* + H^*$	Close packed	0.96 ± 0.07	0.67 ± 0.05	0.07
	Step	0.80 ± 0.07	0.71 ± 0.06	0.10
	All	0.87 ± 0.05	0.70 ± 0.04	0.10
$CH_2^* + ^* \rightarrow CH^* + H^*$	Close packed	1.02 ± 0.07	0.73 ± 0.04	0.09
	Step	0.75 ± 0.16	1.09 ± 0.11	0.25
	All	0.91 ± 0.11	0.88 ± 0.07	0.22
$CH^* + ^* \rightarrow C^* + H^*$	Close packed	0.87 ± 0.07	0.97 ± 0.07	0.09
	Step	0.71 ± 0.11	1.19 ± 0.08	0.18
	All	0.75 ± 0.06	1.12 ± 0.06	0.15
$C_2H_6(g) + 2^* \rightarrow C_2H_5^* + H^*$	Step	0.86 ± 0.03	0.75 ± 0.03	0.03
$C_2H_5^* + ^* \rightarrow C_2H_4^* + H^*$	Step	1.05 ± 0.22	0.75 ± 0.08	0.16
$C_2H_4^* + ^* \rightarrow C_2H_3^* + H^*$	Step	0.86 ± 0.18	1.45 ± 0.15	0.18
$C_3H_8(g) + 2^* \rightarrow C_3H_7^* + H^*$	Step	0.76 ± 0.06	1.11 ± 0.06	0.09
$C_3H_6^* + ^* \rightarrow C_3H_5^* + H^*$	Step	1.04 ± 0.07	1.13 ± 0.05	0.08
Hydrocarbon group	All	0.84 ± 0.04	0.94 ± 0.03	0.21
$H_2(g) + 2^* \rightarrow 2H^*$	Close packed	0.67 ± 0.06	0.69 ± 0.04	0.08
	Step	0.54 ± 0.14	0.60 ± 0.08	0.11
	All	0.61 ± 0.07	0.65 ± 0.04	0.10
Universal	All	0.69 ± 0.03	1.11 ± 0.02	0.27

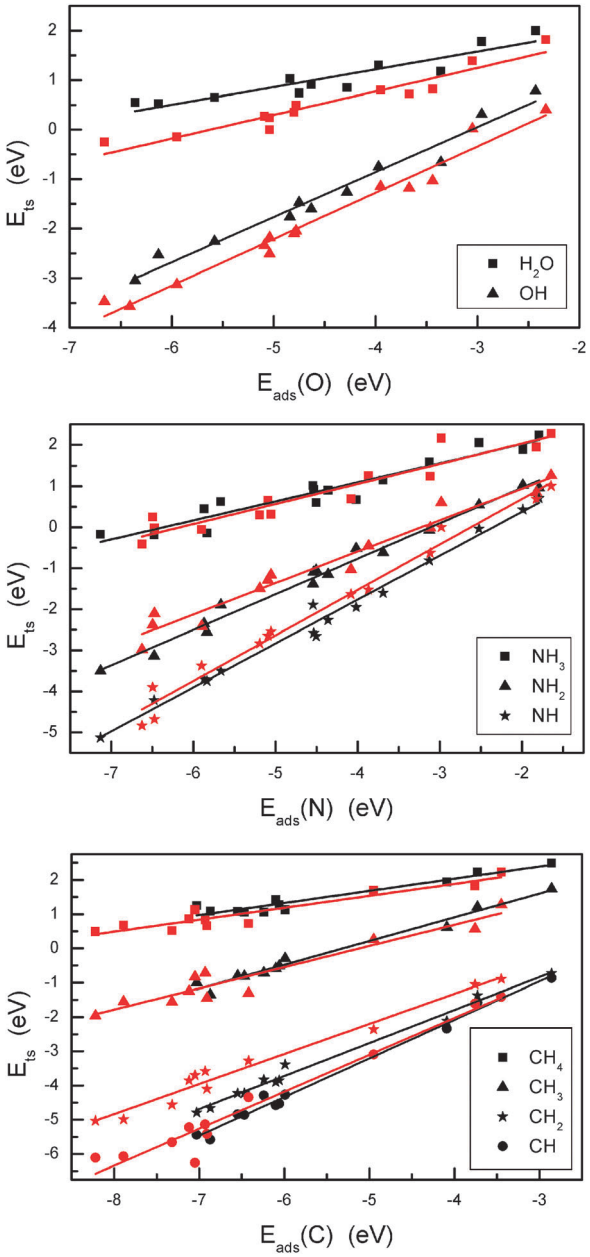

Fig. 3 The transition state energies of dehydrogenation reactions plotted against the adsorption energies of (a) O, (b) N and (c) C with respect to their gas-phase energies. The black and red colors indicate the results on close-packed and step surfaces respectively.

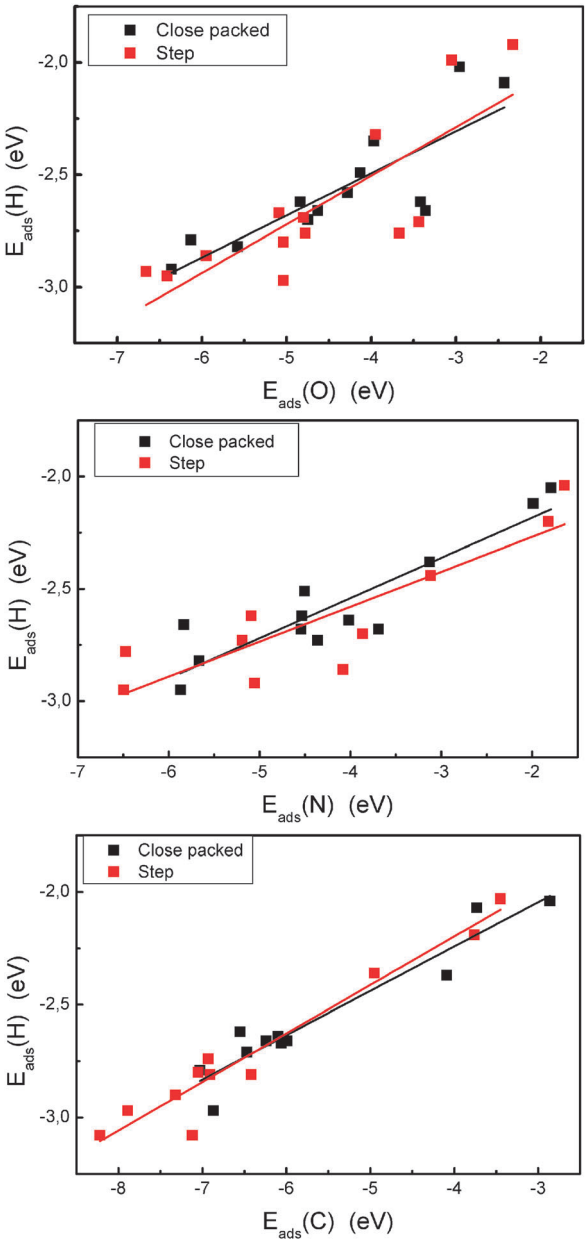

Fig. 4 The adsorption energies of H plotted against the adsorption energies of (a) O, (b) N and (c) C with respect to their gas-phase energies.

atoms (those atoms in contact with the surface). Because the transition state for dehydrogenation reactions is very similar over close-packed and stepped surfaces or a nanoparticle, there is no major geometrical effect for the single TS scaling relation and the BEP relation for all treated hydrogenation/dehydrogenation steps, and all points fall on one line in Fig. 2. For a single reaction, however, there can be a significant electronic effect going from a close-packed surface to a more under-coordinated surface, such as a step or a nanocluster. This is a particular feature of hydrogenation/dehydrogenation reactions and somewhat different from many other bond-breaking reactions on transition metal surfaces, where steps are typically many orders of magnitude more reactive than the close-packed surfaces.[10,32]

If we now more generally consider a transition state scaling relation to represent a general correlation between the energy of the transition state and some combination of relevant adsorption energies, then the BEP relation is one such particular choice of linear combination of the relevant adsorption energies. One may then well ask the question: "what linear combination of relevant energies of adsorption intermediates is the best representation of a given reaction?" This question we shall attempt to address in a subsequent piece of work based on a statistical viewpoint.[33]

Conclusions

We have presented a universal transition state scaling relation for dehydrogenation reactions over close-packed and stepped surfaces as well as nanoparticles of transition metals. One

simple relation is demonstrated to cover a very broad class of hydrogenation/dehydrogenation surface chemistry over transition metals, since all of the investigated reactions, metals, and surface geometries can be reasonably well approximated by one universal linear transition state scaling relation. This holds promise that in the future the search for new hydrogenation catalysts may be facilitated by the fact that a first rough initial screening can be carried out based on this general linear energy relation without the need for performing full DFT calculations. Together with the adsorbate scaling relations for various reaction intermediates, the universal BEP relation for (de)hydrogenation reactions can become a tool with predictive power and give a fast and semi-accurate first-hand knowledge for a number of catalytic reactions which can then subsequently be analyzed in greater detail.

Acknowledgements

The Center for Atomic-scale Materials Design is funded by The Lundbeck Foundation. The SUNCAT Center for Interface Science and Catalysis at SLAC is funded by the U.S. Department of Energy. We thank the Danish Center for Scientific Computing (DCSC) and the Catalysis for Sustainable Energy (CASE) initiative funded through the Danish Ministry of Science, Technology, and Innovation for financial support.

Notes and references

1 J. K. Nørskov, T. Bligaard, J. Rossmeisl and C. H. Christensen, *Nat. Chem.*, 2009, **1**, 37.
2 J. K. Nørskov, F. Abild-Pedersen, F. Studt and T. Bligaard, *Proc. Natl. Acad. Sci. U. S. A.*, 2011, **108**, 937.
3 M. Neurock, *Ind. Eng. Chem. Res.*, 2010, **49**, 10183.
4 M. G. Evans and M. Polanyi, *Trans. Faraday Soc.*, 1938, **34**, 11.
5 V. Pallassana and M. Neurock, *J. Catal.*, 2000, **191**, 301.
6 Z.-P. Liu and P. Hu, *J. Chem. Phys.*, 2001, **114**, 8244.
7 A. Logadottir, T. H. Rod, J. K. Nørskov, B. Hammer and C. J. H. Jacobsen, *J. Catal.*, 2001, **197**, 229.
8 J. K. Nørskov, T. Bligaard, A. Logadottir, S. R. Bahn, L. B. Hansen, M. V. Bollinger, H. S. Bengaard, B. Hammer, Z. Sljivancanin, M. Mavrikakis, Y. Xu, S. Dahl and C. J. H. Jacobson, *J. Catal.*, 2002, **209**, 275.
9 A. Michaelides, Z.-P. Liu, C. J. Zhang, A. Alavi, D. A. King and P. Hu, *J. Am. Chem. Soc.*, 2003, **125**, 3704.
10 S. Wang, B. Temel, J. Shen, G. Jones, L. C. Grabow, F. Studt, T. Bligaard, F. Abild-Pedersen, C. H. Christensen and J. K. Nørskov, *Catal. Lett.*, 2011, **141**, 370.
11 P. Crawford, B. McAllister and P. Hu, *J. Phys. Chem. C*, 2009, **113**, 5222.
12 J. Cheng, P. Hu, P. Ellis, S. French, G. Kelly and C. M. Lok, *J. Phys. Chem. C*, 2008, **112**, 1308.
13 D. Loffreda, F. Delbecq, F. Vigné and P. Sautet, *Angew. Chem., Int. Ed.*, 2009, **48**, 4978.
14 F. Abild-Pedersen, J. Greeley, F. Studt, J. Rossmeisl, T. R. Munter, P. G. Moses, E. Skúlason, T. Bligaard and J. K. Nørskov, *Phys. Rev. Lett.*, 2007, **99**, 016105.
15 F. Studt, F. Abild-Pedersen, T. Bligaard, R. Z. Sørensen, C. H. Christensen and J. K. Nørskov, *Science*, 2008, **320**, 1320.
16 M. P. Andersson, T. Bligaard, A. Kustov, K. E. Larsen, J. Greeley, T. Johannessen, C. H. Christensen and J. K. Nørskov, *J. Catal.*, 2006, **239**, 501.
17 G. Jones, J. G. Jakobsen, S. S. Shim, J. Kleis, M. P. Andersson, J. Rossmeisl, F. Abild-Pedersen, T. Bligaard, S. Helveg, B. Hinnemann, J. R. Rostrup-Nielsen, I. Chorkendorff, J. Sehested and J. K. Nørskov, *J. Catal.*, 2008, **259**, 147.
18 H. Falsig, B. Hvolbæk, I. S. Kristensen, T. Jiang, T. Bligaard, C. H. Christensen and J. K. Nørskov, *Angew. Chem., Int. Ed.*, 2008, **47**, 4835.
19 A. Hellman, E. J. Baerends, M. Biczysko, T. Bligaard, C. H. Christensen, D. C. Clary, S. Dahl, R. van Harrevelt, K. Honkala, H. Jónsson, G. J. Kroes, M. Luppi, U. Manthe, J. K. Nørskov, R. A. Olsen, J. Rossmeisl, E. Skúlason, C. S. Tautermann, A. J. C. Varandas and J. K. Vincent, *J. Phys. Chem. B*, 2006, **110**, 17719.
20 P. Ferrin, D. Simonetti, S. Kandoi, E. Kunkes, J. A. Dumesic, J. K. Nørskov and M. Mavrikakis, *J. Am. Chem. Soc.*, 2009, **131**, 5809.
21 G. A. Somorjai and Y. Li, *Top. Catal.*, 2010, **53**, 311.
22 N. Schumacher, A. Boisen, S. Dahl, A. A. Gokhale, S. Kandoi, L. C. Grabow, J. A. Dumesic, M. Mavrikakis and I. Chorkendorff, *J. Catal.*, 2005, **229**, 265.
23 J. Cheng and P. Hu, *J. Am. Chem. Soc.*, 2008, **130**, 10868.
24 The Dacapo plane wave/pseudopotential DFT code is available as open source software at http://wiki.fysik.dtu.dk/dacapo.
25 B. Hammer, L. B. Hansen and J. K. Nørskov, *Phys. Rev. B: Condens. Matter Mater. Phys.*, 1999, **59**, 7413.
26 D. Vanderbilt, *Phys. Rev. B: Condens. Matter*, 1990, **41**, 7892.
27 H. J. Monkhorst and S. D. Pack, *Phys. Rev. B: Solid State*, 1976, **13**, 5188.
28 M. P. Andersson, F. Abild-Pedersen, I. N. Remediakis, T. Bligaard, G. Jones, J. Engbæk, O. Lytken, S. Horch, J. H. Nielsen, J. Sehested, J. R. Rostrup-Nielson, J. K. Nørskov and I. Chorkendorff, *J. Catal.*, 2008, **255**, 6.
29 G. Henkelman and H. Jónsson, *J. Chem. Phys.*, 2000, **113**, 9978.
30 F. Abild-Pedersen and M. P. Andersson, *Surf. Sci.*, 2007, **601**, 1747.
31 R. Alcalá, M. Mavrikakis and J. A. Dumesic, *J. Catal.*, 2003, **218**, 178.
32 J. K. Nørskov, T. Bligaard, B. Hvolbæk, F. Abild-Pedersen, I. Chorkendorff and C. H. Christensen, *Chem. Soc. Rev.*, 2008, **37**, 2163.
33 T. Bligaard, *et al.*, in preparation.

PCCP

RSC Publishing

PAPER

DFT based study of transition metal nano-clusters for electrochemical NH_3 production†

Cite this: *Phys. Chem. Chem. Phys.*, 2013, **15**, 7785

J. G. Howalt,[ab] T. Bligaard,[bcd] J. Rossmeisl[b] and T. Vegge*[ac]

Received 21st December 2012,
Accepted 26th March 2013

DOI: 10.1039/c3cp44641g

www.rsc.org/pccp

Theoretical studies of the possibility of producing ammonia electrochemically at ambient temperature and pressure without direct N_2 dissociation are presented. Density functional theory calculations were used in combination with the computational standard hydrogen electrode to calculate the free energy profile for the reduction of N_2 admolecules and N adatoms on transition metal nanoclusters in contact with an acidic electrolyte. This work has established linear scaling relations for the *dissociative* reaction intermediates NH, NH_2, and NH_3. In addition, linear scaling relations for the *associative* reaction intermediates N_2H, N_2H_2, and N_2H_3 have been determined. Furthermore, correlations between the adsorption energies of N, N_2, and H have been established. These scaling relations and the free energy corrections are used to establish volcanoes describing the onset potential for electrochemical ammonia production and hence describe the potential determining steps for the electrochemical ammonia production. The competing hydrogen evolution reaction has also been analyzed for comparison.

I. Introduction

In the past decade, it has become more apparent than ever that mankind needs to move towards more sustainable energy consumption with significantly smaller carbon footprint per capita.

There are a number of possible ways that could potentially be used to reduce the global carbon footprint and a number of technologies have already been implemented to generate electrical power more or less sustainably, such as, for example, wind turbines, solar cells, biomass fired power plants, *etc.* With time, and with increasing prices of fossil resources, some of these may become economically competitive with fossil resources. A difficult problem to address is that of substituting transportation fuels. To make sustainable transportation fuels economically, one needs not only a competitively inexpensive way to harvest a sustainable source of energy, but also to store the energy in a convenient form with a high enough volumetric and gravimetric energy density, and in a form that can easily be transferred to a vehicle. Since catalysis can facilitate the efficient synthesis of chemicals with high energy contents, catalysis plays a key role in many of the potential scenarios for reducing our dependence on fossil resources.

One chemical compound of great versatility is ammonia. Ammonia is primarily used for making fertilizers, ultimately sustaining roughly one-third of the world's population.[1,2] In terms of reducing the carbon footprint, ammonia is interesting for a number of reasons. First, there is potential for improving the sustainability of the already huge industrial catalytic production of ammonia, which is on the order of over 100 million metric tons annually, and responsible for 1–2% of the global energy consumption. Secondly, ammonia is becoming increasingly interesting as a potential transportation fuel.[3] As an energy carrier, ammonia has the benefit that it can be used in the very energy efficient fuel cells such as the solid oxide fuel cell (SOFC) or a direct ammonia fuel cell (DAFC). Furthermore, it has the interesting feature of not emitting CO_2 while having a high energy density that is comparable with traditional fossil fuels, both volumetrically and gravimetrically.[3,4] A highly energy-efficient method for the synthesis of ammonia (NH_3) from molecular nitrogen (N_2) in air is therefore desirable. Currently, ammonia synthesis is achieved by the Haber–Bosch process that initially dissociates the N_2 bond and then protonates each nitrogen atom.[5] This is the *dissociative mechanism*. In contrast, the natural enzymatic process in nitrogenase takes place by initially weakening the N–N bond through successive protonations until the dissociation barrier is low enough that

[a] *Department of Energy Conversion and Storage, Technical University of Denmark, DK-4000 Roskilde, Denmark. E-mail: teve@dtu.dk*
[b] *Center for Atomic-scale Materials Design, Department of Physics, Technical University of Denmark, DK-2800 Kgs., Lyngby, Denmark*
[c] *SUNCAT Center for Interface Science and Catalysis, SLAC National Accelerator Laboratory, 2575 Sand Hill Road, Menlo Park, CA 94025, USA*
[d] *Department of Chemical Engineering, Stanford University, Stanford, CA 94305, USA*

† Electronic supplementary information (ESI) available. See DOI: 10.1039/c3cp44641g

the N–N bond breaks; this process is referred to as the *associative mechanism*.[6] The Haber–Bosch process is energy-intensive and centralized due to the high required temperature and pressure and it is associated with a high capital cost to construct the production plants. What we aim for is the electricity-based production of ammonia utilizing electrochemistry, thus allowing small production scales and the use of renewable energy sources like windmills or solar cells.

In the past several years, numerous experimental[7–21] and theoretical[22–34] studies have examined ammonia synthesis and they offer excellent insight into the challenges faced when developing new catalytic materials for this reaction. It has been shown in previous studies that ammonia synthesis is very structure sensitive on metal surfaces and primarily occurs on the surface steps of Fe and Ru[22,35,36] and one could expect the associative mechanism to be even more structure sensitive. The competing hydrogen evolution reaction (HER) is structure insensitive[37] and we have therefore looked at highly under-coordinated nanoclusters as a way to investigate this discrepancy.

Furthermore, it has been shown that a similar reaction, CO oxidation, can be performed on transition metal nanoparticles consisting of more noble metals at lower temperature[36,40] than traditionally-used catalysts for this reaction. On the basis of the development of density functional theory (DFT), it has become feasible to reliably model chemical reactions.[41] We have used DFT calculations to investigate electrocatalytic production of ammonia. In this work we have studied ammonia synthesis on the highly under-coordinated M12 nanoclusters, see Fig. 1, and hence the extreme domain of possible under-coordination that can be achieved, which earlier has been shown to dramatically change the reactivity of inert metals,[34,38,39] and compare the nanocluster to the traditionally studied fcc(211) surfaces. While previous studies have looked at stepped metal surfaces, the B5 sites in particular,[22,31] we perform all calculations on a consistent calculational basis, so we can directly compare results for the M12 nanocluster with the reference system of a fcc(211) stepped surface. We have investigated the reaction intermediates for the dissociative and associative mechanisms on fcc(211) surfaces and M12 nanoclusters for a large number of transition metals and developed scaling relations similar to stepped and close-packed metal surfaces. Based on vibrational calculations, entropy and zero point energy corrections calculated using statistical mechanics we construct Gibbs free energy diagrams for both reaction pathways. These diagrams can then be used to determine the lowest potential which will make each part reaction exothermic, this is then defined as the onset potential for the overall reaction and can be used to construct volcano plots visualizing the onset potential for the electrochemical ammonia production across the investigated metals.

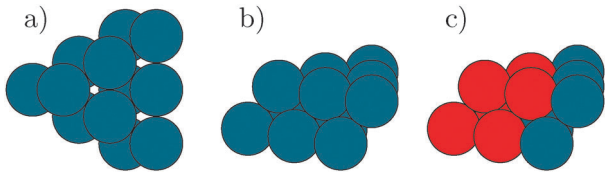

Fig. 1 (a) The M12 nanocluster seen from above. The close-packed structure is shown and the layers arranged as two fcc close-packed layers would be in a normal fcc structure. (b) The M12 nanocluster seen from the side. (c) The front six atoms are the ones with which the intermediates are allowed to bind.

II. Computational method

A. The M12 cluster

The model system we analyze is the M12 nanocluster, which contains 12 metal atoms and has previously served as a model for an under-coordinated and very small nanoparticle.[40] The atoms in the M12 are positioned in two layers, with each layer containing six atoms. Each layer follows the fcc close-packed surface structure creating a triangle, see Fig. 1a. The layers are placed above each other in the same fashion as they would in a normal close-packed slab, see Fig. 1b. For the M12 nanocluster two lattice constants were used for each of the investigated metals. The first lattice constant was determined from calculations of the bulk lattice constants in the fcc structure for each metal (denoted bulk M12). The second lattice constant was determined by allowing the M12 nanocluster to relax the lattice constant until the lowest energy configuration was found (denoted relaxed M12). For both types of M12 nanoclusters the structure was kept fixed during all adsorption calculations of reaction species.

In this study, the analysis was limited to the adsorption sites indicated by the atoms marked with red in Fig. 1c for the reaction intermediates, presented in eqn (3c)–(3h) and (4b)–(4g). These sites are chosen because they are highly under-coordinated and have other features than those of the back side of the clusters which resembles a step closer, but lack the stabilizing terraces and have been analyzed in great detail in ref. 34.

B. DFT calculations

The calculations were carried out with DFT[42,43] using the RPBE exchange correlation functional[44] in the projector augmented wave method[45,46] as implemented in the GPAW code.[47–49] A grid of (3,3) for the finite difference stencils has been used together with a grid spacing of 0.18 Å, at least 20 free bands above the Fermi level, and a Monkhorst–Pack[50] *k*-point sampling of the $2 \times 2 \times 2$. A 7 Å vacuum layer around the nanocluster has been applied. In solving the electronic density self-consistently, the convergence criteria have been chosen such that the changes in energy were $<10^{-5}$ eV and the density was 0.0001 electrons per valence electron and for most systems chosen orders of magnitude lower. Spin polarized calculations were also performed for metals that usually have a magnetic moment, such as Fe, Ni and Co although the magnetic moment could depend on the fixed geometry. In all calculations a Fermi smearing of 0.0001 eV has been used. The atomic simulation environment ASE[51] was used to set up the atomic structure of these systems. All relaxations of the adsorbates (N, H, NH, *etc.*) sitting on the bulk M12 nanocluster were carried out using the BFGS optimizer within ASE.

For the reference calculations on the fcc(211) stepped surface, a slab with five layers was utilized and in the direction following the edge of the step it was repeated once such that

each layer consisted of 3 × 2 atoms. Of the five layers that were employed, the top two were allowed to relax and a vacuum of 7 Å on both sides of the slab was used. The utilized computational criteria only differ from the clusters in that a Monkhorst–Pack *k*-point sampling of 4 × 4 × 1 was used, and the Fermi smearing was 0.0001 eV.

C. Reaction pathways

In the process of forming ammonia electrochemically, it is convenient to model the anode reaction

$$H_2 \rightleftharpoons 2H^+ + 2e^- \quad (1)$$

as the source of electrons and protons. The electrons are transported to the cathode side through an external circuit, while the protons are introduced into the proton conducting electrolyte and sustain the equilibrium and diffuse to the cathode. At the cathode a nitrogen molecule will react with the protons and electrons in the following overall reaction

$$N_2 + 6H^+ + 6e^- \rightarrow 2NH_3, \quad (2)$$

to form ammonia at the catalytically active site.

In this study two pathways to form ammonia have been investigated, the Heyrovski-type[52] reaction for both the associative and dissociative mechanisms. For the Heyrovski-type mechanism, the adsorbed species of NH_x or N_2H_x (x = {0,1,2,3}) are directly protonated, in the following way: the proton directly attaches to the molecule from the electrolyte and the electron comes from the surface and merges with the proton to create a hydrogen bonded to the molecule. In principle, the Tafel-type reaction could also occur, but this requires the reaction barriers for the hydrogenation steps[34,53] to be overcome, and will therefore require a higher temperature to drive the process forward. This is due to the fact that the Tafel reaction[54] requires the proton and the electron to merge to form a hydrogen adatom on the surface first, which then reacts with the adsorbed species of NH_x or N_2H_x (x = {0,1,2,3}). These reaction barriers have not be investigated in the present work.

The Heyrovski-type reactions for the electrochemical ammonia formation are presented below. First, we consider the dissociative Heyrovsky mechanism where the nitrogen molecule is dissociated on the surface and then subsequently protonated (an asterisk, *, denotes a surface site):

$$N_2(g) + 6(H^+ + e^-) + 2^* \rightleftharpoons N_2{}^{**} + 6(H^+ + e^-) \quad (3a)$$

$$N_2{}^{**} + 6(H^+ + e^-) \rightleftharpoons 2N^* + 6(H^+ + e^-) \quad (3b)$$

$$2N^* + 6(H^+ + e^-) \rightleftharpoons NH^* + N^* + 5(H^+ + e^-) \quad (3c)$$

$$NH^* + N^* + 5(H^+ + e^-) \rightleftharpoons NH_2{}^* + N^* + 4(H^+ + e^-) \quad (3d)$$

$$NH_2{}^* + N^* + 4(H^+ + e^-) \rightleftharpoons NH_3{}^* + N^* + 3(H^+ + e^-) \quad (3e)$$

$$NH_3{}^* + N^* + 3(H^+ + e^-) \rightleftharpoons NH_3{}^* + NH^* + 2(H^+ + e^-) \quad (3f)$$

$$NH_3{}^* + NH^* + 2(H^+ + e^-) \rightleftharpoons NH_3{}^* + NH_2{}^* + (H^+ + e^-) \quad (3g)$$

$$NH_3{}^* + NH_2{}^* + (H^+ + e^-) \rightleftharpoons 2NH_3{}^* \quad (3h)$$

$$2NH_3{}^* \rightleftharpoons NH_3{}^* + NH_3(g) + ^* \quad (3i)$$

$$NH_3(g) + NH_3{}^* + ^* \rightleftharpoons 2NH_3(g) + 2^* \quad (3j)$$

Secondly, the associative Heyrovski mechanism is considered, where the nitrogen molecule attaches to the surface and is protonated before the nitrogen–nitrogen bond dissociates. In the equations below, information from the calculations has been used, where the addition of the fourth H to the molecule $N_2H_3{}^*$ weakens the N–N bond so much that the molecule readily dissociates into NH_x species on the surface.

$$N_2(g) + 6(H^+ + e^-) + 2^* \rightleftharpoons N_2{}^{**} + 6(H^+ + e^-) \quad (4a)$$

$$N_2{}^{**} + 6(H^+ + e^-) \rightleftharpoons N_2H^{**} + 5(H^+ + e^-) \quad (4b)$$

$$N_2H^{**} + 5(H^+ + e^-) \rightleftharpoons N_2H_2{}^{**} + 4(H^+ + e^-) \quad (4c)$$

$$N_2H_2{}^{**} + 4(H^+ + e^-) \rightleftharpoons N_2H_3{}^{**} + 3(H^+ + e^-) \quad (4d)$$

$$N_2H_3{}^{**} + 3(H^+ + e^-) \rightleftharpoons NH_2{}^* + NH_2{}^* + 2(H^+ + e^-) \quad (4e)$$

$$NH_2{}^* + NH_2{}^* + 2(H^+ + e^-) \rightleftharpoons NH_3{}^* + NH_2{}^* + (H^+ + e^-) \quad (4f)$$

$$NH_3{}^* + NH_2{}^* + (H^+ + e^-) \rightleftharpoons 2NH_3{}^* \quad (4g)$$

$$2NH_3{}^* \rightleftharpoons NH_3{}^* + NH_3(g) + ^* \quad (4h)$$

$$NH_3{}^* + NH_3(g) + ^* \rightleftharpoons 2NH_3(g) + 2^* \quad (4i)$$

Alternatively, reaction (4d) has the possibility of splitting into NH and NH_2 on the surface and has been observed on some of the metals.

D. Electrochemical modelling

With DFT it is possible to calculate the reaction energy, ΔE, for each of the reaction intermediates described above in the dissociative and associative Heyrovski pathways. This reaction energy is calculated with respect to the gas-phase molecules of hydrogen and nitrogen and a clean M12 nanocluster:

$$\Delta E = E_{M_{12}-N_xH_{y^*}} - \left(E_{M_{12}} + \frac{x}{2}E_{N_2(g)} + \frac{y}{2}E_{H_2(g)}\right), \quad (5)$$

where $E_{M_{12}+N_xH_y}$ is the total energy of the system containing the M12 nanocluster with the adsorbed N_xH_y species, E_{M12} is the total energy of the system containing only the M12 nanocluster, while $E_{N_2(g)}$ and $E_{H_2(g)}$ are the calculated gas-phase energies of nitrogen and hydrogen molecules, respectively.

The reaction energies give information about the catalytic properties for ammonia formation, which we shall elaborate further upon in the discussion of the scaling relations in one of the later sections. However, for a thorough understanding, free energy corrections for each reaction intermediate need to be determined and included in the analysis.

We obtain a reasonable approximation to the free energy from the DFT calculations for the adsorbate relative to the gas-phase molecular nitrogen and hydrogen from the expression:

$$\Delta G = \Delta E + \Delta E_{ZPE} - T\Delta S, \quad (6)$$

where the ΔE_{ZPE} and ΔS are the reaction zero point energy and reaction entropy, respectively, and we have ignored thermal internal energy contributions.

Within the harmonic approximation, it is possible to calculate the vibrational frequencies for all reaction intermediates

using a finite difference method.[55] The surface species were only allowed to vibrate, while the surface atoms were kept fixed and hence the change in free energy of the metal atoms was neglected. From the vibrational frequencies the zero point energy and the entropy under the reaction conditions can be determined. The zero point energy term is given as

$$E_{\mathrm{ZPE}} = \sum_i \frac{1}{2} h\nu_i. \quad (7)$$

The vibrational entropy contribution was calculated explicitly using standard equations from statistical mechanics and is shown below:

$$S_{\mathrm{vib}} = R\sum_i \left(\frac{\Theta_{\mathrm{vi}}/T}{\exp\left(\frac{\Theta_{\mathrm{vi}}}{T}\right) - 1} - \ln\left[1 - \exp\left(\frac{-\Theta_{\mathrm{vi}}}{T}\right)\right] \right). \quad (8)$$

In this expression, the characteristic vibrational temperature, Θ_{vi}, is equal to $h\nu_i/k_{\mathrm{B}}$. Here R is the gas constant, h is Planck's constant, k_{B} is Boltzmann's constant and T is the absolute temperature and ν is the vibrational frequency.

In addition to the entropy and zero point energy corrections we include the effects of the applied potential driving the electrochemical reaction. To include the effect of potential, we use the computational standard hydrogen electrode,[56] which has been successfully applied to describe a number of electrochemical reactions, including the trends in oxygen[57,58] and nitrogen[35] and CO_2 reduction.[59] The procedure of the computational standard hydrogen electrode is briefly outlined below.[56]

The standard hydrogen electrode (SHE) has been chosen as reference potential. The chemical potential (the free energy per H) of $(H^+ + e^-)$ is related to that of $\frac{1}{2}H_2(g)$, see eqn (1). For pH = 0, a potential of $U = 0$ V relative to the SHE and a partial pressure of 1 bar of H_2 in the gas phase at 298 K, the reaction free energy of eqn (1) is equal to the net reaction of eqn (2) at an electrode.

The free energy for the reaction intermediates as defined in eqn (6) was used.

The next step is to incorporate the effects of an applied potential in all reactions involving an electron transfer and for the protons the pH. The free energy shift for a reaction involving n electrons is $-neU$ and hence the free energy reads

$$\Delta G = \Delta E + \Delta E_{\mathrm{ZPE}} - T\Delta S - neU, \quad (9)$$

This holds true for a pH value of 0.

For pH values different from 0, the correction to the free energy of H^+-ions has to be performed for the concentration dependence of the entropy, the shift reads $G(\mathrm{pH}) = -kT\ln[H^+] = kT\mathrm{pH}\ln[10]$.

All calculations presented in the present study are for a pH value of 0.

III. Results and discussion

In this section, we present the adsorption sites for the reaction intermediates, show the corresponding adsorption energies defined in eqn (5) plotted as linear scaling relations (a linear relation between different reaction intermediates) for this geometric structure, and introduce the corrections to the free energy. With these tools, the construction of volcano plots shows the onset potential for each of the reaction mechanisms when electrochemical N_2 fixation is possible.

A. Adsorption sites

We will use adsorption on the ruthenium M12 nanocluster as an illustration because the adsorption sites for this metal resemble the characteristics of all the metals studied here. Among the studied metals, from the very reactive metals such as Sc, Ti, and Nb to the very noble metals such as Au, Ag, and Cu, there are small variations in the adsorption sites. However, the M12 nanocluster has many similar types of adsorption sites, which can be divided into the usual adsorption-site subgroups such as hollow, bridge, ontop. Each of the adsorption sites in each subgroup will be slightly geometrically different and hence for each of the metals the specific electronic properties will diversify which of the specific sites are most stable. But the type of sites is close to identical throughout the investigated metals across all reaction intermediates. In Fig. 2, the adsorption sites on the ruthenium M12 nanocluster can be seen.

In Fig. 2(1) the adsorption site for N_2 is shown. The nitrogen molecule prefers to bind in a disigma type bond to the surface where the nitrogen atoms are bonded to two different metal atoms on the surface. Here the most stable sites were edges. For some sites on most of the metals, bonding of the N_2 molecule

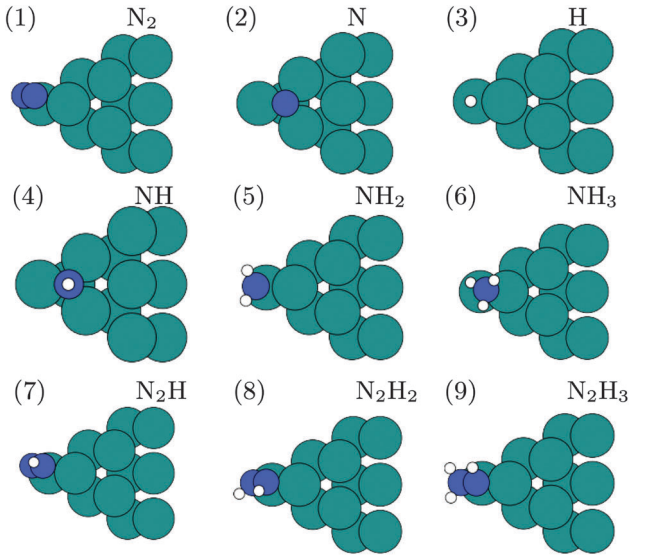

Fig. 2 The most stable adsorption sites for the reaction intermediates in both the dissociative and associative mechanisms on the ruthenium M12 nanocluster. The dark atoms are nitrogen, the small atoms are hydrogen and the light atoms are ruthenium. The adsorption sites for the adsorbates presented for the M12 nanocluster are only representative of the type of adsorption site (hollow, bridge, ontop) and not the actual bonding site for the other metals, which means a N atom could bind more strongly to another hollow site on a different metal studied in this work.

vertically to the surface was possible, where one atom was attached to the surface while the other atom was away from the surface acting as an antenna. The difference in adsorption energy between these two types of bonds is on the order of 0.1 to 0.3 eV. It should be noted that for the very reactive metals, the N_2 molecule had very few stable adsorption configurations since the splitting of the N–N bond and creation of two N* on the surface is exothermic. Furthermore, the barrier for this splitting is in the literature shown to be very low compared to the noble metals.[60]

The nitrogen adatom adsorbs on a hollow site. For hydrogen, the H_2 molecule was very rarely stable on the surface and would split into two hydrogen adatoms on the surface. The hydrogen bonding site is shown here to be a bridge site, but the difference in energy between the different types of adsorption sites was very small. NH, NH_2 and NH_3 bind to hollow, bridge and ontop sites, respectively, see Fig. 2(4–6).

The N_2H_x species on the M12 nanoclusters prefer to bond to a bridge site, where each N atom is bonded to a different metal atom, similarily to a di-sigma bonding. The configuration changes slightly depending on the number of hydrogen atoms in the surface species. Looking carefully at the figures of the N_2H_x, in Fig. 2(7–9), it is possible to see an increase in the internal bonding length as the number of hydrogen is increased and that one of the nitrogen atoms is further away from the metal atom than the other nitrogen atom. This represents the internal weakening of the N–N bond and is a key factor in the associative mechanism and the weakening of the bond between the metal and nitrogen atom. The molecule is therefore mostly bonded through one of the nitrogen atoms.

B. Scaling relations

In earlier studies it has been shown that for hydrogen containing adsorption species (such as NH_x, OH_x, CH_x, and SH_x) linear scaling relations exist that describe the adsorption energies for all species adsorbed onto either a closed packed or a stepped surface.[61] This means that the adsorption energies of AH_x (A being one of the backbone parts mentioned earlier, C, N, O, or S) on a given number of metals scale with the corresponding adsorption energy of A adsorbed onto the surface:

$$\Delta E_{AH_x} = \alpha(x)\Delta E_A + \kappa(x). \quad (10)$$

Here $\alpha(x)$ is the slope of the scaling relation, while $\kappa(x)$ is a constant. In previous studies, $\kappa(x)$ was the factor influenced by the geometric structure (whether it is a closed-packed, a stepped or another kind of surface) while the slope $\alpha(x)$ was found to be close to a constant for different surface types.

The slope is to a large extent dependent on the adsorbates number of hydrogen *versus* the maximum number of possible hydrogen in AH_x (it is 3 for NH_3).[61] The dependency on the hydrogen is such that:

$$\alpha(x) = \frac{x_{max} - x}{x_{max}}, \quad (11)$$

where x_{max} is the maximum number of hydrogen that can bond to the central atom, *i.e.* 3 for N, while the valency is defined as $(x_{max} - x)$. It should be noted that these relations exist (but vary) for different vicinal surfaces/adsorption sites. The relations are therefore useful for understanding the basic underlying trends, but one should keep in mind the complexity arising from variations in adsorption sites.

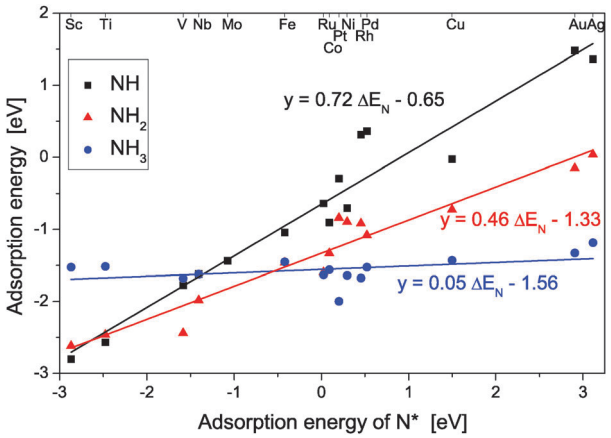

Fig. 3 The scaling relations for NH_x species on the relaxed M12 nanoclusters consisting of transition metals. The adsorption geometries are chosen as the most stable calculated ones.

In Fig. 3 the adsorption energy for NH, NH_2 and NH_3 is plotted as a function of the adsorption energy of N adatoms on the relaxed M12 nanocluster. There exist a linear relation for all NH_x species on this very under-coordinated structure. The slopes follow to a large extent the predicted ones from eqn (11). For NH, NH_2, and NH_3 the slopes are 0.72, 0.46, and 0.05. For both the bulk M12 and the relaxed M12 nanoclusters and the stepped surface fcc(211) the trend for the slope is the same, see Fig. S1–S4 in the ESI,† and the scaling relation holds true for both lattice constants. The only difference is an electronic effect that shifts the binding energy of a metal with the bulk lattice constant along the line to the adsorption energy of the metal with the relaxed lattice constant. The adsorption energies for the reaction species show that the bulk lattice constant M12 nanocluster structure is more reactive than the relaxed M12 nanocluster. This is to be expected due to the effects of stress and strain that have been shown preciously by Nørskov *et al.*[62] The values of the slopes are in good agreement with what we would have expected from the results obtained in earlier studies of the scaling relations for these species on close-packed and stepped surfaces. We cannot directly compare these calculated scaling relations with the previous described relations of NH_x species, since the underlying computational *ab initio* codes are different. Therefore, reference calculations of similar relations for a lower number of stepped fcc(211) surfaces have been carried out and the slopes $\alpha(x)$ and the constants $\kappa(x)$ are presented in Table 1. The variations in the constants between the two systems are very small and close to the uncertainty of DFT calculations. It is therefore not possible to define a noticeably geometrical effect when going from the stepped fcc(211) surface to this highly under-coordinated surface. However, the electronic effect (which is the movement down the line) is somewhat more noticeable, in the order of

Table 1 The energy scaling relations for all reaction intermediates for ammonia synthesis on the M12 nanocluster for both relax and bulk lattice constant structures and compared with the fcc(211) stepped surface. The energy relation with respect to an adsorbed N. It has to be noted that the number of metals in this study is not as large as on the M12 nanocluster calculations. The figures of the scaling relations for stepped surfaces can be found in the ESI

	fcc(211)		M12	
Adsorbate	$\alpha(y,x)$	κ (eV)	$\alpha(y,x)$	κ (eV)
N_2	0.31	−0.47	0.26	0.60
H	0.23	−0.49	0.2	−0.48
NH	0.65	−0.47	0.72	−0.65
NH_2	0.39	−1.32	0.46	−1.33
NH_3	0.16	−1.51	0.05	−1.56
N_2H	0.57	0.21	0.77	0.05
N_2H_2	0.54	0.01	0.66	−0.15
N_2H_3	0.46	−0.25	0.50	−0.28

0.1–0.6 eV for the bulk M12 nanoclusters. For the relaxed M12 nanoclusters the electronic effect is small. Comparing these effects with the previous obtained shifts between close-packed and stepped surfaces the geometrical effect is minor.[61,63]

The fixation of the metals in the M12 structure will, however, influence the calculated adsorption energies and hence effect the determined scaling relations. Structures with or without adsorbates would all have had lower energy, if the structures were allowed to relax fully but this study is focused on determining trends in such under-coordinated structures. Calculations with completely free metal atoms will be difficult to investigate systematically for the examined metals.

In Fig. 4, the scaling relations for the adsorption energy of a N_2 molecule and an H adatom are plotted against the adsorption energy of N adatoms. The slope for the adsorption energies of 0.2 for H adatoms lies close to what previously has been documented in the literature.[35] The scaling relation for a H adatom is systematic and there is only a minor electronic effect between the bulk M12 and the relaxed M12 nanoclusters, see Fig. S5 in the ESI.† The shift between the M12 nanocluster calculations and the fcc(211) stepped calculations for H is again minor and there are no signs of a noticeable geometric effect, see Fig. S6 in the ESI.†

However, for the N_2 scaling relation there is a significant variation in the slope. The bulk M12 nanocluster has a slope of 0.46, while the relaxed M12 nanocluster gives a slope of 0.26, see Fig. S7 in the ESI.† The values for the relaxed M12 correspond very well to the reference calculations on the fcc(211) stepped surface, see Fig. S6 in the ESI,† which gives a slope of 0.31; the slope for N_2 scaling of 0.3 was reported in the literature for both stepped and close-packed surfaces.[61]

The variation in the adsorption energy of N_2 between the bulk M12 and relaxed M12 nanocluster calculations originates from a combination of an electronic effect from the relaxation of the lattice constant, causing a shift along the scaling relation line, and a geometric effect caused by different adsorption geometries for the reactive metals compared to the noble metals. For the reactive metals, the adsorption sites are disigma bonded while for the more noble metals N_2 is adsorbed as an antenna on the surface, which could explain the big change observed specifically for the reactive metals. This difference in adsorption geometry can influence the strength of the adsorption when changing the overall reactivity of the nanocluster going from one M12 lattice constant to another. For the other reaction intermediates studied in this work and N_2 on the noble metals, one nitrogen atom is mainly bound to the surface, while for N_2 on the reactive metals, both nitrogen atoms are adsorbed onto the surface. The adsorption sites for the adsorbed N_2 molecule are different on the stepped fcc(211) surface where the N_2 molecule is bonded to the edge and terrace at the same time.[32,34,35] The consequences of this dramatic change are that the associative mechanism on the bulk M12 nanoclusters seems to be more active. The same tendencies are seen for the other important reaction intermediates NH_3 and N_2H. These three reaction intermediates are key reaction species for the associative mechanism and therefore a shift in scaling relations is very interesting.

In Fig. 5, the linear scaling relations for the N_2H_x adsorbates are shown. In the plot only the adsorption energies calculated for the N_2H, N_2H_2, and N_2H_3 species are included, since adsorbates containing more hydrogen spontaneously split into

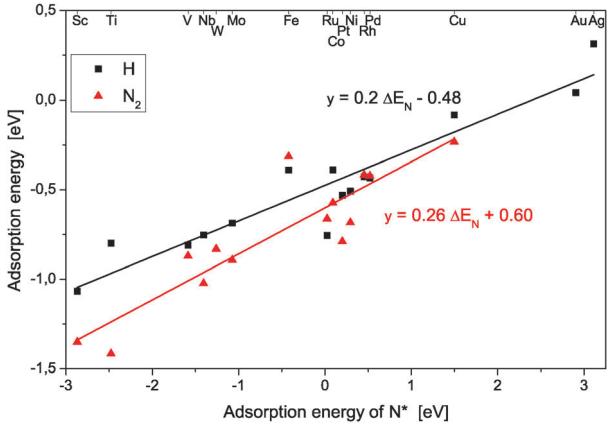

Fig. 4 The scaling relations for N_2 and H species on the M12 nanoclusters consisting of transition metals. The adsorption positions are chosen as the most stable ones.

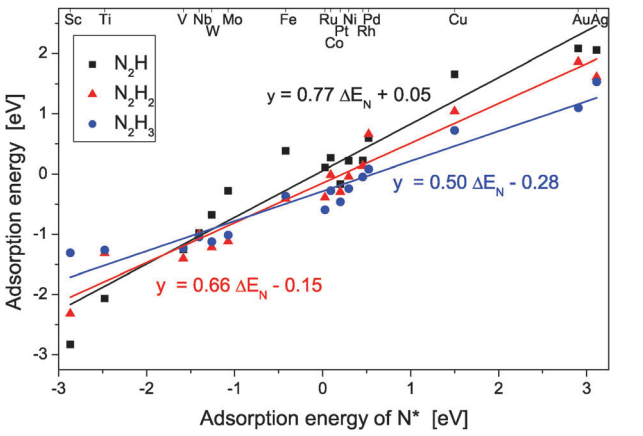

Fig. 5 The scaling relations for N_2H_x species on the M12 nanoclusters consisting of transition metals. The adsorption positions are chosen as the most stable ones.

two molecules, ranging over NH, NH_2, NH_3 to NH_3(g). The slopes for the species are 0.77, 0.66 and 0.50 for N_2H, N_2H_2 and N_2H_3 respectively. The slopes for N_2H and N_2H_2 species are different than those of the reference system of the stepped fcc(211) surface, see Fig. S8 in the ESI.† These relations again present a change in the mechanics for the associative mechanism for the under-coordinated reaction sites. To compare with the substantial effect effects between the bulk M12 and relaxed M12 nanoclusters are observed for N_2, there is no change between the two systems, see Fig. S9–S11 in the ESI,† indicating that the electronic effect on N_2 is higher because the N_2 is bonded to two sites, whereas N_2H_x species are bonded mostly to one site.

The simple underlying argument for scaling relations for AH_x species (where A is N in this case) does not hold for more complicated molecules, such as the A_2H_x molecules considered in this work. The internal bonding of orbitals in the A–A backbone will make a derivation similar to the one carried out for AH_x species much more complicated and may depend more strongly on the local adsorption environment; *i.e.* whether both backbone atoms bind to the surface or only one, and how will the hydrogen atoms bind to one or both backbone atoms and how this may effect the bonding.

C. Entropy and zero point energy corrections

The established linear scaling relations greatly simplify the adsorption energies for all reaction intermediates on all involved metals. As a reference the gas-phase entropy of nitrogen and hydrogen molecules has been used. The conditions for which the corrections have been calculated are ambient conditions, room temperature and 1 bar. The corrections for the zero point energy E_{ZPE} and for the entropy S have been calculated using statistical mechanics for the surface intermediates, see eqn (7) and (8), respectively, and for the gas phase species table values have been used.[64,65]

The calculated thermodynamic corrections are presented in Table 2. These thermodynamic corrections have been calculated for all adsorption species on the Ru M12 nanocluster and have been used as a first order approximation for the entropy and zero point energy terms for the other metals and later tested on Mo. It is reasonable to expect that the difference in the correction terms across the metals is small because the type of adsorption site for each reaction intermediate is similar.

IV. Volcano plots

Using the tools described above, it is possible to create plots visualizing the onset potential for electrochemical nitrogen fixation. This method was introduced in ref. 58 for the electrolysis of water on oxide surfaces.

In this analysis, the reaction free energy can be used directly as a simple measure of electrocatalytic activity. The reaction free energy for each elementary step can be expressed as functions of the applied bias U and the adsorption energy ΔE_N or the reaction free energy ΔG_N of the nitrogen adatom (N*). This is possible because the linear scaling relations

Table 2 The thermodynamic corrections for the reaction intermediates on the M12 nanocluster calculated at 298 K. These corrections are based on statistical thermodynamics calculated using harmonic vibration of adsorbates on the surface

Molecule	ZPE (eV)	TS (eV K^{-1})
Gas-phase		298 K
N_2(g)	0.211	0.592
H_2(g)	0.344	0.404
NH_3(g)	0.985	0.596
M12 nanocluster		298 K
N*	0.076	0.020
H*	0.171	0.014
N_2*	0.182	0.033
NH*	0.365	0.032
NH_2*	0.713	0.041
NH_3*	1.036	0.058
N_2H*	0.480	0.057
N_2H_2*	0.796	0.067
N_2H_3*	1.135	0.063

combined with the approximation that the free energy corrections at the Ru M12 nanocluster describe all important trends for the electrocatalytic activity. All protonation steps for both the *dissociative* and *associative* mechanisms include removal of a proton and an electron from the surrounding electrolyte and addition of a hydrogen to the adsorbed molecule. A dependency on the applied potential will therefore be a direct result of this framework. In the following, the method to determine the onset potential as a function of the free energy of an adsorbed nitrogen adatom will be illustrated.

The free energy of a basic protonation reaction where both reaction intermediates (initial and final state) are bonded to the surface, *e.g.* eqn (3d), can be described solely by the reactants taking active part in the electron transfer. The result is a simplification of the reaction described in eqn (3d) to the following reaction:

$$\begin{aligned} &NH^* + 2(H^+ + e^-) \rightleftharpoons NH_2^* + (H^+ + e^-), \\ &\Delta G_{dis,2} = \Delta G_{NH_2^*} - \Delta G_{NH^*} \end{aligned} \quad (12)$$

which describes the change in free energy of the reaction as defined in eqn (9). Inserting the general expression for the scaling relations formulated in eqn (10) into the equation above, the change in free energy for this part reaction is given as a function of the nitrogen binding energy, ΔE_N, and the applied potential, U.

$$\begin{aligned} \Delta G_{dis,2} &= \Delta G_{NH_2^*} - \Delta G_{NH^*} \\ &= \alpha_{NH_2}\Delta E_N + \kappa_{NH_2} + E_{ZPE,NH_2} - T\Delta S_{NH_2} - eU \\ &\quad - (\alpha_{NH}\Delta E_N) + \kappa_{NH} + E_{ZPE,NH} - T\Delta S_{NH} - 2eU \\ &= (\alpha_{NH_2} - \alpha_{NH})\Delta E_N + eU \\ &\quad + (\kappa_{NH_2} + E_{ZPE,NH_2} - T\Delta S_{NH_2}) \\ &\quad - (\kappa_{NH} + E_{ZPE,NH} - T\Delta S_{NH}). \end{aligned} \quad (13)$$

Inserting the derived numbers from the scaling relations presented in Table 1 and the calculated free energy corrections

from Table 2 into eqn (13) and subsequently converting ΔE_N to ΔG_N yield:

$$\Delta G_{dis,2} = -0.26\Delta E_N - 0.34\ eV + eU$$
$$= -0.26(\Delta G_N - 0.23\ eV) - 0.34\ eV + eU$$
$$= -0.26\Delta G_N - 0.28\ eV + eU, \quad (14)$$

where 0.23 eV is the calculated change in energy going from adsorption energy to reaction free energy for an adsorbed nitrogen adatom. The next step that must be taken is to apply a potential such that each forward reaction has a negative free energy change and the onset potential is defined when $\Delta G_{dis,2} = 0$. This ensures that the reaction occurs spontaneously, as long as the protonation barrier is low. Applying this constraint to eqn (14), the minimum onset potential needed to drive this specific reaction is given by:

$$U = 0.26/e \times \Delta E_N + 0.28\ V \quad (15)$$

where e is the elementary charge.

This procedure can be done for all pure protonation steps and plotting the obtained expressions in one plot will form a volcano describing the necessary onset potential which makes each part reaction exothermic. Fig. 6 shows both the associative and dissociative processes. The associative process is purely electrochemical, whereas the dissociative process involves the non-electrochemical (thermal) step, *i.e.* the splitting of the N–N bond, which has to be dealt with separately as outlined below.

The volcano plot for the associative mechanism can be understood utilizing the method behind eqn (13)–(15), and the two solid lines in Fig. 6 form a volcano. These part reactions are the ones that limit the associative electrochemical ammonia synthesis. The two solid lines form a volcano, where the lowest onset potential for driving the associative ammonia synthesis electrochemically is close to $U = -0.45$ V. None of the investigated metals are, however, at the optimal reaction free energy of a nitrogen adatom at −0.5 eV. The closest metals are divided into two groups, one consisting of the more reactive metals Mo, V and Nb and the other group consisting of Fe being by far the closest metal and Ru, Pt and Co further away. Here Ru and Fe are already well known good heterogeneous catalyst materials for the Haber–Bosch process and are unfortunately even better HER catalysts. Finding that the optimum for the associative mechanism lies between Mo and Fe fits very well with the active site in the enzyme nitrogenase which is the iron molybdenum cofactor.[28] Employing this methodology, effects such as coverage dependence, and the dissociation of N_2 or desorption of NH_3 in particular are not included and will have an effect on the predicted efficiency. However, this analysis suggests that alloy particles with free energies of −0.5 eV for adsorbed N adatoms should be good catalysts for the associative mechanism.

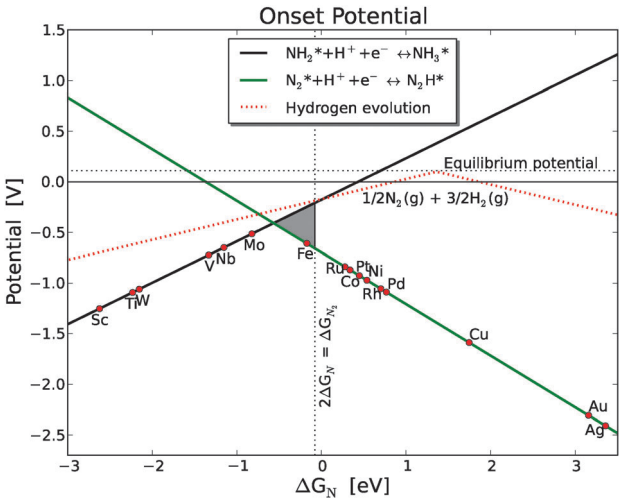

Fig. 6 Volcano plot for the associative and dissociative mechanisms with the free energy ΔG_{N^*} as a descriptor. The competing reaction of creating hydrogen on the surface is also shown as the dotted lines. The two solid lines indicate the limiting potential for the associative mechanism. For the dissociative mechanism the gray area is added as a potential area which could be more favorable for the dissociative mechanism. The efficiency in this area is dependent on the dissociation of the N_2 molecule on the surface. At the top of the gray area the dissociative mechanism will be comparable to HER.

The above-mentioned framework does not describe the main challenges of the dissociative mechanism because it lacks the description of the dissociation of N_2 on the surface. Furthermore, this description will not form one of the two legs to create the volcano (in this case the so-called right leg), see Fig. 6 where the solid black line is the electrochemical limiting reaction for the dissociative mechanism. The reason for this behavior is the scaling relations and that the slopes depend on the number of hydrogen vacancy in the adsorbed molecule. The lines describing the necessary onset potential for the dissociative mechanisms will therefore have slopes with the same sign and almost the same size. The consequence of this behavior will be that the limitations to the electrochemical reaction will only be described for the reactive metals and lack for the noble metals. This description suggests that the electrochemical nitrogen fixation efficiency will be perfect over the noble metals. However, this picture is not correct, since the main hindrance for the noble metals is the N_2 dissociation. The dissociation of N_2 is not affected by the potential and is normally seen as a heterogeneous reaction step and will have activation barriers that is much higher for noble metals than for reactive metals described by the Brøndsted–Evans–Polanyi lines.[60] For the good dissociation catalysts (the reactive metals) the hydrogen evolution reaction is preferred compared to ammonia production. This is the reason why a shift of the volcano utilizing the structure (in)sensitivity to relatively enhance the ammonia production with respect to HER is interesting.

Another method is therefore needed to describe the limitations for the dissociative mechanism on the right leg. Three limitations that should be satisfied for the dissociation of N_2 to be possible on the surfaces are:

(1) It should be preferred to have a nitrogen molecule bonded to the surface. The free energy of N_2* should hence be negative. This break-point is located at $\Delta G_N = 0.03$ eV.

(2) The reaction free energy of N_2(g) to 2N* should be negative and hence exothermic. This corresponds to $\Delta G_N = 0$ eV

and describes the point where the nitrogen atoms are able to bind to the surface.

(3) The gain in reaction free energy for the dissociation reaction of N_2* to 2N* on the surface should be negative, hence leading to a more stable end configuration. Using the linear scaling relations and free energy corrections for both N and N_2, a point can be determined where the gain in free energy for this part reaction is zero. This occurs at the reaction free energy of nitrogen adatoms at −0.08 eV.

The most conservative limit has been implemented as a horizontal line in Fig. 6. Together with the line defining the limiting onset potentials, this limit adds a triangle to the existing associative volcano and this triangle is marked with gray.

These three possible ways of looking at the limiting step for the dissociative mechanism give an estimate of the upper and lower bounds when the dissociative mechanism will be limited by the dissociation. Including one of the other proposed limitations only shift the top of the volcano by 0.11 eV on the *x*-axis and only have a minor change in the onset bias. The added triangle only marks a potential increase in electrocatalytic activity and is to some degree uncertain. Here it is worth noting that in the gray marked area the vertical line is the best case scenario, while the two lines are the worst case.

Comparing the onset potential for ammonia and hydrogen production it is only at the very top of the volcano that there is a possibility of ammonia production requiring a lower onset potential than hydrogen production. As it seems from this volcano it would still be marginally preferred to create hydrogen. However, there will be effects not included in this analysis that will have an effect on the efficiency of the catalyst and on the competition between ammonia and hydrogen production such as coverage, adsorbate–adsorbate effects, the surrounding electrolyte affecting the equilibrium. Furthermore, the fixed geometry used in this study could also influence the results. But it is important to see this study as a trend study to understand to some degree how under-coordinated reactive sites can act as ammonia catalysts.

The volcano plot in Fig. 6 shows the potential determining steps of both the dissociative and associative mechanisms when using the free energy corrections calculated for the adsorbed reaction intermediates within the harmonic approximation. Leaving out the free energy corrections would yield a minor shift for the top of the volcano where the free energy for an adsorbed nitrogen adatom shifts from −0.5 eV to −0.6 eV while the onset potential shifts to 0.4 eV, see Fig. S12 in the ESI.† The potential determining step remains the same for the new volcano and the overall trend is the same, however NH_3 would be favored compared to HER. The fact that the top of the volcano is positioned close to the same free energy of the adsorbed nitrogen adatom indicates that the overall trends for these very under-coordinated reaction sites are to a large degree independent of the calculated free energy corrections.

V. Conclusion

A theoretical analysis of the highly under-coordinated reaction sites of forming ammonia electrochemically on pure transition metal electrodes indicates that the associative mechanism could yield ammonia at an onset potential around −0.6 to −0.45 V with respect to SHE. Here, the hydrogen reaction will be a competing reaction and have a slightly lower onset potential and hence should be preferred. The most promising candidate for electrochemical ammonia production through the associative mechanism is Mo but closely followed by Fe. Alloy materials with reactivities between that of Mo, Fe and Ru could also be candidates, especially if they can hinder the HER and still be good catalysts for NH_3 production. Additionally, alloys with a reactivity such that the free energy of N adsorbed onto the surface is in the vicinity of −0.5 eV. However, even for these very under-coordinated structures there is still a gap between HER and electrochemical ammonia production in terms of onset potential for the potential determining steps. Though this problem could potentially be solved by further utilizing the structure (in)sensitivity, this remains the main challenge for the electrochemical ammonia production.

For the dissociative mechanism a proposed onset potential of −0.5 to −0.1 could be obtained with a preferred ammonia production with respect to HER for the potential determining steps. However, for the dissociative mechanism N_2 dissociation barrier of splitting the N_2 molecule has not been included since this would require a purely thermally activated Langmuir-type mechanism for one elementary step combined with the electrochemical onset potential. Instead an estimate of the equilibrium of having N adatoms compared to N_2 molecules on the surface has been established and this will hence act as a cut-off for the noble metals and describe to some extent the limitations for these metals for the dissociation of a nitrogen molecule on the surface. The cutoff could vary depending on the detailed treatment from a free energy of N adatoms of −0.08 eV to 0.03 eV, which gives the overall uncertainty of approximately 0.1 V in onset potential for the potential determining steps.

Acknowledgements

The authors would like to acknowledge the Danish Center for Scientific Computing for supercomputer access. The Center for Atomic-scale Material Design (CAMD) and the Catalysis for Sustainable Energy (CASE) initiative is funded by the Danish Ministry of Science, Technology and Innovation. This work was funded in part by the U.S. Department of Energy under contract number DE-AC02-76SF00515.

References

1 V. Smil, Detonator of the population explosion, *Nature*, 1999, **400**, 415.
2 V. Smil, *Enriching the earth: Fritz Haber, Carl Bosch, and the Transformation of World Food Production*, Massachusetts Institute of Technology, 2001.
3 A. Klerke, C. H. Christensen, J. K. Nørskov and T. Vegge, Ammonia for hydrogen storage: challenges and opportunities, *J. Mater. Chem.*, 2008, **18**(20), 2304–2310.
4 D. R. Lide, *CRC Handbook of Chemistry and Physics*, CRC Press, 90th edn, 2009.

5 F. Haber and G. van Oordt, Über die Bildung von Ammoniak aus den Elementen, *Z. Anorg. Chem.*, 1905, **47**, 42–44.
6 L. Stryer, *Biochemistry*, W.H. Freeman, New York, 4th edn, 1995.
7 G. Ertl, Z. Paal and S. B. Lee, Structure sensitivity in the iron single-crystal catalyzed synthesis of ammonia, *Appl. Surf. Sci.*, 1981, **8**, 231–249.
8 G. Ertl, M. Weiss and S. B. Lee, Role of potassium in the catalytic synthesis of ammonia, *Chem. Phys. Lett.*, 1979, **60**, 391–394.
9 N. D. Spencer, R. C. Schoonmaker and G. A. Somorjai, Structure sensitivity in the iron single-crystal catalyzed synthesis of ammonia, *Nature*, 1981, **294**, 643–644.
10 G. Ertl, S. B. Lee and M. Weiss, Kinetics of nitrogen adsorption on fe(111), *Surf. Sci.*, 1982, **114**, 515–526.
11 G. Ertl, S. B. Lee and M. Weiss, Adsorption of nitrogen on potassium promoted fe(111) and (100) surfaces, *Surf. Sci.*, 1982, **114**, 527–545.
12 N. D. Spencer, R. C. Schoonmaker and G. A. Somorjai, Iron single crystals as ammonia synthesis catalysts: effect of surface-structure on catalyst activity, *J. Catal.*, 1982, **74**, 129–135.
13 G. Ertl, Primary steps in catalytic synthesis of ammonia, *J. Vac. Sci. Technol., A*, 1983, **1**, 1247–1253.
14 L. Volpe and M. Boudart, Ammonia synthesis on molybdenum nitride, *J. Phys. Chem.*, 1986, **90**, 4874–4877.
15 D. R. Strongin, J. Carrazza, S. R. Bare and G. A. Somorjai, The importance of C7 sites and surface-roughness in the ammonia synthesis reaction over iron, *J. Catal.*, 1987, **103**, 213–215.
16 D. R. Strongin and G. A. Somorjai, The effects of potassium on ammonia synthesis over iron single-crystal surfaces, *J. Catal.*, 1988, **109**, 51–60.
17 J. A. Dumesic and A. A. Trevino, Kinetic simulation of ammonia synthesis catalysis, *J. Catal.*, 1989, **116**, 119–129.
18 L. M. Aparicio and J. A. Dumesic, Ammonia synthesis kinetics: surface chemistry, rate expressions, and kinetic analysis, *J. Mater. Chem.*, 2008, **18**, 2304–2310.
19 M. Boudart, Ammonia synthesis: the bellwether reaction in heterogeneous catalysis, *Top. Catal.*, 1994, **1**, 405–414.
20 A. Nielsen, *Ammonia: catalysis and manufacture*, Springer-Verlag, 1995.
21 G. Marnellos and M. Stoukides, Ammonia synthesis at atmospheric pressure, *J. Mater. Chem.*, 1988, **282**, 98–100.
22 S. Dahl, A. Logadottir, R. C. Egeberg, J. H. Larsen, I. Chorkendorff, E. Törnqvist and J. K. Nørskov, Role of steps in N2 activation on Ru(0001), *Phys. Rev. Lett.*, 1999, **83**, 1814–1817.
23 S. Dahl, E. Törnqvist and I. Chorkendorff, Dissociative adsorption of N2 on Ru(0001): a surface reaction totally dominated by steps, *J. Catal.*, 2000, **192**, 381–390.
24 S. Dahl, J. Sehested, C. J. H. Jacobsen, E. Törnqvist and I. Chorkendorff, Surface science based microkinetic analysis of ammonia synthesis over ruthenium catalysts, *J. Catal.*, 2000, **192**, 391–399.
25 T. Murakami, T. Nishikiori, T. Nohira and Y. Ito, Electrolytic synthesis of ammonia in molten salts under atmospheric pressure, *J. Am. Chem. Soc.*, 2003, **125**, 334–335.
26 R. Kojima and K. Aika, Molybdenum nitride and carbide catalysts for ammonia synthesis, *Appl. Catal., A*, 2001, **219**, 141–147.
27 T. H. Rod, A. Logadottir and J. K. Nørskov, Ammonia synthesis at low temperatures, *J. Chem. Phys.*, 2000, **112**, 5343–5347.
28 B. Hinnemann and J. K. Nørskov, Modeling a central ligand in the nitrogenase femo cofactor, *J. Am. Chem. Soc.*, 2003, **125**, 1466–1467.
29 A. Logadottir, T. H. Rod, J. K. Nørskov, B. Hammer, S. Dahl and C. J. H. Jacobsen, The Brønsted–Evans–Polanyi Relation and the Volcano Plot for Ammonia Synthesis over Transition Metal Catalysts, *J. Catal.*, 2001, **197**(2), 229–231.
30 A. Logadottir and J. K. Nørskov, Ammonia synthesis over a Ru(0001) surface studied by density functional calculations, *J. Catal.*, 2003, **220**, 273–279.
31 A. Hellman, K. Honkala, I. N. Remediakis, A. Logadottir, A. Carlsson, S. Dahl, C. H. Christensen and J. K. Nørskov, Ammonia synthesis and decomposition on a ru-based catalyst modeled by first-principles, *Surf. Sci.*, 2009, **603**, 1731–1739.
32 A. Hellman, E. J. Baerends, M. Biczysko, T. Bligaard, C. H. Christensen, D. C. Clary, S. Dahl, R. van Harrevelt, K. Honkala, H. Jónsson, G. J. Kroes, M. Luppi, U. Manthe, J. K. Nørskov, R. A. Olsen, J. Rossmeisl, E. Skulason, C. S. Tautermann, A. J. C. Varandas and J. K. Vincent, Predicting catalysis: understanding ammonia synthesis from first-principles calculations, *J. Phys. Chem. B*, 2006, **110**, 17719–17735.
33 T. Song and P. Hu, Insight into the adsorption competition and the relationship between dissociation and association reactions in ammonia synthesis, *J. Chem. Phys.*, 2007, **127**, 234706.
34 K. Honkala, A. Hellman, I. N. Remediakis, A. Logadottir, A. Carlsson, S. Dahl, C. H. Christensen and J. K. Nørskov, Ammonia synthesis from first-principles calculations, *Science*, 2005, **307**, 555–558.
35 E. Skúlason, T. Bligaard, S. Gudmundsdottir, F. Studt, J. Rossmeisl, F. Abild-Pedersen, T. Vegge, H. Jónsson and J. K. Nørskov, A theoretical evaluation of possible transition metal electro-catalysts for N_2 reduction, *Phys. Chem. Chem. Phys.*, 2012, **14**, 1235–1245.
36 C. J. H. Jacobsen, S. Dahl, P. L. Hansen, E. Törnqvist, L. Jensen, H. Topsoe, D. V. Prip, P. B. Moenshaug and I. Chorkendorff, Structure sensitivity of supported ruthenium catalysts for ammonia synthesis, *J. Mol. Catal. A: Chem.*, 2000, **163**, 19–26.
37 R. Gomez, A. Fernandez-Vega, J. M. Feliu and A. Aldaz, Hydrogen evolution on platinum single crystal surfaces: effects of irreversibly adsorbed bismuth and antimony on hydrogen adsorption and evolution on platinum (100), *J. Phys. Chem.*, 1993, **97**(18), 4769–4776.
38 M. Haruta, S. Tsubota, T. Kobayashi, H. Kageyama, M. J. Genet and B. Delmon, Low-Temperature Oxidation

of CO over Gold Supported on TiO_2, α-Fe_2O_3, and Co_3O_4, *J. Catal.*, 1993, **144**, 175–192.
39 J. Kleis, J. Greeley, N. A. Romero, V. A. Morozov, H. Falsig, A. H. Larsen, J. Lu, J. J. Mortensen, M. Dułak, K. S. Thygesen, J. K. Nørskov and K. W. Jacobsen, Finite Size Effects in Chemical Bonding: from Small Clusters to Solids, *Catal. Lett.*, 2011, **141**, 1067–1071.
40 T. Jiang, D. J. Mowbray, S. Dobrin, H. Falsig, B. Hvolbaek, T. Bligaard and J. K. Nørskov, Trends in co oxidation rates for metal nanoparticles and close-packed, stepped, and kinked surfaces, *J. Phys. Chem. C*, 2009, **113**, 10548.
41 J. K. Nørskov, T. Bligaard, J. Rossmeisl and C. H. Christensen, Towards the computational design of solid catalysts, *Nat. Chem.*, 2009, **1**, 37–46.
42 P. Hohenberg and W. Kohn, Inhomogeneous electron gas, *Phys. Rev. B: Solid State*, 1964, **136**(3), B864–B871.
43 W. Kohn and L. J. Sham, Self-consistent equations including exchange and correlation effects, *Phys. Rev. Sect. A*, 1965, **140**(4), A1133–A1138.
44 B. Hammer, L. B. Hansen and J. K. Nørskov, Improved adsorption energetics within density-functional theory using revised Perdew-Burke-Ernzerhof functionals, *Phys. Rev.*, 1999, **59**(11), 7413–7421.
45 P. E. Blöchl, C. J. Först and J. Schimpl, Projector augmented wave method: *ab-initio* molecular dynamics with full wave functions, *Bull. Mater. Sci.*, 2003, **26**, 33.
46 P. E. Blöchl, Projector Augmented Wave Method, *Phys. Rev. B: Condens. Matter Mater. Phys.*, 1994, **50**(24), 17953–17979.
47 J. J. Mortensen, L. B. Hansen and K. W. Jacobsen, Real-space grid implementation of the projector augmented wave method, *Phys. Rev. B: Condens. Matter Mater. Phys.*, 2005, **71**, 33.
48 J. J. Mortensen, *et al.*, Electronic structure calculations with gpaw: a real-space implementation of the projector augmented-wave method, *J. Phys.: Condens. Matter*, 2010, **22**, 253202.
49 The GPAW code is available as a part of the CAMPOS software: http://www.camd.dtu.dk/Software.
50 H. J. Monkhorst and J. D. Pack, Special points for brillouin-zone integrations, *Phys. Rev. B: Solid State*, 1976, **13**(12), 5188–5192.
51 The ASE code is available as a part of the CAMPOS software: http://www.camd.dtu.dk/Software.
52 J. Heyrovski, A theory of overpotential, *Recl. Trav. Chim. Pays-Bas*, 1927, **46**(8), 582–585.
53 S. Wang, V. Petzold, V. Tripkovic, J. Kleis, J. G. Howalt, E. Skulason, E. M. Fernandez, B. Hvolbaek, G. Jones, A. Toftelund, H. Falsig, M. Björketun, F. Studt, F. Abild-Pedersen, J. Rossmeisl, J. K. Nørskov and T. Bligaard, Universal transition state scaling relations for (de)hydrogenation over transition metals, *Phys. Chem. Chem. Phys.*, 2011, **13**(46), 20760–20765.
54 J. Tafel, On the polarization during cathodic hydrogen evolution, *Z. Phys. Chem.*, 1905, **50**, 641.
55 T. Vegge, T. Rasmussen, T. Leffers, O. B. Pedersen and K. W. Jacobsen, Atomistic simulations of cross-slip of jogged screw dislocations in copper, *Philos. Mag. Lett.*, 2001, **81**, 137–144.
56 J. K. Nørskov, J. Rossmeisl, A. Logadottir, L. Lindqvist, J. R. Kitchin, T. Bligaard and H. Jónsson, Origin of the overpotential for oxygen reduction at a fuel-cell cathode, *J. Phys. Chem. B*, 2004, **108**(46), 17886–17892.
57 J. Rossmeisl, A. Logadottir and J. K. Nørskov, Electrolysis of water on (oxidized) metal surfaces, *Chem. Phys.*, 2005, **319**, 178–184.
58 J. Rossmeisl, Z.-W. Qu, G.-J. Kroes and J. K. Nørskov, Electrolysis of water on oxide surfaces, *J. Electroanal. Chem.*, 2007, **607**, 83–89.
59 A. A. Peterson, F. Abild-Pedersen, F. Studt, J. Rossmeisl and J. K. Nørskov, How copper catalyzes the electroreduction of carbon dioxide into hydrocarbon fuels, *Energy Environ. Sci.*, 2010, **3**, 1311–1315.
60 S. G. Wang, B. Temel, J. A. Shen, G. Jones, L. C. Grabow, F. Studt, T. Bligaard, F. Abild-Pedersen, C. H. Christensen and J. K. Nørskov, Universal Brønsted-Evans-Polanyi Relations for C–C, C–O, C–N, N–O, N–N, and O–O Dissociation Reactions, *Catal. Lett.*, 2011, 141.
61 F. Abild-Petersen, J. Greeley, F. Studt, J. Rossmeisl, T. R. Munter, P. G. Moses, E. Skulason, T. Bligaard and J. K. Nørskov, Scaling properties of adsorption enemies for hydrogen containing molecules on transition metal surfaces, *Phys. Rev. Lett.*, 2007, **99**, 016105–016108.
62 M. Mavrikakis, B. Hammer and J. K. Nørskov, Effect of Strain on the Reactivity of Metal Surfaces, *Phys. Rev. Lett.*, 1998, **81**(13), 2819–2822.
63 J. K. Nørskov, T. Bligaard, B. Hvolbæk, F. Abild-Pedersen, I. Chorkendorff and C. H. Christensen, The nature of the active site in heterogeneous metal catalysis, *Chem. Soc. Rev.*, 2008, **37**, 2163–2171.
64 R. J. Silbey, R. A. Alberty and M. G. Bawendi, *Physical Chemistry*, Wiley, 4th edn, 2005.
65 C. J. Cramer, *Physical Chemistry*, John Wiley & Sons, Ltd., 2nd edn, 2004.

Electrochemical ammonia production on molybdenum nitride nanoclusters

J. G. Howalt[1,2] and T. Vegge*[1]

[1]*Department of Energy Conversion and Storage, Technical University of Denmark, DK-4000 Roskilde, Denmark*

[2]*Center for Atomic-scale Materials Design, Technical University of Denmark, DK -2800 Kgs. Lyngby, Denmark*

Abstract

Theoretical investigations of electrochemical production of ammonia at ambient temperature and pressure on nitrogen covered molybdenum nanoparticles are presented. Density functional theory calculations are used in combination with the computational hydrogen electrode approach to calculate the free energy profile for electrochemical protonation of N_2 and N adatoms on cuboctahedral Mo_{13} nanoparticles. Pathways for electrochemical ammonia production via direct protonation of N adatoms and N_2 admolecules with an onset potential as low as -0.5 V and generally lower than -0.8 V on both a nitrogen covered or clean Mo nanoparticle. Calculations presented here show that nitrogen dissociation at either nitrogen vacancies on a nitrogen covered molybdenum particle or at a clean molybdenum particle is unlikely to occur at ambient conditions due to very high activation barriers of 1.8 eV. The calculations suggest that the nitrogen will be favored at the surface compared to hydrogen even at potentials of -0.8 V and the Faradaic losses due to HER should be low.

I. INTRODUCTION

Ammonia is a chemical compound of great interest and versatility, which is primarily used for making fertilizer; ultimately sustaining roughly one-third of the World's population.[1, 2] In terms of reducing the carbon footprint, ammonia is interesting for a number of reasons. Improving the sustainability of the already huge industrial catalytic production of ammonia, which is on the order of over 100 million metric tons annually and responsible for 1-2% of the global energy consumption would reduce cost of producing ammonia. Ammonia is also becoming increasingly interesting as a potential transportation fuel [3]. As an energy carrier, ammonia has the benefit that it can be used in very energy efficient fuel cells, such as solid oxide fuel cells (SOFC) or a direct ammonia fuel cells (DAFC) [4]. Furthermore, it has the interesting feature of not emitting CO_2 while having a high energy density that is comparable with traditional fossil fuels, both volumetric and gravimetric [3, 5]. A highly energy-efficient method for the synthesis of ammonia (NH_3) from molecular nitrogen (N_2) is therefore desirable. Currently, ammonia synthesis is achieved by the Haber-Bosch process, in which N_2 is initially dissociated and subsequently each nitrogen atom is protonated [6], *i.e.* the *dissociative* mechanism. The Haber-Bosch process is energy-intensive and centralized due to the required high temperature and pressure and it is associated with a high capital cost to construct the production plants.

Over the years, numerous experimental [7–21] and theoretical [22–34] studies have examined ammonia synthesis and they offer excellent insight into the challenges faced when developing new catalytic materials for ammonia synthesis. It has been shown in previous studies that ammonia synthesis is very structure sensitive on metal surfaces and primarily occurs on the surface steps of Fe and Ru [22, 35, 36]. Whereas, the competing hydrogen evolution reaction (HER) is structure insensitive [37]. Nanoclusters offer a way to increase the selectivity for NH_3 production.

The natural enzymatic process for ammonia production in Nitrogenase takes place by initially weakening the N-N bond through successive electrochemical protonation, until the dissociation barrier is low enough to break the N-N bond; this process is referred to as the *associative* mechanism [38]. In this paper, we present a pathway for electrochemical reduction of nitrogen into ammonia on molybdenum nanoclusters, which could ultimately become sustainable through utilization of renewable electricity sources like windmills or solar

cells.

We have previously identified Mo nanoclusters as a primary candidate for electrochemical production of NH_3 via the associative mechanism [39] and shown that at potentials relevant for NH_3 production, nitrogen will adsorb preferentially over hydrogen [35], thereby minimizing the traditional Faradaic losses due to the competing HER [37]. These findings render nitrogen covered Mo nanoclusters as a prime candidate for electrochemical ammonia production.

In this paper, we investigate nitride formation and reduction on molybdenum nanoclusters as well as the competing hydrogen adsorption process. The potentials required for ammonia production through direct protonation of adsorbed nitrogen adatoms and molecules through the associative mechanism are presented. The dissociation barrier for N_2 molecules at various nitrogen coverages will also be presented.

II. COMPUTATIONAL METHOD

A. DFT calculations

The calculations were carried out with density functional theory (DFT) calculations [40, 41] using the RPBE exchange correlation functional [42] along with the projector augmented wave method [43, 44] as implemented in the GPAW code [45–47]. A grid of (3,3) for the finite difference stencils have been used together with a grid spacing of 0.18 Å, at least 20 free bands above the Fermi level and a Monkhorst-Pack [48] k-point sampling of 2×2×2. A 7 Å vacuum layer around the nanocluster has been applied. When solving the electronic density self-consistently, the convergence criteria have been chosen such that the changes were $\leq 10^{-5}$ eV for the energy and 10^{-4} electrons per valence electron for the density. In all calculations, a Fermi smearing of 10^{-4} eV has been used. The atomic simulation environment ASE [49] was used to set up the atomic structure of these systems. All structural (and atomic) relaxations of the adsorbates (N, H, NH, etc.) attached on the $Mo_{13}N_x$ nanocluster were carried out using the BFGS and FIRE [50] optimizers within ASE. In the determination of transition states and activation barriers the nudged elastic band (NEB) method [51–53] has been used with a spring constant of 1 eV/Å^2. To precisely determine the transition state configuration and the corresponding minimum energy pathway between initial and final

states, the climbing image method [53] was used as the final step in the NEB calculations.

B. The $Mo_{13}N_x$ cluster

The system of interest is the cuboctahedral molybdenum particle containing 13 atoms. The clean molybdenum structure is shown in Fig. 1a. It has a molybdenum atom as the center and a shell of 12 molybdenum atoms [54–56]. The particle was allowed to relax to find its optimum lattice constant and is through the whole study allowed to fully relax in all directions. The Mo_{13} particle is of particular interest because it is highly undercoordinated and molybdenum binds nitrogen stronger than hydrogen; hence giving rise to a nitrogen coverage on the nanocluster.

There are two relevant adsorption sites on the molybdenum particle surface. The first adsorption site is the three-fold hollow site with three nearest metal neighbors, marked with 1, and the second adsorption site is a four-fold hollow site with four closest metal neighbors, marked with 2. Two images for the filling of the nitrogen skin are shown in 1b) (half-filled skin) and 1c) (filled skin).

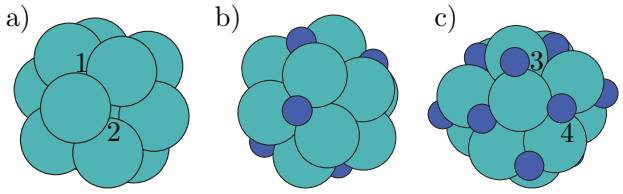

FIG. 1. *a) The clean Mo_{13} nanocluster. b) the $Mo_{13}N_7$ nanocluster after adsorption of seven nitrogen atoms (the dark atoms). c) the $Mo_{13}N_{14}$ with a filled nitrogen skin. The clean cuboctahedral nanoparticle, a), has two special adsorption sites, where the three-fold hollow is marked with 1 and the four-fold hollow site is marked with 2. In the filled nitrogen skin, the four-fold hollow adsorption sites have changed into a bridge site and is now marked 3 on c), while the geometry is kept for the adsorbed nitrogen atoms in the original three-fold hollow sites (marked with 4).*

In the case of a full nitrogen skin, two types of bonding exists for the nitrogen adatoms. One is the three-fold hollow site, *e.g.*, the atom marked 3 in Fig. 1c. The other adsorption sites is a bridge site with two molybdenum atoms (marked 4 in Fig. 1c). In the process of filling the nitrogen skin, the adsorption sites change from a four-fold hollow site to a bridge site; the change will be discussed further in a later section.

C. Reaction pathways

In the process of describing the production of ammonia electrochemically, it is convenient to model the anode reaction

$$H_2 \rightleftharpoons 2H^+ + 2e^- \tag{1}$$

as the source of electrons and protons. The electrons are transported to the cathode side through an external circuit, while the protons are introduced into the proton-conducting electrolyte keeping up the equilibrium while diffusing to the cathode. At the cathode, nitrogen will react with protons and electrons in one of two reactions to form ammonia. At the catalytic active site the reaction for the nitrogen admolecule is

$$N_2 + 6H^+ + 6e^- \rightarrow 2NH_3 \tag{2}$$

and for the nitrogen adatom

$$N + 3H^+ + 3e^- \rightarrow NH_3. \tag{3}$$

In this study, formation of ammonia through these pathways has been investigated at different nitrogen coverages. The reduction processes on the molybdenum cluster has been simulated using the Heyrovski-type [57] reaction for both the protonation of nitrogen adatoms and nitrogen admolecules; the Heyrovski-type mechanisms is a process where the proton is directly attached to an adatom or admolecule from the electrolyte and the electron comes from the surface and merges with the proton to create a hydrogen atom bonded to the molecule. In this study, the adsorbed species of nitrogen adatoms or nitrogen admolecules are directly protonated and the following species are created on the surface; NH_x or N_2H_x (x=$\{0,1,2,3\}$). In principle, a Tafel-type reaction also exists, but it requires the reaction barriers for the hydrogenation steps [34, 58] and will therefore require a higher temperature to drive the process forward. This is due to the fact, that the Tafel-type reaction [59] requires that the proton and electron to first merge on the surface to form a hydrogen adatom, and then the hydrogen adatom reacts with the adsorbed species of NH_x or N_2H_x (x=$\{0,1,2,3\}$).

The calculated reaction pathways for the electrochemical ammonia production is presented below. First, the reaction pathway of direct protonation of the nitrogen adatoms on the surface is considered. Here, a nitrogen adatom is directly protonated and after successive protonations, the formed ammonia is released from the surface. This process removes

nitrogen atoms from the surface and would therefore require a regeneration of the nitrogen adatoms on the surface to retain the skin. Therefore, this presented pathway below does not describe the full catalytic cycle; only the nitride reduction.

$$\mathrm{Mo_{13}N_x\text{-}N} + 3(\mathrm{H^+ + e^-}) \rightleftharpoons \mathrm{Mo_{13}N_x\text{-}NH} + 2(\mathrm{H^+ + e^-}) \tag{4a}$$

$$\mathrm{Mo_{13}N_x\text{-}NH} + 2(\mathrm{H^+ + e^-}) \rightleftharpoons \mathrm{Mo_{13}N_x\text{-}NH_2} + (\mathrm{H^+ + e^-}) \tag{4b}$$

$$\mathrm{Mo_{13}N_x\text{-}NH_2} + (\mathrm{H^+ + e^-}) \rightleftharpoons \mathrm{Mo_{13}N_x\text{-}NH_3} \tag{4c}$$

$$\mathrm{Mo_{13}N_x\text{-}NH_3} \rightleftharpoons \mathrm{Mo_{13}N_x} + \mathrm{NH_3(g)} \tag{4d}$$

Regeneration of the nitride will have to happen through N_2 dissociation on the surface.

$$\mathrm{Mo_{13}N_x} + \mathrm{N_2(g)} \rightleftharpoons \mathrm{Mo_{13}N_x - N_2} \tag{5}$$

$$\mathrm{Mo_{13}N_x - N_2} \rightleftharpoons \mathrm{Mo_{13}N_{x+2}} \tag{6}$$

This reaction is a heterogeneous reaction and will require low activation barriers to allow for preferential nitride regeneration over ammonia production.

Next, the *associative Heyrovski mechanism* is considered, where a nitrogen molecule is directly protonated until it splits into two molecules in the form of NH_x species that later form gaseous ammonia. In the equations below, information from the calculations have been used, where the addition of the fourth H to the molecule N_2H_3* weakens the internal N-N bond sufficiently such that the molecule readily dissociates into NH_x species on the surface.

$$\mathrm{Mo_{13}N_x - N_2} + 6(\mathrm{H^+ + e^-}) \rightleftharpoons \mathrm{Mo_{13}N_x - N_2H} + 5(\mathrm{H^+ + e^-}) \tag{7a}$$

$$\mathrm{Mo_{13}N_x - N_2H} + 5(\mathrm{H^+ + e^-}) \rightleftharpoons \mathrm{Mo_{13}N_x - N_2H_2} + 4(\mathrm{H^+ + e^-}) \tag{7b}$$

$$\mathrm{Mo_{13}N_x - N_2H_2} + 4(\mathrm{H^+ + e^-}) \rightleftharpoons \mathrm{Mo_{13}N_x - N_2H_3} + 3(\mathrm{H^+ + e^-}) \tag{7c}$$

$$\mathrm{Mo_{13}N_x - N_2H_3} + 3(\mathrm{H^+ + e^-}) \rightleftharpoons \mathrm{Mo_{13}N_x - NH_3 - NH} + 2(\mathrm{H^+ + e^-}) \tag{7d}$$

$$\mathrm{Mo_{13}N_x - NH_3 - NH} + 2(\mathrm{H^+ + e^-}) \rightleftharpoons \mathrm{Mo_{13}N_x - NH_3 - NH_2} + (\mathrm{H^+ + e^-}) \tag{7e}$$

$$\mathrm{Mo_{13}N_x - NH_3 - NH_2} + (\mathrm{H^+ + e^-}) \rightleftharpoons \mathrm{Mo_{13}N_x - NH_3 - NH_3} \tag{7f}$$

$$\mathrm{Mo_{13}N_x - NH_3 - NH_3} \rightleftharpoons \mathrm{Mo_{13}N_x} + 2\mathrm{NH_3(g)} \tag{7g}$$

The reaction steps described above are either purely electrochemical or thermal steps and together they describe the full catalytic cycle of the $Mo_{13}N_x$ particle for ammonia synthesis.

D. Electrochemical modelling

With DFT it is possible to calculate the reaction energy, ΔE, for each of the reaction intermediates described above in the direct protonation of nitrogen adatoms and nitrogen admolecules following the Heyrovski type protonation process. This reaction energy is calculated with respect to the gas phase molecules of hydrogen and nitrogen and the right corresponding $Mo_{13}N_x$ nanocluster:

$$\Delta E = E_{Mo_{13}N_x - N_zH_y^*} - (E_{Mo_{13}N_x} + \frac{z}{2}E_{N_2(g)} + \frac{y}{2}E_{H_2(g)}), \tag{8}$$

where $E_{Mo_{13}N_x - N_zH_y}$ is the total energy of the combined system of the $Mo_{13}N_x$ and the adsorbed N_zH_y adsorbates, $E_{Mo_{13}N_x}$ is the total energy of the system containing only the $Mo_{13}N_x$ nanocluster, while $E_{N_2(g)}$ and $E_{H_2(g)}$ are the calculated gas-phase energies of nitrogen and hydrogen molecules, respectively.

The reaction energies provides information about the catalytic properties for ammonia formation. However, for a thorough understanding, free energy corrections for each reaction intermediate needs to be determined and included in the analysis. The expression of the free energy relative to the gas phase of molecular nitrogen and hydrogen is

$$\Delta G = \Delta E + \Delta E_{ZPE} - T\Delta S, \tag{9}$$

where ΔE_{ZPE} and ΔS are the reaction zero point energy and reaction entropy, respectively.

The corrections for the zero point energy and entropy have been taken from a previous study [39], where the harmonic approximation was applied, the vibrational frequencies calculated for the reaction intermediates studied in this work and the corrections (ZPE and S) [60, 61] at ambient conditions.

In addition to the entropy and zero point energy corrections, an applied potential driving the electrochemical reaction will influence the free energy for the reactions. To include the effect of an applied potential, the computational hydrogen electrode [62] has been employed, which has previously been very successful in describing a number of electrochemical reactions, including the trends in oxygen [63–65] and nitrogen [35, 39] and CO_2 reduction. [66] The procedure of the computational standard hydrogen electrode is briefly outlined below.

The standard hydrogen electrode (SHE) is chosen as the reference potential. The chemical potential (the free energy per H) of $H^+ + e^-$ is related to that of $\frac{1}{2}H_2(g)$, see eq. 1. For

an applied potential of U = 0 V relative to the SHE and a partial pressure of 1 bar of H_2 in the gas phase at 298 K and pH = 0, the reaction free energy of eq. 1 is equal to the net reaction of eq. 4a - 4c and eq. 7a - 7f at an electrode.

The next step is to incorporate the effects of an applied potential in all reactions involving an electron transfer and for the protons the pH. The free energy shift for a part reaction involving n electrons is -neU and hence the change in free energy reads

$$\Delta G = \Delta E + \Delta E_{ZPE} - T\Delta S - neU, \tag{10}$$

where the pH value is set to zero. For pH values different from 0, the correction to the free energy of H^+-ions, there is a correction to the entropy arising from the concentration dependence and gives a shift of $G(pH) = -kT \cdot \ln[H^+] = kT \cdot pH \cdot \ln[10]$. All calculations presented in the present study are for a pH value of 0.

To drive the electrochemical reaction forward, the reaction should be exergonic, *i.e.* the change in free energy for each part reaction described in eq. 4a - 4c and eq. 7a - 7f has to be exothermic. From eq. 10, it is evident that the applied potential can be tuned such that the reaction steps involving a proton transfer can be made exothermic and the specific applied potential ensuring this criteria is denoted the "onset" potential. As an example, the onset potential for part reaction 4b is determined in the following way:

$$\begin{aligned} \Delta G_{dis,2} &= \Delta G_{NH_2^*} - \Delta G_{NH^*} \\ &= \Delta E_{NH_2} + E_{ZPE,NH_2} - T\Delta S_{NH_2} - eU \\ &\quad - (\Delta E_{NH} + E_{ZPE,NH} - T\Delta S_{NH} - 2eU). \end{aligned} \tag{11}$$

The next step is to apply a potential such that each forward reaction has negative free energy change and the onset potential is defined when $\Delta G_{dis,2} = 0$. The onset potential for each part reaction can then be calculated as:

$$\begin{aligned} U &= (\Delta E_{NH} + E_{ZPE,NH} - T\Delta S_{NH}) \\ &\quad - (\Delta E_{NH_2} + E_{ZPE,NH_2} - T\Delta S_{NH_2}). \end{aligned} \tag{12}$$

Applying the potential U ensures that the reaction occurs spontaneously, as long as the protonation barrier is low.

III. RESULTS AND DISCUSSION

A. Stability of the nitrogen skin

1. The energetics of the nitrogen and hydrogen skins

In the investigation of the nitrogen coverage on the cuboctahedral structure, the first sites of interest for nitrogen adsorption are the three-fold hollow sites, marked with 1 in Fig. 1a. These sites are known to adsorb nitrogen most strongly [32, 39].

The addition of nitrogen adatoms to the molybdenum nanoparticle has been carried out adding the nitrogen adatoms to three-fold hollow sites. For the first additions of nitrogen adatoms the particle changes shape to optimize the adsorption of nitrogen adatoms. For the fifth nitrogen addition, the adsorption in the three-fold hollow site again follow the cuboctahedral shape. The adsorption free energies of the first eight nitrogen atoms are shown in Fig. 2, (dark filled line), where 0 is the free energy of the clean Mo_{13} nanocluster and the respective number of $1/2N_2$ in gas phase. The graph shows that the adsorption free energies are strongest for the first additions and are then reduced when more nitrogen are added to the surface. The average binding energy for the nitrogen adatoms is presented with a dotted dark line in Fig. 2. The higher the nitrogen coverage, the smaller the structural changes.

The adsorption of hydrogen on the cuboctahedral molybdenum nanoparticle is carried out by adding hydrogen to the three fold hollow sites. In Fig. 2, the adsorption free energy of hydrogen is plotted with a pale red color and forms almost a straight line. There is no observed restructuring of the nanocluster.

2. The Nitrogen skin under reaction conditions

With respect to coverage, the competition between nitrogen (dark filled line) and hydrogen (the light dashed line) at an applied potential of -0.8 V in Fig. 2 shows that nitrogen will be preferred on the surface with overpotential as high as -0.8 V with respect to SHE. Overpotential of up to -0.8 V have previously been shown to be sufficient for the production of ammonia on a Mo model system surface [39].

The results for molybdenum nanocluster covered with either nitrogen or hydrogen shows

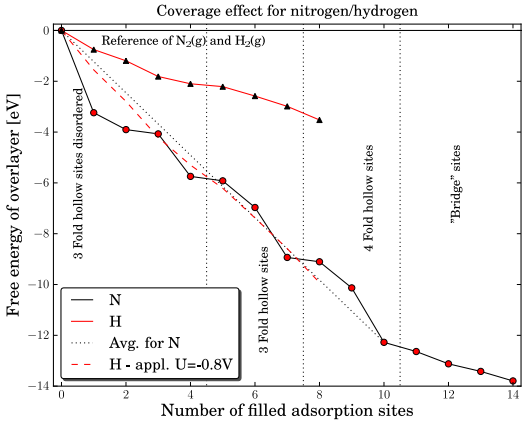

FIG. 2. *The free energy for covering the Mo13 cuboctahedral nanoparticle with either nitrogen or hydrogen. The filled dark line shows the filling of the nitrogen skin and the dark dotted line shows the average free energy of binding nitrogen to the surface. The light colored line shows the free energy of adsorbing hydrogen, while the dashed light colored line shows the free energy of adsorbed hydrogen with an external applied potential of -0.8 V.*

that it is indeed interesting to investigate the production of ammonia on this nitrogen skinned molybdenum particles because the particle should preferentially have nitrogen on the surface under reaction conditions. The stronger nitrogen bonds compared to hydrogen should subsequently result in reduced Faradaic losses due to lower hydrogen evolution on the molybdenum nanocluster under reaction conditions for ammonia production. The next step is to determine the electrochemical properties of the $Mo_{13}N_x$ nanoparticle with respect to the direct protonation of nitrogen adatoms or the associative pathway from an adsorbed N_2 molecule at nitrogen vacancy sites.

B. High nitrogen coverage

1. *Direct protonation of the nitrogen skin*

Our calculations show that a nitrogen skin is stable with respect to hydrogen. The first thing to investigate in the determination of the electrochemical properties of the molybdenum nanocluster is thus the direct protonation of the nitrogen skin. The filled skin has two nitrogen adsorption sites, the three-fold hollow site and the bridge site.

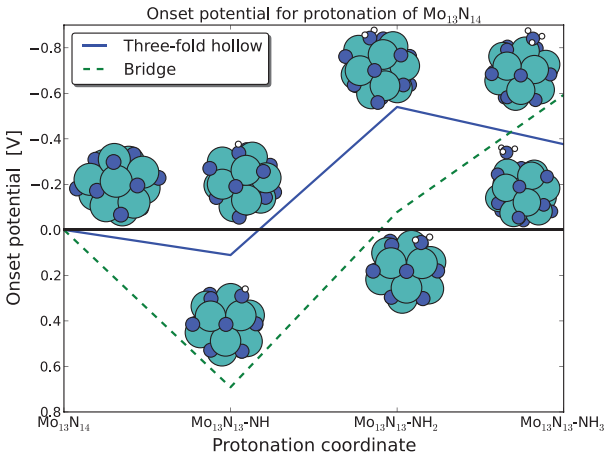

FIG. 3. *The onset potential for each protonation reaction of a nitrogen adatom originating from the $Mo_{13}N_{14}$ nanocluster structure. The onset potential for the three-fold site, dark filled line, and the bridge site, light dashed line, are close to -0.5 V.*

Calculations performed on the filled skin are shown in Fig. 3 where the onset potential is the potential required to make each part reaction exothermic. The figure shows that the onset potential is close to -0.5 V for ammonia production with respect to SHE for both nitrogen adsorption sites. The geometry of the reaction intermediates for each of the reaction pathways is presented in Fig. 3. The geometries of NH are either a bridge site or a three-fold hollow site. For both NH_2 species it is a bridge site, where the geometry of the NH_2 in the three-fold hollow pathway has been moved from the three-fold hollow site to a bridge site during the relaxation of the system. The most stable adsorption site of NH_3 for both studied reaction pathways is the on top sites. A comprehensive electronic charge analysis of the preferred protonation sites has not been performed due to the large associated variations in the geometrical relaxations of the small nanoclusters, but the observations of the adsorption geometries are in good agreement with observed geometries for NH_x adsorption structures presented in literature [32, 35, 39, 67].

For the further direct protonation of the $Mo_{13}N_x$ nanoclusters, similar onset potentials for reduction of the nitrogen skin are observed. For structures with high nitrogen coverage, the lowest onset potentials are on the order of -0.6 V to -0.8 V, see Fig. 1 in ESI. These calculations indicate that the nitrogen skin can be protonated to create ammonia and a nitrogen vacancy site at the surface.

When a $Mo_{13}N_x$ nanocluster adsorbs a nitrogen molecule, there are two pathways for the

further process. The nitrogen molecule can either go through the associative mechanism and create ammonia directly or dissociate into two nitrogen adatoms and hence regenerate the nitrogen skin. The dissociation will be discussed first.

2. N_2 dissociation

One way of regenerating a nitrogen skin is by adsorption and dissociation of N_2 molecules into two N adatoms on the surface filling up two vacancy sites. Here, we investigate the partially reduced $Mo_{13}N_{10}$ cluster that display a very stable final configurations for the adsorbed N adatoms.

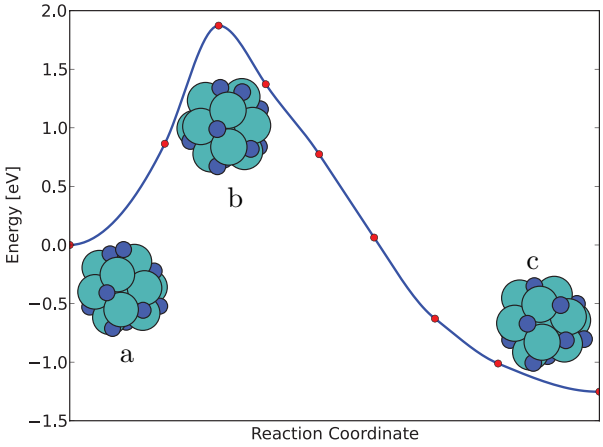

FIG. 4. *The dissociation of N_2 on the $Mo_{13}N_{10}$ nanocluster calculated using the nudged elastic band method. The initial state of adsorbed N_2, marked with a, the transition state is marked with b and the final state is marked with c.*

The minimum energy path for the N_2 dissociation on the $Mo_{13}N_{10}$ can be seen in Fig. 4. Here, the initial and final state configuration together with the transition state is shown. The barrier for the splitting of N_2 is found to be 1.72 eV, indicating that splitting of N_2 is not possible on an almost filled nitrogen skin on the molybdenum particle.

3. The associative mechanism

The direct protonation of N_2 admolecules has been thoroughly investigated on the almost filled nitrogen skin on the molybdenum cluster. Two different reaction pathways were studied

at two different nitrogen coverages. The higher nitrogen coverage ($Mo_{13}N_{12}$) is presented here, while the lower nitrogen coverage case ($Mo_{13}N_{10}$) can be seen in the supplementary material, the main results from both cases are the same.

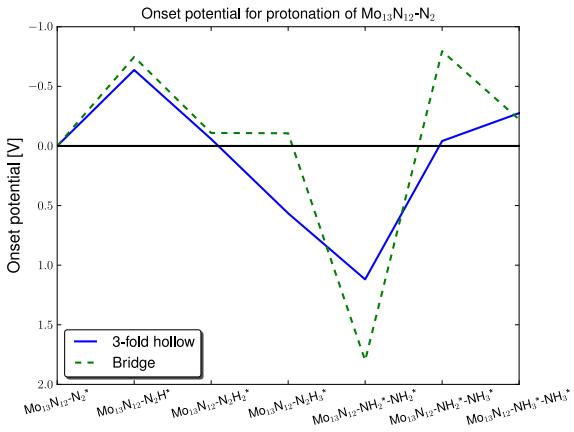

FIG. 5. *Onset potentials for all part reactions for protonation of an adsorbed nitrogen molecule on the $Mo_{13}N_{12}$ nanocluster. For the bridge site, the light dashed line, the onset potential is -0.75 V and for the three-fold site, the dark filled line, the onset potential is -0.6 V.*

The $Mo_{13}N_{12}$-N_2 is the system with the highest nitrogen coverage that can adsorb a nitrogen molecule in a nitrogen vacancy site. The nitrogen molecule has two possible adsorption sites, one is a three-fold hollow site and the other is a bridge site. The vacancy site barely adsorbs the N_2 molecule; the reaction free energy for adsorption is -0.07 eV with the three-fold hollow site as the most stable one. The reason for the weak adsorption of the nitrogen molecules is a steric hindrance caused by the nearby adsorbed nitrogen atoms Fig. 5 shows the onset potentials for driving the protonation of N_2. For both nitrogen pathways, the most endothermic reaction step is the first protonation. Here, the onset potential is around -0.6 V for the three-fold hollow site, marked by the dark filled line, and -0.75 V for the bridge site, marked by the light dashed line. For the pathway taking place on the bridge site, only the first three protonation steps are shown, since the onset potential for the pathway in the three-fold hollow site is lower. During the fourth protonation of N_2H_3 at the three-fold hollow site, the molecule prefers to dissociate into two NH_2 molecules. The protonation and splitting of the N-N bond is strongly exothermic, where the reaction free energy of this step is 1 eV downhill. It was possible to find a semi-stable N_2H_4 configuration, but the creation of this reaction intermediate on the surface is 0.9 eV uphill.

The associative mechanism was also examined on a more reduced cluster ($Mo_{13}N_{10}$). The adsorption energy of the nitrogen molecule is stronger, -1.2 eV, and the onset potentials for the individual part reactions for ammonia formation are presented in Fig. 2 in the ESI where an onset potential of -0.6 V in the best case.

With onset potentials of less than -0.8 V for all protonation processes, both the direct protonation of surface nitrogen and the associative pathways for N_2, shows that the protonation of nitrogen adatoms and admolecules into ammonia is possible.

C. The hydrogen competition

With an adsorption energy of -0.06 eV for N_2, in the case $Mo_{13}N_{12}$ and a corresponding adsorption energy of hydrogen adatoms at -0.65 eV, the hydrogen adatoms will preferential bind to the nitrogen vacancy sites. Lower nitrogen coverage increases the adsorption energy of nitrogen molecules. It increase from -0.06 eV to -2.56 eV at the clean molybdenum particle, while the corresponding adsorption energies of hydrogen is almost constant, rising from -0.66 eV to -0.74 eV. The adsorption energies can be seen in table I.

System	ΔG_{N_2} [eV]	ΔG_H [eV]	ΔG_H [eV] (U = -0.6V)
$Mo_{13}N_{12}$	-0.06	-0.66	-1.26
$Mo_{13}N_{11}$	-0.43	-0.71	-1.31
$Mo_{13}N_{10}$	-1.2	-0.73	-1.33
$Mo_{13}N_9$	-1.13	-0.59	-1.19
Mo_{13}	-2.56	-0.74	- 1.34

TABLE I. *The most stable adsorption energies of nitrogen molecules and hydrogen adatoms at different nitrogen coverages. The last column presents the binding energy of hydrogen at an applied potential of -0.6 V, which is potential at what ammonia creation is possible.*

The pathways studied at the high nitrogen coverage show that the hydrogenation of the nitrogen adatoms and admolecules is possible at reasonable overpotentials, but the dissociation is an issue with a huge activation barrier. This will lead to formation of ammonia from adsorbed nitrogen, but the nitrogen skin will be reduced under reaction conditions

because the dissociation will not lead to a regeneration of the nitrogen skin. Furthermore, the adsorption of nitrogen molecules with respect to hydrogen adatoms is not preferential at high nitrogen coverage.

At a coverage of 10 nitrogen atoms, N_2 binds with -1.2 eV, compared to a hydrogen adsorption energy of θG_H = -0.73 eV (see table I). Fig. 2 in the ESI shows that the potential required for electrochemical ammonia production is -0.6 V. At this potential, the formation of H on the surface will have a reaction free energy of -1.33 eV, while the protonation of N2 will have a reaction free energy of only -0.4 eV. It is therefore expected that H will first cover the unoccupied nitrogen vacancy sites. When all sites are filled, the protonation of N_2 will proceed because the formation of H_2(g) will be 0.13 eV uphill and at the potential required for electrochemical ammonia production all reaction steps for ammonia production will be exergonic. Adsorbate-adsorbate interactions may however lower, e.g., the free energy barrier for producing gas phase hydrogen at high coverage, but quantification would require a more detailed analysis.

Overall, this will lead to reduction of the nitrogen skin and hydrogen adsorption at high nitrogen coverage. On the other hand, adsorption energies at low nitrogen coverage show that nitrogen will be preferred over hydrogen at these conditions.

D. Low nitrogen coverage

From the study of the N_2 dissociation, the direct protonation of the nitrogen skin, the protonation of N_2 and the competing adsorption of hydrogen, we find that the skin will most likely not be completely filled with nitrogen. Even at low nitrogen coverages the onset potential for the direct protonation is still less than -0.6 V, see Fig 3 in the ESI. Nitrogen adatoms on the surface for any given nitrogen coverage will be protonated into ammonia at potentials lower than -0.6 V. In the following, the dissociation and reduction of N_2 molecules are carried out on a clean molybdenum surface with either N_2 or two N adatoms adsorbed.

As see in table I, N_2 adsorbs with 2.5 eV while two nitrogen atoms adsorb with 4 eV. In comparison the hydrogen binding energy is only -0.74 eV and with an applied potential of -0.8 V the hydrogen is bonded -1.54 eV and hence still weaker than N_2.

1. N_2 dissociation

The dissociation of nitrogen molecules is a crucial reaction step. The free energy of the N_2 and 2N on the surface gives rise to a very exothermic splitting of N_2. According to the Brøndsted-Evans-Polanyi [68] relations one would expect a lower activation barrier. This is not the case, the activation barrier for this system is still around 1.8 eV and will be rate limiting at room temperature, see Fig. S4 in the ESI.

2. Associative mechanism

Two routes for the associative pathways are presented in Fig. 6. The first route is pathway 1, which is a process where first one of the nitrogen atoms is directly protonated until ammonia is formed and then continues with protonation of the second nitrogen until formation of ammonia is achieved. This results in a splitting of the nitrogen bond at the third addition of a hydrogen atom (the 3^{rd} protonation coordinate). The second part of the first route is protonation of the second nitrogen atom. The crucial step is the last protonation of the NH_2 to NH_3, where an onset potential of -0.6 V is required. This route presents a pathway for formation of the nitrogen skin, but the onset potentials for the nitrogen adatom (4^{th} and 5^{th} protonation coordinate) is positive and hence should occur instantaneously at reaction conditions and therefore a nitrogen build up is most likely not happen.

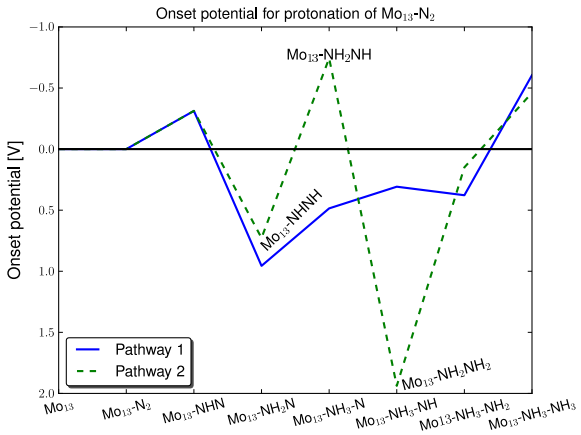

FIG. 6. *The onset potential of the protonation of the N_2 molecule on the 'clean' Mo_{13} particle.*

The second route is going through NH-N, NH-NH and NH_2-NH and then breaking of the

N-N bond where NH and NH_3 are formed on the surface. The issues for this route are both the formation of NH_2-NH and the formation of NH_3. These steps require an onset potential of -0.7 V and -0.45 V, respectively. The graph shows that the fourth protonation step, where the N-N breaking occurs, is very exothermic.

E. Desorption of ammonia

One issue that has not been illustrated with the use of the onset potential for the presented pathways of ammonia formation is desorption of ammonia from the surface. In this study the very reactive metal molybdenum is being studied and according to literature and the Sabatier principle the best catalysts are the ones that have just the 'right' reactivity. Too reactive metals have issue of getting products of the surface and too weak metals will have issues in the formation of the products.

Two nitrogen coverages have been chosen to illustrate desorption of ammonia from the molybdenum nanocluster. One case is the high coverage of nitrogen (the $Mo_{13}N_{10}$ cluster) and the other case a low coverage of nitrogen (the Mo_{13} cluster). In both cases the molybdenum nanoclusters have two ammonia molecules adsorbed. The different ways of desorbing the two ammonia molecules were studied. The reference system for calculating the desorption energy of ammonia is the free ammonia particle and the respective ammonia molecule(s) in gas phase.

In the case of high nitrogen coverage the energy for desorption of ammonia from the surface is as low as 0.38 eV and in the worst-case scenario it is 0.51 eV. These desorption barriers will not be a major issue under ambient reaction conditions. Desorption of ammonia will be slightly hindered, but not the end that it will lower the activity of the catalyst by many orders of magnitude.

In the other case, the low nitrogen coverage, the values of the desorption energy of ammonia are in the best case 0.16 eV and in the worst case 0.40 eV. These are low thermodynamic barriers for desorption of ammonia from the surface. These calculations indicate that the electrochemical production of ammonia should not be thermally hindered.

IV. CONCLUSIONS

Our theoretical study of the nitrogen covered molybdenum nanoparticle at ambient temperature and pressure indicate that these particles have potential for creating ammonia with low onset potential both at low and high nitrogen coverage. Faradaic losses due to the competing HER are reduced compared to other model systems presented in the literature. On the molybdenum nanoparticles nitrogen should be favored on the surface with applied potentials as high as -0.8 V.

At high nitrogen coverage, the pathways for creating ammonia are both the direct protonation of the nitrogen adatoms from the nitrogen coverage on the molybdenum nanoparticle and the protonation of an adsorbed nitrogen molecule adsorbed in the created nitrogen vacancy. The required onset potentials for both reaction pathways are on the order of -0.7 V to -0.5 V. The competition between hydrogen adatoms and nitrogen admolecules will be an issue at high nitrogen coverage, where hydrogen is preferred.

At low nitrogen coverage, the associative mechanism should require onset potentials of -0.6 V. Nitrogen admolecules are preferred at these conditions compared to hydrogen adatoms.

The dissociation of nitrogen at both low and high nitrogen coverage have very high activation barriers of around 1.8 eV, effectively blocking the dissociative mechanism at ambient conditions.

Desorption energies of ammonia from the surface is varying from 0.1 eV to 0.5 eV. These desorption barriers should not make the ammonia production on the molybdenum thermally hindered at ambient conditions and room temperature.

The present study shows that molybdenum nanoclusters are promising electrocatalysts for ammonia production. Nitrogen molecules are found to bind preferentially over hydrogen on certain partially and fully reduced nitrogen skins on molybdenum nanoclusters at the potentials needed for electrochemical ammonia production through the associative mechanism.

ACKNOWLEDGMENTS

The authors would like to acknowledge the Danish Center for Scientific Computing for supercomputer access. The Center for Atomic-scale Material Design (CAMD) and the Catalysis for Sustainable Energy (CASE) initiative is funded by the Danish Ministry of Science, Technology and Innovation.

---

[1] V. Smil. Detonator of the population explosion. *Nature*, 400(415), 1999.

[2] V. Smil. Enriching the earth: Fritz Haber, Carl Bosch, and the Transformation of World Food Production. *Massachusetts Institute of Technology*, 2001.

[3] A. Klerke, C. H. Christensen, J. K. Nørskov, and T. Vegge. Ammonia for hydrogen storage: challenges and opportunities. *Journal of Materials Chemistry*, 18(20):2304–2310, 2008.

[4] T. Vegge, R.Z. Sørensen, A. Klerke, J.S. Hummelshøj, T. Johannessen, J.K. Nørskov, and C.H. Christensen. *Indirect hydrogen storage in metal ammines*, pages 533–568. British Welding Research Association, 2008.

[5] D. R. Lide. *CRC Handbook of Chemistry and Physics*. CRC Press, 90th edition, 2009.

[6] F. Haber and G. van Oordt. Über die Bildung von Ammoniak aus den Elementen. *Zeitschrift für anorganische Chemie*, 47:42–44, 1905.

[7] G. Ertl, Z. Paal, and S. B. Lee. Structure sensitivity in the iron single-crystal catalyzed synthesis of ammonia. *Applied Surface Science*, 8:231–249, 1981.

[8] G. Ertl, M. Weiss, and S. B. Lee. Role of potassium in the catalytic synthesis of ammonia. *Chemical Physics Letters*, 60:391–394, 1979.

[9] N. D. Spencer, R. C. Schoonmaker, and G. A. Somorjai. Structure sensitivity in the iron single-crystal catalyzed synthesis of ammonia. *Nature*, 294:643–644, 1981.

[10] G. Ertl, S. B. Lee, and M. Weiss. Kinetics of nitrogen adsorption on fe (111). *Surface Science*, 114:515–526, 1982.

[11] G. Ertl, S. B. Lee, and M. Weiss. Adsorption of nitrogen on potassium promoted fe (111) and (100) surfaces. *Surface Science*, 114:527–545, 1982.

[12] N. D. Spencer, R. C. Schoonmaker, and G. A. Somorjai. Iron single crystals as ammonia synthesis catalysts: Effect of surface-structure on catalyst activity. *Journal of Catalysis*,

74:129–135, 1982.

[13] G. Ertl. Primary steps in catalytic synthesis of ammonia. *Journal of Vacuum Science & Technology A-Vacuum Surfaces and Films*, 1:1247–1253, 1983.

[14] L. Volpe and M. Boudart. Ammonia synthesis on molybdenum nitride. *Journal of Physical Chemistry*, 90:4874–4877, 1986.

[15] D. R. Strongin, J. Carrazza, S. R. Bare, and G. A. Somorjai. The importance of C7 sites and surface-roughness in the ammonia synthesis reaction over iron. *Journal of Catalysis*, 103:213–215, 1987.

[16] D. R. Strongin and G. A. Somorjai. The effects of potassium on ammonia synthesis over iron single-crystal surfaces. *Journal of Catalysis*, 109:51–60, 1988.

[17] J. A. Dumesic and A. A. Trevino. Kinetic simulation of ammonia synthesis catalysis. *Journal of Catalysis*, 116:119–129, 1989.

[18] L. M. Aparicio and J. A. Dumesic. Ammonia synthesis kinetics: surface chemistry, rate expressions, and kinetic analysis. *Journal of Materials Chemistry*, 18:2304–2310, 2008.

[19] M. Boudart. Ammonia synthesis: The bellwether reaction in heterogeneous catalysis. *Topics in Catalysis*, 1:405–414, 1994.

[20] A. Nielsen. Ammonia: Catalysis and manufacture. *Springer-Verlag*, 1995.

[21] G. Marnellos and M. Stoukides. Ammonia synthesis at atmospheric pressure. *Journal of Materials Chemistry*, 282:98–100, 1988.

[22] S. Dahl, A. Logadottir, R.C. Egeberg, J.H. Larsen, I. Chorkendorff, E. Törnqvist, and J.K. Nørskov. Role of steps in N2 activation on Ru(0001). *Physical Review Letters*, 83:1814–1817, 1999.

[23] S. Dahl, E. Törnqvist, and I. Chorkendorff. Dissociative adsorption of N2 on Ru(0001): A surface reaction totally dominated by steps. *Journal of Catalysis*, 192:381–390, 2000.

[24] S. Dahl, J. Sehested, C. J. H. Jacobsen, E. Törnqvist, and I. Chorkendorff. Surface science based microkinetic analysis of ammonia synthesis over ruthenium catalysts. *Journal of Catalysis*, 192:391–399, 2000.

[25] T. Murakami, T. Nishikiori, T. Nohira, and Y. Ito. Electrolytic synthesis of ammonia in molten salts under atmospheric pressure. *Journal of the American Chemical Society*, 125:334–335, 2003.

[26] R. Kojima and K. Aika. Molybdenum nitride and carbide catalysts for ammonia synthesis.

Applied Catalysis A: General, 219:141–147, 2001.

[27] T. H. Rod, A. Logadottir, and J. K. Nørskov. Ammonia synthesis at low temperatures. *Journal of Chemical Physics*, 112:5343–5347, 2000.

[28] B. Hinnemann and J. K. Nørskov. Modeling a central ligand in the nitrogenase femo cofactor. *Journal of the American Chemical Society*, 125:1466–1467, 2003.

[29] A. Logadottir, T. H. Rod, J. K. Nørskov, B. Hammer, S. Dahl, and C. J. H. Jacobsen. The Brønsted-Evans-Polanyi Relation and the Volcano Plot for Ammonia Synthesis over Transition Metal Catalysts. *Journal of Catalysis*, 197(2):229–231, 2001.

[30] A. Logadottir and J. K. Nørskov. Ammonia synthesis over a ru (0001) surface studied by density functional calculations. *Journal of Catalysis*, 220:273–279, 2003.

[31] A. Hellman, K. Honkala, I. N. Remediakis, A. Logadottir, A. Carlsson, S. Dahl, C. H. Christensen, and J. K. Nørskov. Ammonia synthesis and decomposition on a ru-based catalyst modeled by first-principles. *Surface Science*, 603:1731–1739, 2009.

[32] A. Hellman, E. J. Baerends, M. Biczysko, T. Bligaard, C. H. Christensen, D. C. Clary, S. Dahl, R. van Harrevelt, K. Honkala, H. Jónsson, G. J. Kroes, M. Luppi, U. Manthe, J. K. Nørskov, R. A. Olsen, J. Rossmeisl, E. Skulason, C. S. Tautermann, A. J. C. Varandas, and J. K. Vincent. Predicting catalysis: Understanding ammonia synthesis from first- principles calculations. *Journal of Physical Chemistry B*, 110:17719–17735, 2006.

[33] T. Song and P. Hu. Insight into the adsorption competition and the relationship between dissociation and association reactions in ammonia synthesis. *Journal of Chemical Physics*, 127:234706, 2007.

[34] K. Honkala, A. Hellman, I. N. Remediakis, A. Logadottir, A. Carlsson, S. Dahl, C. H. Christensen, and J. K. Nørskov. Ammonia synthesis from first-principles calculations. *Science*, 307:555–558, 2005.

[35] E. Skúlason, T. Bligaard, S. Gudmundsdottir, F. Studt, J. Rossmeisl, F. Abild-Pedersen, T. Vegge, H. Jónsson, and J.K. Nørskov. A theoretical evaluation of possible transition metal electro-catalysts for N2 reduction. *Phys. Chem. Chem. Phys.*, 14:1235–1245, 2012.

[36] C.J.H Jacobsen, S. Dahl, P.L. Hansen, E. Törnqvist, L. Jensen, H. Tøpsoe, D.V. Prip, P.B. Moenshaug, and I. Chorkendorff. Structure sensitivity of supported ruthenium catalysts for ammonia synthesis. *Journal of Molecular Canalysis A-Chemical*, 163:19–26, 2000.

[37] R. Gomez, A. Fernandez-Vega, J. M. Feliu, and A. Aldaz. Hydrogen evolution on platinum

single crystal surfaces: effects of irreversibly adsorbed bismuth and antimony on hydrogen adsorption and evolution on platinum (100). *The Journal of Physical Chemistry*, 97(18):4769–4776, 1993.

[38] L. Stryer. *Biochemistry, 4th ed.* W.H. Freeman, New York, 4th edition, 1995.

[39] J. G. Howalt, T. Bligaard, J. Rossmeisl, and T. Vegge. Dft based study of transition metal nano-clusters for electrochemical nh_3 production. *Phys. Chem. Chem. Phys.*, 15:7785–7795, 2013.

[40] P. Hohenberg and W. Kohn. Inhomogeneous electron gas. *Physical Review*, 136(3B):B864–B871, 1964.

[41] W. Kohn and L. J. Sham. Self-consistent equations including exchange and correlation effects. *Physical Review*, 140(4A):A1133–A1138, 1965.

[42] B. Hammer, L.B. Hansen, and J.K. Nørskov. Improved adsorption energetics within density-functional theory using revised Perdew-Burke-Ernzerhof functionals. *Phys. Review*, 59(11):7413–7421, 1999.

[43] P. E. Blöchl, C. J. Först, and J. Schimpl. Projector augmented wave method: ab-initio molecular dynamics with full wave functions. *Bulletin of Materials Science*, 26(33):33–41, 2003.

[44] P. E. Blöchl. Projector Augmented Wave Method. *Physical Review B*, 50(24):17953–17979, 1994.

[45] J. J. Mortensen, L. B. Hansen, and K. W. Jacobsen. Real-space grid implementation of the projector augmented wave method. *Physical Review B*, 71(33):035109, 2005.

[46] J. Enkovaara et. al. Electronic structure calculations with gpaw: A real-space implementation of the projector augmented-wave method. *Journal of Physics: Condensed Matter*, 22(253202), 2010.

[47] The GPAW code is available as a part of the CAMPOS software: http://www.camd.dtu.dk/Software.

[48] H.J. Monkhorst and J.D. Pack. Special points for brillouin-zone integrations. *Physical Review B*, 13(12):5188–5192, 1976.

[49] The ASE code is available as a part of the CAMPOS software: http://www.camd.dtu.dk/Software.

[50] E. Bitzek, P. Koskinen, F. Gähler, M. Moseler, and P. Gumbsch. Structural relaxation made

simple. *Physical Review Letters*, 97(12):170201, 2006.

[51] H. Jónsson, G. Mills, and K. W. Jacobsen. Nudged elastic band method for finding minimum energy paths of transitions. *Classical and Quantum Dynamics in Condensed Phase Simulations*, edited by B. J. Berne, G. Ciccotti, D. F. Coker (World Scientific, Singapore, 1998):385, 1998.

[52] G. Henkelman and H. Jónsson. Improved tangent estimate in the nudged elastic band method for finding minimum energy paths and saddle points. *J. Chem. Phys.*, 113:9978, 2000.

[53] G. Henkelman, B.P. Uberuaga, and H. Jonsson. A climbing image nudged elastic band method for finding saddle points and minimum energy paths. *J. Chem. Phys.*, 113(22):9901–9904, DEC 8 2000.

[54] A.A. Peterson, L.C. Grabow, T.P. Brennan, B. Shong, C. Ooi, D.M. Wu, C.W. Li, A. Kushwaha, A.J. Medford, F. Mbuga, L. Li, and J.K. Nørskov. Finite-size effects in o and co adsorption for the late transition metals. *Topics in Catalysis*, 55(19-20):1276–1282, 2012.

[55] S. H. Huh, H. K. Kim, and G. H. Lee. Critical cluster size of metallic cr and mo nanoclusters. *Physical Review B*, 62(4):2937–2943, 2000.

[56] T. Vystavel, S. A. Koch, G. Palasantzas, and J. Th. M. De Hosson. In situ transmission electron microscopy studies on structural dynamics of transition metal nanoclusters. *J. Mater. Res.*, 20(7):1785–2943, 2005.

[57] J. Heyrovski. A theory of overpotential. *Recueil des Travaux Chimiques des Pays-Bas*, 46(8):582–585, 1927.

[58] S. Wang, V. Petzold, V. Tripkovic, J. Kleis, J. G. Howalt, E. Skulason, E. M. Fernandez, B. Hvolbaek, G. Jones, A. Toftelund, H. Falsig, M. Björketun, F. Studt, F. Abild-Pedersen, J. Rossmeisl, J. K. Nørskov, and T. Bligaard. Universal transition state scaling relations for (de)hydrogenation over transition metals. *Physical Chemistry Chemical Physics*, 13(46):20760–20765, 2011.

[59] J. Tafel. On the polarization during cathodic hydrogen evolution. *Zeitschrift fur physikalische Chemie*, (50):641, 1905.

[60] R. J. Silbey, R. A. Alberty, and M. G. Bawendi. *Physical Chemistry.* Wiley, 4th edition, 2005.

[61] C. J. Cramer. *Physical Chemistry.* John Wiley & Sons, Ltd., 2nd edition, 2004.

[62] J. K. Nørskov, J. Rossmeisl, A. Logadottir, L. Lindqvist, J. R. Kitchin, T. Bligaard, and H. Jónsson. Origin of the overpotential for oxygen reduction at a fuel-cell cathode. *Journal*

of Physical Chemistry B, 108(46):17886–17892, 2004.

[63] J. Rossmeisl, A. Logadottir, and J. K. Nørskov. Electrolysis of water on (oxidized) metal surfaces. *Chem. Phys*, 319:178–184, 2005.

[64] J. Rossmeisl, Z.-W. Qu, G.-J. Kroes, and J.K Nørskov. Electrolysis of water on oxide surfaces. *Journal of Electroanalytical Chemistry*, 607:83–89, 2007.

[65] J.S. Hummelshøj, J. Blomquist, S. Datta, T. Vegge, J. Rossmeisl, K.S Thygesen, A. C. Luntz, K.W. Jacobsen, and J.K. Nørskov. Communications: Elementary oxygen electrode reactions in the aprotic li-air battery. *Journal of Chemical Physics*, 132(7):071101, 2010.

[66] A. A. Peterson, F. Abild-Pedersen, J. Rossmeisl F. Studt, and J.K Nørskov. How copper catalyzes the electroreduction of carbon dioxide into hydrocarbon fuels. *Energy & Environmentral Science*, 3:1311–1315, 2010.

[67] F. Abild-Petersen, J. Greeley, F. Studt, J. Rossmeisl, T. R. Munter, P.G. Moses, E. Skulason, T. Bligaard, and J. K. Nørskov. Scaling properties of adsorption enemies for hydrogen containing molecules on transition metal surfaces. *Physical Review Letters*, 99:016105–016108, 2007.

[68] S. Wang, B. Temel, J. Shen, G. Jones, L.C. Grabow, F. Studt, T. Bligaard, F. Abild-Pedersen, C.H. Christensen, and J.K. Nørskov. Universal brønsted-evans-polanyi relations for c–c, c–o, c–n, n–o, n–n, and o–o dissociation reactions. *Catalysis Letters*, 141(3):370–373, 2011.

The role of oxygen and water on molybdenum nanoclusters for electro catalytic ammonia production

J. G. Howalt[1, 2], T. Vegge*[1]

Address: [1] Department of Energy Conversion and Storage, Technical University of Denmark, DK-4000 Roskilde, Denmark
[2] Center for Atomic-scale Materials Design, Department of Physics, Technical University of Denmark, DK-2800 Kgs. Lyngby, Denmark

Email: Tejs Vegge – teve@dtu.dk

* Corresponding author

Abstract

The presence of water often gives rise to oxygen adsorption on catalyst surfaces and occupies important surfaces sites, resulting in a decrease or a total hindrance of other chemical reactions taking place at that site. In this study, we present theoretical investigations of the influence of oxygen adsorption and reduction on molybdenum nanocluster electro catalysts for electrochemical reduction N_2 to NH_3 with the purpose of understanding oxygen and water poisoning of the catalyst. Density functional theory calculations are used in combination with the computational hydrogen electrode approach to calculate the free energy profile for electrochemical protonation of O and N_2 atoms on cuboctahedral Mo_{13} nanoclusters. The calculations show that the molybdenum nanocluster will preferentially bind oxygen over nitrogen and hydrogen at relevant potentials. The potentials required to reduce oxygen off the surface are -0.72 V for all oxygen coverages studied, and it should therefore be the potential needed to (re)activate the nanocluster for electrochemical ammonia production. At lower oxygen coverages, nitrogen molecules can adsorb to the surface and electrochemical ammonia production at potentials between -0.45 V and -0.7 V are observed.

Keywords

Ammonia; Electrocatalysis; Density Functional theory, Molybdenum Oxide; Nanoparticles

Introduction

Molybdenum nanoclusters have been identified as a prime candidate for electrochemical ammonia production with seemingly low Faradaic losses to hydrogen evolution [1, 2]. To produce ammonia electrochemically, one can either use a liquid or a solid electrolyte, which will effectively require wet conditions in order to obtain sufficient protonic conduction [3,4]. The presence of water may give rise to oxygen adsorption on the surface and the oxygen atoms can occupy or block important surfaces sites. The adsorbed oxygen atom can either decrease or totally hinder other chemical reactions taking place at that site. Oxygen poisoning of the surface is indeed a main inhibitor for ammonia production [5, 6]. In this paper, the presence of oxygen, e.g. resulting from a reaction with water from the solid electrolyte, will be investigated to understand the implications it has on the catalytic properties for electrochemical ammonia production. In addition, the blocking of active sites by oxygen has been explored; together with a determination of reduction pathways to electrochemically reduce the blocking oxygen atoms off the surface.

Computational Method

DFT calculations

The calculations were carried out with density functional theory (DFT) calculations [7, 8] using the RPBE exchange correlation functional [9] along with the projector augmented wave method [10, 11] as implemented in the GPAW code [12–14]. A grid of (3,3) for the finite difference stencils have been used together with a grid spacing of 0.18 Å, a minimum of 20 free bands above the Fermi level and a Monkhorst-Pack [15] k-point sampling of 2×2×2. A 7 Å vacuum layer around the nanocluster has been applied. When solving the electronic density self-consistently, the convergence criteria have been chosen such that the changes were ≤ 10^{-5} eV for the energy and 10^{-4} electrons per valence electron for the density. In all calculations, a Fermi smearing of 10^{-4} eV has been used. The atomic simulation environment ASE [16] was used to set up the atomic structure of these systems. All structural (and atomic) relaxations of the adsorbates (N, H, O, NH, etc.) attached on the Mo_{13} nanocluster were carried out using the BFGS and FIRE [17] optimizers within ASE.

Electrochemical modelling

The procedure for electrochemical reduction of nitrogen molecules through the associative mechanism is outlined in Refs. [2,18]. It was shown that the associative mechanism is the preferred route for electrochemical ammonia production, where the protonation of the nitrogen molecules give rise to a weakened N-N bond and subsequent splitting at the third or fourth protonation step. The dissociative mechanism, the other route for electrochemical ammonia production, is due to high dissociation barriers (1.8 eV) of N_2 not taking place at the surface.

For the purposes of analyzing the reduction of oxygen, a two-step electron transfer process was assumed and simulated using the Heyrovsky-type [19] reaction. In an acidic environment, the reaction comprises of these elementary reaction steps:

$$O^*+2(H^++e^-)\rightleftharpoons OH^*+(H^++e^-)$$

$$OH^*+(H^++e^-)\rightleftharpoons H_2O^*$$

$$H_2O^*\rightleftharpoons H_2O(g)+^*,$$

where e^- is an electron in the electrode, H^+ is a proton in the electrolyte and * is a surface site. The reference potential is set to that of the standard hydrogen electrode, and the computational hydrogen electrode approach was employed to describe the effects of an applied external potential U on the electrons and the concentration of protons in the electrolyte [20–22], where $1/2\,H_2\rightleftharpoons H^++e^-$. As an example, the adsorption energy of O* was calculated as $\Delta E_O=E_{surface/O}-E_{surface}-E_{H_2O(g)}+E_{H_2(g)}$, where $E_{surface/O}$ and $E_{surface}$ are total energies of the molybdenum nanocluster with and without the specific oxygen atom, $E_{H_2(g)}$ and $E_{H_2O(g)}$ are gas phase energies of hydrogen and water. Molecular O_2 is not expected to be present under operating conditions. The adsorption energies are corrected with zero-point energy, E_{ZPE}, and entropy, TS, contributions at room temperatures.

$$\Delta G=\Delta E+\Delta E_{ZPE}-T\Delta S-neU+kT\cdot\ln[H^+]=\Delta E+\Delta E_{ZPE}-T\Delta S-neU+2.3\cdot kT\cdot pH, \quad (1)$$

Here, the pH value is set to 0 and the values of the free energy corrections for all the oxygen containing species were found in literature [23].

Results

Oxygen adsorbed in nitrogen vacancies

We have previously shown that partially reduced nitrogen covered molybdenum nanoclusters are promising catalysts for electrochemical production of ammonia [2]. N_2 adsorption is preferred over H in nitrogen vacancy sites at lower nitrogen coverages at the potential of U= -0.6 V needed for electrochemical ammonia production through the associative mechanism [2]. Adsorption of oxygen atoms is presented in Fig. 1, where they have been adsorbed at the vacant bridge site.

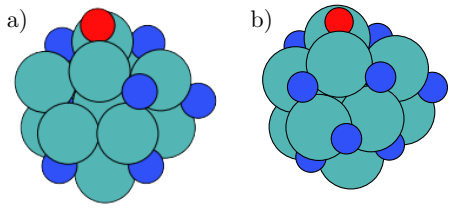

Figure 1: a) Adsorption of oxygen at a nitrogen vacancy site on $Mo_{13}N_{10}$, and b) Adsorption of oxygen at a nitrogen vacancy site on $Mo_{13}N_{12}$. Oxygen is adsorbed in the bridge site in both cases.

The free energies for adsorbing oxygen are shown in Table 1, where the energies for nitrogen and hydrogen are also listed. The table shows that oxygen will be the preferred adsorbate, with much higher adsorption energies of -1.58 eV increasing to -2.15 eV. It is evident that if water is present, the vacancy sites will be filled with oxygen and hence blocks the active sites. This will block nitrogen molecules from adsorbing to this site and stop the electrochemical formation of ammonia from this

site.

Table 1: Stability of nitrogen, hydrogen and oxygen with (U = -0.6 V) and without an applied potential at nitrogen vacancy sites on the $Mo_{13}N_x$ nanocluster. The potential required to produce ammonia electrochemically at partially nitrogen covered molybdenum nanoclusters was shown to be U = -0.6 V [2]. The energies are given with respect to H_2O (g), H_2 (g) and N_2 (g).

	ΔG_{N2} [eV]	ΔG_H [eV]	ΔG_H (U = -0.6V)	[eV] ΔG_O [eV]
$Mo_{13}N_{12}$	-0.06	-0.66	-1.26	-1.58
$Mo_{13}N_{11}$	-0.43	-0.71	-1.31	-2.24
$Mo_{13}N_{10}$	-1.2	-0.73	-1.33	-2.33
$Mo_{13}N_9$	-1.13	-0.59	-1.19	-2.15

To free the active sites for N_2 adsorption and subsequent electrochemical ammonia production, oxygen needs to be removed from the surface sites. One way of re-activating the molybdenum nanocluster for electrochemical ammonia production is to reduce the oxygen electrochemically. The reduction of oxygen will form water, which will be less strongly bound to the active site and make it possible to bind N_2 preferentially.

In the case of oxygen adsorption on the more nitrogen rich molybdenum nanoclusters, Table 2 shows the required potentials for the two-proton transfer steps in the reduction of oxygen.

The potentials range from -1.28 to -1.62 V for the second protonation step. The second protonation steps, the formation of H_2O, are hindered by the adsorbed nitrogen atoms that is present around the adsorption site of O, OH and H_2O at the surrounding three fold hollow sites. The required high potential will limit the removal of oxygen from the partially nitrogen covered molybdenum surface and oxygen will therefore constitute a very strong blocking of the active sites and subsequently limit the ammonia production rate through the associative mechanism on the nitrogen covered molybdenum nanoclusters.

Direct reduction of the residual nitrogen skin will, however, still be possible and the potential will not be influenced by the presence of oxygen and the nitrogen skin will be reduced electrochemically at -0.6 V as shown in Ref. [2] for a water free environment.

Table 2: Reduction of oxygen adsorbed on the $Mo_{13}N_x$ nanocluster.

	$U_{O\rightarrow OH}$ [V]	$U_{OH\rightarrow H2O}$ [V]
$Mo_{13}N_{12}O$	-0.35	-1.62

$Mo_{13}N_{11}O$	-0.97	-1.25
$Mo_{13}N_{10}O$	-1.18	-1.28
$Mo_{13}N_9O$	-0.72	-1.41

An oxygen skin

The electrochemical production of ammonia will not only occur on nitrogen covered molybdenum clusters, but could also take place at very low or no nitrogen coverage [2]. A clean molybdenum nanocluster in contact with nitrogen, hydrogen and water will preferentially adsorb oxygen on the surface, see Fig. 2. The figure shows the total adsorption free energies of oxygen, nitrogen and hydrogen as the coverage evolves and until saturation of oxygen and nitrogen is obtained on the surface. The oxygen skin is approximate 1-2 eV more energetically favored than a nitrogen skin at low coverages. At higher coverages, the oxygen skin becomes even more energetically favored. The consequence is that oxygen will be preferred on the surface compared to nitrogen and hydrogen. If water is present, the surface is expected to have an oxygen coverage.

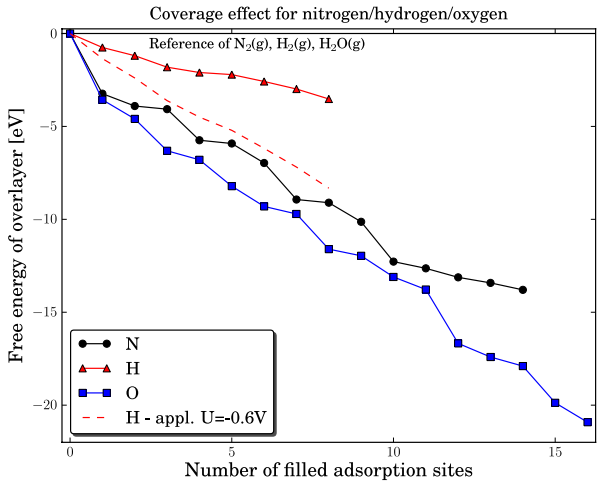

Figure 2: The total free energy for covering the Mo_{13} nanocluster with either nitrogen, hydrogen or oxygen. The filled dark line shows the filling of the nitrogen skin, while the filled blue line shows the evolution of oxygen coverage. The light colored line shows the adsorption of hydrogen, while the dashed light colored line shows adsorption of hydrogen at an external applied potential of -0.6 V, which is the potential needed for electrochemically ammonia production previously determined for the clean and nitrogen covered molybdenum nanocluster [2].

A cyclic pattern is seen in the binding energy for both nitrogen and oxygen adatoms, corresponding roughly to 10 electrons. Fig. 1 in the supporting material shows the d-band of the molybdenum nanocluster as the oxygen coverage increases and it is observed that the d-band broadens and the energetically lower lying d-orbitals are filled.

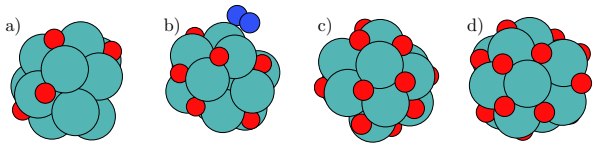

Figure 3: a) The $Mo_{13}O_6$ nanocluster, b) the $Mo_{13}O_9$ nanocluster with N_2 adsorbed, c) the $Mo_{13}O_{12}$ with an almost filled oxygen skin, d) the $Mo_{13}O_{16}$ with a filled oxygen skin. At the $Mo_{13}O_{16}$, the oxygen adsorption sites are a mix of three fold hollow sites and bridge sites.

The preferred adsorption sites for oxygen atoms are the three fold hollow sites, see Fig. 3a. When all the three fold sites are filled, the oxygen atoms will adsorb in the four fold hollow sites, see Fig. 3c. After additional adsorption of a few oxygen atoms the surface has greatly distorted. The restructuring allows a higher filling of oxygen on the surface, see Fig. 3d. The maximum filling of the surface increases to 16 oxygen atoms and further additions of oxygen atoms are energetically un-favored. At a near full overlayer, the binding of oxygen are asymmetric where oxygen now binds in a mix of a three fold hollow site and a bridge site.

Reduction of the oxygen overlayer

At the fully oxygen covered molybdenum nanocluster, nitrogen molecules cannot adsorb to the surface. Therefore, a full oxygen skin eliminates electrochemical ammonia production. It is therefore necessary to reduce the surface, in order to create active sites for nitrogen adsorption. To fully investigate the reduction of oxygen on a partially or fully oxygen covered molybdenum nanocluster, the reduction of all adsorbed oxygen atoms should, in principle, be analysed. This is, however, not computationally feasible and instead up to three representative adsorbed oxygen atoms are reduced at each investigated oxygen coverage. Each of the chosen oxygen atoms represents an unique oxygen adsorption position and the coverage ranges from 16 oxygen atoms to only one oxygen atom. The potentials for the two proton transfer processes are presented in Table 3. For other proton transfer processes (not shown), the local geometries around the adsorption site can hinder both protonation steps, but most often the second protonation is hindered. One such hindrance can be the movements from the adsorption site of the OH species to an on top site, where the H_2O specie is energetically most stable. Such movement requires a restructuring of the local environment, and hence the protonation step can become energetically very endothermic. The largest variation is therefore seen for the second protonation step. For the presented reduction steps of OH, the required potentials are in the range of -0.2 to -0.7 V. The formation of OH from O will require a negative potential to stabilize the OH specie compared to the O atom, and in most cases the potential required are in the range of -0.3 V to -0.7 V.

For most of the studied coverages, the reaction free energies for desorption of H_2O off the surface are either low or exergonic. In general, desorption energies are lower than 0.4 eV, but for a single adsorbed oxygen atom, it is as high as 1.2 eV. Water should therefore desorb thermally from the surface, except at very low oxygen coverages.

The study of oxygen reduction produces adsorption energies for O, OH, H_2O at

different coverages. No apparent correlation is found between the adsorption energies of E_O, E_{OH} and E_{H2O}, see Fig. 2 and Fig. 3 in the supporting material, in contrast to what has previously been observed on metal surfaces, where scaling relations are applicable for OH species on close-packed and stepped surfaces for low coverages [24]. The close packed and stepped surfaces typically have less restructuring during the adsorption of O, OH and H_2O.

On the molybdenum nanocluster surface, larger local restructuring takes place when either O is added or removed and when either O or OH is protonated. The restructuring of the molybdenum cluster involves all atoms in the nanocluster. This is an effect of the small size of the nanocluster, where the local impact from an adsorption or a reduction step influences the whole nanocluster.

The lowest required potential for water formation at the different coverages is in the range of -0.3 V to -0.7 V. These values are lower than the required potential needed to form ammonia on the molybdenum nanocluster [2]. Overall, it seems that it is possible to reduce oxygen of the surface at moderate potential of -0.72 V.

The potential required for reduction of a surface oxygen atom indicates that the nanoclusters can be reactivated after exposure to air or water from the electrolyte or the fabrication process.

Formation of ammonia at relative high oxygen coverage

Nitrogen molecules are not able to adsorb to neither an oxygen vacancy site nor ontop of an oxygen atom at high oxygen coverages. Once the oxygen skin has been partially reduced, the nitrogen molecules adsorb onto the surface at the oxygen vacancy sites, see Fig. 3b. The adsorption of nitrogen become stable at a coverage of less than 10 oxygen atoms, see Table 4. The adsorption energies of N_2 are varying from -1.0 eV to -1.8 eV depending on the oxygen coverage. The corresponding hydrogen adsorption energies are lower, ranging from -0.65 eV to -0.86 eV, and nitrogen molecules are therefore preferred over hydrogen on the surface at zero applied potential. At an applied potential of -0.6 V, which is the potential shown to electrochemically produce ammonia on the clean molybdenum nanocluster, the reaction free energy of adsorbing either a hydrogen atom (coming from H^+ and e^-) or a nitrogen molecule will at certain coverages be in favor of H ($Mo_{13}O_8$ and $Mo_{13}O_6$) and others of N_2 ($Mo_{13}O_9$ and $Mo_{13}O_7$).

Table 4: The adsorption free energies of nitrogen and hydrogen with and without an applied potential on a partly oxygen covered Mo_{13} nanocluster.

	ΔG_{N2} [eV]	ΔG_H [eV]	ΔG_H [eV] (U = -0.6 V)
$Mo_{13}O_{12}$	No binding	-0.23	0.43
$Mo_{13}O_{10}$	0.33	-0.84	-1.44
$Mo_{13}O_9$	-1.82	-0.72	-1.32

$Mo_{13}O_8$	-1.02	-0.75	-1.35
$Mo_{13}O_7$	-1.77	-0.86	-1.46
$Mo_{13}O_6$	-0.93	-0.65	-1.25

For nitrogen molecules adsorbed at a vacancy site on either $Mo_{13}O_9$ or $Mo_{13}O_6$, the potential for driving the electrochemical production of ammonia can be determined. These nanoclusters were selected to describe the two regimes with strong and weak N_2 adsorption compared to hydrogen adsorption, respectively. On the $Mo_{13}O_9$ nanocluster, N_2 is bound most strongly at an applied potential of -0.6 V, while hydrogen is bound stronger on the $Mo_{13}O_6$ nanocluster. Investigations of the associative pathway on the $Mo_{13}O_9$ nanocluster, shows the first protonation step to require an onset potential of -0.7 V. The onset potentials are shown in Fig. 4 for the following electrochemical reaction steps:

$$NN^* + 6(H^+ + e^-) \rightarrow$$

$$NHN^* + 5(H^+ + e^-) \rightarrow$$

$$NH_2N^* + 4(H^+ + e^-) \rightarrow$$

$$NH_3^* + N^* + 3(H^+ + e^-) \rightarrow$$

$$NH_3^* + NH^* + 2(H^+ + e^-) \rightarrow$$

$$NH_3^* + NH_2^* + (H^+ + e^-) \rightarrow$$

$$NH_3^* + NH_3^*$$

The x-axis show the adsorbed reaction intermediate for each protonation step and NH_2N denotes a doubly protonated nitrogen molecule with the N-N backbone intact, while NH_3-NH denotes NH_3 and NH adsorbed on the surface. Five pathways were studied, and all of had the first initial protonation step to be the potential limiting step with identical required onset potentials.

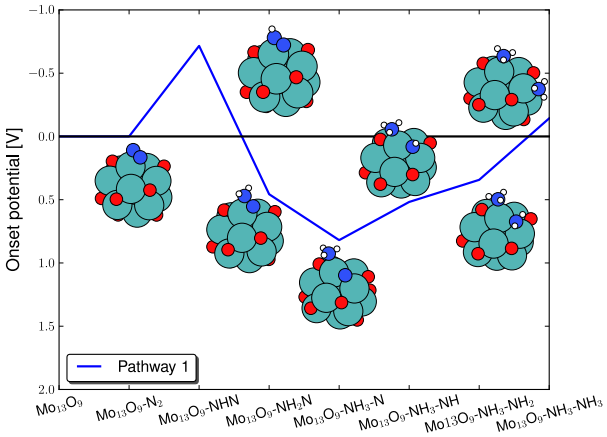

Figure 4: Diagram of the required applied potential to make each reaction step

exergonic for electrochemical ammonia production on the $Mo_{13}O_9$ through the associative mechanism. For all five studied reaction pathways, the highest required potential is -0.7 V for the first protonation step.

For a more reduced oxygen skin, e.g. the $Mo_{13}O_6$ nanocluster, the energetics of the electrochemical production of ammonia are much more diverse. Here, two routes are very favorably, demanding only potentials of around -0.45 V, to drive the electrochemical production of ammonia, see Fig. 5. The routes not shown require potentials of -0.85 V to -1.3 V. The reaction intermediates for the preferred ammonia formation route have been used as the bottom x-axis. The blue filled line on Fig. 5 shows that the rate-limiting step is the last protonation; while for the alternative route, marked with the green dashed line and the corresponding reaction intermediates have been used as the top x-axis in Fig. 5, the rate-limiting steps are found to be both the third and the last protonation step. The limiting step for this reaction path is the formation of the NH_2-NH intermediate on the surface. The reaction is then followed by a very exergonic reaction step, where the N-N bond breaks. In both pathways, the N-N bond breaking in the associative process is very exergonic and no apparent activation barrier is observed for the N-N cleavage at either the third or fourth protonation step. The onset potential presented here for electrochemical ammonia production is similar to those obtained in previous studies on both clean and nitrogen covered molybdenum nanoclusters [2].

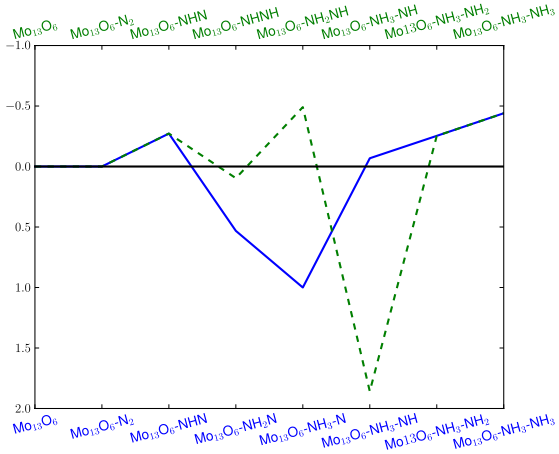

Figure 4: Diagram of the required applied potential to make each reaction step exergonic for electrochemical ammonia production on the $Mo_{13}O_6$ through the associative mechanism. The limiting reaction is the last protonation to form the second ammonia on the surface requiring a potential of -0.45 V to become exergonic.

Instead of protonating the adsorbed nitrogen molecule, the potential could drive the reduction of oxygen. In Table 5, the potentials for driving the oxygen reduction processes are presented. Here, a potential of -0.77 V is required for the high oxygen coverage case, while the last reduction step for the lower oxygen coverage requires significantly larger potentials, i.e. -1.3 V to -1.75 V, to make the reaction exergonic. H_2O is found to be unstable on $Mo_{13}O_6$, while $Mo_{13}O_9$ has a stable adsorption of water.

Table 5: The required potentials for reducing oxygen at two oxygen coverages when nitrogen molecules are present on the partly covered oxygen surfaces.

	$U_{O\rightarrow OH}$ [V]	$U_{OH\rightarrow H2O}$ [V]
$Mo_{13}O_9$-N_2	-0.53	-0.77
$Mo_{13}O_6$-N2	-0.26	-1.30

Competing reaction mechanisms

A procedure to determine the possible reaction pathways on the $Mo_{13}O_9$ nanocluster with N_2 adsorbed with an applied potential U = -0.7 V, such that electrochemical ammonia production is exergonic, is presented. Three possible mechanisms must be considered: the reduction of N_2 to ammonia, hydrogen adsorption and evolution, and last the reduction of oxygen and subsequently formation of water. Here, we assume that the adsorption of H with N_2 present on the surface will be equal to adsorption of H on a surface without N_2 present.

The reaction free energies of forming H, OH, and N_2H at U = -0.7 V are: $\Delta G[N_2{*}+(H^+{+}e^-) \rightarrow N_2H{*}] = 0$ eV, $\Delta G[(H^+{+}e^-) \rightarrow H{*}] = -1.42$ eV, $\Delta G[O{*}+(H^+{+}e^-) \rightarrow OH{*}] = -0.17$ eV, respectively. The reaction step with the lowest reaction free energy is hydrogen adsorption on the surface. For adsorbed hydrogen, the next step will be formation of H_2(g) with a reaction free energies of $\Delta G[H{*}+(H^+{+}e^-) \rightarrow H_2(g)] = 0.02$ eV. The next reaction to occur on the surface will therefore be the reduction O to OH at -0.17 V. For this reaction intermediate, the next reaction will produce H_2O with a reaction free energies of $\Delta G[OH{*}+(H^+ {+}e^-) \rightarrow H_2O{*}] = 0.08$ eV. Small energy differences between the next protonation, but N_2H will be formed on the surface.

The subsequent reaction intermediates for ammonia formation are exergonic at U = -0.7 V. The initial production of an overlayer of H is followed by reduction of O into OH, until the electrochemical reduction of N_2 becomes possible. When the ammonia molecules have desorbed from the surface, adsorption of N_2 is 0.4 eV more stable than H, which would make the adsorption of nitrogen at a vacancy site energetically favorable. At higher pH-values this difference would increase in favour of N_2 adsorption, as given by eq. 1. Because of the very small difference between the formation of N_2H, H_2O and H_2(g) a Faradaic loss due to hydrogen evolution should be expected and a reduction of the oxygen skin on the surface would also be expected at this oxygen coverage and potential.

For the $Mo_{13}O_6$ nanocluster with N_2 adsorbed at an applied potential of U = -0.45 V, the preferred mechanism is the following. First hydrogen is bound to the surface, then O is reduced to OH and then finally the reduction of N_2 can take place. Here, the reaction free energy for production of gas phase hydrogen is $\Delta G[H{*}+(H^+{+}e^-) \rightarrow H_2(g)] = 0.20$ eV and for water formation is $\Delta G[OH+(H^+{+}e^-) \rightarrow H_2O{*}] = 0.59$ eV, while ΔG for all electrochemical reaction steps for ammonia production, see Fig. 5, are zero or lower as in the previous example on the $Mo_{13}O_9$ nanocluster.

In the discussion of the preferential reactions on the $Mo_{13}O_9$ and $Mo_{13}O_6$ nanoclusters, adsorbate-adsorbate interactions are not included due to the large computational cost associated with a comprehensive investigation. This is a

potentially significant assumption, since the adsorption energies may decrease with higher coverage [25]. For hydrogen evolution on the $Mo_{13}O_6$ nanocluster, this could have the consequence that the free energy barrier for producing gas phase hydrogen molecules is lowered.

The results for ammonia production on a partially oxidized molybdenum nanocluster indicates that the formation of ammonia on the molybdenum nanocluster is possible at a low onset potential, but with a low Faradaic efficiency due to the parasitic formation of both adsorbed H or OH on $Mo_{13}O_9$ and $Mo_{13}O_6$. Adsorption of nitrogen seems to hinder the further reduction of OH at lower oxygen coverages. This indicates that the nanocluster should be fully reduced, i.e. no oxygen present on the surface, before nitrogen is able to reach the catalyst surface. Small amounts of oxygen in the form of water may however be present in the electrochemical cell, e.g. from the solid proton conduction electrolyte, without limiting the electrochemical production of ammonia does not seem to be limited at low oxygen coverages.

Conclusions

Density functional theory calculations have been employed to investigate the adsorption and reduction of oxygen on molybdenum nanoclusters. The computational hydrogen electrode was used to determine potentials for reduction of nitrogen and oxygen and the hydrogen evolution reaction.

First, a partially nitrogen covered molybdenum nanocluster was exposed to oxygen and the adsorption of oxygen atoms was shown to be stronger than both hydrogen atoms and nitrogen molecules. The consequence is that the presence of water will lead to preferential oxygen adsorption at the nitrogen vacancy sites. The reduction of the oxygen atoms at the nitrogen rich molybdenum nanocluster was studied, and the potentials more negative than -1.25 V. The main challenge is the second protonation step, where the reaction step is very dependent on the local environment. The oxygen atom will bind to the vacancy site blocking the adsorption of nitrogen molecules and thereby greatly reduce the efficiency of the nitrogen rich molybdenum nanocluster as an electro catalyst for ammonia production through the associative mechanism. A direct reduction of the nitrogen skin will, however, still be possible at -0.6 V.

A clean molybdenum nanocluster in contact with oxygen, hydrogen and nitrogen will preferentially form an oxygen skin. Nitrogen adsorption on an oxygen covered molybdenum nanocluster is impossible, and therefore the reduction of an oxygen overlayer was studied. It was found that the reduction requires potentials of -0.29 V to -0.72 V to successfully produce water from adsorbed oxygen atoms. The desorption of water has low free energy barriers. With oxygen coverage of nine or less oxygen atoms, adsorption of nitrogen and hydrogen becomes possible. The electrochemical production of ammonia for adsorbed nitrogen molecules at partial oxygen coverage will only require potentials of -0.45 V to -0.7 V to make the reaction exergonic. These onset potentials are similar to values reported in earlier studies of electrochemical ammonia production on molybdenum nanocluster with or without a nitrogen skin [2]. At the potentials needed to make the ammonia production exergonic, hydrogen is found to be present on the surface, and a reduction of oxygen to OH is observed, before electrochemical production of ammonia is possible.

On the basis of the work presented here, we propose that molybdenum nanoclusters can be re-activated for ammonia production by electrochemical reduction of the adsorbed oxygen resulting from, e.g. the presence of water in the solid electrolyte, at a potential of approximate -0.7 V.

Supporting Information

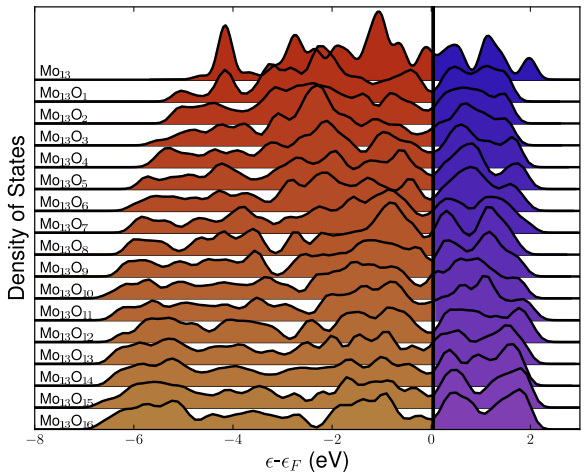

Figure 1: The d-band of molybdenum nanoclusters as the oxygen coverage evolves.

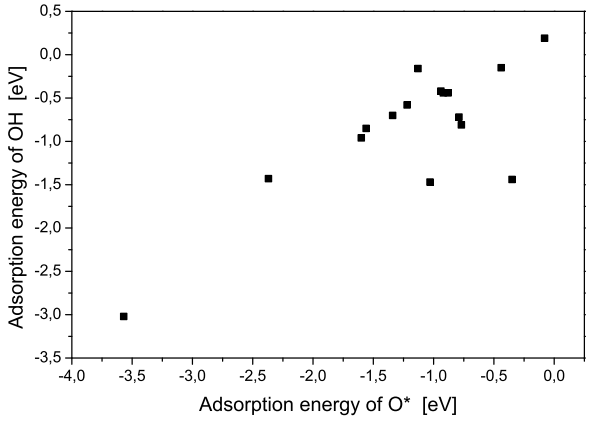

Figure 2: The adsorption energy of OH plotted as a function of adsorption energy of O for the oxygen covered molybdenum nanoclusters.

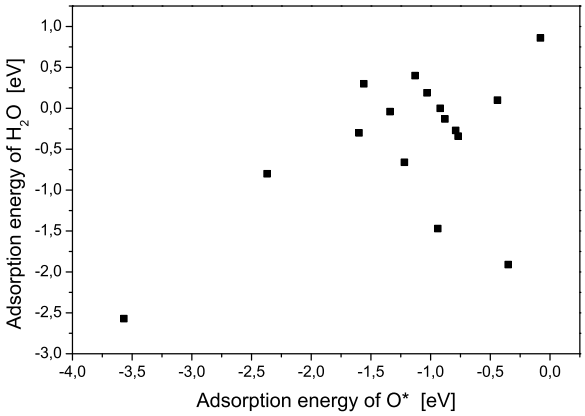

Figure 3: The adsorption energy of H_2O plotted as a function of adsorption energy of O for the oxygen covered molybdenum nanoclusters.

Acknowledgements

The authors would like to acknowledge the Danish Center for Scientific Computing for supercomputer access. The Catalysis for Sustainable Energy (CASE) initiative is funded by the Danish Ministry of Science, Technology and Innovation.

References

. [1] Howalt, J. G.; Bligaard, T.; Rossmeisl, J.; Vegge, T. *Phys. Chem. Chem. Phys.,* 2013, *15*, 7785-7795.

. [2] Howalt, J. G.; Vegge, T. *Phys. Chem. Chem. Phys.*, in press.

. [3] Sone, Y.; Ekdunge, P.; Simonsson, D. *J. Electrochem. Soc.,* 1996, *143,* 1254-1259

. [4] Kreuer, K.-D.; Paddison, S.; Spohr, E.; Schuster, M. *Chem. Rev.* 2004, *104*, 4637-4678

. [5] Fastrup, B.; Nygård Nielsen, H. *Catalysis Letters* 1992, *14*, 233-239.

. [6] Kuchaev, V.; Shapatina, E.; Avetisov, A. *Russian Journal of Electrochemistry,* 2009*, 45*, 983-995.

. [7] Hohenberg, P.; Kohn, W. *Physical Review*, 1964, *136(3B)*, B864-B871.

. [8] Kohn, W.; Sham, L. J. *Physical Review* 1965, *140(4A)*, A1133-A1138.

. [9] Hammer, B.; Hansen, L.; Nørskov, J. *Phys. Review* 1999, *59*, 7413-7421.

. [10] Blöchl, P. E. *Physical Review B* 1994, *50*, 17953-17979.

. [11] Blöchl, P. E.; Först, C. J.; Schimpl, J. *Bulletin of Materials Science* 2003, *26*, 33-41.

. [12] Mortensen, J. J.; Hansen, L. B.; Jacobsen, K. W. *Physical Review B* 2005, *71,* 035109.

. [13] Enkovaara, J. *Journal of Physics: Condensed Matter*, 2010, *22,* 253202.

. [14] The GPAW code is available as a part of the CAMPOS software: http://www.camd.dtu.dk/Software.

. [15] Monkhorst, H.; Pack, J. *Physical Review B,* 1976, *13*, 5188-5192.

. [16] The ASE code is available as a part of the CAMPOS software: http://www.camd.dtu.dk/Software.

. [17] Bitzek, E.; Koskinen, P.; Gähler, F.; Moseler, M.; Gumbsch, P.; *Physical Review Letters* 2006, *97*, 170201.

. [18] Skúlason, E.; Bligaard, T.; Gudmundsdottir, S.; Studt, F.; Rossmeisl, J.; Abild-Pedersen, F.; Vegge, T.; Jónsson, H.; Nørskov, J. *Phys. Chem. Chem. Phys.* 2012, *14*, 1235-1245.

. [19] Heyrovski, J. *Recueil des Travaux Chimiques des Pays-Bas* 1927, *46*, 582-585.

. [20] Rossmeisl, J.; Logadottir, A.; Nørskov, J. Chem. Phys. 2005, *319*, 178-184.

. [21] Rossmeisl, J.; Qu, Z.-W.; Kroes, G.-J.; Nørskov, J. *Journal of Electroanalytical Chemistry* 2007, *607*, 83-89.

. [22] Hummelshøj, J.; Blomquist, J.; Datta, S.; Vegge, T.; Rossmeisl, J.; Thygesen, K.; Luntz, A.; Jacobsen, K.; Nørskov, J. *Journal of Chemical Physics* 2010, *132*, 071101.

. [23] Nørskov, J. K.; Rossmeisl, J.; Logadottir, A.; Lindqvist, L.; Kitchin, J. R.; Bligaard, T.; Jónsson, H. *Journal of Physical Chemistry B* 2004, *108*, 17886-17892.

. [24] Abild-Petersen, F.; Greeley, J.; Studt, F.; Rossmeisl, J.; Munter, T. R.; Moses, P.; Skúlason, E.; Bligaard, T.; Nørskov, J. K. *Physical Review Letters* 2007, *99*, 016105-016108.

. [25] Getman, R. B.; Schneider, W. F. *ChemCatChem* 2010, *2*, 1450-1460.

.